Development of advanced electrode materials for high-performance supercapacitors

Dongwei Du

A thesis submitted in fulfilment of the requirements for the degree of Doctor of Philosophy
in the

University of Warwick

Supervised by:
Prof. Shanwen Tao

January 2018

Contents

List of Figures

List of Tables

List of Schemes

Acknowledgements

Firstly, I would like to express my sincere thanks to my supervisor Prof. Shanwen Tao, for his invaluable supervision, guidance and motivation throughout the PhD study. Without his support and encouragement, it is impossible to complete this work.

I would like to thank all the group members, ex-group members and colleagues, Dr. Rong Lan, Dr. Wei Xu, Dr. Sivaprakash Sengodan, Mr. John Humphreys, Mr Shigang Chen, Dr. Maoshuai Li and Dr. Guannan Hu, for their help and meaningful discussions, which inspire me a lot. I would also like to thank Dr. Shangfeng Du, my master's supervisor, without his encouragement, I may not start this PhD.

Thanks to the chemical engineering staff: Prof. Andre C. van Veen, who is my progress reviewer during the PhD, for giving me many constructive advices; our technician Mr. John Piller, for his technical support in solving the instrument issues and making proper units for my experiments.

I would like to thank my friends, Mr Zaicheng Wang, Dr. Yidong Zhang, Mr. Xiaojun Guo, Mr. Jiachuan Tian, Mr. Yaochen Song, Mr. Yiqiang Yang, Miss Fan Yang, for their support and encouragement when I am down. It's so lucky to know them in my life.

Last but not least, a special thanks to my family, especially my parents, for their unconditional love, support and encouragement all the time. They always support me and respect my choice.

Declaration

The work reported in this PhD thesis is the original work of the author and has not been published elsewhere except for the following publications.

Publication List

1. **Du, D.**, Lan, R., Humphreys, J., Amari H., & Tao, S. (2018) Preparation of nanoporous nickel-copper sulfide on carbon cloth for high-performance hybrid supercapacitors. *Electrochimica Acta, 273*, 170-180.

2. **Du, D.**, Lan, R., Humphreys, J., Xu, W., Xie, K., Wang, H., & Tao, S. (2017). Synthesis of $NiMoS_4$ for high-performance hybrid supercapacitors. *Journal of The Electrochemical Society*, *164*(12), A2881-A2888.

3. **Du, D.**, Lan, R., Xie, K., Wang, H., & Tao, S. (2017). Synthesis of $Li_2Ni_2(MoO_4)_3$ as a high-performance positive electrode for asymmetric supercapacitors. *RSC Advances*, *7*(22), 13304-13311.

4. **Du, D.**, Lan, R., Humphreys, J., & Tao, S. (2017). Progress in inorganic cathode catalysts for electrochemical conversion of carbon dioxide into formate or formic acid. *Journal of Applied Electrochemistry*, 1-18.

5. **Du, D.**, Lan, R., Xu, W., Beanland, R., Wang, H., & Tao, S. (2016). Preparation of a hybrid $Cu_2O/CuMoO_4$ nanosheet electrode for high-performance asymmetric supercapacitors. *Journal of Materials Chemistry A*, *4*(45), 17749-17756.

6. **Du, D.**, Lan, R., Humphreys, J., Sengodan, S., Xie, K., Wang, H., & Tao, S. (2016). Achieving both high selectivity and current density for CO_2 reduction to formate on nanoporous tin foam electrocatalysts. *ChemistrySelect*, *1*(8), 1711-1715.

7. Xu, W., **Du, D.**, Lan, R., Humphreys, J., Wu, Z., & Tao, S. (2017). Highly active Ni–Fe double hydroxides as anode catalysts for electrooxidation of urea. *New Journal of Chemistry*, *41*(10), 4190-4196.

8. Xu, W., **Du, D.**, Lan, R., Humphreys, J., Miller, D. N., Walker, M., Wu, Z., Irvine, J. T. S., & Tao, S. (2016). Electrodeposited NiCu bimetal on carbon paper as stable non-noble anode for efficient electrooxidation of ammonia. *Applied Catalysis B: Environmental*.

9. Xu, W., Lan, R., **Du, D.**, Humphreys, J., Walker, M., Wu, Z., & Tao, S. (2017). Directly growing hierarchical nickel-copper hydroxide nanowires on carbon fiber cloth for efficient electrooxidation of ammonia. *Applied Catalysis B: Environmental*, *218*, 470-479.

10. Humphreys, J., Lan, R., **Du, D.**, Xu, & Tao, S. Promotion effect of proton-conducting oxide $BaZr_{0.1}Ce_{0.7}Y_{0.2}O_{3-\delta}$ on the catalytic activity of Ni towards ammonia synthesis from hydrogen and nitrogen. *International Journal of Hydrogen Energy*. (In press)

11. Sengodan, S., Lan, R., Humphreys, J., **Du, D.**, Xu, W., Wang, H., & Tao, S. (2018). Advances in reforming and partial oxidation of hydrocarbons for

hydrogen production and fuel cell applications. *Renewable and Sustainable Energy Reviews*, *82*, 761-780.

12. Cowin, P. I., Lan, R., Petit, C. T., **Du, D.**, Xie, K., Wang, H., & Tao, S. (2017). Conductivity and redox stability of new perovskite oxides $SrFe_{0.7}TM_{0.2}Ti_{0.1}O_{3-\delta}$ (TM= Mn, Fe, Co, Ni, Cu). *Solid State Ionics*, *301*, 99-105.

Abstract

The demand for high-performance electrochemical energy storage devices is ever-growing as they are critical components for portable electronics, electric vehicles, and efficient storage media for energy from renewable sources. Electrochemical capacitors (also called supercapacitors) are emerging as one of the most promising candidates due to their rapid charge rate, high power density, good rate capability and excellent lifespan. However, their usage is significantly limited by the disadvantages of low energy density. The main aim of this work is to develop advanced electrode materials for supercapacitors with improved energy density while maintaining high power density and long cycle life.

In this thesis, we have developed four novel electrode materials based on the transition metals of Ni and Cu for supercapacitor applications, including the metal oxides ($Li_2Ni_2(MoO_4)_3$ and $Cu_2O/CuMoO_4$) and metal sulfides ($NiMoS_4$-A and Ni-Cu-S). These materials were prepared via different techniques, such as combustion, chemical co-precipitation and hydrothermal. Their physical properties were characterized by X-ray diffraction (XRD), scanning electron microscope (SEM) and transmission electron microscopy (TEM) etc. Their electrochemical behaviours were evaluated by cyclic voltammetry (CV), galvanostatic charge-discharge (GCD) and cycling stability etc. To further measure the performance in practical energy storage devices, the materials were tested with a two-electrode configuration. All the four materials were used as positive electrodes, which were paired with proper activated carbon (AC) or nitrogen-doped graphene (NG) negative electrodes to assemble asymmetric supercapacitors (ASCs).

At a current density of 1 A g^{-1}, the $Cu_2O/CuMoO_4$ electrode exhibits a high specific capacitance of 4264 F g^{-1}, superior to the1137 F g^{-1} of the $Li_2Ni_2(MoO_4)_3$, 706.5 F g^{-1} of the $NiMoS_4$-A, and 938.6 F g^{-1} of the Ni-Cu-S. In terms of the ASCs, the $Cu_2O/CuMoO_4$//AC ASC could expand the operation voltage to 1.7 V, at which the energy density can reach 75.1 Wh kg^{-1} with a power density of 420 W kg^{-1}. The $NiMoS_4$-A//AC ASC displays a high energy density of 35 Wh kg^{-1} at an average power density of 400 W kg^{-1}. Meanwhile, it exhibits excellent cycle stability, maintaining 82% of the initial capacitance after 10000 charge-discharge cycles at 5 A g^{-1}. These good results suggest that the developed materials are promising for high-performance supercapacitor applications.

Abbreviations

AC	Activated carbon
ACN	Acetonitrile
AGM	Absorbent glass mat
ALD	Atomic layer deposition
ASC	Asymmetric supercapacitor
BET	Brunauer–Emmett–Teller
C_A	Areal capacitance
C_s	Specific capacitance
CE	Counter electrode
CNT	Carbon nanotube
CP	Conducing polymer
CV	Cyclic voltammetry
CVD	Chemical vapor deposition
DEC	Diethyl carbonate
DMC	Dimethyl carbonate
DME	Dimethoxyethane
DSC	Differential scanning calorimetry
E	Energy density
EC	Ethylene carbonate
EDL	Electrical double-layer
EDLC	Electrical double-layer capacitor
EDX	Energy-dispersive X-ray spectroscopy
EIS	Electrochemical impedance spectroscopy
EMI-TFSI	ethyl-methylimmidazolium-bis(trifluoromethane-sulfonyl)imide
ESM	Eggshell membrane
FESEM	Field emission scanning electron microscopy
GCD	Galvanostatic charge-discharge
GNS	Graphene nanosheets
GO	Graphene oxide
HRTEM	High-resolution transmission electron microscopy
HSC	Hybrid supercapacitor

I	Current
m	Mass
MWCNT	Multi-walled carbon nanotube
ND	Nanodiamond
NG	Nitrogen-doped graphene
NHE	Normal hydrogen reference electrode
P	Power density
PANI	Polyaniline
PC	Propylene carbonate
PE	polyethylene
PEDOT	Poly(3,4-ethylenedioxythiophene)
PEO	Polyethyleneoxide
PP	Polypropylene
PPy	Polypyrrole
PTFE	Polytetrafluoroethylene
PVA	Poly-(vinyl alcohol)
RE	Reference electrode
R_{ct}	Charge transfer resistance
R_s	Equivalent series resistance
rGO	Reduced graphene oxide
sat.	Saturated
SCE	Saturated calomel electrode
SEM	Scanning electron microscope
SHE	Standard hydrogen electrode
SSC	Symmetric supercapacitor
SWCNT	Single-walled carbon nanotube
t_c	Charging time
t_D	Discharging time
Δt	Time change
$TEABF_4$	Tetraethylammonium tetrafluoroborate
TEM	Transmission electron microscopy
TG	Thermogravimetric analysis
XRD	X-ray diffraction

UGF	Ultrathin-graphite foam
UV-Vis	Ultraviolet–visible
V	Cell voltage
ΔV	Potential change
WE	Working electrode
W_o	Warburg impedance
v	Scan rate

CHAPTER 1 Introduction

1.1 Background

Energy and power demands keep increasing year by year due to the fast development of the world. Traditional energy supply is mainly based on the combustion of fossil fuels which causes many environmental issues, such as global warming and sea level rise [1]. On the other hand, the availability of fossil fuels is decreasing. As a consequence, extensive research efforts have been dedicated to developing clean and renewable energy resources, such as solar, wind and wave [2]. However, energy generated from these sources are usually in the form of electricity, and the places with sufficient resources are usually far away from the areas with high energy demand. Therefore, it is of great importance to harvest the energy in combination with efficient electrical energy storage technologies. In addition to the industrial level energy management, the electrical energy storage systems are also critical components for portable electronics and electric vehicles in daily life [3].

Rechargeable batteries are considered as the promising energy storage devices. However, the power density and cycling life of batteries (e.g. Nickel metal hydride batteries and Li-ion batteries) are limited by the materials used, which are less effective to fulfil today's requirements [4]. In contrast, electrochemical capacitors, also known as supercapacitors, have attracted significant attention in recent years due to their rapid charge-discharge rate, high powder density, and outstanding life span [5]. Fig.1.1 demonstrates the power and energy density of various electrical energy storage devices [6]. Supercapacitors can bridge the gap between conventional capacitors and batteries, and they are also crucial for complementing or replacing batteries under some circumstances especially when high power is needed with short duration, such as flash light in cameras, and back-up power for electric vehicle during acceleration [3].

Although supercapacitors are promising candidates for many high power applications, their usage is significantly limited by the disadvantages of low energy density. Consequently, it is necessary to develop high power supercapacitors

without sacrificing the power density and cycling life [7]. As is known, the energy density (E) of a supercapacitor is determined by its specific capacitance (C) and cell voltage (V) according to the following equation [8]:

$$E = \frac{1}{2}CV^2 \tag{1.1}$$

Accordingly, two efficient strategies are proposed to improve the energy density: one is to discover novel electrode materials, or to make the existing materials with different nanostructures to achieve high capacitance; the other is to increase the overall cell voltage [9].

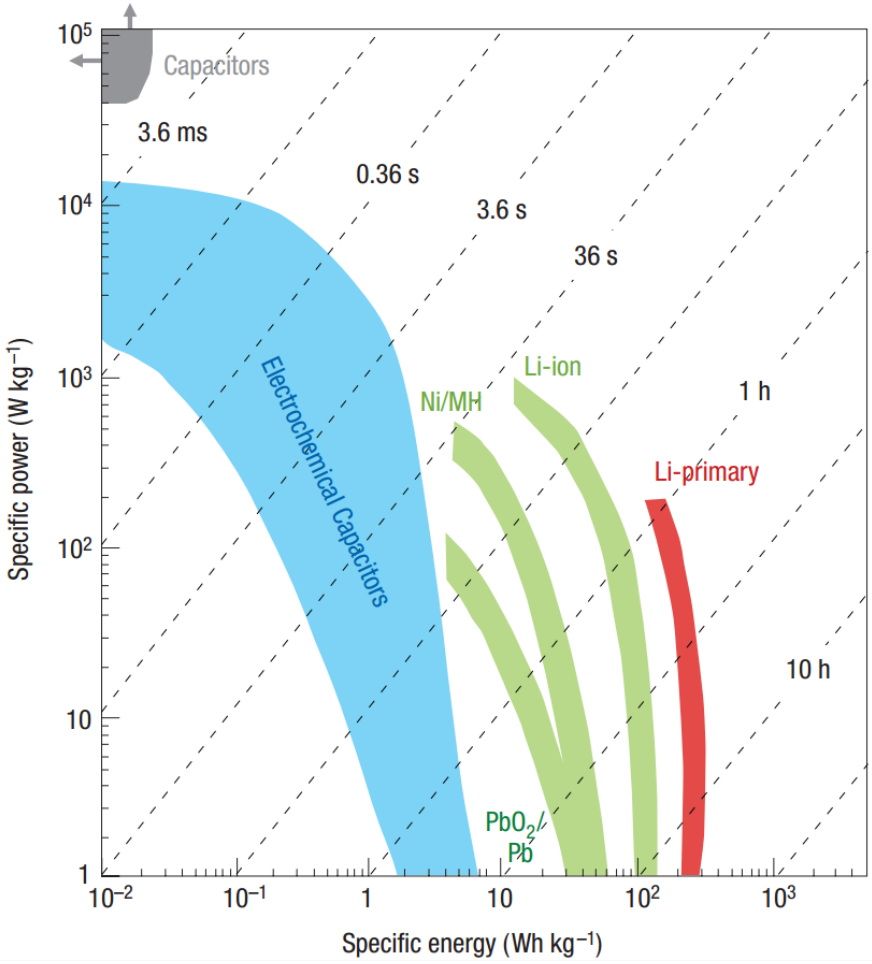

Fig. 1.1 Specific power against specific energy, also called a Ragone plot, for various electrical energy storage devices [6].

During the past decades, many efforts have been made to explore new materials for supercapacitors. The commonly studied materials are high surface area carbon [10, 11], transition metal oxides [12, 13] and conducting polymers [14, 15]. Currently, only a few of carbon-based materials are commercially available while

they can only provide a low energy density of 3-4 Wh kg^{-1} [3]. Due to the different energy storage mechanisms (details will be introduced in chapter 2), transition metal based materials could exhibit higher energy density [16, 17], therefore, further research should be conducted to make them meet the requirements of practical application.

1.2 Research aims and objectives

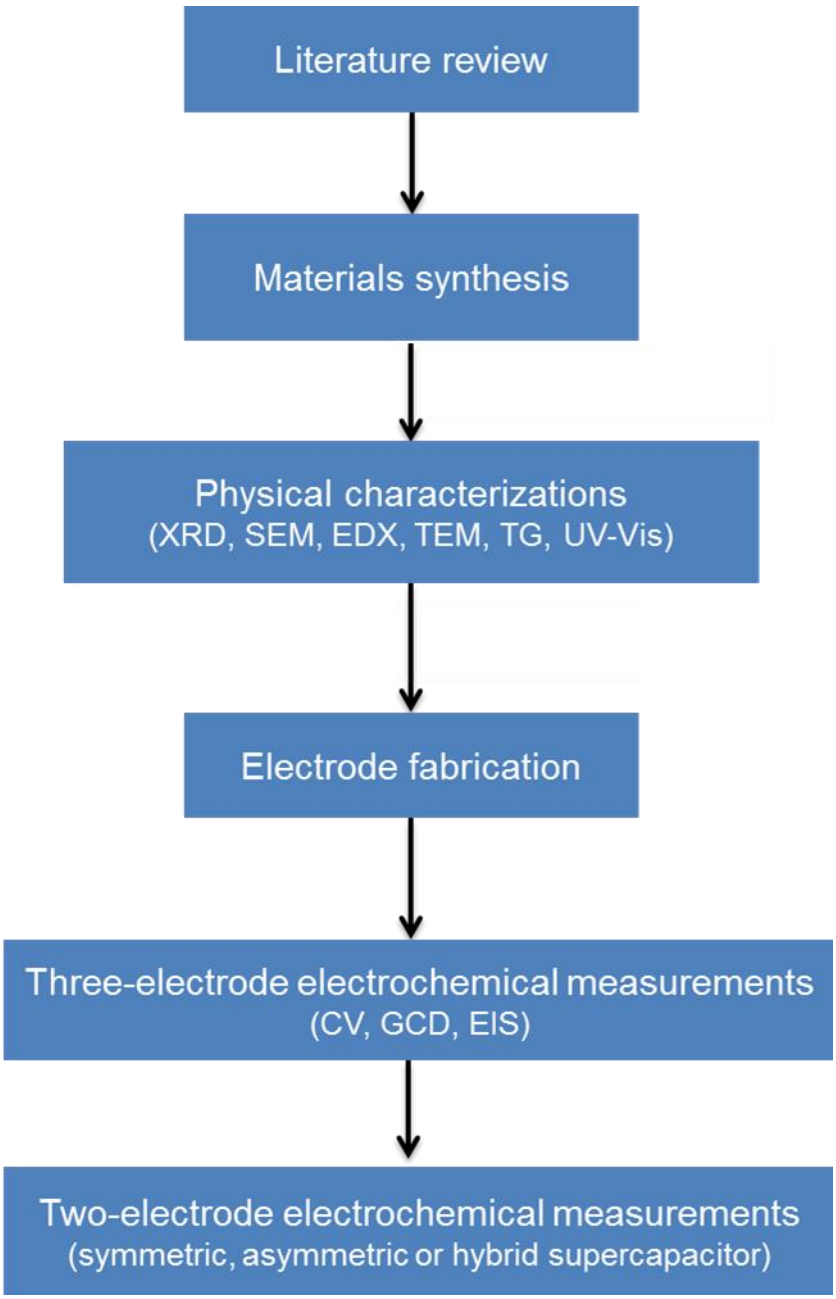

Scheme 1.1 Schematic illustration of methodology.

As discussed above, the main challenge for supercapacitors is to improve their energy density while maintaining the properties of high power density and long cycle life, and the feasible method is to enhance the capacitance and cell voltage according to equation 1.1. Wider operation potential window of supercapacitors can be provided by using organic or ionic based electrolytes. However, these electrolytes are only suitable for some specific type of materials such as carbon materials [18]. Additionally, they are usually expensive, volatile, flammable and toxic which limit the wide applications. Another promising approach is to fabricate asymmetric supercapacitors (ASCs) which can broaden the cell voltage in aqueous electrolyte. Since the electrode material plays a key role in determining the performances of a supercapacitor, the main aim of this thesis is to develop advanced electrode materials for high-performance supercapacitors in aqueous electrolytes. To pursue good electrochemical performance for supercapacitors, most of the materials prepared in this research are nanostructured. It is important to apply appropriate techniques to evaluate their physical and electrochemical characterisations. A general description of procedures to investigate the materials is illustrated in Scheme 1.1.

- Firstly, synthesize active materials via a designed technique, such as hydrothermal, chemical co-precipitation etc.
- Secondly, characterize physical properties of the prepared materials with a variety of methods, including X-ray diffraction (XRD), scanning electron microscope (SEM), energy-dispersive X-ray spectroscopy (EDX), transmission electron microscopy (TEM), thermogravimetric analysis (TG) and ultraviolet–visible (UV-Vis) spectroscopy.
- Next, prepare the working electrode based on the active materials: mix the active materials with conducting reagent and binder, and then coat them onto a conductive substrate; directly use the self-support materials as electrodes.
- Evaluate the electrochemical behaviours of the fabricated electrode by cyclic voltammetry (CV), galvanostatic charge-discharge (GCD) and electrochemical impedance spectroscopy (EIS) in a three-electrode system.
- Finally, further test the electrode in a practical energy storage device with a two-electrode configuration. Specifically, pair the electrode with a negative

electrode to assemble a symmetric or asymmetric supercapacitor. Measure the CV, GCD and cycling stability performances.

1.3 Organization of the thesis

The structure of this thesis is summarized as follows.

Chapter 1 provides the background information and research aims of this thesis.

Chapter 2 reviews charge storage mechanisms for supercapacitors, electrode materials discussed in existing literatures (carbon-based materials, metal oxides/hydroxides, metal nitrides, metal sulfides and conducting polymers), electrolytes, and supercapacitor configurations.

Chapter 3 briefly introduces the fundamentals of the applied physical and electrochemical characterization methods involved in this thesis. Specifically, the physical techniques are XRD, SEM, EDX, TEM, TG and UV-Vis, and the electrochemical measurements includes CV, GCD and EIS.

Chapter 4 describes the fabrication of activated carbon (AC) and nitrogen-doped graphene (NG) electrodes. Their capacitive performances are investigated with a three-electrode system and a two-electrode system (symmetric supercapacitor) respectively. AC and NG are used as the negative electrode materials for chapter 5-8.

Chapter 5 focuses on the synthesis of a NASICON-type metal oxide $Li_2Ni_2(MoO_4)_3$. General characterizations of the compound are conducted, including morphology, thermal stability and charge storage performance in aqueous LiOH and NaOH electrolytes.

Chapter 6 introduces a hypothermal method to prepare a nanostructured metal oxide composite of $Cu_2O/CuMoO_4$. Its physical properties and electrochemical behaviours as a positive electrode for supercapacitors are investigated.

Chapter 7 describes the synthesis of a nickel-molybdenum sulfide compound ($NiMoS_4$) using a co-precipitation method. The supercapacitor performances of materials with and without calcination process are compared.

In Chapter 8, nanoporous nickel-copper sulfide supported on carbon cloth are prepared by sulfurizing the nickel-copper carbonate hydroxide precursor through an anion exchange reaction. Physical and electrochemical properties of the electrode are explored.

Chapter 9 summarises the major contributions of the thesis and compared the four positive electrode materials from different aspects. Future works for the supercapacitors is suggested based on the present findings.

CHAPTER 2 Literature review

2.1 Energy storage mechanisms for batteries and supercapacitors

As we introduced in chapter 1, batteries and supercapacitors are two major technologies for electrochemical energy storage at present. The capacity of the secondary batteries originates from intercalation/de-intercalation of ions in the crystalline structure of electrode materials which is usually achieved via redox reactions. For instance, the charge-discharge of the conventional lithium-ion batteries work on the principle of intercalation/de-intercalation of Li ions [19, 20]. $LiCoO_2$ is a common cathode material for lithium-ion batteries. During the charge process, Li ions are extracted from the crystalline framework to convert $LiCoO_2$ into Li_xCoO_2, while a reversible process occurs during discharging. It should be noted that phase change of the electrode material is involved in the intercalation/de-intercalation process and the charge storage is determined by the ions diffusion.

As for the supercapacitors, the capacitance is mainly involved in the reactions in the surface region, and they can be classified into two categories according to the charge storage mechanisms: electrical double-layer capacitors (EDLCs) and pseudocapacitors.

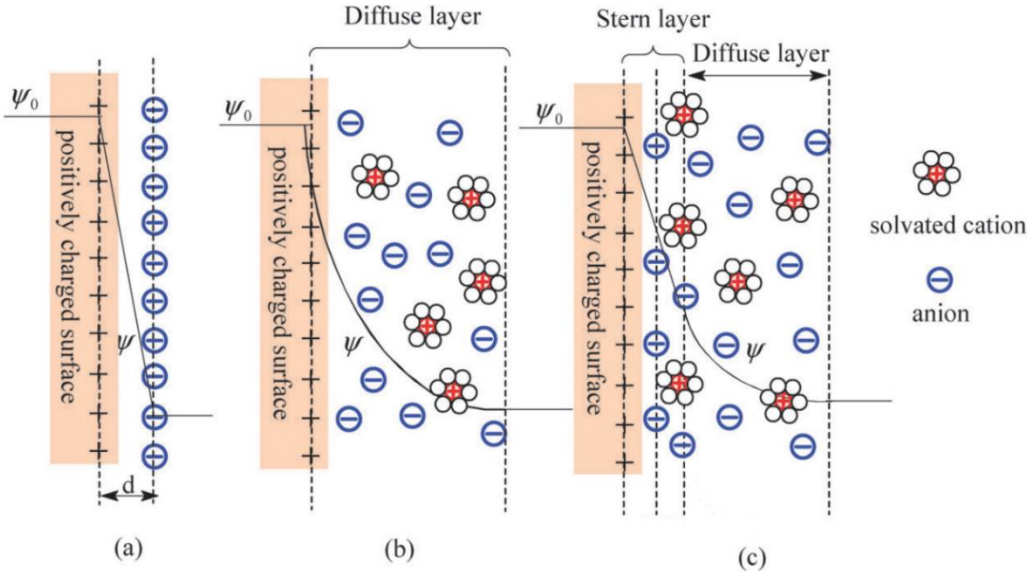

Fig. 2.1 Models of the electrical double layer at a positively charged surface [10]: (a) the Helmholtz model, (b) the Gouy–Chapman model, and (c) the Stern model.

EDLCs store charges via electrostatically adsorption/desorption of the electrolyte ions at the electrode/electrolyte interface. The electrical double-layer (EDL) model was firstly developed by von Helmholtz in the 19th century [21], and he supposed that the opposite charges were separated at electrode/electrolyte interface in an atomic distance (Fig. 2.1a). In consideration of the distribution of electrolyte ions in the electrolyte, Gouy and Chapman improved the model by introducing a diffuse layer (Fig. 2.1b) [22]. However, the Gouy-Chapman model failed to explain highly charged EDLs. Later, Stern combined the two models, giving two layers to describe the ion distribution, the internal stern layer and the diffuse layer (Fig. 2.1c) [23], which is commonly accepted at present. The capacitance of the EDL (C_{dl}) can be considered as a combination of the stern type capacitance (C_H) and the diffuse layer type capacitance (C_{diff}), following the equation [10]:

$$\frac{1}{C_{dl}} = \frac{1}{C_H} + \frac{1}{C_{diff}} \tag{2.1}$$

The EDL behaviours are demined by a lot of factors such as the electrode surface, the type of electrolyte ions, the solvent, etc [10].

The capacitance of an EDLC is similar to a parallel plate capacitor. Therefore its specific capacitance can be described as [8, 24]:

$$C = \frac{\varepsilon_r \varepsilon_0 A}{d} \tag{2.2}$$

where ε_r is the dielectric constant of the electrolyte, ε_0 is permittivity of the vacuum, A is the specific surface area of the electrode, and d is the effective distance between the ions and the electrode, which is also known as Debye length with an extremely small length of 6-10 Angstroms. Based on equation 2.2, we can predict that larger capacitance will be achieved with larger surface area and there should be a linear relationship between them. However, the capacitance is not simply linear to the surface area since the solvated ions cannot access the micropores at small size, which inhibits the formation of double layer. Besides the large surface area, high conductivity is another key factor to reach high capacitance for the electrode. Therefore, carbon-based materials with high surface area have been widely used as active materials for EDLCs [25-27]. As no faradaic process is involved in the EDLCs, destruction caused by phase change or swelling rarely occurs for the active materials, leading to a long cycle life.

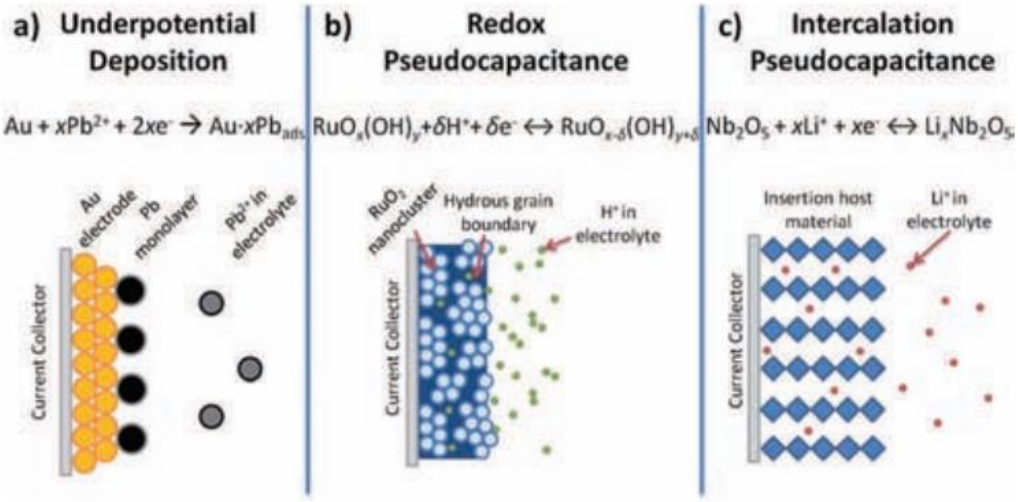

Fig. 2.2 Different types of mechanisms that can produce pseudocapacitance: (a) underpotential deposition, (b) redox pseudocapacitance, and (c) intercalation pseudocapacitance [28].

On the contrary, for the pseudocapacitors, the energy storage capability is associated with the fast and reversible faradaic reaction between the electrolyte and the active species on the electrode surface at characteristic potentials. The ions in the electrolyte pass the double layer, interacting with the atoms in the electrode surface. Fig. 2.2 illustrates three different types of redox mechanisms that can generate pseudocapacitance [28]: (a) underpotential deposition, (b) redox pseudocapacitance, and (c) intercalation pseudocapacitance. Underpotential deposition is a phenomenon of reduction of metal cations onto a different metal's surface at a less negative potential (compared with its redox potential). Monolayer of lead adsorbed on the gold surface is a typical example. Redox pseudocapacitance is produced through electrochemically adsorption of ions onto the electrode surface accompanied by a faradaic charge-transfer. In intercalation pseudocapacitance case, ions intercalate into the crystalline structure of the active materials, coupled with faradaic charge-transfer but no phase change. These three mechanisms vary from different kinds of materials, but the relationship between the potential and the charge stored at the electron/electrolyte interface for all of them follows [29]:

$$E \sim E^0 - \frac{RT}{nF} In(\frac{X}{1-X}) \tag{2.3}$$

where E is the potential (V), R is the ideal gas constant (8.314 $J \cdot mol^{-1} \cdot K^{-1}$), T is the absolute temperature (K), n is the number of electrons, F is the Faraday constant (96485 $C \cdot mol^{-1}$), and X is the fractional coverage of the surface. The capacitance (C, F g^{-1}) can be expressed as [28]:

$$C = (\frac{nF}{m})\frac{X}{E} \tag{2.4}$$

where m is the molecular weight of the active material. As X is not always proportional to E, the capacitance is not constant. The most common pseudocapacitive materials are conducting polymers (e.g., polypyrrole (PPy), polyaniline (PANI)) and transition metal oxides such as MnO_2 RuO_2 and Fe_3O_4. Since the faradaic processes are involved in pseudocapacitors, they usually possess higher specific capacitance and energy density but lower power density (faradaic process is slower than non-faradaic process) and stability compared with EDLCs.

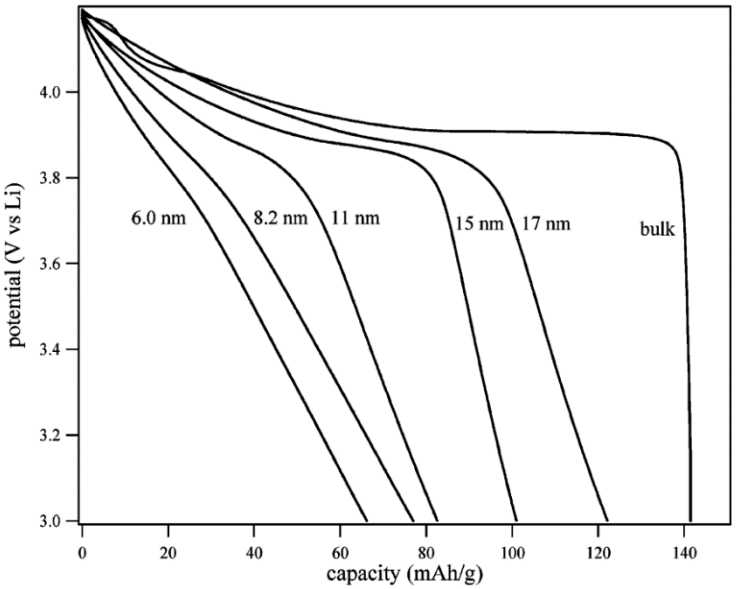

Fig. 2.3 The effect of crystallite size for discharge curves of $LiCoO_2$ [30].

As mentioned above, both battery-type materials and pseudocapacitive materials store charges via faradaic reactions. It is believed that battery-type materials usually display voltage plateau in the charge-discharge curves while pseudocapacitive materials exhibit a linear trend between the amount of charge stored and the charging potential [9]. However, the boundary between battery-type materials and pseudocapacitive materials is not very clear. For example, $LiCoO_2$ is a typical battery-type material, exhibiting voltage plateau at bulk state (Fig. 2.3) [30]. When the particle size reduces to 17 nm or less, the voltage plateau is

gradually fading out over the entire discharge process. With the particle size at 6 nm, it performs an almost linear discharge curve (Fig. 2.3) This fact indicates that pseudocapacitance can emerge when a battery-type material is at nano-size scale. In addition to $LiCoO_2$, many other battery materials, such as Ni/Co oxides/hydroxides [31, 32], MoO_3 [33, 34], and Bi_2O_3 [35] have also been investigated as electrode materials for pseudo-supercapacitors.

It is supposed that cyclic voltammetry (CV) measurement could provide insights into the kinetic properties of a material. Basically, the current response of an electrode at various scan rates follows the equation [34, 36]:

$$i = av^b \tag{2.5}$$

where i is the measured current response, v is the scan rate, and a and b are adjustable parameters. This means the current at a fixed potential has a power law dependence on the scan rate. Since the kinetic properties of battery-type materials and pseudocapacitive materials are different, specifically, battery-type materials are controlled by diffusion process while pseudocapacitive materials are not. For typical battery materials, $b = 0.5$, the current represents the diffusion-controlled faradaic component. For the capacitive or pseudocapacitive behaviour, the current is linear to the scan rate and the value of b equals to 1. However, recently studies found that many materials cannot be simply classified as either battery or capacitor, and the two charge storage mechanisms contribute together to the overall performance. In this respect, the current at a fixed potential can be treated as a combination of surface capacitive effect ($k_1 v$) and diffusion-controlled faradaic effect ($k_2 v^{1/2}$), which can be expresses as [37]:

$$i = k_1 v + k_2 v^{1/2} \tag{2.6}$$

or

$$i/v^{1/2} = k_1 v^{1/2} + k_2 \tag{2.7}$$

where v is the scan rate. By degerming the values of k_1 and k_2, it is possible to work out the specific current contribution at each potential. Furthermore, the fraction of the charge stored from capacitive effect and diffusion-controlled faradaic process could be extracted quantitatively.

2.2 Electrode materials

2.2.1 Carbon-based materials

It is well known that that carbon materials have been frequently used as EDLC electrode for supercapacitors due to the advantages of abundance, low cost, non-toxicity, high conductivity, high specific surface area, high chemical stability, and wide operating temperature range [38]. Various carbon materials have been studied for supercapacitors, such as activated carbon (AC), carbon nanotubes (CNTs), carbon aerogels, and graphene.

2.2.1.1 Activated carbon (AC)

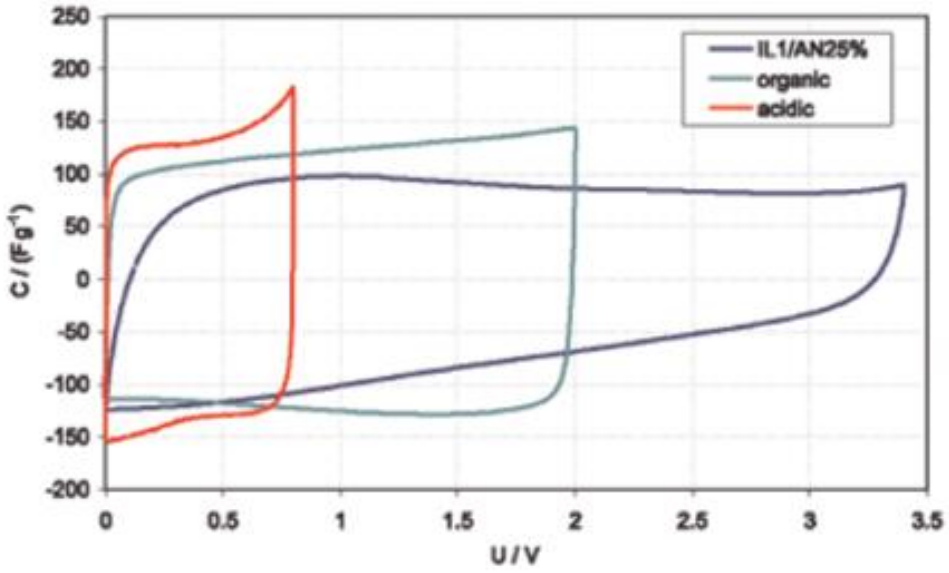

Fig. 2.4 CV curves of AC in three different electrolytic media at 5 mV s^{-1} [39].

AC is the most widely used carbon material. AC usually possesses large specific surface area more than 2000 m^2 g^{-1} and offers a capacitance of 100-300 F g^{-1} in aqueous electrolyte and less than 150 F g^{-1} in organic electrolyte. Fig. 2.4 shows the typical CV behaviours of AC in different electrolytes: aqueous, organic and ionic liquid (IL) [39]. As the charge is accumulated at the electrode/electrolyte interface, the specific capacitance of AC depends on the specific surface area. However, the specific capacitance is not always proportional to the specific surface area because of the broad pore size distribution of AC, which are micropores (<2

nm), mesopores (2-50 nm), macropores (> 50 nm) [40, 41]. Kierzek *et al.* found that a large portion of micropores were not accessible to the electrolyte ions which limited the specific capacitance of AC [42]. Therefore, we can know that not only the specific surface area, but also the pore size distribution significantly determines the performance of AC for EDLC. Furthermore, to achieve an optimal specific capacitance, the pore size should match with the ion size. It has been reported that a pore size about 0.4 nm is efficient to form double layer in aqueous solution, while a pore size around 0.8 nm is suitable for organic electrolyte [43, 44]. In 2008, Largeot *et al.* prepared carbide derived carbon at temperatures from 400 to 1000 °C and characterized the pore structure using BET technique [45]. The porosity properties of the carbon samples are shown in Table 2.1. The electrolyte used was an EMI-TFSI ionic liquid and the size of TFSI and EMI ions were calculated as 0.79 and 0.76 nm respectively. The pore size dependent capacitance is displayed in Fig. 2.5, which clearly reveals the pore size effect. The normalized capacitance increased when the pore size was increased from 0.6 nm and reached a maximum value at 0.7 nm. Then the capacitance kept decreasing with the increasing pore size until 1.1 nm. The results can be well explained by the charge storage of carbons: when the pore size is in the same range as the ion size, each of the pore could accommodate only one ion, at which the pores are perfectly adapted to the ion size and the ion adsorption is achieved in a most efficient way by reducing the free space. Larger pores will cause the increase of distance between the pore wall and the centre of the ion thus leading to a lower capacitance. While with the small pores, less space is available for EDL charging since the ions cannot get into. Therefore, it is important to select proper electrode/electrolyte couple to maximize the capacitance. It should be noted that the electrolyte salts are usually solvated or hydrated by the solvent, for example, PC-solvated Li^+ ions are formed in a $LiBF_4$/PC electrolyte, so the solvated ion size should be considered [44].

However, excessive activation on the specific surface area or pore distribution is not a good strategy to boost the performance of AC, since these processes will lead to low material density and conductivity, thus lowering the volumetric energy density and rate capability [10].

Table 2.1 Carbide derived carbon porosity measurements using Ar gas sorption technique [45].

Preparation temperature (°C)	BET specific surface area (m^2 g^{-1})	Pore volume (cc g^{-1})	Average pore width (nm)	Maximum pore width[a] (nm)
400	1113	0.51	0.65	1.12
500	1140	0.50	0.68	1.18
550	1202	0.51	0.72	1.29
600	1269	0.60	0.74	1.23
700	1401	0.66	0.76	1.41
800	1595	0.79	0.81	1.54
1000	1625	0.81	1.10	2.80

[a] 85% of pore volume is below this size.

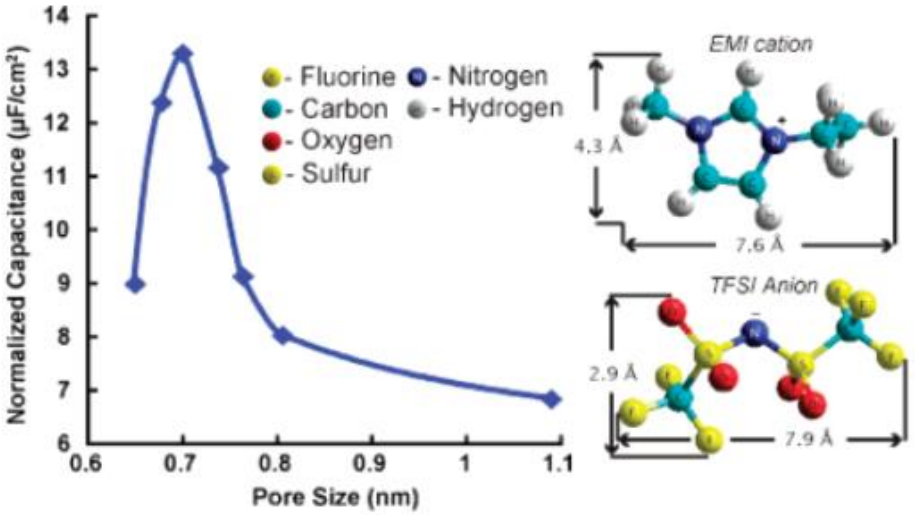

Fig. 2.5 The capacitance of carbide derived carbon as a function of pore size [45].

Besides the larger specific surface area and proper pore size, the surface functionalization is another important parameter to improve the capacitive performance of carbon materials. Surface functionalization is generally achieved by introducing heteroatoms (oxygen, nitrogen, boron and sulphur) into the carbon materials, which could improve their wettability by the electrolyte and induce faradaic charge transfer processes, resulting in an increment in capacitance [46, 47]. For example, Li *et al.* recently prepared a nitrogen-doped AC with high specific surface area up to 2900 m^2 g^{-1} and nitrogen content at 4 wt% [48]. The synthesized AC exhibited good electrochemical performance with a high specific capacitance of 185 F g^{-1} in an organic electrolyte. Moreover, the material also

showed excellent rate capability and cycling stability, and 76.3% capacitance was retained after 8000 cycles in an assembled cell.

2.2.1.2 Carbon Nanotubes (CNTs)

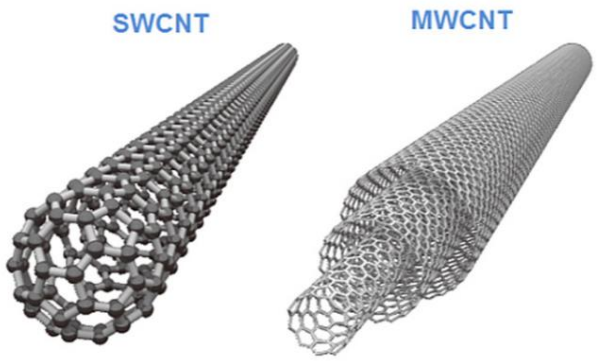

Fig. 2.6 Atomic structures of single-walled carbon nanotubes (SWCNTs) and multi-walled carbon nanotubes (MWCNTs) [49].

In addition to AC, carbon nanotubes (CNTs), including single-walled carbon nanotubes (SWCNTs) and multi-walled carbon nanotubes (MWCNTs) (Fig. 2.6), have been proposed as promising electrode materials for supercapacitors because of the superior electrical conductivity, and good mechanical and thermal stability [50]. However, the relatively small surface area restricts the capacitance of CNTs. Niu *et al.* prepared a MWCNT-based electrode with a specific surface area of 430 $m^2\ g^{-1}$ for supercapacitors, getting specific capacitances of 102 and 49 F g^{-1} at 1 and 100 Hz in H_2SO_4 electrolyte [51]. Researchers have undertaken various methods to improve the surface area of CNTs. For example, Frackowiak *et al.* successfully realised MWCNTs with a specific surface area up to 1035 $m^2\ g^{-1}$ by a KOH activation process [52]. The activated CNTs displayed an improved capacitance in both aqueous and organic electrolytes. Compared with MWCNTs, SWCTNs often exhibit better permeance due to the larger specific surface area, higher aspect ratio and easier accessibility for electrolyte ions [17]. A specific capacitance as high as 180 F g^{-1} was achieved with a SWCNT electrode [53]. The increased capacitance could be attributed to the reduced resistance by heat treatment and enhanced specific surface area. Studies have indicated that aligned CNTs are more efficient than entangled CNTs for capacitive performance as their unbundled structures provide more mesopores, low resistance and fast ion

transportation [54, 55]. Kim *et al.* reported a vertically CNT electrode synthesized via water-assisted chemical vapor deposition (CVD), which showed excellent performances [56]: in 1 M H_2SO_4 electrolyte, the specific capacitance, energy density and power density at current density of 20 A g^{-1} were 200 F g^{-1}, 20 Wh kg^{-1} and 40 kW kg^{-1}, respectively. It should be mentioned that in many cases, CNTs are used as additives to other active materials since they can offer good support and enhance conductivity [57].

2.2.1.3 Graphene

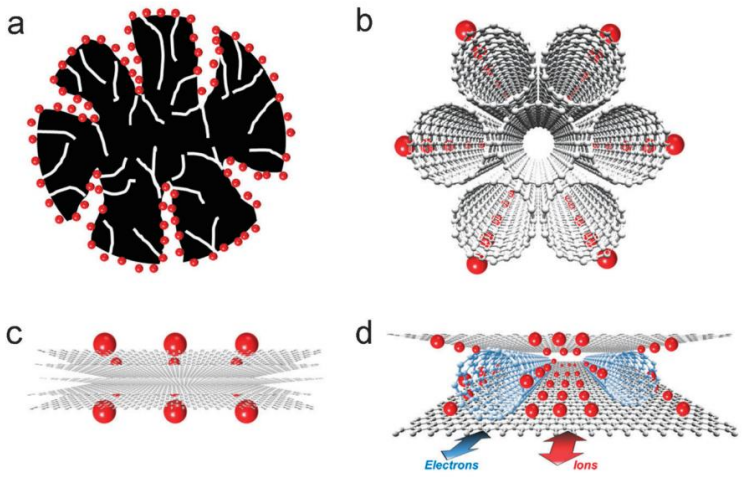

Fig. 2.7 Comparison of different carbon materials for supercapacitors: (a) AC, (b) CNTs, (c) Graphene sheets, (d) Graphene/CNT composite [58].

Graphene is composed of two-dimensional single-layer sp^2-hybridized conjugated carbon atoms. Because of its high electrical conductivity, superior mechanical properties, and large specific surface area, graphene has been widely studied as a high-performance electrode material for supercapacitors [59]. The theoretical specific surface area of graphene is 2630 m^2 g^{-1}, providing a theoretical specific capacitance of up to 526 F g^{-1} in aqueous electrolyte [58, 60, 61]. Graphene is supposed to be superior to other carbon materials, including AC and CNTs. Fig. 2.7 compares the benefits and drawbacks of AC, CNTs and graphene sheets. For AC, many regions are not available for electrolyte ions which limits its specific capacitance (Fig. 2.7a); for CNTs, although they hold high conductivity, they are easy to form bundles and thus only the outer surface is accessible by electrolyte ions (Fig. 2.7b); for graphene, it tends to form irreversible agglomerates due to the

van der Waals interactions, so the ions are impossible to access the inner layers which lowers the specific capacitance (Fig. 2.7c).

Normally, only around 40% of the theoretical capacitance value of graphene can be obtained. Wang *et al.* prepared a graphene electrode by reducing the graphene oxide (GO) synthesized via a modified Hummers's method with hydrazine, delivering a maximum specific capacitance of 205 F g^{-1} in KOH electrolyte [11]. Lee *et al.* fabricated a mesoporous graphene nanoball electrode via a CVD technique, achieving a specific capacitance of 206 F g^{-1} in H_2SO_4 solution [62]. Dey *et al.* reported a copper foam (CuF) integrated three-dimensional rGO network which delivered a high specific capacitance approaching the theoretical value of graphene, specifically, 623 F g^{-1} at 1 A g^{-1} and 427 F g^{-1} at 10 A g^{-1} [63].

Many methods have been proposed to improve the performance of graphene. For example, Cheng *et al.* developed a graphene/CNTs composite electrode to counter the graphene restacking problem [58]. The addition of CNTs not only reduced agglomeration of graphene sheets (Fig. 2.7d), but also improved the conductivity of the composite. Consequently, an excellent electrochemical performance with a specific capacitance of 290.6 F g^{-1} was obtained. To dope the graphene with substituent heteroatoms is another efficient way to enhance its capacitive behaviours. Sun *et al.* reported a facile hydrothermal method to simultaneously fulfil N-doping and GO reduction with urea [64]. The produced high-level nitrogen-doped graphene (10.13 atom%) displayed a high capacitance of 326 F g^{-1} and outstanding cycling stability (no degradation after 2000 cycles).

2.2.2 Metal oxides/hydroxides

In general, metal oxides/hydroxides can provide higher capacitance and energy density compared with the carbon materials because they store energy not only from the electrochemical adsorption/desorption of ions at the electrode/electrolyte interface but also from faradaic reactions between the electrode and the electrolyte within proper potential. As mentioned previously, both battery-type materials and pseudocapacitive materials store charges via faradaic reactions, some of the studies interchangeably describe the two types of materials. To avoid confusion, the

terminology used here is consistent with the cited papers. To date, the metal oxides/hydroxides investigated for supercapacitors include MnO_2, RuO_2, V_2O_5, NiO, $Ni(OH)_2$, Co_3O_4, $Co(OH)_2$, Fe_2O_3 etc.

2.2.2.1 RuO_2

It is known that hydrous RuO_2 was the first material introduced for pseudo-supercapacitors by Conway's group [65]. After that, RuO_2 has been extensively investigated due to its high specific capacitance, wide potential window, reversible redox reactions and long cycle life [17]. It was found that only around 10% of the capacitance was derived from the electrical double-layer while the remaining was contributed by redox pseudocapacitance [3]. The pseudocapacitive behaviours of RuO_2 are based on highly reversible transitions between Ru(II)/Ru(III), Ru(III) /Ru(IV) and Ru(IV)/ Ru(VI) which can be described as [66]:

$$RuO_x(OH)_y + \delta H^+ + \delta e^- \leftrightarrow RuO_{x-\delta}(OH)_{y+\delta} \qquad (2.8)$$

The performance of Ru oxides is determined by many factors such as the degree of crystallinity, the water content, the particle size etc. Zheng *et al.* reported a hydrous RuO_2 electrode annealed at 150 ^oC with amorphous phase that can reach 720 F g^{-1} [67]. When they increased the annealing temperature to convert the RuO_2 into crystalline phase, the specific capacitance dramatically dropped, specifically, 144 F g^{-1} at 200 ^oC and only 19.2 F g^{-1} at 400 ^oC. These results revealed that the proton can easily permeate into the hydrous RuO_2 in amorphous phase while they were difficult to intercalate into a well crystallized structure. Dmowski *et al.* demonstrated that hydrous RuO_2 was a mixed electron-proton conductor, and a maximum specific capacitance would be achieved when electron and proton conducting pathways are balanced [68]. It is found that electron conduction is supported by RuO_2 nanocrystals, while proton conduction is supported by the boundaries between the nanocrystals. The volumes of the RuO_2 nanocrystals and the hydrous grain boundaries will change with different water content. Therefore, the volume of the electronic and protonic pathways strongly depends on the water content. Table 2.2 gives the specific capacitance of $RuO_2 \cdot xH_2O$ as a function of water content. Hu *et al.*'s work indicated that the interparticle electronic conductivity of $RuO_2 \cdot xH_2O$ could be improved by nanostructuring the particle size to around 3 nm as well as mixing with AC, which maximized the utilization during

charge-discharge for supercapacitors, obtaining a specific capacitance of 1340 F g^{-1} at 25 mV s^{-1} [69].

Table 2.2 Specific capacitance of $RuO_2 \cdot xH_2O$ as a function of water content [68].

$RuO_2 \cdot xH_2O$ x mole %H_2O ± 7%	Specific capacitance (F g^{-1}) ± 4.8%
2.11	505
0.84	740
0.58	850
0.48	735
0.35	365
0.14	250
0.02	125

2.2.2.2 MnO_2

Despite the excellent capacitive performance of Ru-based materials, the relatively high cost and environmental harmfulness limit their wide application in supercapacitors. As an alternative approach, researchers have made great effort to seek less-expensive and environmentally friendly materials with similar electrochemical behaviours of RuO_2. MnO_2 has been proposed as a promising electrode material for supercapacitors due to its low cost, low toxicity as well as high theoretical capacitance up to 1370 F g^{-1} [3]. The capacitance of the manganese oxides can be attributed to the reversible redox transitions between Mn(II)/Mn(III), Mn(III)/Mn(IV) and Mn(IV)/Mn(VI). The mechanism can be expressed by the following equation [3]:

$$MnO_x(OZ)_y + \delta Z^+ + \delta e^- \leftrightarrow MnO_{x-\delta}(OZ)_{y+\delta} \qquad (2.9)$$

where Z^+ indicates the protons or alkali metal cations (Li^+, Na^+, K^+) in the electrolyte, and $MnO_x(OZ)_y$ and $MnO_{x-\delta}(OZ)_{y+\delta}$ represent the Mn in different oxidation states [3].

In general, MnO_2 exhibits a typical rectangular CV curve in aqueous electrolyte with a potential window around 1.0 V as shown in Fig. 2.8 [70], but its specific capacitance is only ca. 200 F g^{-1}, far lower than the theoretical value. It is supposed that MnO_2 electrode often suffers from low surface area and poor electronic conductivity (10^{-5}–10^{-6} S cm^{-1}), in other word, the charge storage of MnO_2 only

occurs at a thin surface layer instead of the bulk material. Therefore, to enhance the surface area via changing the morphology of MnO_2 have been attempted to improve its electrochemical performance. Wu synthesized MnO_2 with different morphologies of nanorod (15-35 nm in diameter) and nanowire (8-16 nm) by controlling the electrodeposition potential [71]. Due to the higher surface area of the nanowires, a higher specific capacitance of 350 F g^{-1} was reached on the nanowire electrode versus 243 F g^{-1} on the nanorod electrode. Recently, Kashale *et al.* prepared a 2D aligned MnO_2 micro-flower electrode by a simple chemical bath deposition technique, which exhibited a high capacitance of 376 F g^{-1} at a current density of 5 mA cm^{-2} in Na_2SO_4 solution [72].

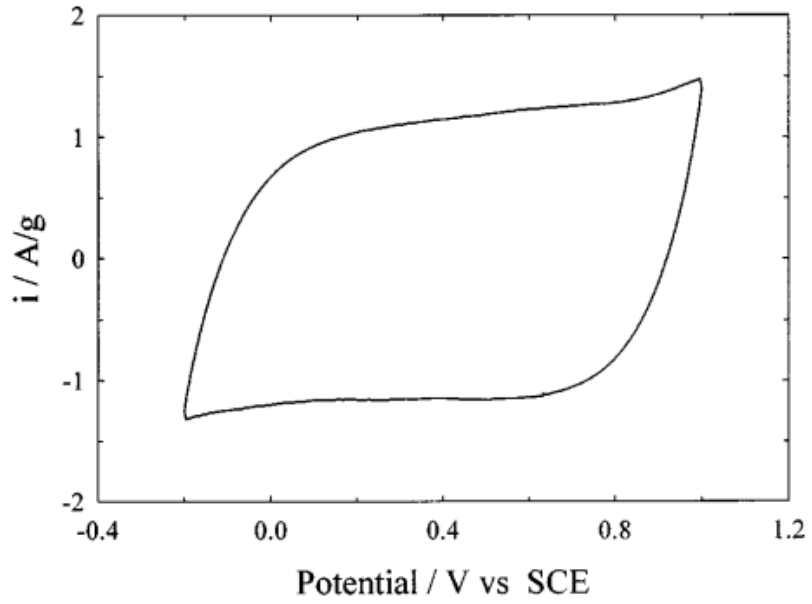

Fig. 2.8 Cyclic voltammogram of $MnO_2 \cdot nH_2O$ at 5 mV s^{-1} in 2 M KCl electrolyte [70].

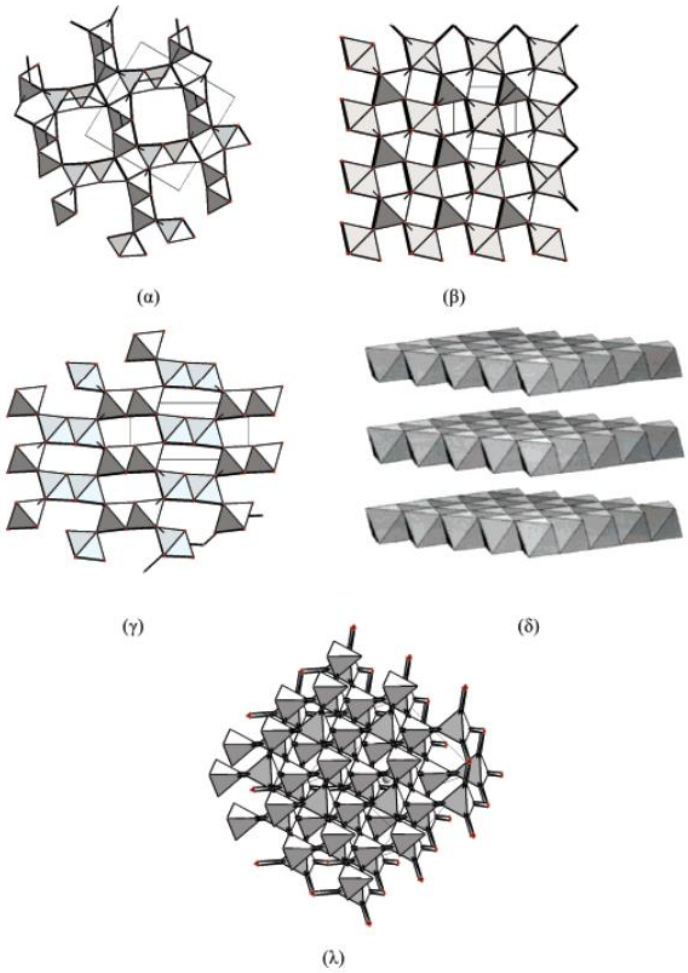

Fig. 2.9 Crystal structures of α-, β-, γ-, δ- and λ-MnO_2 [73].

Besides the morphology, the crystal structure also plays an important role in determining the pseudocapacitive performance of MnO_2. Naturally, there are five types of crystal structures for MnO_2: α, β, γ, δ and λ. As shown in Fig. 2.9, α, β and γ have a 1D tunnel structure, while δ and λ possess 2D and 3D tunnel structures, respectively [73]. As capacitive behaviours are based on the intercalation/deintercalation of electrolyte ions into the crystals, only some of the structures could provide sufficient gaps and proper sized tunnels to accommodate the ions. Devaraj and Munichandraiah compared the supercapacitor performance of five crystallographic structures of MnO_2 in Na_2SO_4 solution, and the measured specific capacitance values were in the order of $\alpha = \delta > \gamma > \lambda > \beta$ [73]. The large tunnel size in α-MnO_2 and large interlayer separation of δ-MnO_2 are the favourable factors for the high specific capacitances while the narrow tunnels in β-MnO_2 is unsuitable for transporting ions.

Incorporating MnO_2 with other conductive and high surface area materials is another way to improve its performance. Yang *et al.* fabricated a MnO_2/graphene composite electrode with a specific capacitance of 450 F g^{-1} at 1 A g^{-1} [74]. Meanwhile, the composite showed outstanding cycle performance with no capacitance loss over 5000 cycles. Chen and co-workers reported a MnO_2/CNT sponge electrode reaching 1230 F g^{-1} (based on mass of MnO_2) in 1 M Na_2SO_4 with excellent stability of only 4% degradation after 10000 cycles at 5 A g^{-1} [75]. The symmetric MnO_2/CNT device exhibited a superior energy density of 31 Wh kg^{-1}.

2.2.2.3 V_2O_5

V_2O_5 has been extensively studied as pseudocapacitive electrode due to its layered structure and various oxidation states (+2 to +5), low cost and easy procedure for fabrication. Nevertheless, performance of V_2O_5 is still limited by its poor electrical conductivity (10^{-2}–10^{-3} S cm^{-1}) and low lithium-ion diffusion coefficient [76]. Developing nanostrurured V_2O_5 is an effective approach to enhance its performance because nanoscale material possesses large surface area and short diffusion paths. Saravanakumar *et al.* synthesized an interconnected V_2O_5 nanoporous network and explored its supercapacitor performance in K_2SO_4 solution [77]. It was discovered that the nanoporous structure could provide nanochannels for ion diffusion thus improving ions accessibility. A high specific capacitance of 316 F g^{-1} was achieved. Zhu and co-workers fabricated a 3D V_2O_5 nanosheet electrode via a hydrothermal treatment followed by a freeze-drying process (Fig. 2.10a) [78]. The resulting architectures were highly interconnected and porous (Fig. 2.10b), possessing a large surface area of 133 m^2 g^{-1}, which facilitated the electrolyte transport and provided numerous active sites for energy storage. Consequently, a specific capacitance as high as 451 F g^{-1} was obtained with the energy density up to 107 Wh kg^{-1} at a power density of 9.4 kW kg^{-1} (Fig. 2.10c). In addition to constructing 3D V_2O_5, 3D current collector was employed to promote the electrochemical performance. Liang *et al.* embedded V_2O_5 nanowires in a 3D porous Ni current collector for supercapacitor application [79]. The Ni current collector not only worked as a conductive framework, but also enlarged

the active area for redox reactions. A high specific capacitance of 832 F g^{-1} with an energy density of 115.7 Wh kg^{-1} was observed in aqueous Na_2SO_4 electrolyte.

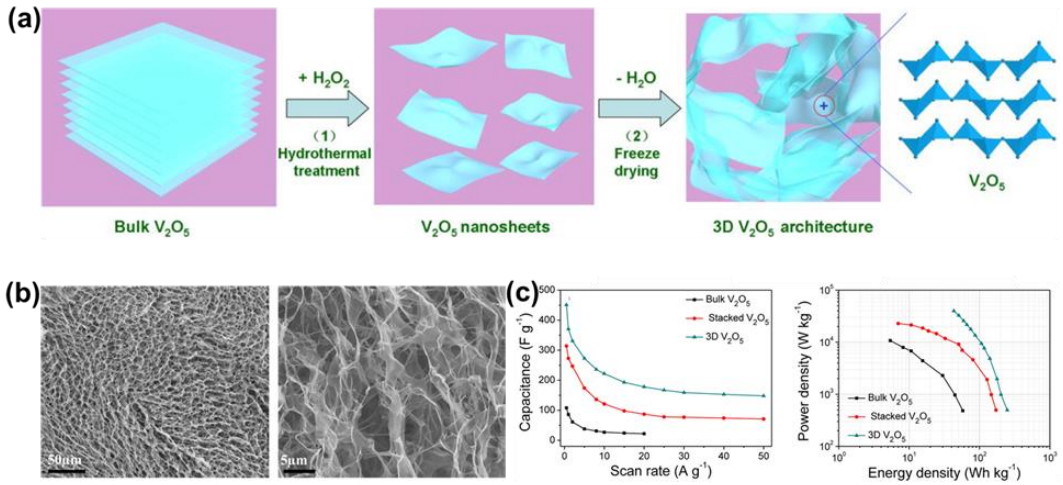

Fig. 2.10 (a) Schematics of the fabrication steps of the 3D V_2O_5; (b) Typical field emission scanning electron microscopy (FESEM) images of the 3D V_2O_5; (c) Specific capacitances calculated from GCD at various current densities, and power density and energy density for different electrodes [78].

Similar to other metal oxides, to composite V_2O_5 with conductive carbon materials is an efficient approach to boost its supercapacitor performance. Chen *et al.* prepared a V_2O_5/CNT composite electrode through a hydrothermal process, which displayed a specific capacitance up to 440 F g^{-1} at a current density of 0.25 A g^{-1} in 1 M Na_2SO_4 [80]. A rodlike V_2O_5/rGO (reduced graphene oxide) nanocomposite electrode was fabricated for high-performance supercapacitors [76]. It exhibited high specific capacitance (537 F g^{-1}), high power density (74.58 Wh kg^{-1}), and good cycling stability.

2.2.2.4 Ni/Co oxides/hydroxides ($NiO/Ni(OH)_2$ and $Co_3O_4/Co(OH)_2$)

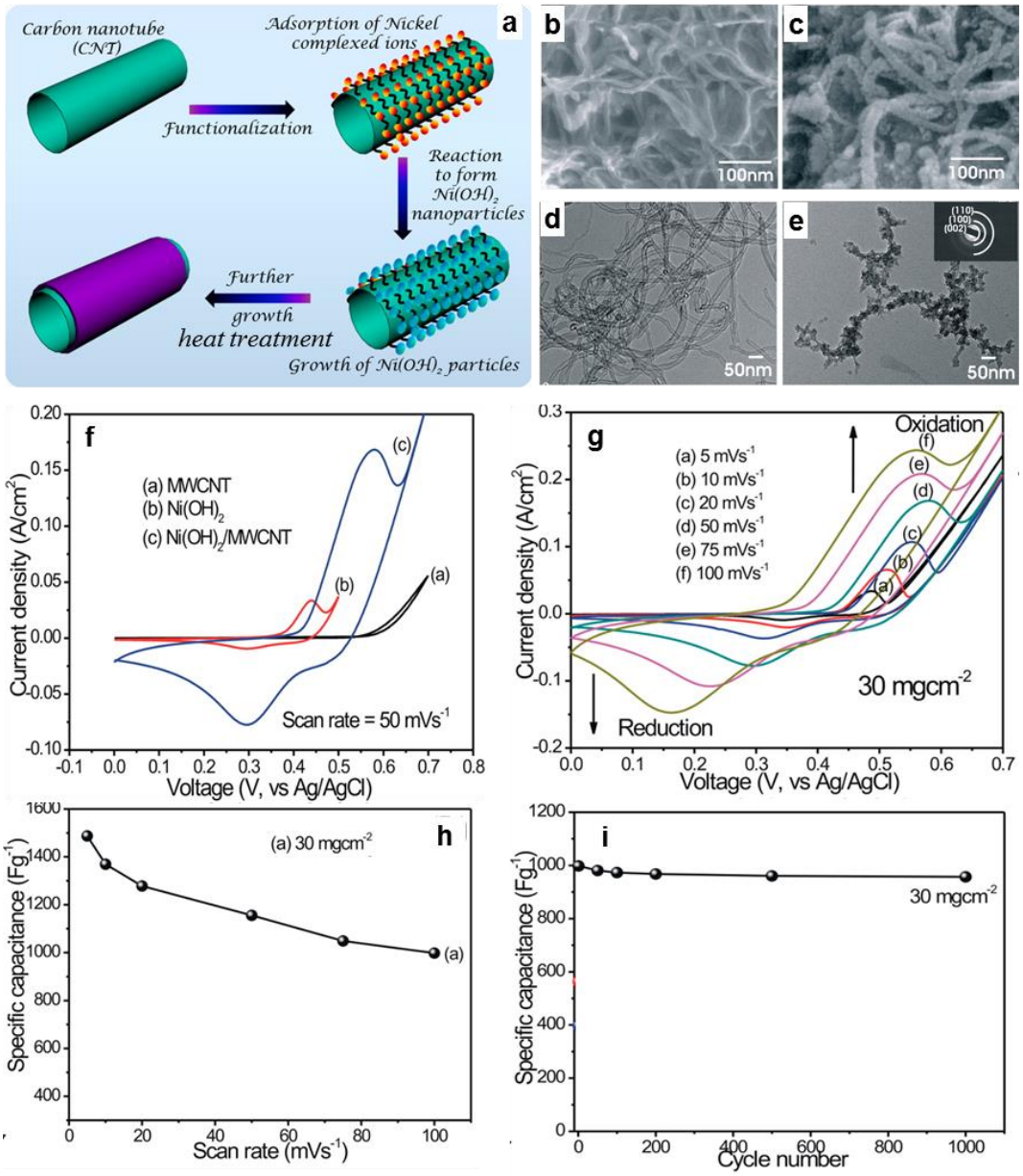

Fig. 2.11 (a) Schematics of the fabrication steps of the nanocrystalline $Ni(OH)_2$ onto multiwalled carbon nanotubes (MWCNTs) which is denoted as $Ni(OH)_2$/MWCNT. Typical FESEM images of (b) pristine MWCNT and (c) $Ni(OH)_2$/MWCNT. TEM images of (d) pristine MWCNT and (e) $Ni(OH)_2$/MWCNT. (f) CV curves of MWCNT, $Ni(OH)_2$, and $Ni(OH)_2$/MWCNT. (g) CV curves of the $Ni(OH)_2$/MWCNT at different scan rate. (h) Specific capacitances of $Ni(OH)_2$/MWCNT at different scan rate. (i) Cycling stability of $Ni(OH)_2$/MWCNT at 100 mV s^{-1} [81].

Nanostructured Ni/Co oxides/hydroxides have been investigated as promising electrode materials for supercapacitors due to their ultrahigh theoretical specific capacitances (e.g., 3750 F g^{-1} for NiO, and 3560 F g^{-1} for Co_3O_4), low cost and environmental friendliness [13]. Charge storage in Ni/Co oxides/hydroxides is accomplished via reversible redox between Ni^{2+}/Ni^{3+} or Co^{2+}/Co^{3+} states in alkaline electrolytes [28]. Various nanostructures, such as nanowires, nanosheets, nanoflowers, nanobelts, have been developed to enhance the supercapacitor performances by providing larger surface area and short ion diffusion and transport pathways. For instance, Vijayakumar *et al.* synthesized NiO using microwave heating method at different calcination temperature [82]. Results indicated that the 300 ^oC calcined NiO showed nanoflake structure and exhibited a maximum specific capacitance of 401 F g^{-1} at 0.5 mA cm^{-2}. Yuan *et al.* designed mesoporous Co_3O_4 nanosheet arrays on a Ni foam substrate, and this unique 3D structure endowed fast ion and electron transport and good structural stability, delivering a high specific capacitance of 2735 F g^{-1} at 2 A g^{-1} with negligible degradation over 3000 cycles [83]. Hu *et al.* compared the supercapacitor performance of $Ni(OH)_2$ and $Co(OH)_2$ films prepared by a simple electrodeposition method [84]. It was found that $Ni(OH)_2$ delivered higher specific capacitance than $Co(OH)_2$ (2217 F g^{-1} versus 549 F g^{-1} at 1.0 mA cm^{-2}) while the $Co(OH)_2$ presented better rate capability and energy efficiency.

Although the Ni or Co oxides/hydroxides usually exbibit high specific capacitances, they still suffer from terrible rate capability and poor cycling stability due to the low conductivity and large volume change during the charging-discharging processes [17]. For example, Lu *et al.* fabricated $Ni(OH)_2$ nanowall films which exhibited a very high specific capacitance of 2675 F g^{-1} at 5 mA cm^{-2}, but the specific capacitance dramatically dropped to 1150 F g^{-1} when the current density increased to 30 mA cm^{-2} [85]. To alleviate these issues and further improve the electrochemical performances, these materials are frequently composited with carbon materials. Liao *et al.* reported an electrode based on Co_3O_4 nanoparticles on vertically aligned graphene nanosheets (Co_3O_4/graphene), obtaining a high specific capacitance of 3482 F g^{-1} which was close to the theoretical value [86]. Dubal *et al.* developed $Ni(OH)_2$/MWCNT composites for flexible supercapacitors by growing $Ni(OH)_2$ nanoparticles onto MWCNTs which is illustrated in Fig.

2.11a [81]. SEM and TEM images demonstrated that the sponge-like $Ni(OH)_2$ was uniformly coated on the MWCNT network (Fig. 2.11b-e). The high conductivity of the MWCNTs and porous structure facilitated the ion insertion/extraction and electron transport in the $Ni(OH)_2$/MWCNT electrode, resulting in a high specific capacitance of 1487 F g^{-1} at a scan rate of 5 mV s^{-1} with good rate capability (998 F g^{-1} at 100 mV s^{-1}) and long-term stability (4% fading after 1000 cycles) (Fig. 2.11f-i).

However, it should be noted that NiO/$Ni(OH)_2$ and Co_3O_4/$Co(OH)_2$ have an inherent defect, in that their working potential range is small, usually around 0.5 V [13].

2.2.2.5 Iron oxides/hydroxides (Fe_2O_3, Fe_3O_4 and FeOOH)

Iron oxides/hydroxides are good candidate materials for supercapacitor electrodes due to their high theoretical capacitance, suitable negative working potential window, cost-effectiveness, earth-abundance, and environmental friendliness [87]. Since the iron oxides/hydroxides naturally react with acidic solution, the employed electrolytes are usually alkaline (e.g., KOH) or neutral (e.g., Li_2SO_4, Na_2SO_4). However, even with suitable electrolyte, the resultant capacitance and power capability of iron oxides/hydroxides are severely restricted by their poor conductivity (e.g., around 10^{-14} S cm^{-1} for Fe_2O_3) [13, 18]. To address this issue, many efforts have been devoted, in which designing rational morphologies especially nanostructures to shorten the diffusion paths for electrons is an effective approach. Chen *et al.* investigated the pseudocapacitive performance of a layered FeOOH nanosheet electrode in Li_2SO_4 electrolyte, obtaining a specific capacitance of 310.3 F g^{-1} [88]. Li *et al.* fabricated Fe_2O_3 nanoneedles on ultrafine Ni nanotube arrays, with which an improved specific capacitance up to 418.7 F g^{-1} at 10 mV s^{-1} as well as good cycling stability (93.3% capacitance retention after 5000 cycles) in 1 M Na_2SO_4 electrolyte were achieved [89]. Lu and co-workers prepared oxygen-deficient Fe_2O_3 nanorods through thermal treatment of FeOOH under N_2 atmosphere for supercapacitors [90]. Because the number of active sites and donor density were promoted by the oxygen vacancies, the as-synthesized Fe_2O_3

electrode yielded a high areal capacitance of 382.7 mF cm^{-2} with excellent long-term stability (less than 5% decay after 10000 cycles) in LiCl solution.

To composite iron materials with other conductive materials is another promising way to improve their supercapacitor performance. For instance, a Fe_3O_4/rGO nanocomposite delivered a specific capacitance of 220.1 F g^{-1} with no capacitance loss over 3000 cycles in KOH solution [91]. Very recently, Liu *et al.* successfully fabricated an electrode based on Ti-doped FeOOH quantum dots decorated on graphene sheets, exhibiting an exceptional areal capacitance of 3322 mF cm^{-2} with outstanding cycling stability (around 95% capacitance was maintained after 6000 cycles) and good flexibility [92].

2.2.2.6 Binary metal oxides

In recent years, binary metal oxides have received a lot of attention as electrode materials for supercapacitors, such as $NiCo_2O_4$, $ZnCo_2O_4$, $CoFe_2O_4$, $NiMoO_4$, $CoMoO_4$, $MnMoO_4$, $FeMoO_4$, and $Ag_6Mo_{10}O_{33}$ [93-99]. It is reported that binary metal oxides can exhibit better electrochemical performance than unitary metal oxides due to the synergistic effect and combined capacitive contribution of the individual components [100]. The urchin-like $NiCo_2O_4$ nanorods synthesized by a simple hydrothermal method exhibited a superior specific capacitance of 1650 F g^{-1} at 1 A g^{-1} and 9.2% capacitance loss after 2000 cycles at a high charge-discharge rate of 8 A g^{-1} [93]. Wang *et al.* reported that the $CoFe_2O_4$ hollow microspheres displayed enhanced electrochemical performance due to the unique, hollow multi-shell structure which provided more active surface area for charge storage, demonstrating a specific capacitance of 1790 F g^{-1} at 2 A g^{-1} with excellent durability (98% retention after 500 cycles) [95]. Guo *et al.* prepared a binder free electrode by growing $NiMoO_4$ nanowires on flexible carbon cloth, obtaining a high specific capacitance of 1587 Fg^{-1} at 6.25 A g^{-1} [97]. However, because of the structural deformation during the rapid chare/discharge process, only 76.9% capacitance was retained after 4000 cycles.

2.2.2.7 Other metal oxides

In addition to the above-mentioned metal oxides, other materials such as TiO_2 [101,

102], MoO_3 [34, 103], Bi_2O_3 [104, 105], etc. have also been explored as promising electrode materials for supercapacitor applications. TiO_2 nanoparticles coated on porpous graphene prepared via an atomic layer deposition (ALD) method only showed a capacitance of 84 F g^{-1} [102]. Chang *et al.* demonstrated a MoO_3 nanosheets graphene composite where the graphene functioned as conductive channels and active interface centres, and offered better interconnectivity between MoO_3 nanosheets, leading to an improved capacitance of 291 F g^{-1} at 2 mV s^{-1} aqueous Na_2SO_4 electrolyte [103]. By introducing oxygen vacancies into Bi_2O_3, Liu *et al.* developed an oxygen-deficient Bi_2O_3 graphene (r-Bi_2O_3/GN) electrode which offered more active sites and faster charge transfer, resulting in an ultrahigh areal capacitance of 6675 mF cm^{-2} and an excellent gravimetric capacitance of 681 F g^{-1} at 1 mA cm^{-2} [104].

2.2.3 Metal nitrides

In recent years, metal nitride materials have gradually entered into researchers' horizon as electroactive materials for supercapacitors due to their high electrical conductivity and chemical stability in common aqueous electrolyte [3].

2.2.3.1 TiN

Titanium nitride (TiN) is one of the most frequently studied nitride materials with super electrical conductivity (4000–55500 S cm^{-1}) [106]. However, Choi and Kumta's work demonstrated that TiN electrode was not stable in alkaline electrolyte, specifically, only 28% of its initial specific capacitance was retained after 400 cycles in KOH solution [107]. Lu *et al.* found that the capacitance loss was due to the irreversible electrochemical oxidation of TiN during the charging-discharging process [108]. They firstly proposed a poly(vinyl alcohol) (PVA)/KOH gel electrolyte to stabilize the TiN nanowire electrode, which successfully supressed the oxidation reaction. A specific capacitance of 123 F g^{-1} at 10 mV s^{-1} and 18% capacitance degradation after 15000 cycles were observed. Capacitive performance of TiN could be improved by combining with other materials such as graphene. For example, Tian *et al.* synthesized a graphene-TiN nanotube array electrode, exhibiting a specific capacitance of 333.7 F g^{-1} at 1 A g^{-1} with 86.1% capacitance retention after 1000 cycles [109].

2.2.3.2 VN

Vanadium nitride (VN) is another promising electrode material for supercapacitor owing to the large specific capacitance (1340 F g^{-1}) and good electrical conductivity ($\sigma_{bulk} = 1.67 \times 10^4$ S cm^{-1}). Xu and co-workers prepared 1D VN nanofibers using electrospinning followed by high-temperature ammonization [110]. The VN nanofibers exhibited a specific capacitance of 291.5 F g^{-1} at 0.5 A g^{-1} in aqueous KOH electrolyte. However, the VN can be electrochemically oxidized to vanadium oxide (VO_x) during the charging-discharging process, which will cause severe degradation as VO_x is soluble in aqueous solution [111]. Therefore, only 50% capacitance was maintained on the VN nanofiber electrode after 1000 cycles. To improve the stability of VN, a PVA/LiCl gel electrolyte was developed by Li's group [111]. It was discovered that the cycling stability of VN nanowire electrode can be significantly enhanced with the PVA/LiCl gel electrolyte, specifically, a capacitance retention up to 95.3% was obtained after 10000 cycles, much higher than the value got in 5M LiCl solution (14.1%). TiN-VN composite particles with core-shell structure were prepared for supercapacitors application, showing a specific capacitance of 170 F g^{-1} at 2 mV s^{-1} [112]. Similarly, Zhou and co-workers fabricated TiN-VN core-shell structured mesoporous fibres, which combined high specific capacitance of VN and better rate capability of TiN, demonstrating high specific capacitance (247.5 F g^{-1} at 2 mV s^{-1}) and good rate capability (160.8 F g^{-1} at 50 mV s^{-1}) [113].

2.2.3.3. Other metal nitrides

In addition to TiN and VN, many other nitrides have been applied as electrode materials for supercapacitors. Balogun *et al.* fabricated nickel nitride (Ni_3N) nanosheets on a carbon cloth substrate by a hydrothermal method [114]. The electrode displayed a specific capacitance of 990 F g^{-1} at 10 mA cm^{-2} with good rate capability (800 F g^{-1} at 40 mA cm^{-2}). Very recently, Xiao *et al.* reported a salt-templating approach for synthesis of 2D MoN nanosheet electrode (Fig. 2.12a) [115]. The capacitive behaviours of the electrode were compared in a variety of electrolytes, including H_2SO_4, Li_2SO_4, $NaSO_4$, K_2SO_4, $MgSO_4$ and KOH (Fig. 2.12b-c). A highest volumetric capacitance of 928 F cm^{-3} was obtained at 2 mV s^{-1} in H_2SO_4 solution. Moreover, an excellent cycling stability was observed with

over 95% volumetric capacitance retention after 25000 cycles (Fig. 2.12d), which can be attributed to the fast electron transport in the 2D MoN. Gryglewicz *et al.* synthesised an iron nitride activated carbon composite (Fe_2N@AC) as a novel electrode material for supercapacitors [116]. The good distribution of Fe_2N nanoparticles on the mesoporous AC surface greatly maximized the electrochemical performance of the Fe_2N@AC electrode, resulting in an outstanding specific capacitance of 507 F g^{-1} at 0.5 A g^{-1}.

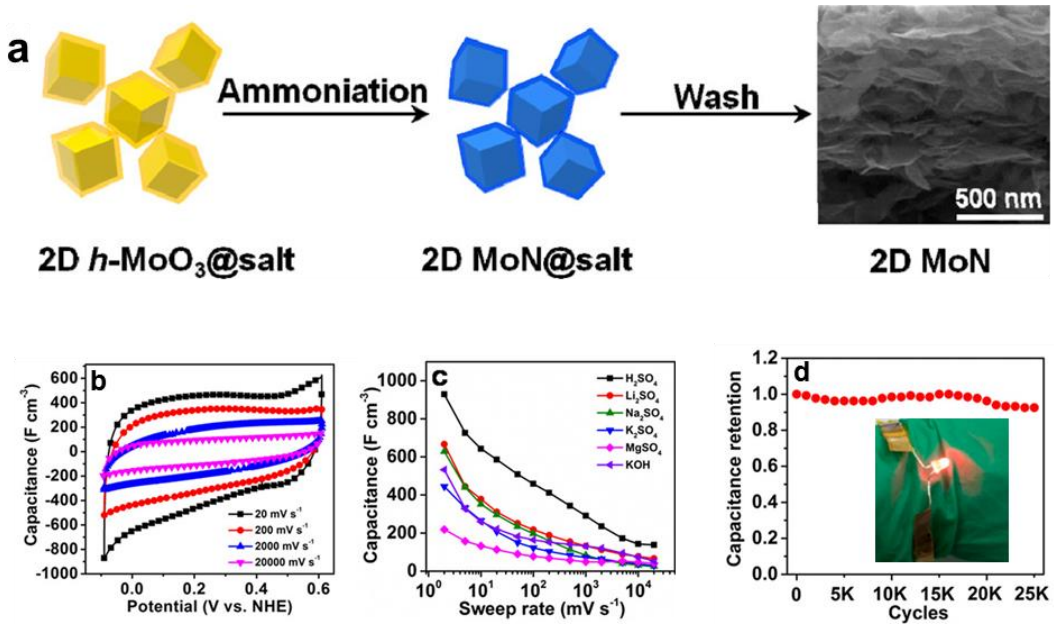

Fig. 2.12 (a) Schematic illustrations of synthesis of 2D MoN; (b) CV curves of 2D MoN in H_2SO_4 at different scan rates; (c) Volumetric capacitance versus sweep rates for different electrolytes; (d) Cycling stability of 2D MoN in H_2SO_4 electrolyte at 100 mV s^{-1} [115].

2.2.4 Metal sulfides

Metal sulfides, usually possess higher electrical conductivity and thermal stability, and richer redox chemistry than their oxide counterparts, therefore they have been supposed as promising electrode materials for supercapacitors [117].

2.2.4.1 Nickel sulfides

As one of the most common of metal sulfides, nickel sulfides can exist in plenty of phases, including NiS, NiS_2, Ni_3S_2, Ni_7S_6 and Ni_9S_8, most of which have been

confirmed holding excellent capacitance performance in alkaline electrolyte. For instance, Guan *et al.* synthesized NiS microflowers with a large surface area of 26.3 m^2 g^{-1}, which exhibited a high specific capacitance of 1122.7 F g^{-1} at 1 A g^{-1}, as well as excellent long-term stability (97.8% capacitance retention after high charge-discharge rate of 10 A g^{-1} for 1000 cycles) [118]. Pang *et al.* prepared different morphologies of NiS_2 (nanocubes, nanospheres and nanoparticles) by controlling the microwave reaction time [119]. The results indicated that electrochemical properties of the materials were related to their microstructures: NiS_2 nanocubes showed the highest specific capacitance (695 F g^{-1} at 1.25 A g^{-1}) while N_2S nanospheres exhibited the best photocatalytic activity towards H_2 evolution. 3D Ni_3S_2 nanosheet arrays supported on Ni foam were fabricated by a one-step hydrothermal approach and then directly applied as the electrode for supercapacitor application [120]. Due to the fast ion transport, large electroactive surface area and high structural stability of the nanosheet arrays, the electrode displayed a superior specific capacitance of 1370.4 F g^{-1} at 2 A g^{-1}, together with good rate capability (952.0 F g^{-1} at 20A g^{-1}) and outstanding cycling stability (8.6% degradation after 1000 cycles at 6 A g^{-1}).

2.2.4.2 Cobalt sulfides

Cobalt sulfide are materials which have very similar electrochemical properties with nickel sulfides. Co-S can form compounds in different stoichiometric compositions according to its phase diagram, such as CoS, CoS_2, Co_2S_3, Co_3S_4, Co_4S_3 and Co_9S_8 [121]. Among these diverse structures, CoS, CoS_2 and Co_9S_8 have been widely applied as electrode materials for supercapacitors.

Lou's group successfully constructed a complex CoS material with hollow structures (CoS-nanoparticle assembled nanoboxes surrounded by CoS-nanosheet, denoted as CoS-NP/CoS-NS DSNBs) for hybrid supercapacitor application [117]. The synthesis procedures are illustrated in Fig. 2.13a. Firstly, Co-based zeolitic imidazolate (ZIF-67) nanocubes were converted into ZIF-67/$Co(OH)_2$-NS via a refluxing process. Secondly, the formed ZIF-67/$Co(OH)_2$-NS was sulfurized by Na_2S to produce CoS-NP/CoS-NS DSNBs. The corresponded SEM and TEM images are shown in Fig. 2.13b-e. Due to the large surface area, suitable mesopores,

and robust structure, the prepared CoS-NP/CoS-NS DSNBs electrode exhibited high electrochemical performances in KOH aqueous electrolyte, specifically, a

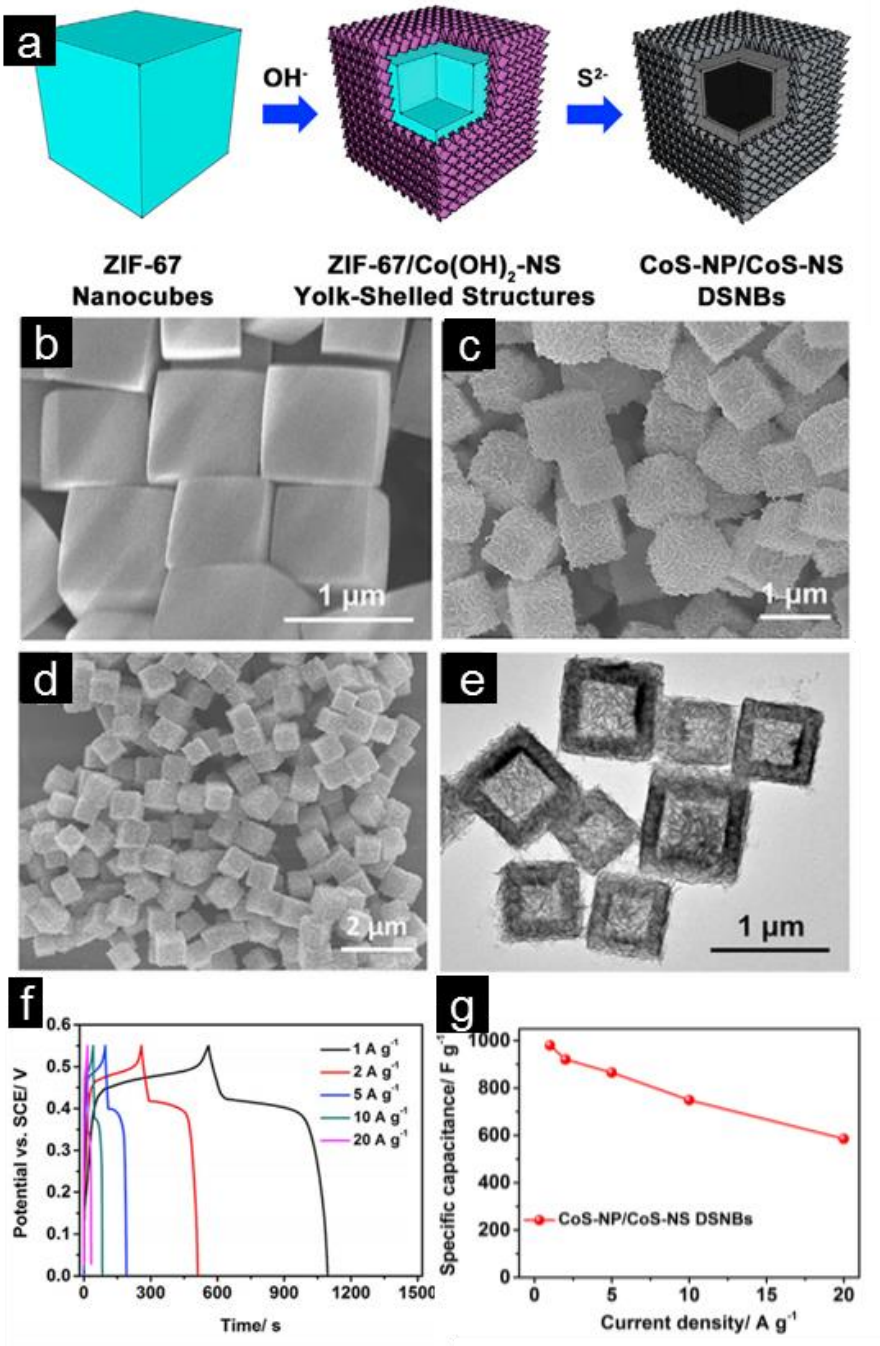

Fig. 2.13 (a) Synthesis procedure for hierarchical double-shelled hollow structures consisting of CoS-nanoparticle-assembled nanoboxes surrounded by CoS nanosheets (CoS-NP/CoS-NS DSNBs). (b) SEM of Co-based zeolitic imidazolate (ZIF-67) nanocubes. (c) SEM of ZIF-67/$Co(OH)_2$-nanosheet (ZIF-67/$Co(OH)_2$-NS). (d) SEM and (e) TEM of CoS-NP/CoS-NS DSNBs. (f) GCD curves and (g) Specific capacitance of CoS-NP/CoS-NS DSNBs at various current densities [117].

specific capacitance of 980 F g^{-1} was achieved at 1 A g^{-1}, and 60% of the capacitance was maintained when the chagre/discharge current increased to 20 Ag^{-1} (Fig. 2.13f-g). Ji and co-workers reported a CoS_2 nanocrystal electrode with porous surface that delivered a specific capacitance of 654 F g^{-1} [122]. Li *et al.* fabricated a Co_9S_8 thin film/nickel foam electrode through an ALD approach, in which the deposited film offered good microstructural crystallinity, low surface roughness, high purity, and high conductivity [123]. The ALD-prepared electrode demonstrated remarkable electrochemical performances with high specific capacitance (1645 F g^{-1} at 3 A g^{-1}), excellent rate capability (1309 F g^{-1} at 45 A g^{-1}), and great long-term stability (5.6% initial capacitance fading after 2000 cylces at 45 A g^{-1}).

2.2.4.3 MoS_2

Molybdenum disulphide (MoS_2) is a layered metal sulfide and it is considered as a good electrode material for electrochemical charge storage devices such as supercapacitors because it can not only deliver EDL capacitance but also offers large pseudocapacitance with varying Mo oxidation states (+2 to +6) [17]. Generally, MoS_2 can exist in three phases including 1T (Trigonal), 2H (Hexagonal) and 3R (Rhombohedral). 1T-MoS_2 holds metallic properties that usually exhibits higher supercapacitor performance. For instance, Acerce and co-workers chemically exfoliated MoS_2 nanosheets with 1T phase for supercapacitor application [124]. The obtained 1T-MoS_2 exhibited 10^7 times more conductive than the semiconducting 2H phase. Fig. 2.14a-b demonstrate the layered structure of the MoS_2 nanosheets. The 1T-MoS_2 nanosheet electrode can electrochemical intercalate many ions such as H^+, Li^+, Na^+ and K^+ with high volumetric capacitance ranging from 400 to 700 F cm^{-3} (Fig. 2.14c-e). Moreover, outstanding cycling stability was achieved with 97% capacitance retention over 5000 cycles in both aqueous and organic electrolytes (Fig. 2.14f). These superior electrochemical properties were mainly attributed to the hydrophilicity and high electrical conductivity of 1T MoS_2. 2H and 3R phases of MoS_2 are not attractive as electrode materials for supercapacitors due to their limited conductivity. To improve the electrothermal performances, they are usually combined with carbon materials or conducting polymers. Firmiano *et al.* prepared a 2H-MoS_2/rGO composite which

exhibited a high specific capacitance of 265 F g^{-1} in 1 M $HClO_4$ aqueous solution [125]. Huang *et al.* fabricated a polyaniline (PANI)/MoS_2 nanocomposite, in which the embedding PANI prevented the restacking of MoS_2 sheets and improved electrolyte/electrode accessibility [126]. Therefore, an enhanced specific capacitance of 575 F g^{-1} was obtained.

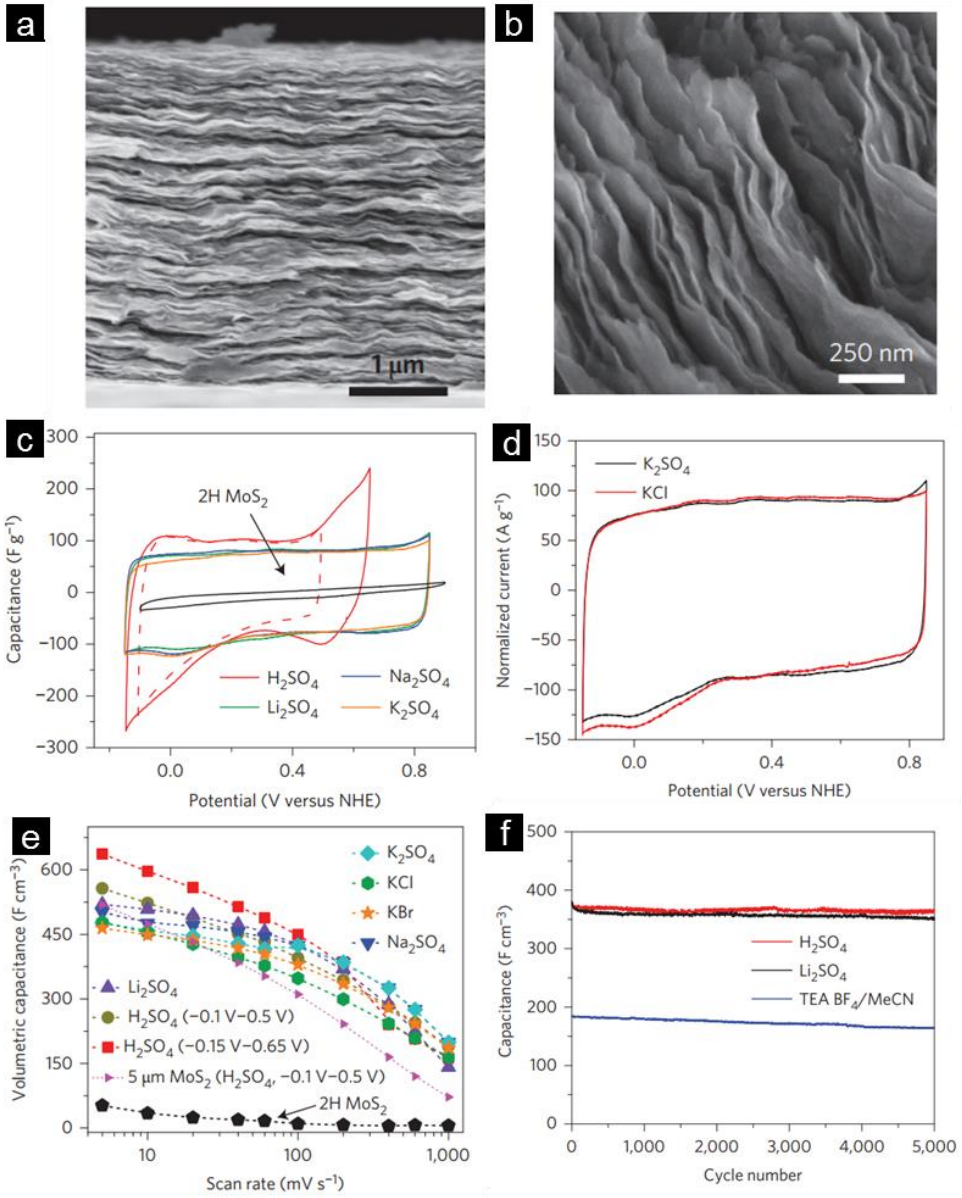

Fig. 2.14 (a-b) SEM images MoS_2 nanosheets. (c) CVs of 1T-MoS_2 electrode in different sulphate-based electrolytes at scan rates of 20 mV s^{-1}. (d) CV curves in 0.5 M K_2SO_4 and 1 M KCl. (e) Volumetric capacitance of the MoS_2 electrode in different electrolytes. (f) Cycling stability of 5000 cycles in 0.5 M H_2SO_4, Li_2SO_4, and 1 M TEA BF_4 in acetonitrile [124].

2.2.4.4 Other metal sulfides (monometallic sulfides)

In addition to the Ni, Co, Mo sulfides, other metal sulfides such as MnS, VS_2, FeS_2, CuS and WS_2 have been investigated as electrode materials for supercapacitors [127-131]. Javed *et al.* directly grew MnS nanoparticles on a carbon textile (CT) via a hydrothermal method and applied it as binder free electrode for supercapacitors [127]. The MnS electrode showed a high specific capacitance of 710.6 F g^{-1} in aqueous LiCl solution. Furthermore, two MnS/CT electrodes were used to fabricate an all-solid-state supercapacitor with PVA-LiCl electrolyte, which exhibited high flexibility (no performance change even bending to 180^o), high power density (52.03 Wh kg^{-1} at 307.5 W kg^{-1}) and excellent stability (92.5% retention even after 10000 charge-discharge cycles). Similarly, a flexible solid-state supercapacitor based on FeS_2 nanospheres supported on carbon paper was developed, performing a capacitance of 484 F g^{-1} at 5 m Vs^{-1} [129]. Huang *et al.* synthesized a CuS nanosheet electrode, which facilitated charge transport and electrolyte diffusion during charge-discharge, delivering a specific capacitance of 833.3 F g^{-1} at 1 A g^{-1} [130].

2.2.4.5 Binary metal sulfides

Besides the monometallic sulfides, binary metal sulfides ($NiCo_2S_4$, $MnCo_2S_4$, Co_2CuS_4, Cu_2WS_4, $CoMoS_4$ etc.) also show good supercapacitor performances because of their unique structural and electrochemical properties [132-136]. Chen *et al.* prepared interconnected $NiCo_2S_4$ nanosheet arrays on a conductive carbon substrate by a one-step electrodeposition method [132]. The electrode based on $NiCo_2S_4$ presented a high capacitance of 1418 F g^{-1} at 5 A g^{-1} with excellent rate capability (1285 F g^{-1} at 100 A g^{-1}). Elshahawy *et al.* synthesized $MnCo_2S_4$ sulphospinel through a multistep hypothermal route in which the Mn-Co-OH precursor was sulphurated by NaS_2 [133]. The mesostructured $MnCo_2S_4$ provided a high specific capacitance of 1402 F g^{-1} at 1 A g^{-1} with excellent stability where 95% of the initial capacitance was maintained after 5000 cycles. Guo *et al.* reported a composite electrode with Co_2CuS_4 nanoparticles anchored on nitrogen doped graphene (Co_2CuS_4/NG) that manifested superior performances to the monometallic CoS/NG and Cu_2S/NG, reaching a high specific capacitance of 1005 F g^{-1} at 1 A g^{-1} [134]. Hu *et al.* found that semiconducting Cu_2WS_4 could be

converted to metallic Cu_2WS_4 via hydrogen incorporation, by which the electrical conductivity was significantly improved (10^{10} times higher), resulting in high supercapacitor performances (583.3 F cm^{-3} at 0.31 A cm^{-3}) [135].

2.2.5 Conducting polymers (CPs)

It is known that conducing polymers (CPs) have been considered as suitable electrode materials for supercapacitors due to their low cost, environmental stability, high electrical conductivity, high storage capacity etc. [3]. The capacitance delivered by CPs depends on redox processes. When the oxidation reaction occurs, the ions transfer from electrolyte into the polymer backbone, and a reversible process takes place during the reduction reaction. It should be noted that the redox reactions not only involve the surface layer but also the entire bulk. Moreover, as no structural changes (e.g., phase transformation) happen throughout the redox reactions, the redox processes are highly reversible.

CPs can be classified into two types according to their charging state: n-doped and p-doped. The positively-charged polymers generated via oxidation are termed as 'p-doped', while the negatively-charged polymers generated via reduction are known as 'n-doped' [3]. The common CPs for supercapacitor applications are polypyrrole (PPy), polyaniline (PANI), and poly(3,4-ethylenedioxythiophene) (PEDOT). Since the n-doping potentials of PPy and PANI are much lower than the reduction potential in a common electrolyte, they can only be p-doped [9]. Consequently, they are mostly employed as positive (cathode) electrode materials. For PANI, protons are required during the charge-discharge process, therefore acidic solution or protic solvent should be selected as electrolyte. Noticeably, CPs can only work properly in a fixed potential range, and working out of the range may cause degradation of the CPs. Hence, it is important to choose a suitable potential window.

Many studies have been conducted about applying CPs to supercapacitors. For instance, Li *et al.* used $FeCl_3$ as an oxidant to polymerize the PEDOT monomers in an aqueous media, and the obtained PEDOT electrode exhibited a specific capacitance of 100 F g^{-1} in 1 M H_2SO_4 solution [14]. Sharma *et al.* synthesized a

stable PPy film electrode with a pulse polymerization method [15]. Results demonstrated that the pulse on time determined the chain size and chain defects whereas the pulse off time controlled the polymer conjugation and orientation. A high specific capacitance of 400 F g^{-1} was obtained in an acidic electrolyte by optimizing the two parameters. Vertically aligned PANI nanowires were prepared for supercapacitors via a galvanostatic current method [137]. The electrode performed a specific capacitance of 950 F g^{-1} at 1 A g^{-1} in aqueous $HClO_4$ electrolyte.

One main problem for CPs is the swell and shrink during the intercalating/deintercalating process, which will result in mechanical destruction of the electrode and degradation of the electrochemical performance during cycling. For example, an electrode made of PPy displayed 50% degradation of its initial capacitance in the first 1000 cycles [138]. Zhu *et al.* observed that the volumetric change during the charge-discharge process caused 29.5% decline in specific capacitance on a PANI electrode after 1000 cycles in 1 M H_2SO_4 solution [139]. To overcome the low stability issue, strategies based on two directions have been proposed: designing proper microstructures and fabricating composite electrodes. Wang and co-workers reported a robust and compact freestanding electrode based on nanocellulose coupled PPy@GO nanocomposites [140]. The electrode yielded excellent stability with over 85% capacitance retention after 16000 cycles at 5 A g^{-1}, as well as a high volumetric capacitance of 198 F cm^{-3}.

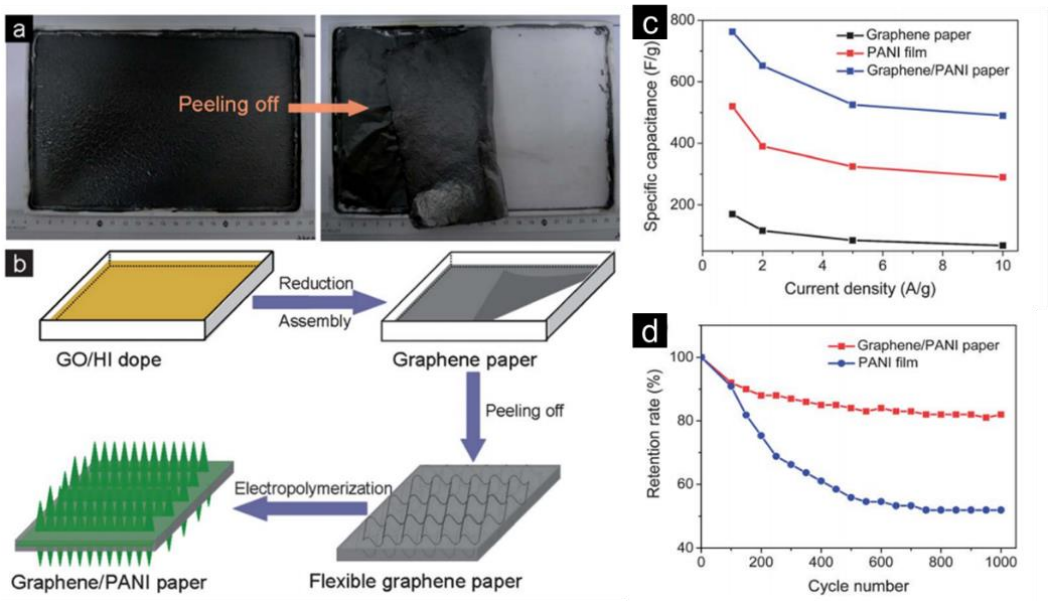

Fig. 2.15 (a) A piece of the peeling-off graphene paper on a Teflon substrate; (b) Schematic illustrations of the preparation process of the graphene–PANI paper; (c) comparison of the specific capacitance at variety of current densities for graphene paper, PANI film and graphene–PANI paper; (d) Cycle stability of PANI film and graphene–PANI paper at a current density of 5 A g^{-1} [141].

Similarly, introducing graphene can also enhance the performance of PANI. Cong *et al.* assembled a flexible graphene/PANI paper composite and compared its performances with graphene paper and PANI film prepared using the same method [141]. Fig. 2.15a shows a piece of graphene paper made by HI reduction, which can be easily peeled-off from the substrate. Fig. 2.15b illustrates the formation process of the graphene/PANI paper. PANI nanorods were directly grown on the graphene paper surface via an electroplomerization approach. Based on the hierarchical structure and synergistic effect of the graphene and PANI, the graphene/PANI paper performed a specific capacitance of 763 F g^{-1} at 1 A g^{-1}, much higher than the 180 F g^{-1} of graphene paper and 520 F g^{-1} of PANI film (Fig. 2.15c). Furthermore, the graphene/PANI electrode presented a better cycling stability than the PANI film, 82% versus 51.9% retention after 1000 cycles (Fig. 2.15d).

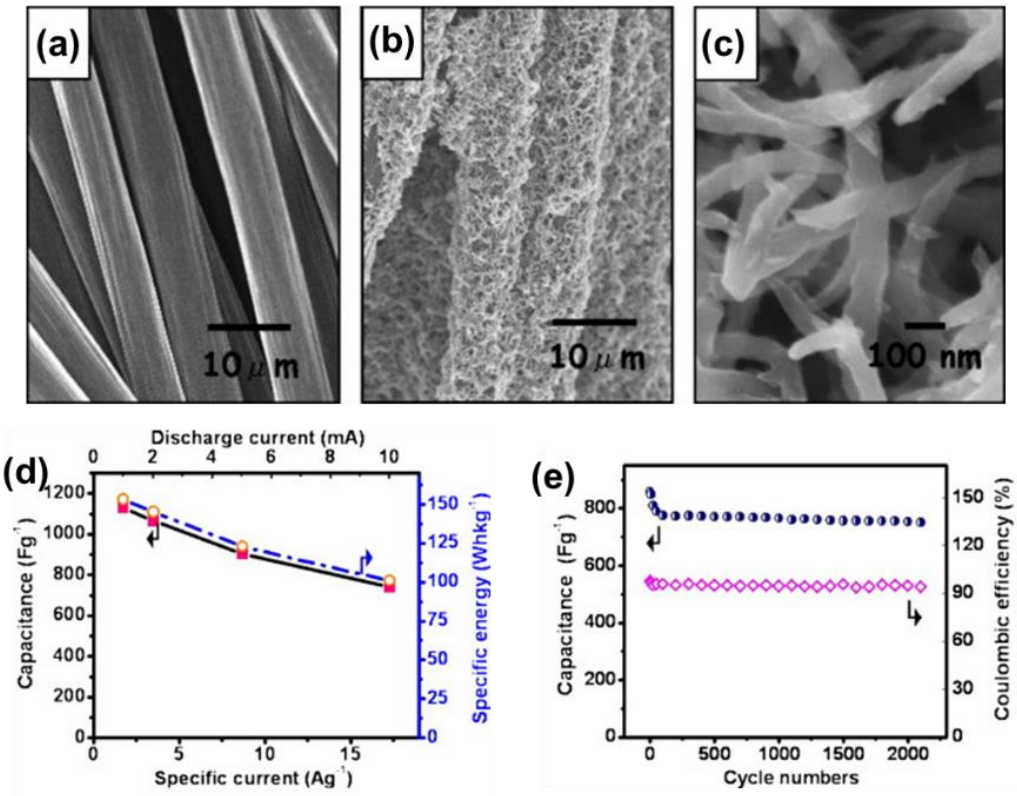

Fig. 2.16 (a) SEM images of original carbon, (b) SEM images of PANI-NWs/CC electrode, (c) higher-magnification SEM image of the PANI-NWs; (d) Specific capacitance (square) and energy (circular) at different current densities, (e) Stability tests of the PANI-NWs/CC electrode at a current density of 8.65 A g^{-1} for 2100 cycles (circular: capacitance; diamond: coulombic efficiency) [142].

In addition to graphene, CNT is another good material to combine with CPs. A nanobrush-like PANI/CNT composite electrode demonstrated a high specific capacitance of 1030 F g^{-1} with high stability (5.5% fading after 5000 cycles) [143]. Horng *et al.* successfully fabricated a PANI nanowire/carbon cloth (PANI-NWs/CC) nanocomposite electrode (Fig. 2.16a-c) [142]. This type of composite delivered an extraordinary gravimetric capacitance of 1079 F g^{-1} (areal capacitance of 1.8 F cm^{-2}) at 1.73 A g^{-1} (Fig. 2.16d), and outstanding cycling stability with 14% capacitance loss after 2100 cycles at 8.65 A g^{-1} (Fig. 2.16e). Kovalenko *et al.* discovered that embedding nanodiamond (ND) powders into CPs could greatly improve their electrochemical performances especially stability [144]. The specific capacitance of PANI-ND (3 wt% ND) electrode increased from 550 F g^{-1} to 640 F g^{-1} after 10000 cycles. The improvement of the electrode durability could be attributed to the toughening ability of the ND nanoparticles which minimized

the volume changes of the PANI during charge-discharge.

2.2.6 Hybrid electrodes

Here, we have introduced almost all kinds of common electrode materials for supercapacitors. Capacitive performances of different electrode materials are summarized in Table 2.3. Each material has its merits and drawbacks. In order to further improve their electrochemical performances, they are usually composite with others to form hybrid materials which could combine the advantages of each individual component. The most common case is metal-based materials combined with carbon materials or conducting polymers, leading to composites with largely boosted conductivity, thereby promoting the final performances including specific capacitance, rate capability and cycling life. Many examples have been discussed above, such as MnO_2/CNT, Co_3O_4/graphene, $Ni(OH)_2$/MWCNT, (PANI)/MoS_2, etc. Combinations between carbon materials and conducting polymers such as graphene/CNTs and PPy-rGO have also been introduced above. In addition, rational designed combinations among metal-based materials can also generate improved electrochemical properties due to the newly formed unique structure and synergistic effect. For instance, Zhao *et al.* found that the $MnCo_2O_4$@$Ni(OH)_2$ core-shell nanoflowers synthesized through a facile hydrothermal method exhibited superior specific capacitance to that of the pure $MnCo_2O_4$ and $Ni(OH)_2$, specifically, 2154, 474 and 590 F g^{-1} for $MnCo_2O_4$@$Ni(OH)_2$, $MnCo_2O_4$ and $Ni(OH)_2$ respectively at 5 A g^{-1} [145].

Table 2.3 Summarized capacitive performances of different electrode materials.

Category	Electrode	Specific capacitance	Electrolyte	Potential range	Cycling performance (capacitance retention)	Ref.
Carbon-based materials	AC	74 F g^{-1} at 0.5 A g^{-1}	1 M Na_2SO_4	-0.2–0.8 V vs. SCE	86.5% after 500 cycles	[146]
	Nitrogen-doped AC	115.8 F g^{-1} at 0.4 A g^{-1}	1.2 M $LiPF_6$ in EC/DEC/DMC (1:1:1)	2.0–4.5 V	76.3% after 8000 cycles	[48]
	MWCNTs	90 F g^{-1}	6 M KOH	0–1.0 V	—	[52]
	SWCNTs	180 F g^{-1} at 1 mA cm^{-2}	7.5 M KOH	0–0.9 V	—	[53]
	Graphene	205 F g^{-1} at 0.1 A g^{-1}	30 wt % KOH	0–1.0 V	90% after 1000 cycles	[11]
	Mesoporous Graphene	206 F g^{-1} at 5 mV S^{-1}	1 M H_2SO_4	-0.5–0.3 V vs. Ag/AgCl	96% after 10000 cycles	[62]
	Graphene/CNT	290.4 F g^{-1} at 0.5 A g^{-1}	1 M KCl	0–1.0 V	100% after 1300 cycles	[58]
	NG	326 F g^{-1} at 0.2 A g^{-1}	6 M KOH	−1.1–0 V vs. SCE	100% after 2000 cycles	[64]
Metal oxides/hydroxides	$RuO_2 \cdot 0.58H_2O$	850 F g^{-1} at 2 mV S^{-1}	0.5 M H_2SO_4	0.2–0.8 V vs. NHE	—	[68]
	$RuO_2 \cdot nH_2O$	1340 F g^{-1} at 25 mV S^{-1}	0.5 M H_2SO_4	0–1.05 V vs. Ag/AgCl	—	[69]
	Amorphous $MnO_2 \cdot nH_2O$	203 F g^{-1} at 2 mA cm^{-2}	2 M KCl	−0.2–1.0 V vs. SCE	100% after 100 cycles	[70]
	MnO_2 nanowires	350 F g^{-1} at 0.1 mA cm^{-2}	0.1 M Na_2SO_4	0–0.9 V vs. SCE	—	[71]
	MnO_2 micro flowers	376 F g^{-1} at 5 mA cm^{-2}	1 M Na_2SO_4	-0.2–0.8 V vs. Ag/AgCl	138% after 2500 cycles	[72]
	MnO_2/graphene	450 F g^{-1} at 1 A g^{-1}	6 M KOH	-1.0–0 V vs. SCE	100% after 5000 cycles	[74]
	MnO_2/CNT sponge	1230 F g^{-1} at 1 mV S^{-1}	1 M Na_2SO_4	-0.2–0.8 V vs. Ag/AgCl	98% after 100000 cycles	[75]
	V_2O_5 nanosheets	451 F g^{-1} at 0.5 A g^{-1}	1 M Na_2SO_4	-1.0–1.0 V	~90% after 4000 cycles	[78]

V_2O_5 nanowires	832 F g^{-1} at 1 A g^{-1}	1 M Na_2SO_4	-1.0–1.0 V	94.6% after 10000 cycles	[79]
V_2O_5 nanowire/CNT	440 F g^{-1} at 0.25 A g^{-1}	1 M Na_2SO_4	0–0.8 V vs. Ag/AgCl	90% after 100 cycles	[80]
V_2O_5 nanorod/rGO	537 F g^{-1} at 1 A g^{-1}	8 M LiCl	-0.3–0.7 V vs. Ag/AgCl	84% after 1000 cycles	[76]
NiO nanoflakes	401 F g^{-1} at 0.5 mA cm^{-2}	2 M KOH	0–0.45 V vs. Ag/AgCl	92% after 500 cycles	[82]
Co_3O_4 nanosheets	2735 F g^{-1} at 2 A g^{-1}	2 M KOH	0–0.45 V vs. SCE	99% after 3000 cycles	[83]
$Ni(OH)_2$	2217 F g^{-1} at 1 mV S^{-1}	1 M NaOH	0–0.5 V vs. Ag/AgCl	—	[84]
$Co(OH)_2$	549 F g^{-1} at 1 mV S^{-1}	1 M NaOH	-0.2–0.5 V vs. Ag/AgCl	—	[84]
$Ni(OH)_2$ nanowalls	2675 F g^{-1} at 5 mA cm^{-2}	1 M NaOH	0–0.45 V vs. SCE	>96% after 500 cycles	[85]
Co_3O_4/graphene	3482 F g^{-1} at 1 mV S^{-1}	2 M KOH	0.25–0.75 V vs. Hg/HgO	>86.2% after 20000 cycles	[86]
$Ni(OH)_2$/MWCNT	1487 F g^{-1} at 5 mV S^{-1}	2 M KOH	0–0.7 V vs. Ag/AgCl	96% after 1000 cycles	[81]
FeOOH nanosheets	310.3 F g^{-1} at 0.13 A g^{-1}	1 M Li_2SO_4	-0.8–-0.1 V vs. Ag/AgCl	—	[88]
FeOOH	1066 F g^{-1} at 1 A g^{-1}	2 M KOH	-1.2–0 V vs. SCE	91% after 10000 cycles	[147]
Fe_2O_3 nanoneedles	418.7 F g^{-1} at 10 mV S^{-1}	1 M Na_2SO_4	-0.8–0 V vs. Ag/AgCl	93.3% after 5000 cycles	[89]
Oxygen-deficient Fe_2O_3 nanorods	382.7 mF cm^{-2} at 0.5 mA cm^{-2}	3 M LiCl	-0.8–0 V vs. SCE	95.2% after 10000 cycles	[90]
Fe_3O_4/rGO	220.1 F g^{-1} at 0.5 A g^{-1}	1 M KOH	-1.0–0 V vs. Hg/HgO	100% after 3000 cycles	[91]
Ti-doped FeOOH	3322 mF cm^{-2} at 2 mA cm^{-2}	1 M Na_2SO_4	-0.9–0 V vs. SCE	94.7% after 6000 cycles	[92]
$NiCo_2O_4$	1650 F g^{-1} at 1 A g^{-1}	3 M KOH	0–0.4 V vs. SCE	91.8% after 2000 cycles	[93]
$MnMoO_4$/$CoMoO_4$	187.1 F g^{-1} at 1 A g^{-1}	2 M NaOH	-0.6–0.4 V vs. Ag/AgCl	98% after 1000 cycles	[94]
$MnCo_2O_4$@$Ni(OH)_2$	2154 F g^{-1} at 5 A g^{-1}	2 M KOH	0–0.45 V vs. SCE	90% after 2500 cycles	[145]
$CoFe_2O_4$	1790 F g^{-1} at 2 A g^{-1}	6 M KOH	0–0.4 V vs. Ag/AgCl	98% after 500 cycles	[95]
$ZnCo_2O_4$ nanorods	1400 F g^{-1} at 1 A g^{-1}	PVA/KOH	0–0.4 V vs. Hg/HgO	97% after 1000 cycles	[96]

	$NiMoO_4$ nanowires	1587 F g^{-1} at 5 mA cm^{-2}	2 M KOH	0–0.65 V vs. SCE	76.9% after 4000 cycles	[97]
	$FeMoO_4$/graphene	135 F g^{-1} at 1 A g^{-1}	1 M Na_2SO_3	-0.75–0.15 V vs. SCE	70.4% after 500 cycles	[98]
	$Ag_6Mo_{10}O_{33}$	398 C g^{-1} at 1 mV S^{-1}	2 M KOH	-0.4–0.85 V vs. Ag/AgCl	68% after 2500 cycles	[99]
	TiO_2 nanotubes	3.24 mF cm^{-2} at 100 mV S^{-1}	0.5 M Na_2SO_4	0–0.8 V vs. Ag/AgCl	96.9% after 10000 cycles	[101]
	TiO_2/graphene	84 F g^{-1} at 10 mV S^{-1}	1 M KOH	-0.05–0.5 V vs. SCE	87.5% after 1000 cycles	[102]
	MoO_3/rGO	291 F g^{-1} at 2 mV S^{-1}	1 M Na_2SO_4	-1.0–0 V vs. Ag/AgCl	>100% after 1000 cycles	[103]
	Bi_2O_3 nanosheets	530 mF cm^{-2} at 1 mA cm^{-2}	1 M KOH	-1.0–0 V vs. Hg/HgO	87% after 2000 cycles	[148]
	Oxygen-deficient Bi_2O_3/graphene	681 F g^{-1} at 1 mA cm^{-2}	6 M KOH	-1.0–0 V vs. Hg/HgO	90% after 1000 cycles	[104]
Metal nitrides	TiN	238 F g^{-1} at 2 mV S^{-1}	1 M KOH	-0.8–0.2 V vs. Hg/HgO	86% after 1000 cycles	[107]
	TiN nanowires	123 F g^{-1} at 10 mV S^{-1}	PVA/KOH	-1.0–0 V vs. Ag/AgCl	82% after 15000 cycles	[108]
	TiN/graphene	333.7 F g^{-1} at 1 A g^{-1}	1 M KOH	-0.8– -0.2 V	86.1% after 1000 cycles	[109]
	VN nanofibers	291.5 F g^{-1} at 0.5 A g^{-1}	1 M KOH	-1.0–0.1 V vs. SCE	50% after 1000 cycles	[110]
	VN nanowires	298.5 F g^{-1} at 10 mV S^{-1}	PVA/LiCl	-1.2–0 V vs. SCE	95% after 10000 cycles	[111]
	Core-shell TiN/VN	170 F g^{-1} at 2 mV S^{-1}	1 M KOH	-1.1–0 V vs. Hg/HgO	89% after 500 cycles	[112]
	Core-shell TiN/VN	247.5 F g^{-1} at 2 mV S^{-1}	1 M KOH	-1.2– -0.2 V vs. SCE	88% after 500 cycles	[113]
	NiN_3 nanosheets	990 F g^{-1} at 10 mA cm^{-2}	6 M KOH	-0.05–0.45 V vs. Ag/AgCl	50% after 2000 cycles	[114]
	MoN nanosheets	928 F cm^{-3} at 2 mV S^{-1}	1 M H_2SO_4	-0.1–0.6 V vs. NHE	>95% after 25000 cycles	[115]
	Fe_2N@AC	507 F g^{-1} at 0.5 A g^{-1}	6 M KOH	-1.1–0 V vs. Hg/HgO	—	[116]
Metal sulfides	NiS nanoflowers	1122.7 F g^{-1} at 1 A g^{-1}	3 M KOH	0–0.45 V vs. Ag/AgCl	97.8% after 1000 cycles	[118]
	NiS_2 nanocubes	695 F g^{-1} at 1.25 A g^{-1}	3 M KOH	0–0.4 V vs. Hg/$HgCl_2$	93.4% after 3000 cycles	[119]
	Ni_3S_2 nanosheets	1370.4 F g^{-1} at 2 A g^{-1}	6 M KOH	0–0.5 V vs. Hg/HgO	91.4% after 1000 cycles	[120]

	CoS	980 F g^{-1} at 1 A g^{-1}	2 M KOH	0–0.55 V vs. SCE	88% after 10000 cycles	[117]
	CoS_2	654 F g^{-1} at 0.5 A g^{-1}	2 M KOH	-0.2–0.45 V vs. Hg/HgO	72% after 600 cycles	[122]
	Co_9S_8	1645 F g^{-1} at 3 A g^{-1}	2 M KOH	-0.1–0.45 V vs. SCE	94.4% after 2000 cycles	[123]
	MoS_2 nanosheets	~700 F cm^{-3} at 5 mV S^{-1}	0.5 M H_2SO_4	-0.15–0.65 V vs. NHE	97% after 5000 cycles	[124]
	MoS_2/rGO	265 F g^{-1} at 10 mV S^{-1}	1 M $HClO_4$	0.25–0.65 V vs. SHE	92% after 5000 cycles	[125]
	MoS_2/PANI	575 F g^{-1} at 1 A g^{-1}	1 M H_2SO_4	-0.4–0.6 V vs. Hg/HgO	98% after 500 cycles	[126]
	MnS	710.6 F g^{-1} at 1 mV S^{-1}	3 M LiCl	0–0.8 V vs. Ag/AgCl	92.47% after 10000 cycles	[127]
	VS_2 nanosheets	155 F g^{-1} at 1 A g^{-1}	6 M KOH	0–0.5 V vs. Ag/AgCl	99% after 5000 cycles	[128]
	FeS_2 nanospheres	484 F g^{-1} at 5 mV S^{-1}	1 M LiCl	-0.8–0.8 V vs. SCE	95.7% after 5000 cycles	[129]
	CuS nanosheets	833.3 F g^{-1} at 1 A g^{-1}	6 M KOH	-0.3–0.3 V vs. Hg/HgO	75.4% after 500 cycles	[130]
	WS_2	2813 μF cm^{-2} at 0.5 A m^{-2}	1 M H_2SO_4	-0.8– -0.2 V vs. Ag/AgCl	~30% after 2000 cycles	[131]
	$NiCo_2S_4$ nanosheets	1418 F g^{-1} at 5 A g^{-1}	1 M KOH	-0.2–0.6 V vs. Ag/AgCl	82.2% after 20000 cycles	[132]
	$MnCo_2S_4$	1402 F g^{-1} at 1 A g^{-1}	2 M KOH	0–0.45 V vs. Ag/AgCl	95% after 5000 cycles	[133]
	Co_2CuS_4/NG	1005 F g^{-1} at 1 A g^{-1}	6 M KOH	-0.1–0.5 V vs. Ag/AgCl	96.3% after 5000 cycles	[134]
	Cu_2WS_4	583.3 F cm^{-3} at 0.31 A cm^{-3}	PVA/LiCl	-0.6–0.6 V	95% after 3000 cycles	[135]
Conducting polymers	PEDOT	100 F g^{-1} at 5 mV S^{-1}	1 M H_2SO_4	0–1.0 V	70% after 17000 cycles	[14]
	PPy	400 F g^{-1}	0.5 M H_2SO_4	-1.0–1.0 V	~60% after 10000 cycles	[15]
	PANI nanowires	950 F g^{-1} at 1 A g^{-1}	1 M $HClO_4$	0–0.7 V vs. SCE	78% after 500 cycles	[137]
	MnO_2 embedded PPy	620 F g^{-1} at 5 mV S^{-1}	0.5 M Na_2SO_4	-0.5–0.5 V vs. Ag/AgCl	90% after 5000 cycles	[138]
	PANI/MWCNT	515 F g^{-1} at 1 A g^{-1}	1 M H_2SO_4	-0.2–0.75 V	94.6% after 1000 cycles	[139]
	PPy@GO	244 F g^{-1} at 0.2 A g^{-1}	2 M NaCl	0–0.8 V	>85% after 16000 cycles	[140]
	Graphene/PANI	763 F g^{-1} at 1 A g^{-1}	1 M H_2SO_4	-0.2–0.8 V vs. Ag/AgCl	82% after 1000 cycles	[141]

PANI/CNT	1030 F g^{-1} at 5 A g^{-1}	1 M H_2SO_4	-0.2–0.7 V vs. SCE	94.5% after 5000 cycles	[143]
PANI nanowires/CC	1079 F g^{-1} at 1.73 A g^{-1}	1 M H_2SO_4	0–0.7 V vs. Ag/AgCl	86% after 2100 cycles	[142]
PANI-ND	640 F g^{-1} at 1 mV S^{-1}	1 M H_2SO_4	-0.6–0.6 V	>100% after 1000 cycles	[144]

Note: SCE: saturated calomel reference electrode; NHE: normal hydrogen reference electrode; SHE: standard hydrogen electrode; AC: activated carbon; NG: nitrogen-doped graphene; rGO: reduced graphene oxide; EC: ethylene carbonate; DEC: diethyl carbonate; DMC: dimethyl carbonate; PC: propylene carbonate; CNT: carbon nanotube; SWCNTs: single-walled carbon nanotubes; MWCNTs: multi-walled carbon nanotubes; PVA: poly(vinyl alcohol); PPy: polypyrrole; PANI: polyaniline; PEDOT: Poly(3,4-ethylenedioxythiophene); CC: carbon cloth; ND: Nanodiamond.

2.3 Electrolyte

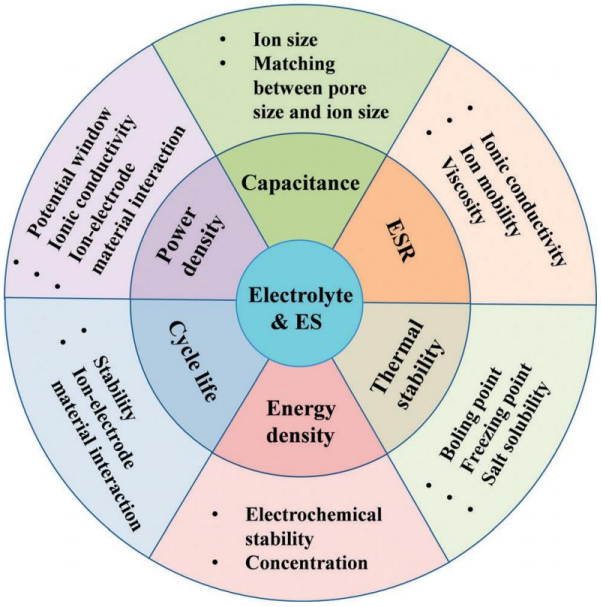

Fig. 2.17 Effects of the electrolyte on supercapacitor performances [149]. (ESR: equivalent series resistance)

Besides the electrode materials, the electrolyte is an essential component which plays a critical role in determining the supercapacitor performances in many aspects such as energy and power density, internal resistance, operating temperature range, cycling life, and so on (Fig. 2.17). Generally, the requirements for an ideal electrolyte include: wide voltage window; high ionic conductivity; high electrochemical and chemical stability; high electrochemical and chemical inertness to the supercapacitor components such as current collectors and packaging; wide operating temperature range; low volatility and flammability; low viscosity; low toxicity; low cost and availability at high purity [3, 149]. Actually, it is difficult to fulfil all the requirements with a single electrolyte, and each electrolyte has its strengths and drawbacks. A large variety of electrolytes have been developed for supercapacitors until now, and they can be classified into four types: aqueous electrolytes, organic electrolytes, ionic liquids, and solid-state polymer electrolytes.

2.3.1 Aqueous electrolytes

Aqueous electrolytes have been extensively employed for supercapacitors due to their low cost, environmental friendliness and easy assembly in air, while organic electrolytes and ionic liquids need to be processed without moisture. Normally, aqueous electrolytes display higher ionic conductivity and lower resistance compared with organic electrolytes and ionic liquids. For instance, the ionic conductivities for 1 M H_2SO_4 and 6 M KOH at 25 ^oC are about 0.8 and 0.6 S cm^{-1}, respectively, which is 10-1000 times higher than the values for organic electrolytes and ionic liquids (e.g., 0.017 S cm^{-1} for 1 M $LiPF_6$ in EC&DME (Dimethoxyethane) (1:1) at 25 ^oC) [150]. Basing on these properties, the electrode in aqueous electrolyte usually exhibit higher specific capacitance. Aqueous electrolytes can be generally grouped into acid, neutral and alkaline solutions, among which H_2SO_4, Na_2SO_4 and KOH are the most frequently used electrolytes. However, the main disadvantage of aqueous electrolytes is their narrow cell voltage window, which largely restricts the energy densities. Since the water will decompose into oxygen and hydrogen when the cell voltage is over 1.23 V, the voltage of aqueous supercapacitors is commonly around 1.0 V (many techniques have been proposed to extend the cell voltage of aqueous supercapacitors which will be discussed later). In addition, the operating temperature for aqueous supercapacitors is in a limited range as water will be freezing and boiling at 0 and 100 ^oC (1 atm), respectively.

2.3.2 Organic electrolytes

Organic electrolytes can offer a voltage as high as 3.5 V, resulting in largely enhanced energy densities for the supercapacitors, which is the major reason why the organic-based supercapacitors dominate the current commercial market [3]. Acetonitrile (ACN) and propylene carbonate (PC) are two typical solvents for organic electrolytes. ACN can dissolve larger amount of salts, but it is toxic and harmful to the environment. On the contrary, PC-based electrolytes are environment friendly, delivering a wide voltage window, wide working temperature, and good conductivity. By combining with tetraethylammonium tetrafluoroborate ($TEABF_4$), a commonly employed organic salt, $TEABF_4$/PC is formed, and it has been widely applied in supercapacitors. Nevertheless, some issues should be noticed when using organic electrolytes. Organic electrolytes are

usually expensive, volatile, flammable and toxic. Additionally, they are water sensitive thus should be processed in a strictly-controlled environment. Water content in the organic electrolytes should be kept below 3-5 ppm, otherwise, significant performance degradation and serious self-discharge will occur [9].

2.3.3 Ionic liquids

Ionic liquids are room temperature molten salts, which are entirely composed of cations and anions and free of any molecular solvent. Ionic liquids typically exhibit good physical and chemical properties, including low vapor pressure, low flammability, high thermal and chemical stability, and broad electrochemical window ranging from 2 to 6 V, typically about 4.5 V, which makes them promising candidates electrolytes for supercapacitors [3]. Moreover, the ionic liquids are solvent free thus with no solvation shell, so the ion size can be well identified. In an ionic liquid, the cation affects the negative potential window while the anion determines the positive window and melting temperature, therefore suitable combination should be designed or selected for supercapacitor applications [151]. Presently, cations of pyrrolidinium, imidazolium or aliphatic quaternary ammonium with anions of PF_6^-, BF_4^-, $TFSI^-$, or FSI^- are the commonly used ionic liquids for supercapacitors [9]. Unfortunately, some shortcomings limit the wide application of ionic liquids, such as low electrical conductivity (usually less than 10 mS cm^{-1}), prohibitive cost and stringent operating conditions (e.g., water-free environment) [152].

2.3.4 Solid-state polymer electrolytes

Solid-state polymer-electrolyte-based supercapacitors have attracted great attention in recent years because of the increasing demand of power supply for portable, wearable, printable and especially flexible electronic devices. The solid polymer electrolytes can serve as ionic conducting media and electrode separator simultaneously [9]. In addition, the solid electrolyte based supercapacitors are easy to fabricate and liquid-leakage free. Generally, the solid polymer electrolytes can be grouped into three types: dry polymer electrolyte, gel polymer electrolyte, and polyelectrolyte [149]. The dry polymer electrolyte is formed of a polymer (e.g., polyethyleneoxide (PEO)) and a salt (e.g., $LiClO_4$) without any solvent, and its

ionic conductivity is derived from the ion transport through the polymer [149]. In terms of the gel polymer electrolyte, the polymer acts as a matrix to accommodate a liquid electrolyte, so the ion transport takes place in the solvent. In polyelectrolyte, no extra salt is required, and the charged polymer chain itself provides the ionic conductivity. Among these, the gel polymer electrolyte possesses the highest conductivity due to the existence of liquid solvent. Based on this, the gel polymer electrolyte has been extensively explored while the reports regarding the other two are very limited. The most common type of gel electrolyte is mixing poly-(vinyl alcohol) (PVA) with an aqueous solution, such as PVA/H_3PO_4, PVA/H_2SO_4, PVA/KOH, PVA/LiCl, and so on [153]. However, it should be noted that there are several limitations with solid polymer electrolytes. For instance, the contact between the electrolyte and the electrode materials especially for the nonporous materials is not efficient which could generate high internal resistance and reduce the utilization of active materials, leading to poor rate capability and low specific capacitance [149].

2.4 Separator

A separator is another critical component in a supercapacitor device, which plays an important role in determining the device performance. It is usually sandwiched between the cathode and anode, which could physically sperate the two electrodes to avoid electrical short circuit. In the meantime, the separator also provides free pathways for the electrolyte ions transport. There are many parameters used to evaluate a separator, such as the permeability, absorbency, chemical stability, thickness, pore size, thermal properties etc. The permeability indicates how easily ions molecules pass through it which has large impact on the internal resistance. The absorbency reveals the wetting ability of a separator to the electrolyte. Good absorbency could reduce the internal resistance. Additionally, the chemical stability could directly influence the cycling stability and device life.

Porous membranes/mats are good candidates to fulfil these requirements and have been widely used as separators for electrochemical energy storage devices. In general, general, the separators can be grouped into porous polymeric membrane, nonwoven mat, and composite separator [154, 155]. Sun et al. compared the effects

of four different separators including nonwoven polypropylene (PP) mat, porous PP membrane, Al_2O_3-coated PP membrane, and cellulose paper on the electrochemical performance of different types supercapacitors in organic electrolytes [156]. For AC based EDLCs with 1 M $TEABF_4$/PC as electrolyte, the specific capacitance and rate capability decreased in the order of cellulose paper > Al_2O_3-coated PP membrane > PP membrane > nonwoven PP mat. In terms of the $LiNi_{0.5}Co_{0.2}Mn_{0.3}O_2$ based hybrid supercapacitors with1 M $LiPF_6$ in EC/DEC/DMC (1:1:1) as electrolyte, the devices with PP membrane and nonwoven PP mat displayed better specific capacitance and rate capability. Moreover, it was also found that the devices with cellulose separator exhibited highest self-discharge rate.

In 2016, Mandake and Karandikar compared the absorbent glass mat (AGM) and polyethylene (PE) separators for MnO_2 based supercapacitors in an aqueous K_2SO_4 electrolyte [157]. For each separator, its thickness showed neglectable impact on the device internal resistance and specific capacitance. The two separators also presented similar capacitance, but the AGM separator could generate lower internal resistance compared with the PE separator. Intestinally, a separator based on eggshell membrane (ESM) was explored for AC supercapacitors using 1 M aqueous Na_2SO_4 electrolyte. The ESM based supercapacitor exhibited good electrochemical performances with low resistance, rapid charge-discharge ability and outstanding cycling stability, which provides a new strategy for preparing low-cost, and stable biologic separator for supercapacitors.

Currently, the study of separators for supercapacitors are rare. Majority of the researches focus on electrode materials, and the tests are usually conducted in a container filled with electrolyte by leving a distance between the anode and cathode instead of using a separator. To assemble a pouch cell or coin cell, cellulose paper is commonly used. Moreover, the solid-state electrolyte can also be functioned as a separator (details in section 2.3.4). In this thesis, the cellulose paper was applied as separator for assembling the pouch cells.

2.5 Supercapacitor configurations

A typical supercapacitor unit cell is an energy storage device very similar to batteries in design, which consists of two electrodes, an electrolyte and a separator. We have summarized verities of electrode materials in section 2.2. According to the electrode materials of the two electrodes, supercapacitors can be classified into three types: symmetric supercapacitors (SSCs), asymmetric supercapacitors (ASCs) and hybrid supercapacitors (HSCs). SSCs are composed of two identical electrodes; ASCs are fabricated with two different electrodes, normally, one is an EDL carbon material and the other is a pseudocapacitance material; HSCs are combined by one battery-type electrode and one supercapacitor-type electrode.

2.5.1 Symmetric supercapacitors (SSCs)

As the positive and negative electrode materials in a SSC are identical, the involved material should work properly in both positive and negative potentials. To fulfil this requirement, the materials applied to SSCs are mainly carbon-based, ruthenium dioxide, manganese oxide, and conducting polymers. Although most of materials can work in both organic and aqueous electrolytes, aqueous electrolytes are highly preferred owing to their high ionic-conductivity, high safety, low cost, environmental friendliness and easy assembly in air [7]. However, in order to prevent the water decomposition at 1.23 V, the operating voltage for aqueous SSCs is usually around 1.0 V, which significantly restricts their energy densities (mostly below 10 Wh kg^{-1}). Galvo *et al.* fabricated an aqueous SSC based on an activated carbon xerogel with working voltage of 1 V [158]. Although its specific capacitance can reach as high as 140 F g^{-1} in Na_2SO_4 solution (single electrode value, device capacitance should be 35 F g^{-1}), its energy density was only about 4.9 Wh kg^{-1}. Chodankar *et al.* reported a MnO_2 SSC with potential window of 1 V, delivering a cell specific capacitance of 145 F g^{-1} with an energy density of 16 Wh kg^{-1} [159].

According to the equation 1.1, we know that the energy stored in a supercapacitor is proportional to square of voltage window [153]. Therefore, extending the operating voltage window would be more efficient than increasing the device capacitance in terms of energy density improvement for aqueous supercapacitors.

Abdulhakeem *et al.* built a SSC with activated graphene foam electrodes, which could reach an upper potential limit of 1.8 V [160]. To avoid oxidation of the electrode material, the cell was measured at 1.6 V, achieving a specific capacitance of 65 F g^{-1} with an energy density of 12 Wh kg^{-1} at a power density of 0.4 kW kg^{-1}, as well as good stability (almost no capacitance loss after 3000 cycles). Wang and co-workers developed a 3D RuO_2 anchored graphene and CNT hybrid foam architecture for high-performance SSCs, demonstrating an operating voltage of 1.5 V with high energy density (39.28 Wh kg^{-1}) and power density (128.01 kW kg^{-1}) [161]. Such high performances can be attributed to the high hydrogen/oxygen evolution overpotentials and enhanced electrochemical stability of the nanocrystalline of RuO_2.

Zhu *et al.* presented a 2.0 V quasi-solid-state symmetric capacitive device based on Fe_2N-Ti_2N (FTN) core-shell nanorod arrays with a gel electrolyte PVA/LiCl [106]. Fig. 2.18A shows the preparation processes of the FTN, specifically, TiO_2 was deposited on a pre-treated carbon fibre on which FeOOH nanorods grew, then the carbon fibre was annealed in ammonia. CV curves confirmed that the FTN electrode was stable from -1.0 to 1.0 V (Fig. 2.18B), thus CV and GCD measurements for the assembled symmetric device were explored within 2.0 V (Fig. 2.18C-D). The device exhibited excellent stability and rate capability (Fig. 2.18E-F), and a high energy density of 48.45 W h kg^{-1} at a power density of 2.7 kW kg^{-1} (Fig. 2.18G). Moreover, due to the high conductivity and redox reaction kinetics of the FTN nanorod structure, an extremely high power density of 27 kW kg^{-1} was achieved at a scan rate of 50 V s^{-1}. Recently, Shan *et al.* boosted the limit of potential window of aqueous SSC to an unbelievable value of 3.0 V by employing layered Mn_5O_8 in aqueous Na_2SO_4 electrolyte [162]. It was discovered that the interaction between Mn^{2+} terminated surface and hydroxylated interphase effectively suppressed the water decomposition. In addition, the layered and bivalence structure significantly facilitated the transport of Na^+, resulting in a high energy density of 23 Wh kg^{-1} with nearly 100% coulombic efficiency after 25000 cycles.

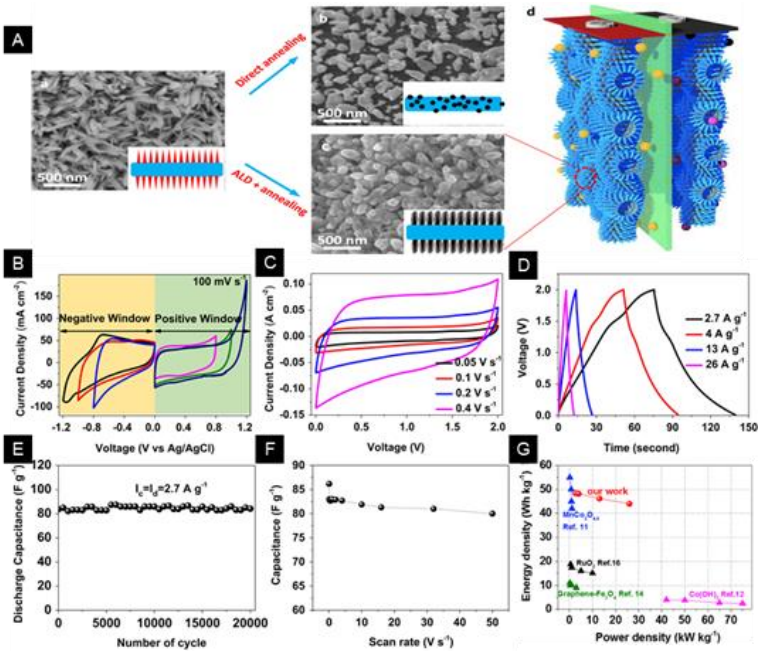

Fig. 2.18 (A) Schematic illustrations of the preparation processes of the Fe_2N-Ti_2N SSC device: (a) FeOOH nanorods grown on carbon fiber; (b) Fe_2N nanoparticles. (c) Fe_2N-Ti_2N core-shell nanorods; (d) Configuration the SSC device. (B) CV curves of Fe_2N-Ti_2N electrode in positive and negative potential range. (C) CV curves. (D) Charge-discharge curves. (E) Cycling stability. (F) Rate performance. (G) Ragone plot of the symmetric device [106].

2.5.2 Asymmetric supercapacitors (ASCs)

ASCs usually possess extended cell voltage since the different positive and negative electrodes exhibit well-separated potential windows, thus delivering high energy density compared with their symmetric counterparts [16]. To assemble an ASC, suitable materials should be selected for positive and negative electrodes. Here we can roughly divide the electrode materials into positive and negative groups according to their working potentials. Note that many materials are feasible for both positive and native electrodes, thus they belong to both two groups in principle. However, these materials are usually the electrode materials for SSCs which has been already discussed in the previous section. Here the materials are categorized based on the roles that they frequently play in ASCs. Positive electrode materials (cathode): Ni/Co oxide/hydroxide/sulfide/nitride (e.g., $Ni(OH)_2$, NiS, Co_3O_4, $NiCo_2O_4$), Mn oxide/sulfide (e.g., MnO_2, MnS), ruthenium oxide (RuO_2), titanium nitride (TiN), conducting polymers (e.g., PANI, PPy, PEDOT); negative

electrode materials (anode): carbon-based materials (e.g., AC, graphene, CNT), iron oxide/nitride (e.g., Fe_2O_3, Fe_3O_4, FeOOH, Fe_2N), vanadium oxide/nitride (e.g., V_2O_5, VN), molybdenum oxide/nitride/sulfide (e.g., MoO_3, MoS_2, Mo_3N_2), and bismuth oxide (Bi_2O_3). Theoretically, materials or their hybrids could form ASCs as long as the two electrodes are from the positive and negative groups receptively.

Depending on the charge storage mechanisms of the two electrodes, ASCs can be divided into two types: the redox//EDLCs type and the redox//redox type [16]. Redox//EDLCs ASCs integrate the features of carbon materials and pseudocapacitive materials which has been extensity investigated. For example, Cao *et al.* reported a MnO_2//graphene ASC which can be operated reversibly between 0 to 2.0 V, delivering an energy density of 25.2 Wh kg^{-1} at a power density of 100 W kg^{-1} in aqueous Na_2SO_4 electrolyte [163]. Ruof *et al.* assembled an ASC with nanoporous $Ni(OH)_2$ thin film grown on ultrathin-graphite foam ($Ni(OH)_2$/UGF) as the positive electrode and activated microwave exfoliated graphite oxide (a-MEGO) as the negative electrode, whose energy density can reach 13.4 Wh kg^{-1} with a cell voltage of 1.8 V [31]. Chen and co-workers fabricated a $NiCo_2S_4$//rGO ASC with 6 M KOH solution as electrolyte, achieving a high energy density of 31.5 Wh kg^{-1} even at a high mass loading of 49.5 mg cm^{-2} [164]. Yang *et al.* developed an all-solid-state ASC based on carbon fibre-supported PPy (CFP/PPy) cathode and rGO/CNT anode by using a potassium polyacrylate/KCl gel electrolyte [165]. Due to the unique structure, the cell displayed a stable potential window of 1.6 V, a high energy density of 28.6 Wh kg^{-1} with a maximum power density at 15.1 kW kg^{-1}, and superior cycle life of 93% retention after 2000 cycles. Additionally, other ASC systems such as RuO_2/TiO_2//AC [166], MnO_2@TiN//activated carbon cloth [167], V_2O_5//rGO [168], and so on, have been extensively investigated and good electrochemical performances have been observed.

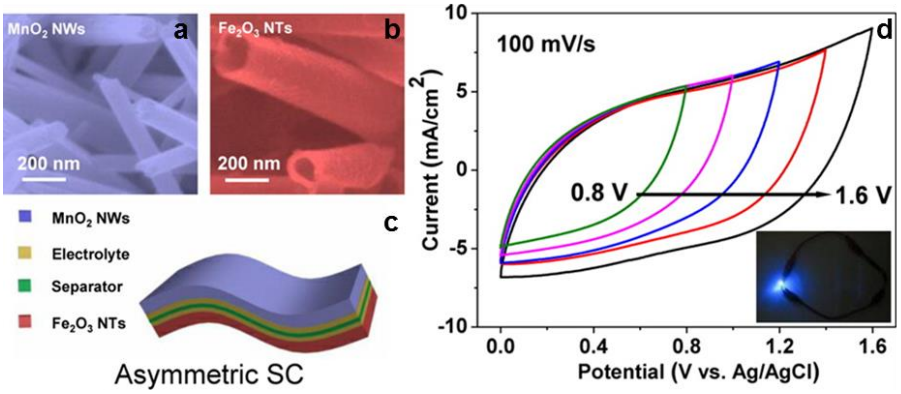

Fig. 2.19 SEM images of (a) MnO_2 nanowires and (b) Fe_2O_3 nanotubes; (c) schematic sketch of the ASC device; (d) CV curves of the assembled ASC device collected at different voltage windows (Inset demonstrates a blue LED powered by the ASC) [12].

As we know, in an ASC, the positive and negative electrodes are connected in tandem, so the attained energy density is limited by the electrode with lower capacitance. Therefore, if the EDLC electrode with low capacitance could be replaced, the energy density of ASCs will be further enhanced. From this point of view, redox//redox-type ASCs have been widely explored. By growing MnO_2 nanowires (NWs) and Fe_2O_3 nanotubes (NTs) on flexible carbon fabrics respectively (Fig. 2.19a-b). Wang *et al.* developed a flexible ASC (Fig. 2.19c) [12]. The special 1D nanostructure of the active materials provided high interfacial area and shorten the ion diffusion path during charge-discharge, resulting in a high specific energy density of 0.55 mWh cm^{-3} with a potential window of 1.6 V (Fig. 2.19d). Similarly, Gu and Wei combined CNT with MnO_2 and Fe_2O_3 to improve their conductivity [169]. Based on the MnO_2/CNT and Fe_2O_3/CNT microfilm electrodes, an all-solid-state stretchable ASC was assembled with PVA/Na_2SO_4 gel electrolyte. The ASC exhibited an extended potential window of 2.0 V, and a supreme energy density of 45.8 Wh kg^{-1} at a power density of 0.41 kW kg^{-1} with exceptional durability (98.9% retention after 10000 cycles at multiple strains).

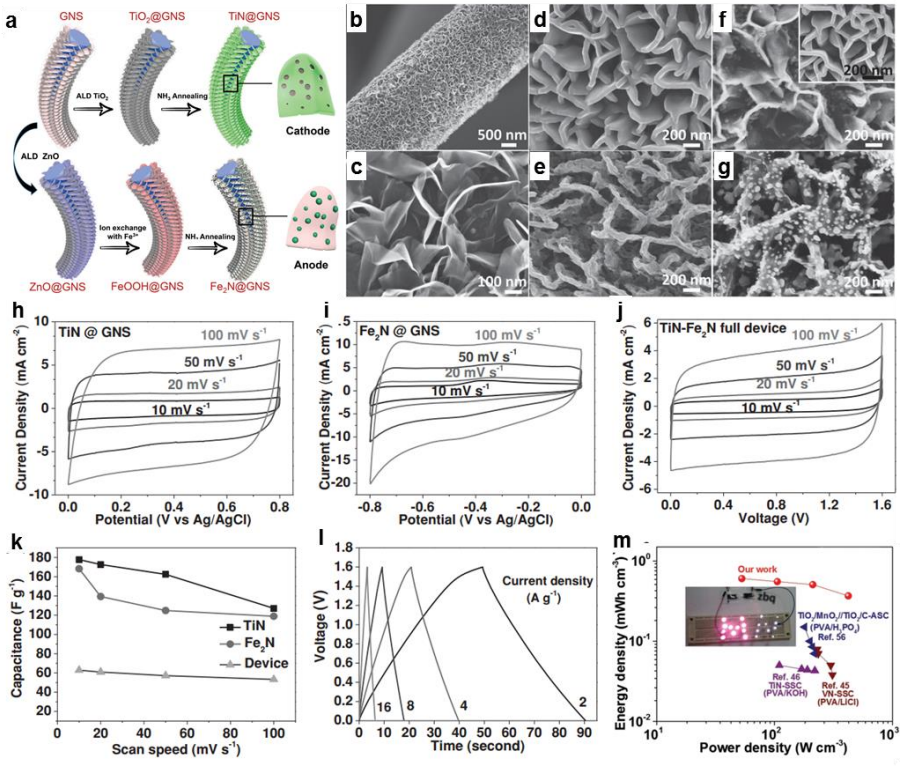

Fig. 2.20 (a) Schematics of the fabrication processes of TiN cathode and Fe_2N anode. SEM images of (b) graphene nanosheets (GNS) grown on carbon fibre, (c) GNS, (d) TiO_2@GNS, (e) TiN@GNS, f) FeOOH@GNS (inset is the ZnO@GNS), g) Fe_2N@GNS. Electrochemical performances of individual electrodes and full cell. CV curves of (h) TiN@GNS, (i) Fe_2N@GNS, (j) ASC; (k) Specific capacitances at different scan rates based on CVs; (l) Charge-discharge curves of the ASC at different current densities; (m) Ragone plots of the ASC (inset shows white and pink LEDs were lit up by the ASC) [170].

Zhu *et al.* reported an all metal nitrides ASC using TiN@GNS (GNS: graphene nanosheets) cathode and Fe_2N@GNS anode, both of which were synthesized via an ALD technique followed by an ammonia annealing process (Fig. 2.20a) [170]. All the materials showed good nanostructures which could enlarge the specific surface area (Fig. 2.20b-g). The TiN@GNS and Fe_2N@GNS exhibited stable performances at potential of 0-0.8 V and -0.8-0 V (vs. Ag/AgCl), respectively, constructing a full device with an overall cell voltage of 1.6 V (Fig. 2.20h-l). Due to the porous structure of TiN and uniform coverage of Fe_2N on the conductive GNS, the device achieved high energy density (15.4 Wh kg^{-1} or 0.55 mWh cm^{-3}) and power density (6.4 kW kg^{-1} or 220 mW cm^{-3}) with outstanding stability (98%

retention after 20000 cycles) (Fig. 2.20m). This work provides a good strategy to prepare high-performance metal nitrides for electrochemical energy storage applications.

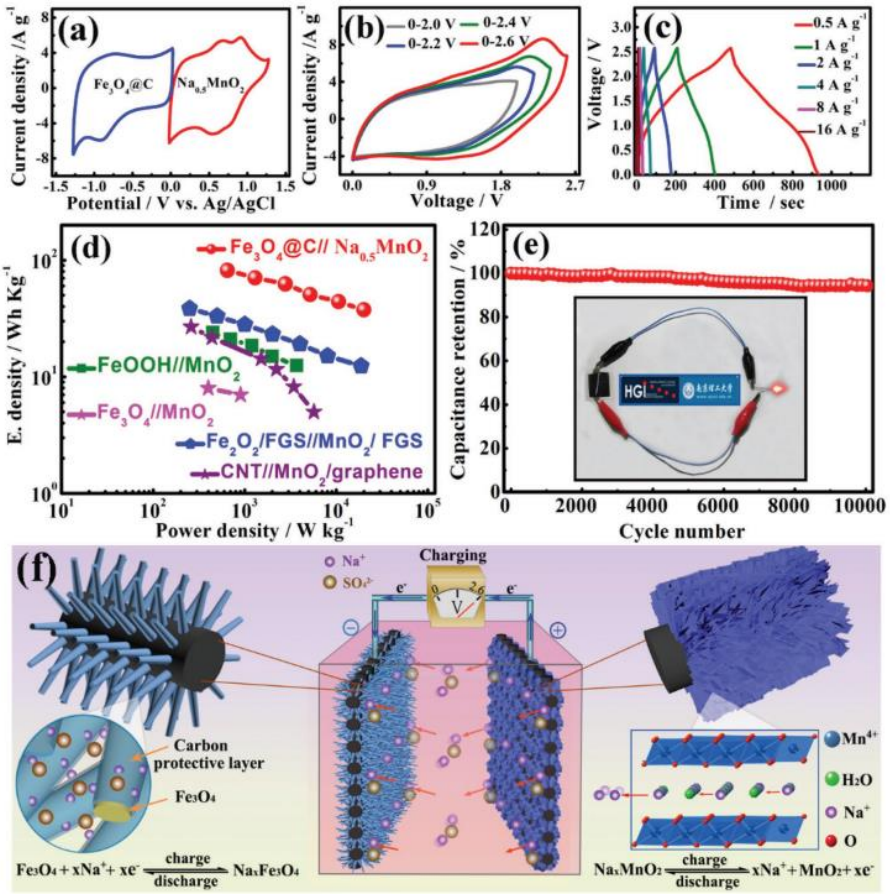

Fig. 2.21 (a) CV curves of the $Na_{0.5}MnO_2$ and the Fe_3O_4@C electrodes at a scan rate of 10 mV s^{-1}. (b) CV curves of the $Na_{0.5}MnO_2$//Fe_3O_4@C ASC in different voltage windows at 50 mV s^{-1}. (c) Charge-discharge curves of the $Na_{0.5}MnO_2$//Fe_3O_4@C ASC between 0 and 2.6 V at different current densities. d) Ragone plots of the $Na_{0.5}MnO_2$//Fe_3O_4@C ASC. (e) Cycling performance in 10000 cycles at 2 A g^{-1} (Inset shows a LED was lit up by the ASC). (f) Schematic electrode structures and charge-storage mechanisms of the anode and cathode [171].

Xia *et al.* found that the potential window of $Na_{0.5}MnO_2$ nanowall arrays and carbon-coated Fe_3O_4 (Fe_3O_4@C) could be extended to well separated ranges of 0-1.3 V and -1.3-0 (vs. Ag/AgCl) respectively in aqueous Na_2SO_4 electrolyte (Fig. 2.21a) [171]. An ASC was constructed by these two smart designed electrodes,

achieving a stable cell voltage of 2.6 V with an extremely high energy density up to 81 Wh kg^{-1} (Fig. 2.21b-d). Moreover, the $Na_{0.5}MnO_2$//Fe_3O_4@C ASC also showed outstanding cycling stability with only 7% fading after 10000 cycles (Fig. 2.21e). These excellent performances of the ASC can be attributed to the coated ultrathin carbon layer on the Fe_3O_4 that largely inhibited the gas evolution, as well as the layered structure of $Na_{0.5}MnO_2$ and nanorod morphology of Fe_3O_4@C which promoted the Na^+ insertion/extraction and charge transport (Fig. 2.21f). In addition to designing suitable electrode materials, an approach based on solution chemistry was proposed to expand the potential window of aqueous electrolyte [172]. A voltage as high as 3.2 V was achieved with a MnO_2//Fe_3O_4 ASC by employing saturated $NaClO_4$ aqueous solution as electrolyte [172]. Due to the high solubility of $NaClO_4$ in water (219.6 g per 100 g water at 25 °C, about 3.3 water molecules exist per one $NaClO_4$ molecule), almost all the hydrogen bonds could be destroyed, leading to a stronger covalent O-H bond, which significantly supressed the water decomposition.

2.5.3 Hybrid supercapacitors (HSCs)

In a hybrid supercapacitor (HSC), one battery-type electrode is serving as energy reservoir while the other capacitor-type electrode offers power capability. Consequently, both high energy and power densities can be simultaneously achieved by HSCs. In some papers, supercapacitors containing Ni/Co based electrode, such as CoS//AC [117] and $NiCo_2O_4$//MnO_2 [173] are described as HSCs. However, it was suggested that nanostructured Ni/Co based electrodes can be considered as pseudocapacitive electrodes rather than battery-type electrodes [16, 28], and we have discussed them in the ASCs part (section 2.4.2). Therefore, here we will only discuss HSCs based on traditional battery-type materials, such as PbO_2//AC, AC//$Li_4Ti_5O_{12}$ and $LiMn_2O_4$//AC.

Gao's group designed a HSC with PbO_2 thin film electrodeposited on a Ti/SnO_2 substrate as positive electrode and AC as negative electrode in H_2SO_4 electrolyte [174]. The HSC exhibited reversible charge-discharge behaviours in the voltage range of 0.8 to 1.8 V, delivering a specific energy density of 29.0 Wh kg^{-1} at a power density of 1.01 kW kg^{-1}. $Li_4Ti_5O_{12}$ is known as a superior battery material

due to its high columbic efficiency, little volume change during charge-discharge and low cost [175]. Kim and co-workers built a HSC based on graphene-wrapped $Li_4Ti_5O_{12}$ negative electrode and AC positive electrode, which was tested in an organic electrolyte between 1.0 and 2.5 V [176]. The prepared HSC achieved a high energy density of 50 Wh kg^{-1} and can even maintain 15 Wh kg^{-1} at an ultrafast charge-discharge rate of 20 s. In addition to AC, CNT is also a promising candidate to construct high-performance HSC with $Li_4Ti_5O_{12}$ [177].

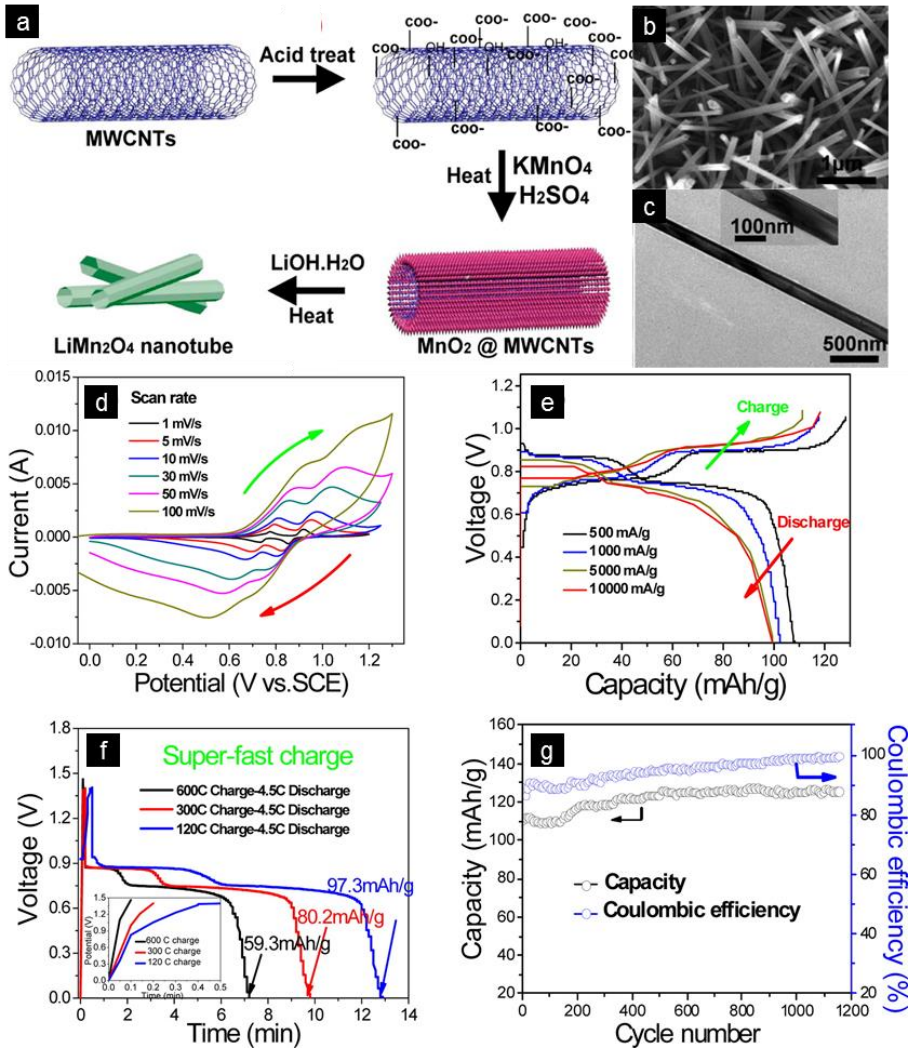

Fig. 2.22 (a) Schematic preparation processes of the $LiMn_2O_4$ nanotube. (b) SEM and (c) TEM of the prepared $LiMn_2O_4$ nanotubes. (d) CV curves of the $LiMn_2O_4$ electrode at different scan rates. (e-f) Charge-discharging curves measured at different current densities in three-electrode system. (g) Cycling performance of $LiMn_2O_4$//AC HSC (the capacity was calculated based on the weight of $LiMn_2O_4$) [178].

$LiMn_2O_4$//AC HSC was firstly presented by Wang and Xia in 2005 [179]. In aqueous Li_2SO_4 solution, the Li-ions were transferred between the two electrodes during charge-discharge process, offering a specific energy of ca. 35 Wh kg^{-1}. Tang *et al.* synthesized $LiMn_2O_4$ nanotube with exposed 400 planes by using MWCNTs template (Fig. 2.22a) [178]. The $LiMn_2O_4$ nanotubes demonstrated a uniform structure with length over 2 μm and width around 80-100 nm (Fig. 2.22b-c). Because of the nanostructure and designed crystal face, the $LiMn_2O_4$ showed excellent electrochemical performances in 0.5 M Li_2SO_4 aqueous electrolyte especially superfast charge capability (Fig. 2.22d-g). Specifically, 53.9% capacity could be maintained when the charging rate increased to 600 C (6 s). By further fabricating with AC electrode, the $LiMn_2O_4$//AC exhibited good cycling stability (no fading after 1200 cycles) and coulombic efficiency.

As mentioned above, many supercapacitor systems have been explored over the past years. The performances of supercapacitors in various device configurations are summarized in Table 2.4.

Table 2.4 Summarized performance of supercapacitors in various device configurations.

Category	Positive electrode (cathode)	Negative electrode (anode)	Electrolyte	Operating voltage	Energy density	Power density	Cycling performance (capacitance retention)	Ref.
SSCs	Activated graphene foam	Activated graphene foam	1 M Na_2SO_4	1.6 V	12 Wh kg^{-1}	0.4 kW kg^{-1}	100% after 3000 cycles	[160]
	Nitrogen-doped 3D graphene	Nitrogen-doped 3D graphene	6 M KOH	0.8 V	15.2 Wh kg^{-1}	35.1 kW kg^{-1}	93.5% after 4600 cycles	[180]
	MnO_2	MnO_2	Cellulose-Na_2SO_4 gel	1.0 V	16 Wh kg^{-1}	2.5 kW kg^{-1}	88% after 2500 cycles	[159]
	MnOOH nanosheets	MnOOH nanosheets	0.5 M $LiNO_3$	1.7 V	32.5 Wh kg^{-1}	0.85 kW kg^{-1}	84.6% after 10000 cycles	[181]
	RuO_2/graphene/CNT	RuO_2/graphene/CNT	2 M Li_2SO_4	1.5 V	39.28 Wh kg^{-1}	0.356 kW kg^{-1}	106% after 8100 cycles	[161]
	Ag-$BiVO_4$	Ag-$BiVO_4$	6 M KOH	1.6 V	38.43 Wh kg^{-1}	2.44 kW kg^{-1}	82% after 4000 cycles	[182]
	Fe_2N@Ti_2N core-shell nanorods	Fe_2N@Ti_2N core-shell nanorods	PVA/LiCl	2.0 V	48.45 Wh kg^{-1}	2.7 kW kg^{-1}	99% after 20000 cycles	[106]
	Mn_5O_8	Mn_5O_8	1 M Na_2SO_4	3.0 V	40 Wh kg^{-1}	—	85% after 25000 cycles	[162]
ASCs	MnO_2	Graphene	1 M Na_2SO_4	2.0 V	25.2 Wh kg^{-1}	0.1 kW kg^{-1}	96% after 25000 cycles	[163]
	RuO_2/TiO_2	AC	1 M KOH	1.4 V	5.7 Wh kg^{-1}	1.207 kW kg^{-1}	90% after 1000 cycles	[166]
	V_2O_5/rGO nanosheets	rGO	1 M KCl	1.6 V	75.9 Wh kg^{-1}	0.9 kW kg^{-1}	—	[168]
	TiN@MnO_2	EACC	5 M LiCl	2.0 V	1.5 mWh cm^{-3}	~1.6 W cm^{-3}	100% after 70000 cycles	[167]
	CFP/PPy	rGO/CNT	Polyacrylate/KCl	1.6 V	28.6 Wh kg^{-1}	0.395 kW kg^{-1}	93% after 2000 cycles	[165]
	$Ni(OH)_2$/UGF	a-MEGO	6 M KOH	1.8 V	13.4 Wh kg^{-1}	65 kW kg^{-1}	63.2% after 10000 cycles	[31]

	$NiMoO_4$ nanosheets	AC	2 M KOH	1.7 V	60.9 Wh kg^{-1}	0.85 kW kg^{-1}	85.7% after 10000 cycles	[183]
	$NiCo_2O_4$@MnO_2 nanosheets	AC	1 M KOH	1.5 V	37.5 Wh kg^{-1}	7.5 kW kg^{-1}	—	[184]
	$NiCo_2S_4$ nanotubes	rGO	6 M KOH	1.6 V	31.5 Wh kg^{-1}	0.157 kW kg^{-1}	—	[164]
	$Li_2Co_2(MoO_4)_3$	rGO	2 M LiOH	1.8 V	71.63 Wh kg^{-1}	0.91 kW kg^{-1}	98% after 8000 cycles	[185]
	MnO_2 nanowires	Fe_2O_3 nanotubes	PVA/LiCl	1.6 V	0.55 mWh cm^{-3}	~0.02 W cm^{-3}	84% after 5000 cycles	[12]
	MnO_2 nanoflowers	Bi_2O_3 nanoflowers	1 M Na_2SO_4	1.8 V	11.3 Wh kg^{-1}	0.35 kW kg^{-1}	80% after 4000 cycles	[35]
	MnO_2/CNT	Fe_2O_3/CNT	PVA/Na_2SO_4	2.0 V	45.8 Wh kg^{-1}	0.41 kW kg^{-1}	98.9% after 10000 cycles	[169]
	PANI nanotubes	MoO_3 nanobelts	1 M H_2SO_4	2.0 V	71.9 Wh kg^{-1}	0.254 kW kg^{-1}	78% after 1000 cycles	[186]
	TiN@GNS	Fe_2N@GNS	PVA/LiCl	1.6 V	15.4 Wh kg^{-1}	—	98% after 20000 cycles	[170]
	$Co(OH)_2$	VN	2 M KOH	1.6 V	22 Wh kg^{-1}	0.16 kW kg^{-1}	>80% after 4000 cycles	[187]
	$Na_{0.5}MnO_2$ nanowalls	Carbon-coated Fe_3O_4 nanorods	1 M Na_2SO_4	2.6 V	81 Wh kg^{-1}	0.647 kW kg^{-1}	93% after 10000 cycles	[171]
	30% MnO_2	30% Fe_3O_4	Saturated $NaClO_4$	3.2 V	24.1 Wh kg^{-1}	0.35 kW kg^{-1}	—	[172]
HSCs	PbO_2	AC	5.3 M H_2SO_4	1.8 V	29 Wh kg^{-1}	1.01 kW kg^{-1}	90% after 4500 cycles	[174]
	AC	$Li_4Ti_5O_{12}$	1 M $LiPF_6$ in EC/DMC (1:1)	2.5 V	50 Wh kg^{-1}	~0.015 kW kg^{-1}	75% after 1000 cycles	[176]

$Li_4Ti_5O_{12}$	CNT	1 M $LiPF_6$ in EC/DMC (1:1)	3.0 V	4.38 mWh cm^{-3}	~0.014 W cm^{-3}	92% after 3000 cycles	[177]
$LiMn_2O_4$	AC	1 M Li_2SO_4	1.8 V	35 Wh kg^{-1}	0.1 kW kg^{-1}	>95% after 20000 cycles	[179]

Note: HSCs: hybrid supercapacitors; ASCs: asymmetric supercapacitors; SSCs: symmetric supercapacitors; AC: activated carbon; rGO: reduced graphene oxide; CNT: carbon nanotube; UGF: ultrathin-graphite foam; GNS: graphene nanosheets; CFP: carbon fiber paper; EACC: Electrochemically activated carbon cloth; a-MEGO: activated microwave exfoliated graphite oxide; PVA: poly(vinyl alcohol); PPy: polypyrrole; PANI: polyaniline; EC: ethylene carbonate; DEC: diethyl carbonate.

2.6 Summary

In this chapter, I have reviewed the charge storage mechanisms and electrode materials for supercapacitors, including the EDLCs and pseudocapacitors. Conventional electrode materials such as carbon-based materials, metal oxides/hydroxides, metal nitrides, metal sulfides, conducting polymers, have been extensively described. It can be seen that the capacitive behaviours of a material are determined by a lot of factors such as the conductivity and microstructures. Depending on the specific characteristics of each material, corresponded methods have been developed to improve its performance, such as combining with carbon materials or conducting polymers to improve the conductivity and rational constructing nanostructures to increase the active sites and short diffusion paths for ions and electrons. In addition to the electrode materials, commonly used electrolytes, namely, aqueous, organic, ionic liquid, and solid-state polymer electrolytes have been discussed while we focus on aqueous supercapacitors in this thesis. The commonly used separators for supercapacitors in both organic and aqueous electrolytes have also been briefly introduced. Further introduction in the cell configuration demonstrates that the electrodes can be assembled into symmetric, asymmetric, and hybrid supercapacitors for practical application. It is also revealed that asymmetric or hybrid cell structure, with carbon materials as the negative electrode, could extend the cell voltage and deliver high energy density.

CHAPTER 3 Methodology

Materials characterisation is an important part in this PhD study. In this chapter, the fundamentals of the applied physical methods, including XRD, SEM, EDX, TEM, TG and UV-Vis are briefly described. In addition, electrochemical techniques used to characterize the electrochemical properties, such as CV, GCD and EIS, are also introduced.

3.1 Physical characterisations

3.1.1 X-ray Diffraction (XRD)

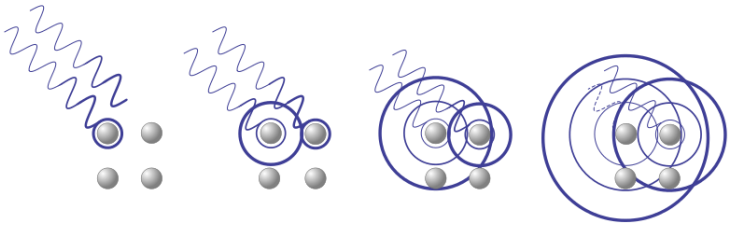

Fig. 3.1 X-rays interact with the atoms in a crystal [188].

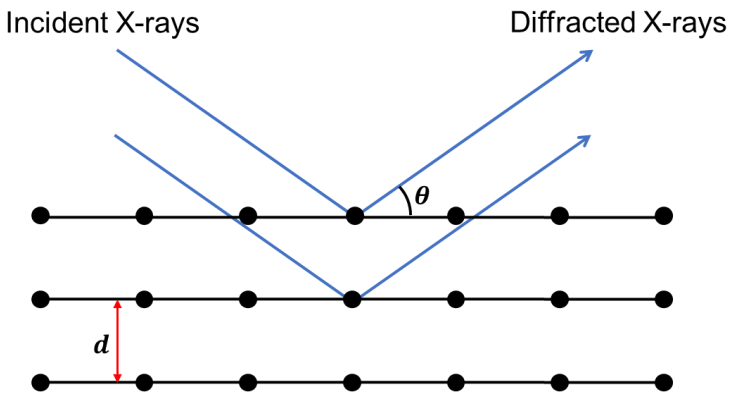

Fig. 3.2 Diffraction of X-rays.

XRD is a common technique to identify the structure, phase, atomic spacing of crystalline materials. As shown in Fig. 3.1, X-rays are scattered by the atoms of a crystal system when passing through it. The scattered waves perform as spherical waves emitted from the atomic centre. Since the atoms are periodically aligned in the crystal, there is fixed phase relationships among these spherical waves. Inevitably, the waves interfere constructively or destructively with each other, so they are intensified in some directions while offset in some other directions,

resulting in the diffraction patterns. Namely, the diffraction spots only appear in specific directions according to the original incident line. This phenomenon can be described mathematically by the Bragg's law:

$$2dsin\theta = n\lambda \tag{3.1}$$

where d is the distance between the parallel planes, θ is the incident angle, n is integer, and λ is the wavelength of X-ray. In Fig. 3.2, the path-length difference between two different X-rays can be determined as $2dsin\theta$, and the X-rays will interfere constructively when their path-length difference equals to an integer multiple of the wavelength.

As the d-spacing varies in different crystals, the corresponding diffraction patterns will be different. From this point of view, it is possible to identify the phases of a sample by comparing the obtained patterns with the standards from the database. However, the materials with same structure will exhibit similar patterns. Therefore, other factors such as the used reagents should be taken into account for indexing a correct material.

Fig. 3.3 Image of Panalytical X'Pert Pro Multi-Purpose Diffractometer (MPD)

In this thesis, all the XRD measurements were carried out on a Panalytical X'Pert Pro Multi-Purpose Diffractometer (MPD) (Fig. 3.3). The results were indexed to the ICCD database by using the software X'pert Highscore.

3.1.2 Electron Microscope

Electron Microscope is a significant technology for scientists to characterize

materials up to nanoscale. Generally, there are two types of electron microscopes, scanning electron microscope (SEM) and Transmission electron microscopy (TEM). A very high magnification can be achieved, typically 10 to half million for SEM and 2000 to one million for TEM. In SEM, electrons interact with the sample surface and the produced signals are collected by a detector (Fig. 3.4a), consequently, SEM is mainly used to examine the material surface. In TEM, electrons with higher energies can penetrate through the sample and then be collected by a detector to form images (Fig. 3.4b). TEM is basically applied to investigate the internal structure of samples.

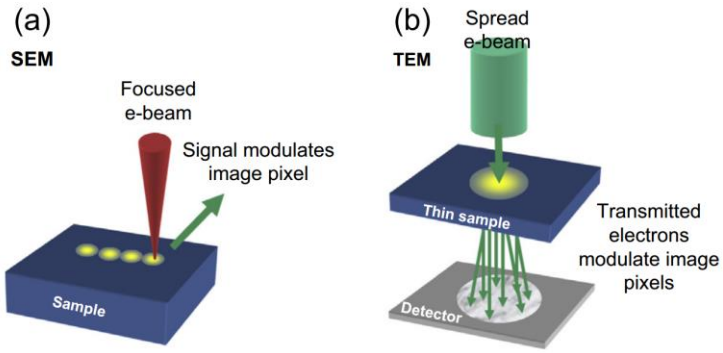

Fig. 3.4 Imaging methodology for (a) SEM and (b) TEM [189].

3.1.2.1 Scanning electron microscope (SEM)

SEM is a wildly used technique to analysis the surface morphology of specimens. Fig. 3.5 shows the layout of core components of a SEM. The electron gun, including the electron source and accelerating anode, accelerates the electrons through 1-30 kV voltage, which generates the incident electrons with energy of 1-30 keV. The electromagnetic condenser lenses focus the electron beam into a fine probe and adjust the beam astigmatism, and then the beam is scanned across the specimen by scan coils [190]. The penetration volume of electrons in the specimen is determined by the energy of the electrons, the types of encountered element in the specimen and the incident beam angle. The penetration depth increases with higher electron energy, incident angel and lighter atomic mass [191]. Normally, the 15-30 keV mode is for routine use while the low voltage operation with 1-5 keV is to reduce the electron penetration and generate high resolution images. The

interactions between the electrons and the specimen create a range of signals which are collected by various detectors to produce images.

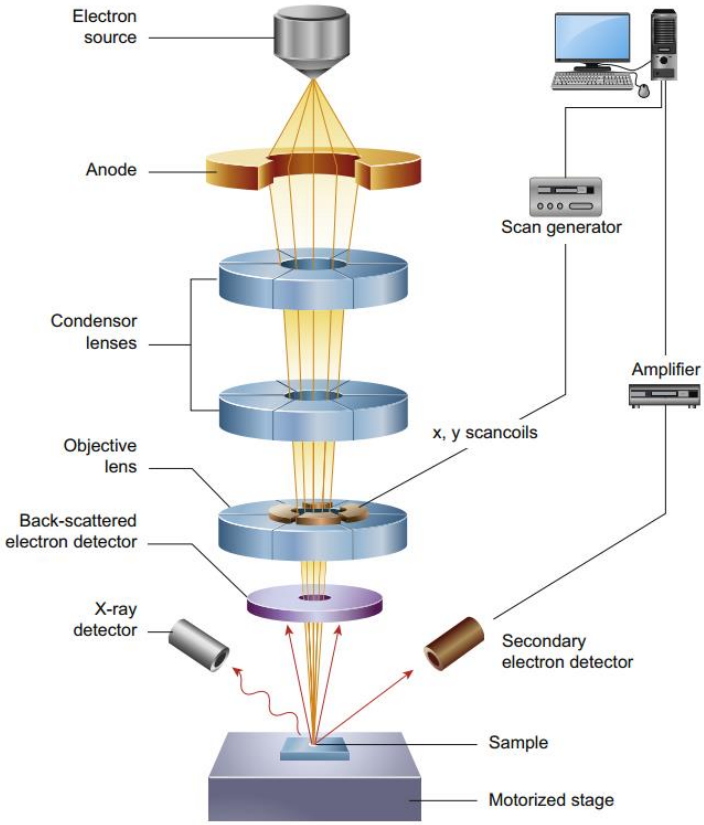

Fig. 3.5 Schematic diagram of the main components of a SEM [189].

In terms of the interactions of the incident primary electrons with the specimen, they can be divided into two classes: elastic scattering and inelastic scattering [192]. In elastic scattering, the direction of the primary electrons can be changed up to 180^{o} without kinetic energy loss, thus their wavelength is not changed. Coherent elastic scattering can cause electron diffraction, which can give the information of a crystal structure. On the contrary, the inelastic scattered electrons experience energy loss and they have a longer wavelength. The lost energy is transferred from the beam electrons to the atoms of specimen which generates varieties of valuable signals for analysing the material. The resulted signals from these interactions hold different physical properties as shown in Fig. 3.6 [193]. The secondary electrons (SEs) are those electrons with low energy (below 50 eV) mainly ejected from the outer shell of a specimen through inelastic scattering interactions. Backscattered electrons (BSEs) are the electrons scattered from nearby region of an atom nucleus after an elastic interaction, and they have much

higher energies than SEs. The Characteristic X-rays are produced via the following process [194]: when the primary electrons knock out an inner-shell electron, the outer-shell electron will jump from higher energy state to refill the vacancy, during which X-rays with specific energy are emitted. Since the X-rays of specific energy are related to the specific elements, they can be used for element analysis, which will be further discussed in EDX section. Auger electrons (AEs) are ejected from atomic layers near the surface and deliver useful message about the surface chemistry. Cathodoluminescence (CL) involves the visible or ultraviolet light emitted from semiconductors. Bremstrahlung X-rays (noncharacteristic X-rays) are generated by deceleration of the primary electrons when transmitting through the atoms.

In this thesis, SEM was employed to study the surface morphology of the prepared materials.

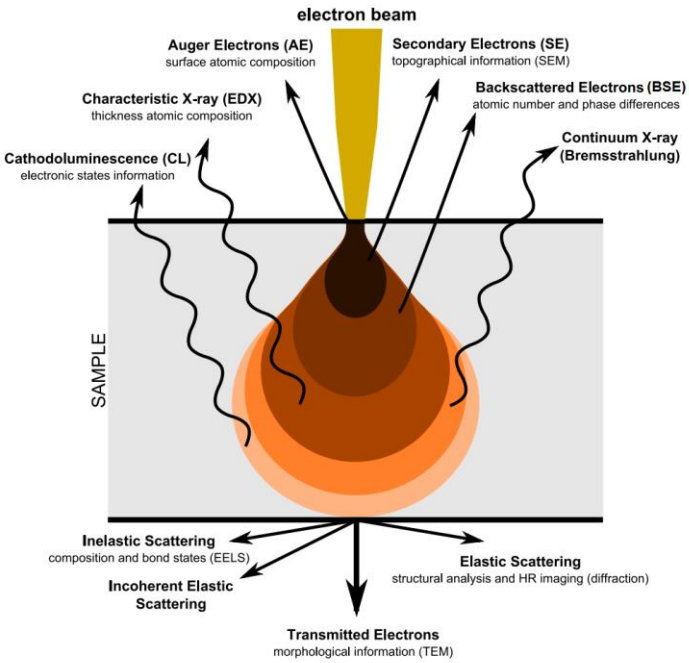

Fig. 3.6 The interaction of incident primary electrons with a specimen [195].

3.1.2.2 Energy-dispersive X-ray spectrometry (EDX)

Energy-dispersive X-ray spectroscopy (EDX) is a technique to analysis the elemental compositions of a specimen. Characteristic X-rays are produced after

the interactions of the incident primary electrons with the specimen as shown in Fig. 3.7a. Specifically, a primary electron with energy E knocks out an inner-shell electron (E_1) of an atom, leaving the atom in an excited energy state. An electron from outer-shell at E_2 orbit jumps into this vacancy. Simultaneously, a photon with energy E_1-E_2 is released, which is known as the characteristic X-ray [194]. The emitted characteristic X-rays are collected and counted by energy difference, which is named as EDX spectrum (Fig. 3.7b). Because the energy difference is matching specific electron configuration of the atom, the specific element in the specimen can be obtained by comparing the signals with the elemental standards. The sensibility of EDX to determine the chemical composition is at least around 1 wt% [196]. In this work, EDX was employed to conduct element identification and element distribution of a selected area (EDX mapping).

Today, most EDX detectors is attached to a SEM. All the SEM and EDX analysis in this thesis was carried out with a ZEISS SUPRA 55-VP instrument (Fig. 3.8).

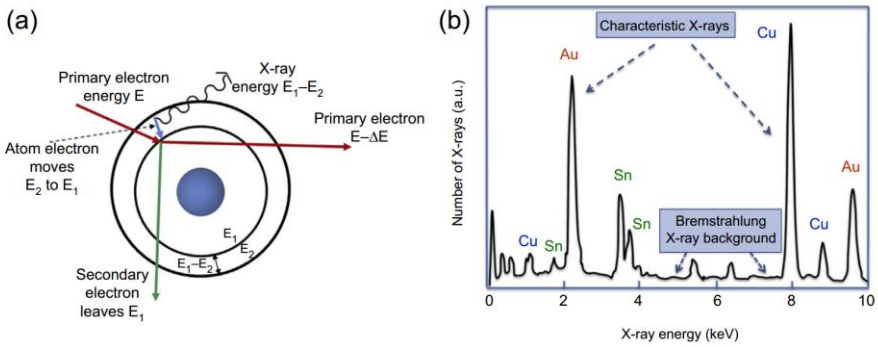

Fig. 3.7 Electron-induced X-ray emission [189]: (a) Generation of Characteristic X-ray. (b) EDX spectrum.

Fig. 3.8 Image of ZEISS SUPRA 55-VP used for SEM and EDX.

3.1.2.3 Transmission electron microscopy (TEM)

Transmission electron microscopy (TEM) is a technique to analyse the internal structure of a sample at nanometre level [197]. Fig. 3.9 shows the layout of core components of a TEM. The electrons are accelerated through the electron gun with energy of 80-300 keV, which enables them to pass through a sample up to thickness of 1 μm. In general, higher energy electrons (200-300 keV) are used for normal characterisation while lower energy electrons (<100 keV) are applied to avoid sample damage for very light elements [198]. The condenser lenses focus the electrons into a beam. The transmitted electrons are focused to form diffraction patterns and images, which can be directly exposed on a phosphor screen. Nevertheless, most TEMs are equipped with digital electron detection systems, such as digitally charged coupled device (CCD), so the images can be digitally recorded.

Similar to SEM, the electrons interact with the sample atoms via elastic and inelastic scattering in TEM. A number of different TEM imaging modes have been developed to analysis a sample from different respects, and the most common modes are: bright-field imaging, high-resolution TEM (HRTEM) and electron diffraction [198-200]. (1) Bright-field imaging: the bright-field refers to the area where most of the electrons reach the image. On the contrary, the area where most electrons are blocked appears dark. Electrons are easy to pass the regions with low thickness, low atomic number and low density. (2) HRTEM: when the sample is ultrathin and possess a uniform thickness, interference patterns are generated due to the interactions of the electron waves with the crystal lattice. These obtained patterns can provide information about atom positions, which is also known as phase contrast. (3) Electron diffraction: with the constructive and destructive interference of the scattered electrons, diffraction patterns which refer to the specific crystal structure and material orientation are formed. By analysis of the electron diffractions, crystal structure and lattice parameters can be identified.

In this thesis, all TEM images were taken with a JEOL 2100 machine (Fig. 3.10).

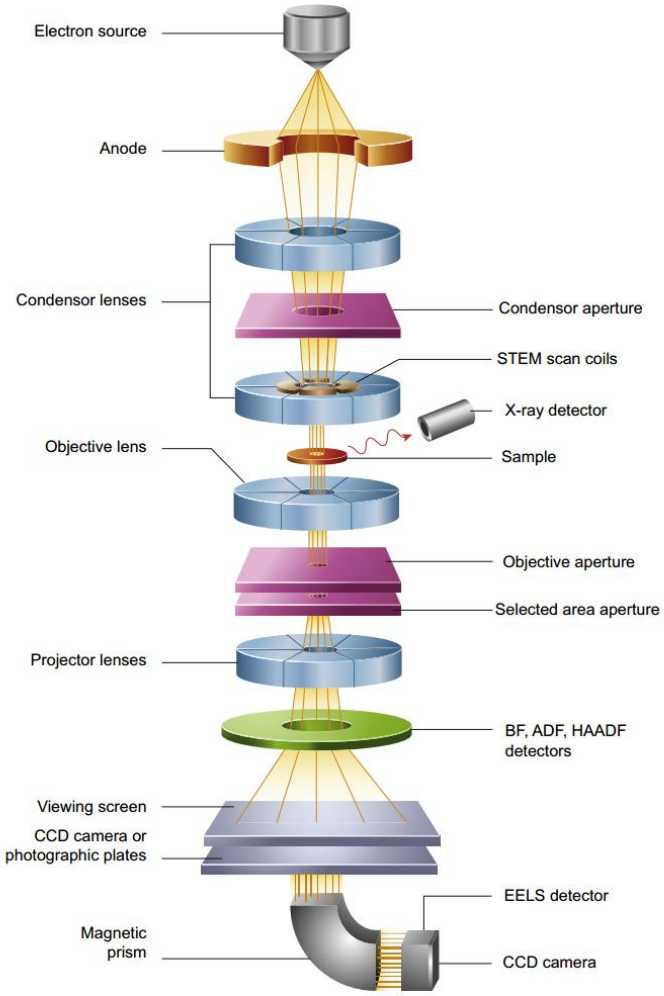

Fig. 3.9 Schematic diagram of the main components of a TEM [189].

Fig. 3.10 Image of JEOL 2100.

3.1.3 Thermal analysis

The thermogravimetric analysis (TG) is a technique in which the mass of a sample is determined as a function of temperature or time. In general, there are three modes for TG with different temperature programs (Fig. 3.11) [201]. In isothermal thermogravimetry mode, the sample mass is recorded against time at constant temperature; in quasi-isothermal thermogravimetry mode, the temperature increases as long as no weight change occurs; in dynamic thermogravimetry, the temperature is controlled to a setting point at a constant heating rate. In this thesis, all the TG tests were conducted in dynamic mode. TG curve can deliver information about thermal stability, compositions, intermediates and residue of a sample.

Beside determining the mass change of a sample, differential scanning calorimetry (DSC) is often applied together to gain more information. DSC measurement is a technique in which the difference energy inputs between a sample and a reference is recorded as a function of temperature [202]. Both the sample and the reference are subjected to the same temperature during the test. The endothermic or exothermic reactions versus temperature can be obtained.

By combing the TG and DSC results, a lot of useful information regarding the sample can be known [201, 203]. For physical phenomena: phase changes, fusion, vaporisation, sublimation, absorption, adsorption, desorption; in terms of chemical phenomena: chemisorption, dehydration, decomposition, oxidation reduction etc. Normally, endothermic processes include phase transitions, dehydration, reduction and some decomposition reactions whereas exothermic reactions include oxidation, crystallization and some decomposition reactions.

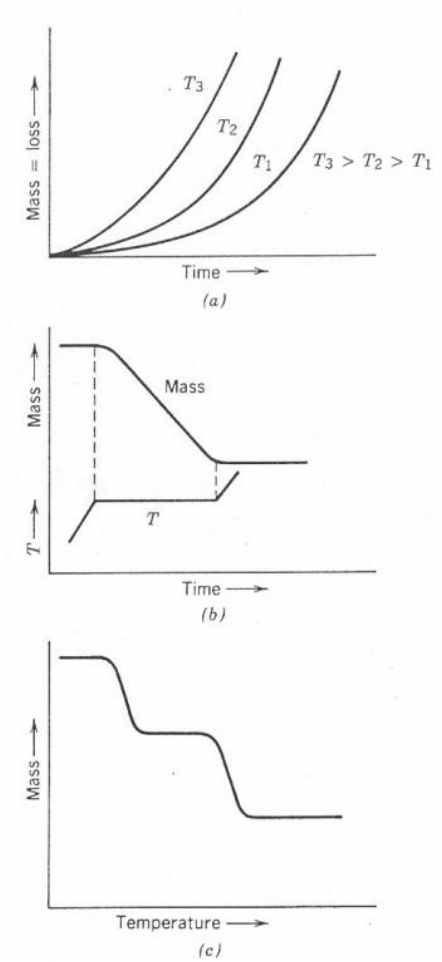

Fig. 3.11 Three modes of thermogravimetry [201]: (a) Isothermal thermogravimetry; (b) quasi-isothermal thermogravimetry; (c) dynamic thermogravimetry.

Fig. 3.12 Image of a NETZSCH 449 F3 thermal analyser.

The thermal analysis in this thesis was obtained on a NETZSCH 449 F3 thermal analyser (Fig. 3.12).

3.1.4 Ultraviolet–visible (UV-Vis) spectroscopy

Ultraviolet-visible (UV-Vis) spectroscopy is a technique to measure the absorption spectroscopy of a beam of light after passing through a sample or the reflection spectroscopy from a sample surface [202]. It is a good method in analysis of materials in chemistry, physics and biochemistry.

Nowadays, the spectral region of most commercial UV-Vis spectrometers is around 200 to 900 nm. The ranges of spectra and their limits are given in Fig. 3.13. Each atom has its orbitals, when the atoms form a molecule by a bond, the atomic orbitals merge and they are occupied by electrons at different energy levels. These electrons can be divided into three categories: single bonding (σ), multiple-bonding (π) and non-bonding (n) [204, 205]. These electrons can absorb energy in the form of ultraviolet or visible light and transmit to excited state or anti-bonding state from ground state. It is believed that the electron promotion is favoured from the highest occupied molecular orbital (HOMO) to the lowest unoccupied molecular orbital (LUMO). Fig. 3.14 demonstrates the details of the transitions [206]. σ-bond electrons have the lowest energy, so they are very stable and difficult to be excited. π-bond and n-bond electrons hold much higher energy, so the excitation is easier. Most of the transitions in the UV-Vis range are based on the left two routes in Fig. 3.14 (lowest energy input required). In a UV-Vis scan, the wavelength is changing over time. When the light energy matches the energy difference for an electronic transition, the light is absorbed by the molecule and the electrons are excited. Since the electronic transition energy is specific for a particular system, the UV-Vis spectroscopy can be used for materials characterisation. Moreover, the absorbance of a sample will be proportional to the amount of the molecules exposed to the light [207]. Therefore, UV-Vis spectroscopy can also be applied to do quantitative evaluation.

UV-Vis spectroscopy analysis is commonly conducted in solutions, but solids can be investigated as well. In this thesis, UV–visible spectra of the solid samples were obtained using a spectrophotometer (Shimadzu UV-2600) (Fig. 3.15). By using a integrating sphere, the diffuse reflection light, which is the reflected incident-light from the sample surface, is measured with barium sulphate as reference.

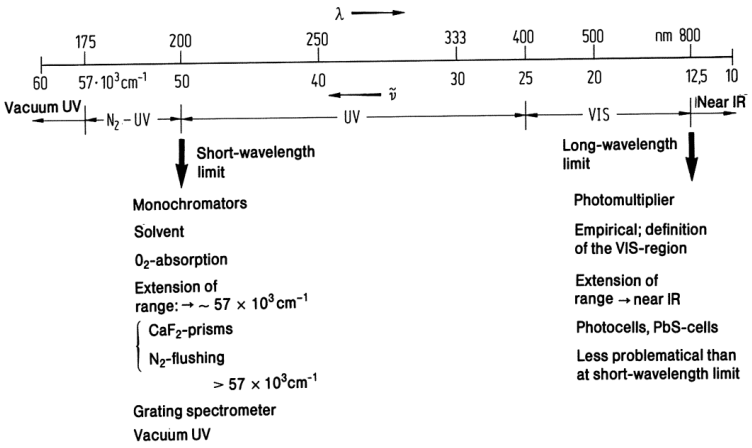

Fig. 3.13 The ranges of UV-Vis spectra and their limits [208].

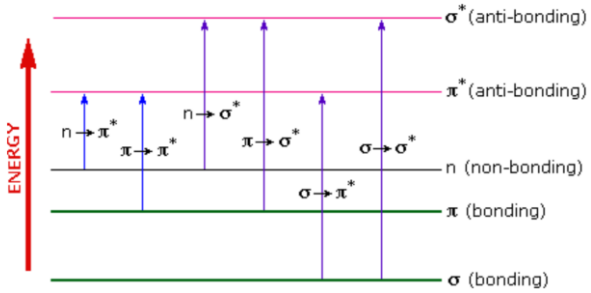

Fig. 3.14 Transitions of the electrons between bonding and anti-bonding states by absorbing of UV-Vis light [206].

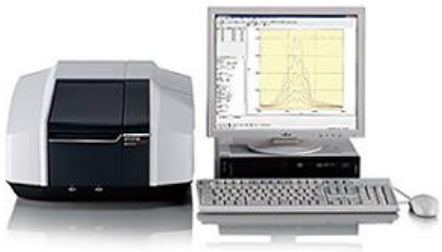

Fig. 3.15 Image of Shimadzu UV-2600.

3.2 Electrochemical measurements

3.2.1 Cell configuration

There are two cell configurations for electrochemical measurements, which are three-electrode and two-electrode modes. As shown in Fig. 3.16, a standard three-electrode system contains a working electrode (WE), which is the electrode for

studying, a counter electrode (CE) and a reference electrode (RE). In this technique, the applied potential on the WE always refer to the RE, and almost no current passes through the RE due to its high resistance. In addition, the RE is often placed as close as possible to the WE to avoid the impact of iR-drop resulted from the internal resistance of the electrolyte. The stable potential of RE makes it highly preferred for electrochemical test. Common REs include Ag/AgCl, Hg/Hg_2SO_4, saturated calomel electrode (SCE) etc. The monitored current response is between WE and CE. CE, also known as the auxiliary electrode, is usually made of inert material which will not react with the electrolyte while just to oxidize or reduce the electrolyte to maintain the current. In this thesis, the RE and CE used in three-electrode mode are Ag/AgCl and platinum mesh respectively. In terms of the two-electrode mode, it is the appropriate set-up for fully assembled cells, which is composed of working and counter electrodes. Unlike three-electrode system, both the applied potential and obtained current are with respect to CE. Two-electrode configuration is close to the final design of a real device, thus representing the performance of the electrode in real application.

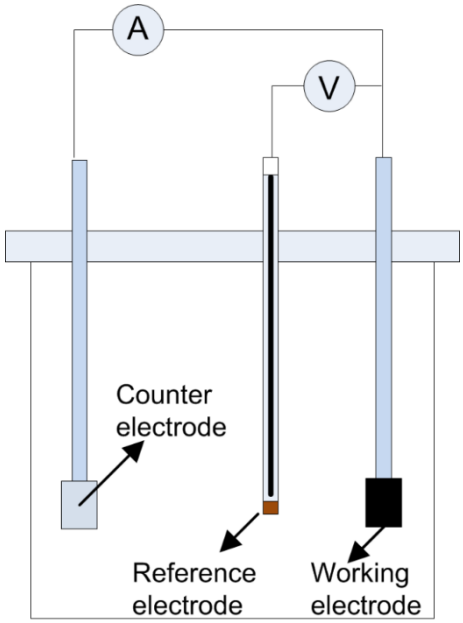

Fig. 3.16 A standard three-electrode system.

3.2.2 Cyclic voltammetry (CV)

CV is one of the most commonly used electrochemical methods. Generally, CV could provide information about kinetics of the electrode reactions, including

heterogeneous and homogeneous electron-transfer steps as well as the coupled chemical reactions [209]. In addition, the reversibility of the reactions, intermediate, phase adsorption could also be examined. Studying the control steps and reaction mechanisms is expected to be the major application of CV. For a new electrochemical system, CV is supposed to be the first-choice to make investigation.

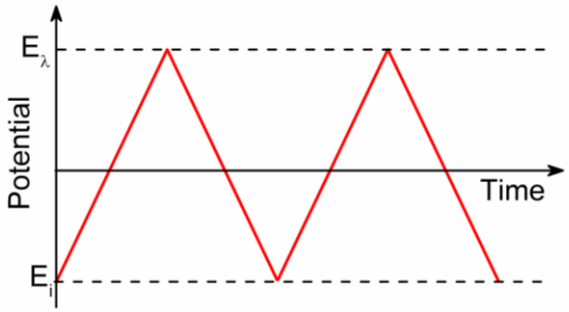

Fig. 3.17 Cyclic voltammetry waveform.

Normally, CV measurement is carried out using a stationary WE in an appropriate electrolyte. A linear potential is applied to the electrode starting from an initial value E_i, after reaching the switching potential E_λ, the potential is reversed and sweeps back to the initial value [210]. In other words, the applied potential is triangular waveform towards time (Fig. 3.17). The cycle could be repeated a number of times if necessary. Notably, scan rate is one of the most significant parameters in CV experiments, usually from several to hundreds of mV s^{-1}. During the scan, current is plotted as a function the applied potential to give the CV curves.

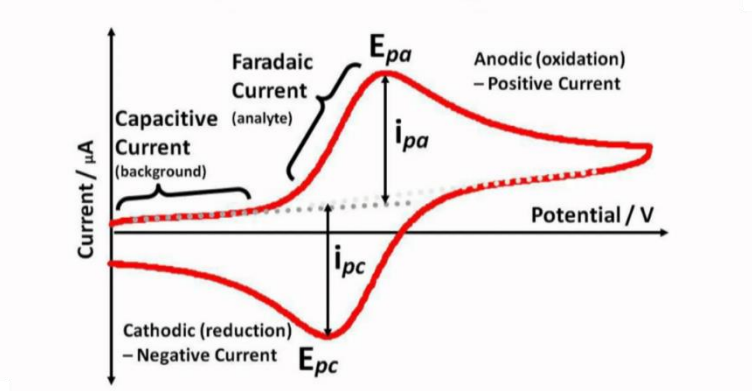

Fig. 3.18 A typical cyclic voltammogram [211].

Fig. 3.18 illustrates a typical CV curve, where $E_{pa}$is anode peak potential, E_{pc} is

cathode peak potential, $i_{pa}$is anode peak current and i_{pc} is cathode peak current. To understand a CV behaviour, it is essential to study the influence of voltage at the electrode surface. The current indicates the quantity of charge transfer. As the potential sweeps from the initial value to the switching value, the surface concentration of the reactant decreases, and the equilibrium is shifting to the state with full conversion of reactant. In addition to the faradaic current generated from oxidation of the chemicals, the capacitive current produced by the EDL formed on the electrode surface also contributes to the current response. The current reaches a maximum i_{pa} and then decays. A similar process is performed in the opposite potential direction.

Based on the CV curve, the standard redox potential can be obtained by [212]:

$$E^0 = 1/2(E_{pa} + E_{pc}) \quad (3.2)$$

The electron transfer between the electrode and the electrolyte is related to the applied potential, namely, the electron transfer rate constant for oxidation and reduction processes can be expressed as [212]:

$$k_{red} = k_0 \exp[(a-1)nF(E-E^0)/(RT)] \quad (3.3)$$

$$k_{ox} = k_0 \exp[(1-a)nF(E-E^0)/(RT)] \quad (3.4)$$

where k_0 is the standard electron transfer rate constant (cm s^{-1}) at E^0, α is the transfer coefficient, n is the number of electrons transferred, F is the Faraday constant (96485 C·mol^{-1}), E is the applied potential, R is the ideal gas constant (8.314 J·mol^{-1}·K^{-1}), and T is the absolute temperature (K).

According to equation 3.3 and 3.4, the electron transfer rate k exponentially increases with the applied potential E, therefore the current will dramatically increase when E increases. This will decrease the concentration of reactant at the electrode surface. The reactant can move from the bulk solution to the electrode via a diffusion process. Since the diffusion coefficients are very small (in the scale of 10^{-5} cm^2·s^{-1}), insufficient reactant can be supplied by the diffusion. The current drops after the reactant used up on the electrode surface. A diffusion layer formed during the reaction, and the mass transport can be described as [212]:

$$m_{trans} = [\pi nFDv/(RT)]^{1/2} \quad (3.5)$$

where D is the diffusion coefficient, ν is the scan rate. There is a competition between the electrode kinetics and mass transport, and the electrochemical behaviour is dominated by the slower step. In this regard, CV could be grouped into three types: If $k_0 >> m_{trans}$, the electron transfer rate is fast enough with respect to the sweep rate, so the established equilibrium is consistent with the thermodynamic prediction. The electrode process is reversible and diffusion controlled; If $k_0 \approx m_{trans}$, the current is determined by both mass transfer and charge transfer, and this is called quasi-reversible; If $k_0 << m_{trans}$, the charge transfer is very low thus dominates the current, and only one reaction (anodic or cathodic) presents an obvious peak in the CV curve. This is the irreversible case. To further quantify the reversibility of electrochemical reactions, a dimensionless parameter Λ is introduced [212]:

$$\Lambda = k_0/m_{trans} = k_0/[\pi nFD\nu/(RT)]^{1/2} \qquad (3.6)$$

The reversible, quasi-reversible and irreversible processes can be distinguished by the value of Λ and k_0 as listed in table 3.1.

Table 3.1 Relationship between electron transfer mechanism and values of Λ and k_0 [212].

reversible	$\Lambda > 10$	$k_0 > 0.35 \cdot \nu^{1/2}$
quasi-reversible	$10 > \Lambda > 10^{-2}$	$0.35 \cdot \nu^{1/2} > k_0 > 3.5 \cdot 10^{-4} \cdot \nu^{1/2}$
irreversible	$\Lambda < 10^{-2}$	$k_0 < 3.5 \cdot 10^{-4} \cdot \nu^{1/2}$

For reversible processes, the peak current follows Randles-Sevcik equation [213]:

$$i_p = 0.4463\,(\frac{F^3}{RT})^{1/2} n^{3/2} A D^{1/2} \nu^{1/2} C_0 \qquad (3.7)$$

At 298 K (25 °C), it is [213, 214]:

$$i_p = 2.686 \times 10^5 n^{3/2} A D^{1/2} \nu^{1/2} C_0 \qquad (3.8)$$

where i_p is the peak current (A), n is the number of electrons transferred, F is the Faraday constant (96485 C·mol^{-1}), R the ideal gas constant (8.314 J·mol^{-1}·K^{-1}), T the absolute temperature (K), A is the area of the working electrode (cm^2), D is the diffusion coefficient (cm^2·s^{-1}), ν is the scan rate (V·s^{-1}), and C_0 is the bulk electrolyte concentration (mol·cm^{-3}).

In this thesis, the materials were prepared for rechargeable energy storage devices, which means reversibility is a fundamental requirement for them. Therefore, all the applied materials performed reversible or quasi-reversible behaviours. CV was firstly used to examine the potential window of the materials. Furthermore, it was also employed to evaluate the specific capacitance of the electrode by the following equation [215, 216]:

$$C_s = \frac{1}{2mv\Delta V} \int I(V)dV \tag{3.9}$$

where C_s is the specific capacitance (F g^{-1}), m is the mass the active materials (g), v is the scan rate (V s^{-1}), I is the current at V (A), dV is the differential potential and ΔV is the potential window (V).

3.2.3 Galvanostatic charge-discharge (GCD)

The GCD is the most straightforward technique to evaluate the performance of energy storage materials, such as the specific capacitance and cycling stability. In a GCD process, a constant current is applied to the working electrode, the resulting potential is recorded as a function of time. When a constant anodic/cathodic current is applied, the reactant is oxidizing/reducing at a constant rate, consequently, the potential changes with the time due to the change of reactant concentration at the electrode surface. After the concentration of reactant deceases to zero, the electrode surface could not effectively accept the electrons provided by the constant current, leading to sharp change of the potential towards a more anodic/cathodic direction.

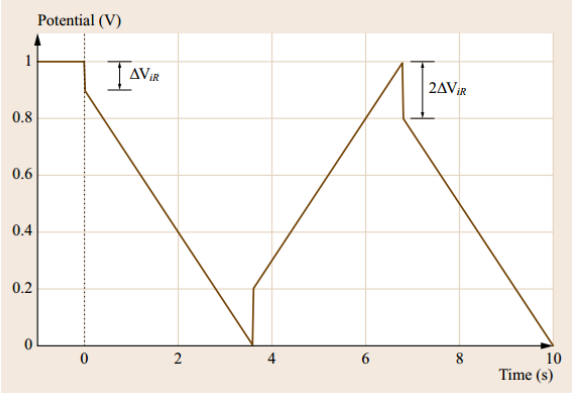

Fig. 3.19 The iR-drop during a charge–discharge cycle switch is twice as large as the voltage drop from a static voltage [24].

In a normal test. the electrode is firstly charged until the potential reaches a setting point, and then the current is suddenly changed to the opposite direction at a same value and the discharge starts. Notably, there is a iR-drop in voltage caused by the internal resistance at moment of when the current is reversed. Moreover, the iR-drop at the charge-discharge switching is twice larger than that from a static voltage (Fig. 3.19).

In this thesis, GCD curves were employed to estimate the specific capacitance and columbic efficiency. In addition, the stability performance was examined through thousands of GCD cycles.

The specific capacitance of the electrode can be calculated from the discharge curves according to the following equation [59]:

$$C_s = \frac{I \times \Delta t}{m \times \Delta V} \tag{3.10}$$

where C_s is the specific capacitance (F g^{-1}), I is the constant discharge current (A), Δt is the discharge time (s), m is the mass of the active materials (g), and ΔV is the potential change excluding the iR drop in the discharge step (V).

The coulombic efficiency can be obtained as the ratio of discharging time and charging time when the charge-discharge current densities are equal with the following equation [217]:

$$\eta = \frac{t_D}{t_C} \times 100\% \tag{3.11}$$

where η is the coulombic efficiency, t_D is the discharging time (s), t_c is the charging time.

Furthermore, the energy density and power density of a full cell can be calculated by the following equations [218, 219]:

$$E = \frac{1}{2} C_s V^2 \times \frac{1}{3.6} \tag{3.12}$$

$$P = 3600 \times \frac{E}{\Delta t} \tag{3.13}$$

where E is the energy density (Wh kg^{-1}), C_s is the specific capacitance (F g^{-1}), V is the capacitor potential window excluding the iR drop (V), P is the power density

(W kg^{-1}) and Δt is the discharge time (s). Ragone plot was obtained with the energy density and power density calculated at a series of discharge rates.

3.2.4 Electrochemical Impedance Spectroscopy (EIS)

EIS is a powerful tool in applied electrochemistry and materials science. In an EIS test, AC sinusoidal signal of potential with small amplitude in a wide frequency range is applied and the current response is recorded. Since the potential magnitude is small enough which will not disturb the equilibrium state of the system during the measurement, it is believed that EIS is a non-destructive technique to investigate an electrochemical system. By alternating the potential frequency over a wide range, the reaction steps take place at different rate constants, thus each process of the impedance component, such as equivalent series resistance (ESR), charge transfer resistance and Warburg impedance etc. could be studied separately.

In a typical EIS measurement, an input of sinusoidal potential generates a sinusoidal current output at the same frequency. The input potential and output current can be expressed as [214]:

$$V(t) = V_0 \cos(\omega t) \tag{3.14}$$

$$I(t) = I_0 \cos(\omega t - \emptyset) \tag{3.15}$$

where $V(t)$ and $I(t)$ are the time-dependent potential and current signals at time t, V_0 and I_0 are the potential and current amplitudes, ω is the angular velocity ($\omega = 2\pi f, f$ is frequency) and $\emptyset$ is the current phase shift. Based on the listed equations, the impedance can be calculated by the Ohm's law [214]:

$$Z(t) = V(t)/I(t) = Z_0 \cos(\omega t) \,/\, \cos(\omega t - \emptyset) \tag{3.16}$$

"Lissajous figure" can be obtained by plotting $V(t)$ on X-axis and $I(t)$ on Y-axis. To further process the data, we can rearrange the potential and current with Euler's formula [214]:

$$exp(j\emptyset) = \cos\emptyset + j\sin\emptyset \tag{3.17}$$

The corresponding input potential and output current can be converted to [214]:

$$V(t) = V_0 \exp(j\omega t) \tag{3.18}$$

$$I(t) = I_0 \exp[j(\omega t - \emptyset)] \tag{3.19}$$

Based on the Ohm's law, the impedance is express as [214]:

$$Z(\omega) = Z_0 \exp(j\emptyset) = Z_0(\cos\emptyset + j\sin\emptyset) \tag{3.20}$$

Finally, we get a complex number to represent the impedance. By plotting the real part on X-axis and the imaginary part on Y-axis, a "Nyquist plot" is obtained. Fig. 3.20 deconstructs an example of Nyquist plot, in which the length |Z| is the impedance, and the angel ∅ is the phase shit.

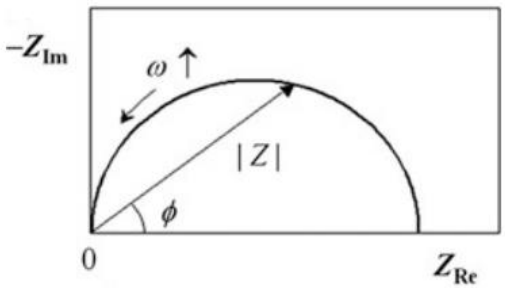

Fig. 3.20 A Nyquist plot example [214]

In a Nyquist plot, the frequency information is not provided while sometimes this is useful. So a "Bode plot" is used to meet the demand. In a Bode plot, the logarithm of absolute impedance value (log |Z|) or phase shift (∅) is plotted against the horizontal axis with logarithm of frequency (logω). The corresponding Bode plot regarding Fig 3.20 is shown in Fig. 3.21.

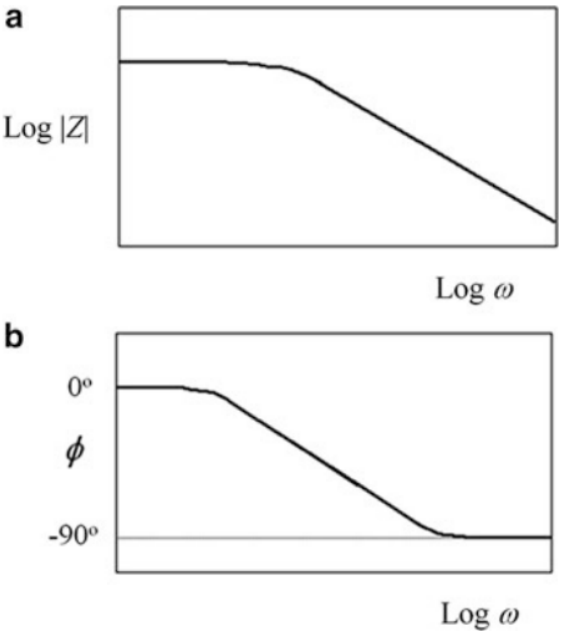

Fig. 3.21 Corresponding Bode plots for Fig. 3.20 [214].

According to measured impedance results, equivalent electronic circuit can be

developed with different physical models, such as resistor, capacitor, Warburg element, and constant phase element (CPE). The Randles circuit is a simple and frequently used equivalent circuit for interpretation of EIS data (Fig. 3.22A). It includes a resistor (R_{ct}, the charge transfer resistance), which is connected in series with the Warburg impedance (W_o), and this combined unit is connected in parallel with a capacitor (C_{dl}, the capacitance of the dielectric layer), finally they are connected in series with another resistor (R_s, the electrolyte resistance). The Nyquist plot is composed of a semicircle in high frequency region followed by a straight line in low frequency region (Fig. 3.22B). The values for R_s and R_{ct} can be easily determined from the Nyquist plot (R_s, the intercept at the X-axis; R_{ct} the diameter of the semicircle). In terms of the double layer capacitance, it follows the equation [220]:

$$\omega = 2\pi f = 1/C_{dl}R_{ct} \tag{3.21}$$

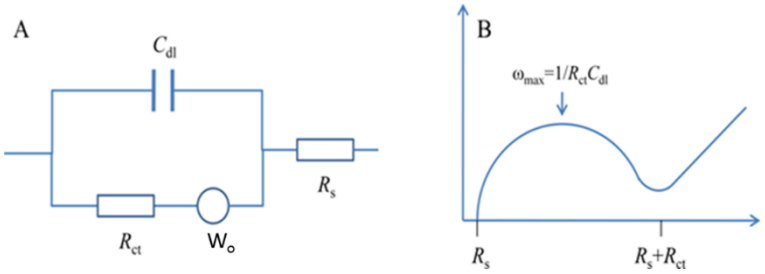

Fig. 3.22 (A) The Randles equivalent circuit and (B) its Nyquist plot [220].

The measured impedance spectra can be modelled in equivalent circuit, and by comparing the simulated and the real results, the electrochemical properties of a cell could be well understood. However, there are some limitations with the equivalent circuits [221]: the equivalent circuit for three or more elements is usually not unique, namely, different circuits can yield exactly the same data; moreover, since the real situation for an electrochemical process could be very complicated, it may be difficult to be represented by ideal circuit elements. Therefore, more attention should be paid when developing an equivalent circuit.

In this thesis, all the impedance measurement was carried out at open circuit with a potential amplitude of 5 mV. Nyquist plot was mainly used to analysis the equivalent series resistance, the charge transfer resistance and the Warburg impedance.

Fig. 3.23 Image of Solartron 1470E/1455A multichannel cell test system.

All the electrochemical measurements including CV, GCD and EIS were carried out on a Solartron 1470E/1455A multichannel cell test system (Fig. 3.23).

CHAPTER 4 Preparation of activated carbon and nitrogen-doped graphene for supercapacitors

4.1 Introduction

It is well known that that carbon materials have been frequently used as EDLC electrode for supercapacitors due to the advantages of abundance, low cost, non-toxicity, high conductivity, high specific surface area, high chemical stability, and wide operating temperature range [38]. Activated carbon (AC) and graphene are two of the most commonly used materials among various carbons.

Many efforts have been made to improve the performance of graphene. Introducing heteroatom of nitrogen into graphene to prepare nitrogen-doped graphene (NG) is a simple and efficient technique to enhance the specific capacitance and cycle stability since it manipulates the local electron donor or acceptor properties of graphene [222]. Plenty of methods have been reported to synthesize NG, such as CVD [223, 224], thermal conversion [225, 226], plasma treatment [227, 228], arc discharge [229, 230], flames [59, 231], and so on. Wei *et al.* prepared NG via a CVD process in a tube furnace with CH_4 and NH_3 as the C and N sources respectively [232]. Hou *et al.* synthesized NG by thermal annealing of graphene oxide (GO) with cyanamide, and the N content can be controlled by changing the annealing temperature [225]. With NH_3 as buffer gas, multi-layered NG was obtained by applying direct current arc discharge between pure graphite rods [229]. However, rigorous reaction conditions and complicated facilities are required to operate these processes, which limits their wide applications.

Very recently, Sun *et al.* demonstrated a hydrothermal method with GO and urea which can achieve N-doping and GO reduction in one step [233]. As shown in Fig. 4.1, during the reaction, ammonia is released from the urea and continually reacts with the GO, introducing high content of nitrogen into the graphene sheets.

In this chapter, GO was firstly prepared via a modified Hummers method. And then, NG was synthesized following the hydrothermal method with urea as the chemical dopant. Physical properties of the commercial AC and the as-prepared

NG were investigated by XRD and SEM. Their supercapacitor behaviours including CV, GCD and cycling stability were measured in three-electrode and two-electrode systems, respectively. Based on the obtained results, proper negative electrodes will be prepared for assembling ASCs in chapter 5-8.

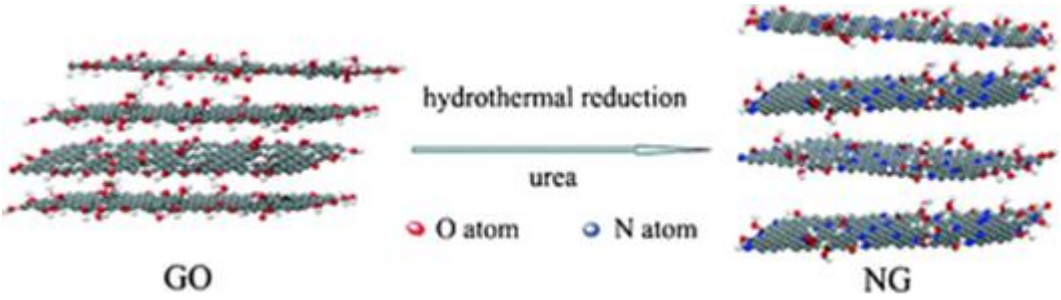

Fig. 4.1 Scheme illustration of the procedure for NG preparation [233].

4.2 Experimental

4.2.1 Preparation of graphene oxide (GO)

GO was synthesized from a modified Hummers method according to the literature [234]. Briefly, 2.0 g of graphite flakes (Sigma-Aldrich) was added to 200 mL of mixture of concentrated H_2SO_4/H_3PO_4 (9:1). 12.0 g of $KMnO_4$ was added slowly under stirring. After that, the mixture was kept at 50 ^oC for 12 h for further reaction. Then, the reaction was cooled to room temperature and poured onto 270 g of ice with 2 mL of 30% H_2O_2 solution, producing a bright yellow mixture. The solid material was collected by centrifuging, and then washed in succession with 5% HCl solution, deionized water and ethanol, respectively. Finally, the resulted GO was dispersed in water at around 20 mg mL^{-1} for further application.

4.2.2 Preparation of nitrogen-doped graphene (NG)

NG was prepared following a previous reported method with urea as the chemical dopant [64]. Briefly, 80 mg GO was dispersed in 70 mL water, and then 24 g urea was added into the suspension under sonication for 2 h. The solution was sealed in a 100 mL Teflon-lined stainless-steel autoclave and kept at 180 ^oC for 12 h. The products were collected by centrifuging, water-washing and drying at 60 ^oC under vacuum overnight.

4.2.3 Preparation of AC and NG working electrodes

The AC working electrode was prepared as follows: a homogeneous slurry composed of the commercial AC (Cabot Pearls 2000, surface area 1500 m^2 g^{-1}) and polytetrafluoroethylene (PTFE) in a mass ratio of 95 : 5 was mixed in water under magnetic stirring. The formed slurry was coated onto Ni foam (1 × 1 cm^2), pressed at 10 MPa, and finally dried at 60 ^oC under vacuum. All the Ni foams used in this thesis are the same and their properties are: porosity 97%, bulk density 0.45 g cm^{-3}, and PPI (pores per inch) 110.

The synthesized NG was mixed with carbon black (Super P) and PTFE in a weight ratio of 90 : 5 : 5. The formed slurry was then coated onto Ni foam (1 × 1 cm^2), pressed at 10 MPa, and finally dried at 60 ^oC under vacuum.

The mass loading of the active materials on each working electrode was about 1-2 mg cm^{-2}.

4.2.4 Physical characterization

X-ray Diffraction (XRD) was carried out to identify the crystal structures on a Panalytical X'Pert Pro Multi-Purpose Diffractometer (MPD) with Cu Kalpha1 radiation working at 45 kV and 40 mA. The morphologies of the samples were investigated with scanning electron microscopy (SEM) (ZEISS SUPRA 55-VP).

4.2.5 Electrochemical measurements

The performance of the prepared working electrode was firstly investigated in a standard three-electrode testing system with a piece of Pt mesh (1 × 1 cm^2) and an Ag/AgCl electrode (sat. KCl) serving as counter and reference electrodes, respectively. To fabricate the AC//AC or NG//NG symmetric supercapacitor (SSC) devices, two identical AC or NG electrodes were used as both positive and negative electrodes. The electrochemical measurements including CV and GCD were carried out on a Solartron 1470E/1455 multichannel cell test system. All the measurements were performed at room temperature with 2 M KOH aqueous solution as electrolyte.

4.3 Results and discussion

4.3.1 Activated carbon (AC)

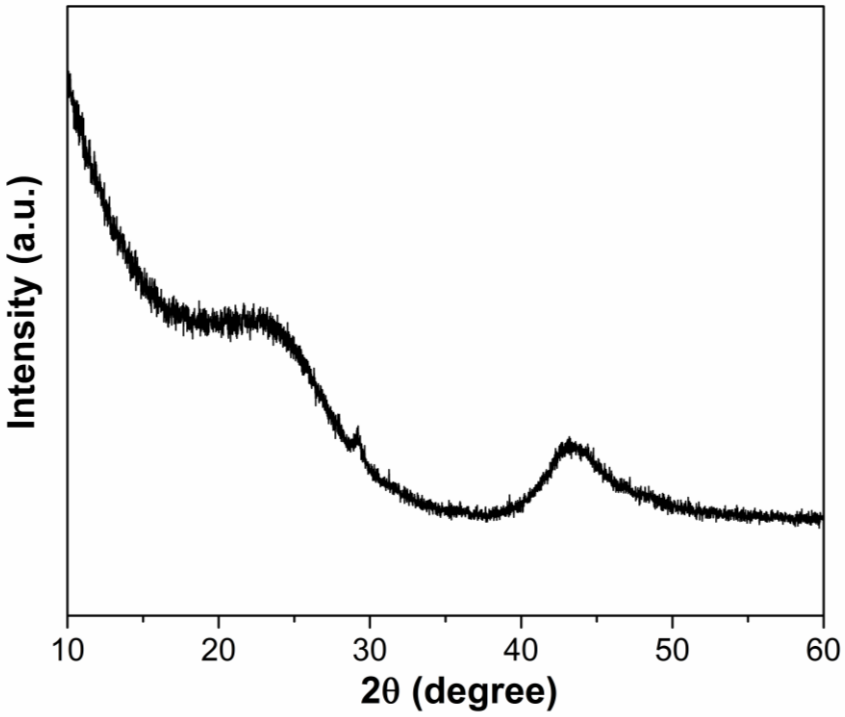

Fig. 4.2 XRD patterns of the AC.

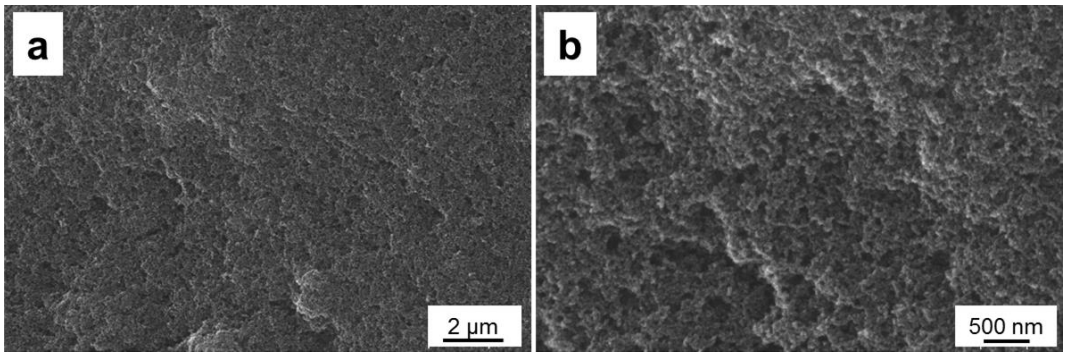

Fig. 4.3 SEM images of the AC.

Fig. 4.2 shows the XRD patterns of the commercial AC. Two broad peaks are observed at $2\theta \approx 23.5^{o}$ and 43.5^{o}, which correspond to the (002) and (100) reflections of the AC, respectively [235, 236]. The broad diffraction peaks indicate that the AC is mainly at amorphous state [237, 238].

The morphological structures of the AC were investigated by SEM. As shown in

Fig. 4.3, the AC is composed of thousands of nanoparticles, forming a porous structure, which could sever as channels for the electrolyte access during charge-discharge.

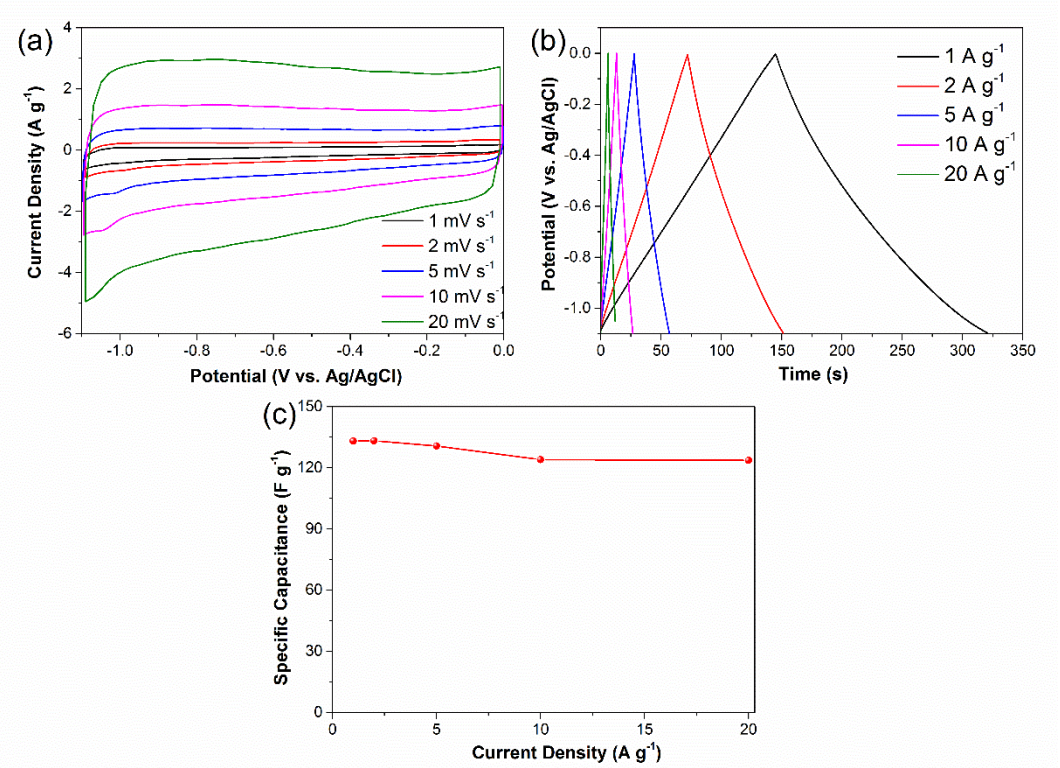

Fig. 4.4 Electrochemical performance of a single AC electrode using a three-electrode cell in 2 M KOH solution. **(a)** CV curves at various scan rates; (b) GCD curves at various current densities; (c) Specific capacitance at various current densities.

AC electrode is commonly used as the negative electrode in asymmetric or hybrid supercapacitors. Therefore, the testing potential range here was selected as -1.1 to 0 V vs. Ag/AgCl. CV curves at different scan rates from 1 to 20 mV s^{-1} are demonstrated in Fig. 4.4a. Apparently, the AC electrode displays typical EDL capacitance property at -1.1 to 0 V (vs. Ag/AgCl) in 2 M KOH electrolyte because the CV curves are nearly rectangular, and no redox peaks can be observed in this potential range. The symmetrical and linear GCD curves also indicate its EDL capacitance feature (Fig. 4.4b). The specific capacitance of the electrode can be calculated from the GCD curves according to equation 3.10. As shown in Fig. 4.4c, the capacitance can reach 133 F g^{-1} at 1 A g^{-1} and notably, the value maintains

around 92.5% even at 20 A g^{-1}, exhibiting excellent rate capability of the AC electrode, which would be an ideal negative electrode in an ASC. The slight decrease in specific capacitance of the AC at high current density is due to the insufficient time for the electrolyte ions to diffuse into inner surface the AC, which limits the contribution to the specific capacitance [239, 240].

In the next step, with AC as both positive and negative electrodes, a SSC was assembled in 2 M KOH solution. Fig. 4.5a presents the CV curves of the SSC with different voltage windows from 0.8 to 1.4 V at a scan rate of 5 mV s^{-1}. Clearly, the SSC delivers a stable performance up to 1.4 V. This is also evidenced by the GCD profiles recorded at a current density of 1 A g^{-1} (Fig. 4.5b). To avoid the water electrolysis, the working voltage of the SSC here was chosen as 1.2 V. Within 1.2 V, the SSC device maintains rectangle shaped CV curves at different scan speeds from 1 to 50 mV s^{-1} (Fig. 4.5c), indicating the EDL behavior. In addition, both the charge and discharge curves at various current densities from 0.5 to 5 A g^{-1} are in straight lines, forming triangle shaped profiles (Fig. 4.5d), which further confirms the capacitive properties. The specific capacitance of a single carbon electrode (C_{carbon}, F g^{-1}) in the SSC can be calculated based on the discharge curves with the formula [241, 242]:

$$C_{carbon} = \frac{4I \times \Delta t}{m \times \Delta V} = 4C_s \quad (4.1)$$

where I is the constant discharge current (A), Δt is the discharge time (s), m is the total mass of active materials in both positive and negative electrodes (g), ΔV is the voltage change excluding the iR drop in the discharge step (V), and C_s is the specific capacitance of the supercapacitor cell. The multiplier 4 is to adjust the capacitance of a two-electrode device to the capacitance of a single electrode. Theoretically, the SSC is composed of two single-electrodes connected in series. The capacitance of the two-electrode cell is half of the value of an individual electrode. In addition, the total mass for the two-electrode cell is twice of an individual electrode. Therefore, the specific capacitance of the two-electrode cell is $\frac{1}{4}$ of the specific capacitance of a single electrode.

According to equation 4.1, the specific capacitances of the AC//AC SSC are calculated in Fig. 4.5e. At a current density of 0.5 A g^{-1}, the capacitance reaches

103 F g^{-1} and this value gradually decreases with the increasing current density, maintaining 59.5 F g^{-1} at 5 A g^{-1}. The degradation of capacitance could be attributed to the incremental iR drop and insufficient active material involved at high current densities.

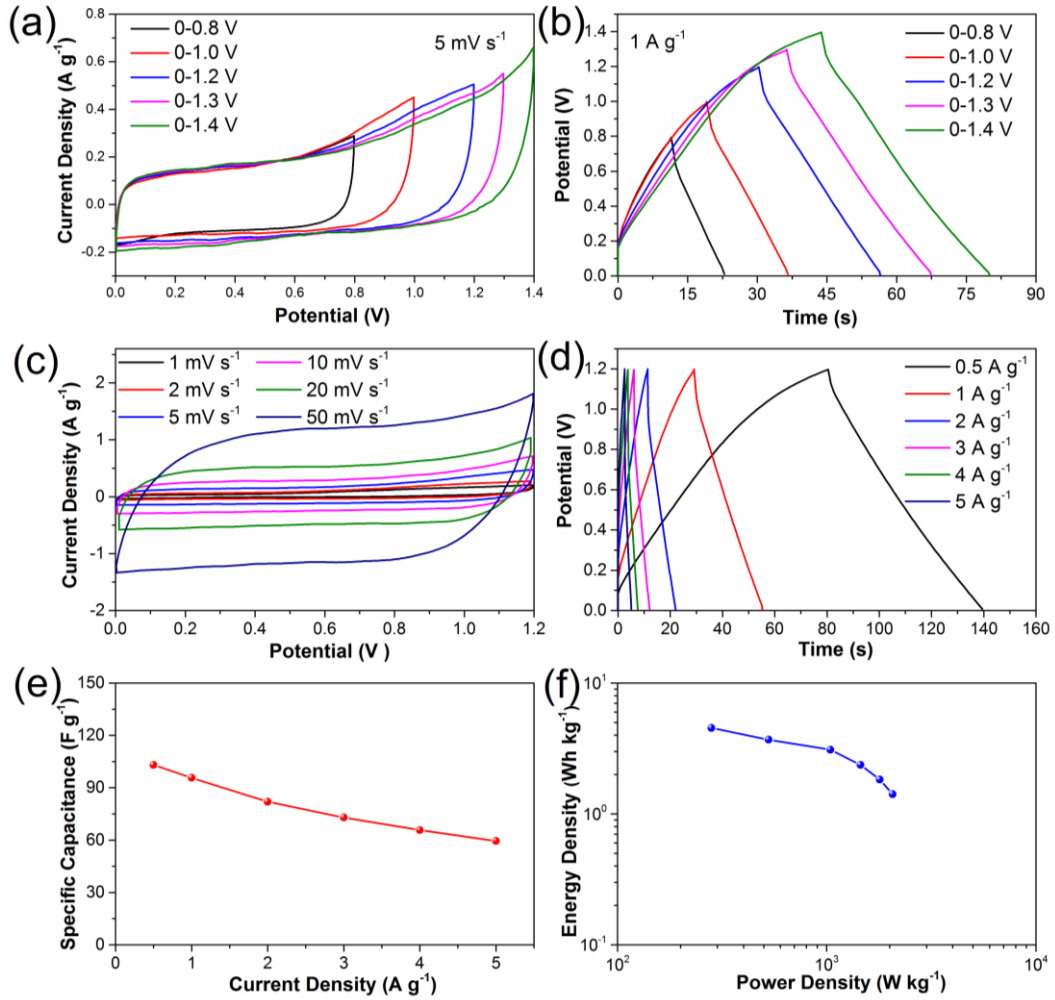

Fig. 4.5 Electrochemical performance of AC//AC SSC. (a) CV curves at different potential windows at 5mV s^{-1}; (b) GCD curves taken at constant current density of 1 A g^{-1} at different potential windows; (c) CV curves with a voltage window of 0 to 1.2 V at various scan rates; (d) GCD profiles at various current densities; (e) Specific capacitance at various current densities; (f) Ragone plots of the SSC device.

Energy and power densities are crucial parameters of a supercapacitor. The energy densities and corresponding power densities of the SSC were obtained using equation 3.12 and 3.13. The resulted energy and power data for the AC//AC SSC

is given by Ragone plot in Fig. 4.5f. The device delivers a highest energy density of 4.5 Wh kg^{-1} at a power density of 281 W kg^{-1}, and an energy density of 1.4 Wh kg^{-1} is retained at a high power density of 2069 W kg^{-1}.

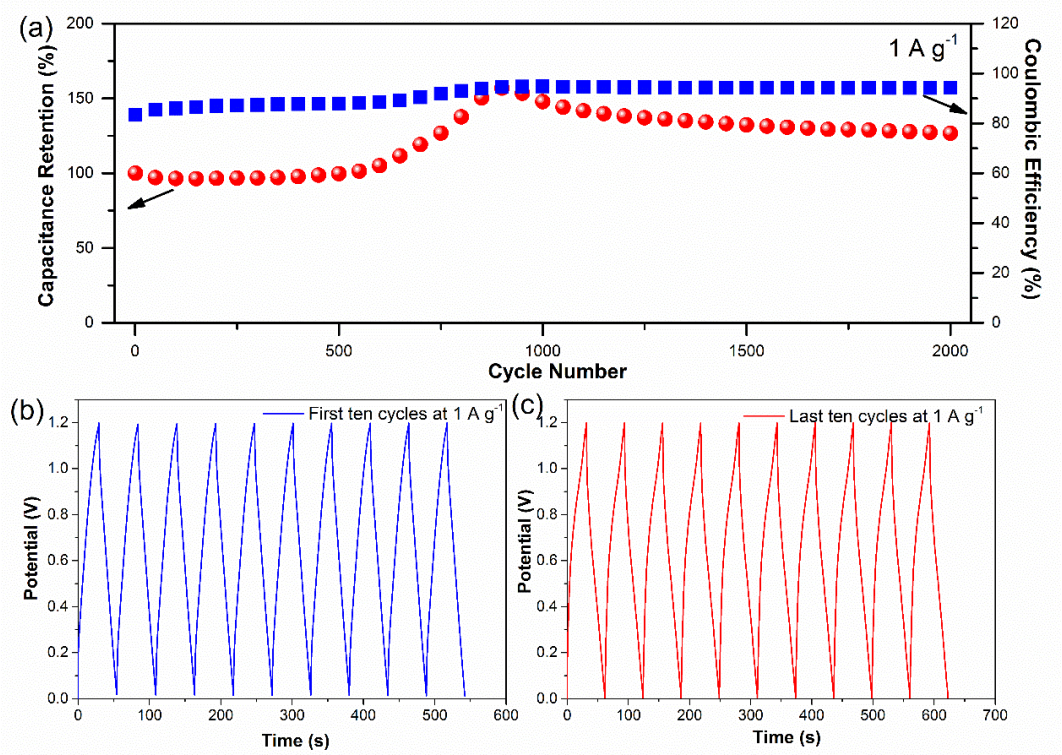

Fig. 4.6 (a) Cycling stability and coulombic efficiency of the fabricated AC//AC SSC for 2000 cycles at a current density of 1 A g^{-1}; (b) First and (c) last ten GCD curves of the AC//AC SSC.

To evaluate stability of the AC//AC SSC, 2000 cycles of consecutive GCD test were conducted at a current density of 1 A g^{-1} (Fig. 4.6a). Obviously, the specific capacitance keeps constant for the first 500 cycles. It is very interesting that the specific capacitance gradually increases to around 150% of the initial value in the following 400 cycles, which could be due to the improvement of surface wetting of the AC by the electrolyte during the repetitive GCD process [243]. When the GCD process goes, the electrolyte may permeate into the inner of the AC structure, making more area available to charge storage [244]. This phenomenon has also been reported by many researchers [245, 246]. In addition, the explanation is also supported by the variation of coulombic efficiency, which is defined as the ratio of discharging time and charging time when the charge discharge current densities are equal. The values were calculated according to equation 3.11. Specifically, the

coulombic efficiency gradually increases from 83% to 95% in the first 900 cycles, then stabilizes at this level for the reaming cycles, indicating the improved ion intercalation/deintercalation by the repetitive GCD process [247]. The specific capacitance exhibits a slightly decrease during the last 1100 cycles, showing an overall capacitance retention of 126% after 2000 cycles, which can also be evidenced by the first and last GCD curves (Fig. 4.6b and c). These results indicate the excellent stability and electrochemical reversibility of the AC//AC SSC.

4.3.2 Nitrogen-doped graphene (NG)

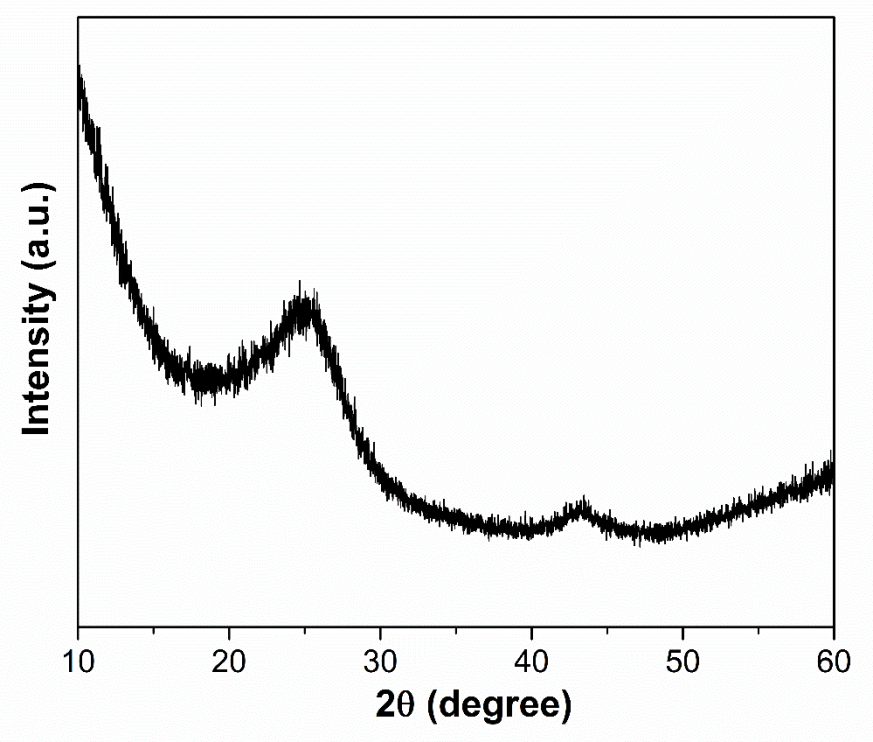

Fig. 4.7 XRD patterns of the NG.

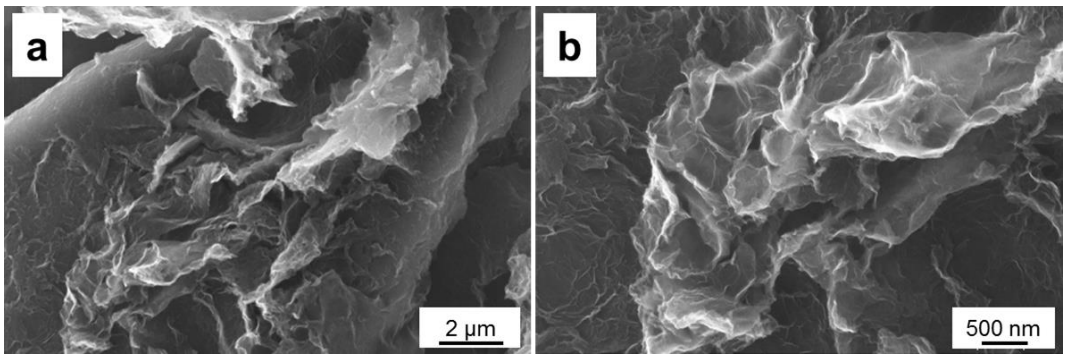

Fig. 4.8 SEM images of the NG.

Fig. 4.7 illustrates the XRD patterns of the as-prepared NG. A major broad peak at around 2θ = 25.3° is observed, which can be assigned to the (002) plane, indicating the successful exfoliation and conversion of graphitic oxide into NG [59, 248]. Additionally, it also suggests that the NG is composed of few layer stacked graphene nanosheets [64]. The weak diffraction peak at 43.5° corresponds to the (100) reflection. These results are in good agreement with the previously reported NG samples [233, 249]. SEM images of the NG are presented in Fig.4.8. Clearly, the NG exhibits an exfoliated and wrinkled nanoplatelet structure, demonstrating its good mechanical flexibility.

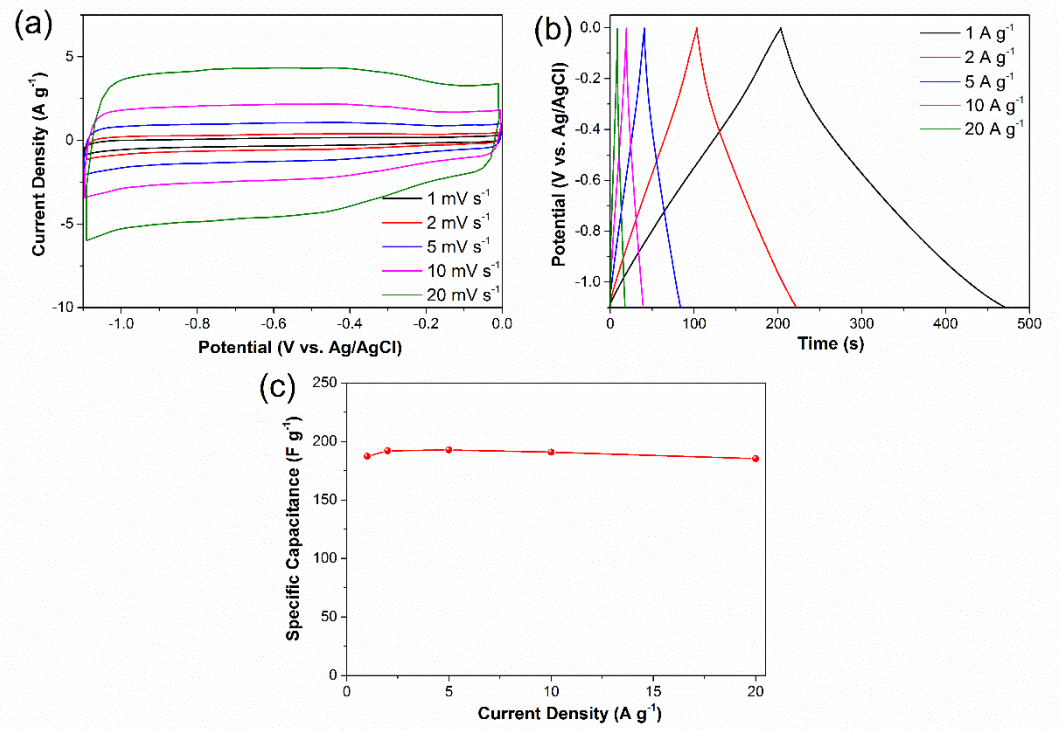

Fig. 4.9 Electrochemical performance of a single NG electrode using a three-electrode cell in 2 M KOH solution. (a) CV curves at various scan rates; (b) GCD curves at various current densities; (c) Specific capacitance at various current densities.

To understand the electrochemical performances of the as-prepared NG electrode, it was measured in a three-electrode cell with 2 M KOH as electrolyte. CV curves at difference scan rates from 1 to 20 mV s^{-1} in the potential range of -1.1 to 0 V vs. Ag/AgCl are displayed in Fig. 4.9a. The electrode exhibits rectangular characteristics while weak peaks at around 0.4 V (vs. Ag/AgCl) are observed,

which could be due to the pseudocapacitance contributed by the functional group attached on the graphene surface. It is consistent with the qusi-triangular GCD curves presented at different charge-discharge current densities (Fig. 4.9b). In addition, the NG electrode demonstrates excellent rate capability, maintaining almost the same capacitance from 1 to 20 A g^{-1} (187 F g^{-1} at 1 A g^{-1} and 185 F g^{-1} at 20 A g^{-1}) (Fig. 4.9c).

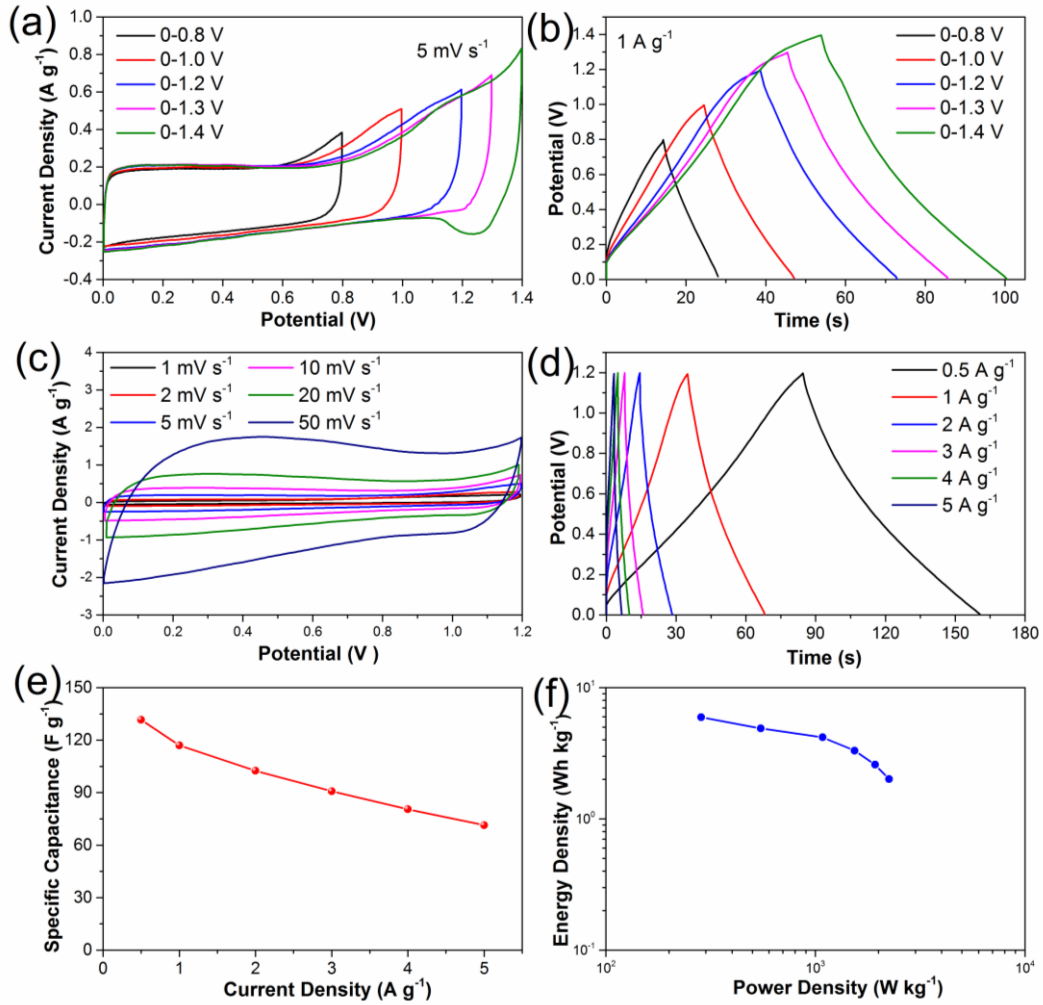

Fig. 4.10 Electrochemical performance of NG//NG SSC. (a) CV curves at different potential windows at 5mV s^{-1}; (b) GCD curves taken at constant current density of 1 A g^{-1} at different potential windows; (c) CV curves with a voltage window of 0 to 1.2 V at various scan rates; (d) GCD profiles at various current densities; (e) Specific capacitance at various current densities; (f) Ragone plots of the SSC device.

To further investigate the electrochemical performances of NG under practical

conditions, a SSC composed of two identical NG electrodes was assembled with 2 M KOH solution as electrolyte. A series of CV measurements with different voltage windows ranging from 0.8 to 1.4 V at a scan rate of 5 mV s^{-1} were carried out to optimize the working potential of the SSC. As Fig. 4.10a shows, the operating voltage window is stable up to 1.2 V. When it extends to 1.4 V, a polarization curve is observed, indicating the electrolysis of water. Fig. 4.10b presents the GCD profiles of different voltage windows recorded at a current density of 1 A g^{-1}. To avoid the water electrolysis, all the following measurements of the SSC were conducted between 0 and 1.2 V. Compared with a standard rectangle, the SSC exhibits a deviation of CV curves at different scan rates from 1 to 50 mV s^{-1} (Fig. 4.10c), which can be attributed to the functional groups on NG surface. The charge and discharge curves measured at various current densities from 0.5 to 5 A g^{-1} are shown in Fig. 4.10d. The curve deviations from a perfect triangle further confirms the pseudocapacitance contributed by the functional groups on NG surface. The specific capacitances of the NG were calculated according to equation 3.10 as shown in Fig. 4.10e. When the current density increases from 0.5 to 5 A g^{-1}, the specific capacitance decreases from 131 to 71 F g^{-1}. The Ragone plots of the NG//NG SSC are displayed in Fig. 4.10f, a maximum energy density of 5.9 Wh kg^{-1} can be delivered at a power density of 285 W kg^{-1}. An energy density of 2.0 Wh kg^{-1} is maintained at a high power density 2248 W kg^{-1}.

The cyclability of the NG//NG SSC device was tested by using repeated GCD measurement at a current density of 1 A g^{-1} (Fig. 4.11a). The slight decrease of the specific capacitance at the initial 200 cycles is possibly related to the loss of electrical contact between the active material and the current collector, and wettability issues [250, 251]. Similar phenomenon can also be found in the literatures [250, 252]. During the following period, the specific capacitance increases due to the improved wettability of the NG by the electrolyte, exhibiting a capacitance retention of 108% after 2000 cycles, which reveals that the accessibility of the electrolyte ions to the active materials does not change over long-term cycling test. This demonstrates the outstanding cycle stability of the SSC. The good stability of the SSC can also be proved by the first and last ten cycles of the GCD test (Fig. 4.11b and c). Moreover, the NG//NG SSC shows good

electrochemical reversibility of 93% coulombic efficiency during the test (Fig. 4.11a).

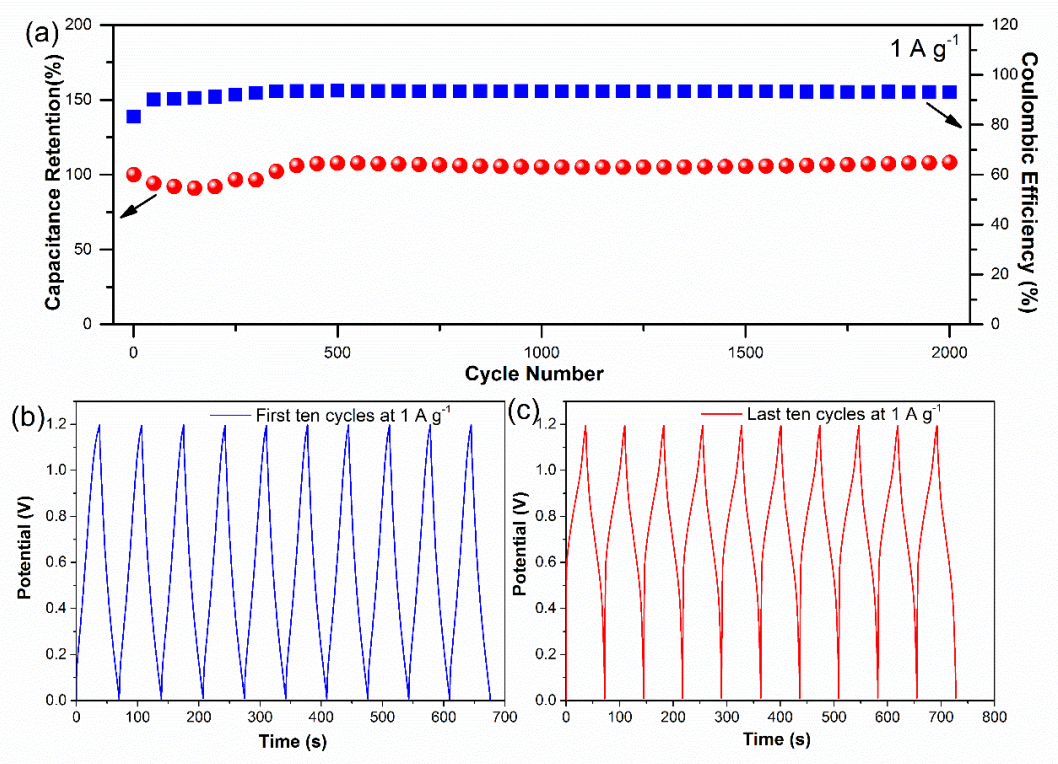

Fig. 4.11 (a) Cycling stability and coulombic efficiency of the fabricated NG//NG SSC for 2000 cycles at a current density of 1 A g^{-1}; (b) First and (c) last ten GCD curves of the NG//NG SSC.

4.4 Conclusions

In summary, NG was synthesized by hydrothermal reaction of GO with urea. Electrochemical performances of commercial AC and the as-prepared NG were firstly measured in a three-electrode system with 2 M KOH as electrolyte. In a negative potential window of -1.1 to 0 V (vs. Ag/AgCl), the AC exhibits a specific capacitance 133 F g^{-1} at a current density of 1 A g^{-1}, while the NG shows a higher specific capacitance of 187 F g^{-1} at the same current density. Even the current density increases to 20 times larger, their capacitance retentions are still over 90%, indicating the excellent rate capability. In addition, the practical performances were investigated under two-electrode mode by fabricating SSCs with two identical electrodes. To avoid the water electrolysis, their working potential was operated at 1.2 V, leading to low energy densities. Specifically, the AC//AC SSC

delivers an energy density of 4.5 Wh kg^{-1} at a power density of 281 W kg^{-1}, and a slightly higher energy density of 5.9 Wh kg^{-1} is achieved by the NG//NG SSC at 285 W kg^{-1}. Nevertheless, their stability is very good, retaining over 100% after 2000 repeated GCD cycles.

Although the SSCs composed of AC and NG cannot deliver high energy density, their outstanding rate capability and stability make them as ideal negative electrodes to fabricate high-performance ASCs, and these applications will be discussed in the following chapters.

CHAPTER 5 Synthesis of $Li_2Ni_2(MoO_4)_3$ as high-performance asymmetric supercapacitor materials

5.1 Introduction

As we mentioned in the previous chapters, among different types of electrochemical energy storage devices, supercapacitors have attracted great interest because of the relatively high power density, fast charge-discharge capability and exceptional cycle life [6, 183, 253-257]. Generally, supercapacitors can be classified into two categories depending on the energy storage mechanisms: EDLCs and pseudocapacitors [8]. EDLCs involve reversible adsorption of the ions at the electrode/electrolyte interface without any chemical reactions, which are commonly related to carbon-based materials with high surface area [258, 259]. In terms of the pseudocapacitors, fast and reversible faradaic reactions at the electrode surface are utilized to contribute the energy storage capability [260, 261]. The pseudocapacitors usually present larger specific capacitance than the EDLCs, however, their lower energy density compared with batteries limits the applications.

Basically, the reversible ion adsorption of the pseudocapacitive materials usually takes place at the electrode surface, which may limit the energy storage capacity. It can be deduced that the energy density could be improved if the fast bulk ion intercalation is achieved because the extra ion adsorption into the active materials will contribute more capacitance. From this point of view, it is important to explore appropriate materials which can allow the fast ion intercalation/deintercalation without the structure destruction. Lukatskaya *et al.* demonstrated the electrochemical intercalation of cations including Li^+, Na^+, K^+, NH_4^+, Mg^{2+} and Al^{3+} from aqueous solutions into the two-dimensional Ti_3C_2 MXene layers [262]. Recently, a NASICON-type compound $Li_2Co_2(MoO_4)_3$ was synthesized and its electrochemical performances was investigated in different alkaline electrolytes [185]. It was found that the $Li_2Co_2(MoO_4)_3$ electrode displayed remarkable specific capacitance as a pseudocapacitive material for supercapacitors, namely, 1055 to 700 F g^{-1} at the current density from 1 A g^{-1} to 50 A g^{-1} in LiOH solution. Moreover, higher specific capacitance was obtained in lithium-based electrolyte

than in sodium and potassium-based electrolytes, which is attributed to the easier intercalation of the small Li ions into the crystallographic structure of the $Li_2Co_2(MoO_4)_3$. As the NASICON-type compounds have a large family, the work opens up a new type of material which could present good supercapacitor performances.

$Li_2Ni_2(MoO_4)_3$, as a member of NASICON-type compounds, has been studied as positive electrode in lithium batteries [263-265], but its application on supercapacitors has not been reported yet. In this chapter, the $Li_2Ni_2(MoO_4)_3$ was synthesized via a combustion method. Its electrochemical properties were firstly evaluated in a three-electrode system in alkaline electrolytes. The specific capacitance reaches 1137 F g^{-1} at 1 A g^{-1} and 717 F g^{-1} at 20 A g^{-1} in 2 M LiOH solution, exhibiting a capacitance retention of 63%. Moreover, the $Li_2Ni_2(MoO_4)_3$ electrode was fabricated with an AC electrode forming an ASC. The ASC displays an energy density as high as 36.5 Wh kg^{-1} at an average power density of 420 W kg^{-1}. It also demonstrates excellent electrochemical stability and reversibility, specifically, the specific capacitance still retains 68% of the initial value with a coulombic efficiency over 95% even after 10000 cycles at 2 A g^{-1}. These results suggest that the prepared $Li_2Ni_2(MoO_4)_3$ is a prospective candidate for the high-performance energy storage devices.

5.2 Experimental

5.2.1 Synthesis of $Li_2Ni_2(MoO_4)_3$

The $Li_2Ni_2(MoO_4)_3$ compound was synthesized by a combustion method similar to a method described in previous studies [263, 265]. The sequential synthesis procedures are described in Scheme 5.1. Specifically, aqueous solutions containing the lithium nitrate, nickel nitrate hexahydrate and ammonium molybdate tetrahydrate were homogeneously mixed with a molar ratio of Li:Ni:Mo at 1 : 1 : 1.5.

Subsequently, citric acid was added to the solution at molar ratio of 1:1 to the total metal ions. The resulted solution was stirred overnight and then heated to boiling at around 100 ^oC to evaporate water. Then the resulted dried precursor was further

heated at 180 °C to obtain black ash. The ash was ground into powders with a agate mortar. Single-phase powders of $Li_2Ni_2(MoO_4)_3$ in yellow were obtained upon annealing the as-prepared powders at 600 °C for 4 h in ambient air. $Na_2Ni_2(MoO_4)_3$ was synthesized using the same method by replacing $LiNO_3$ with $NaNO_3$.

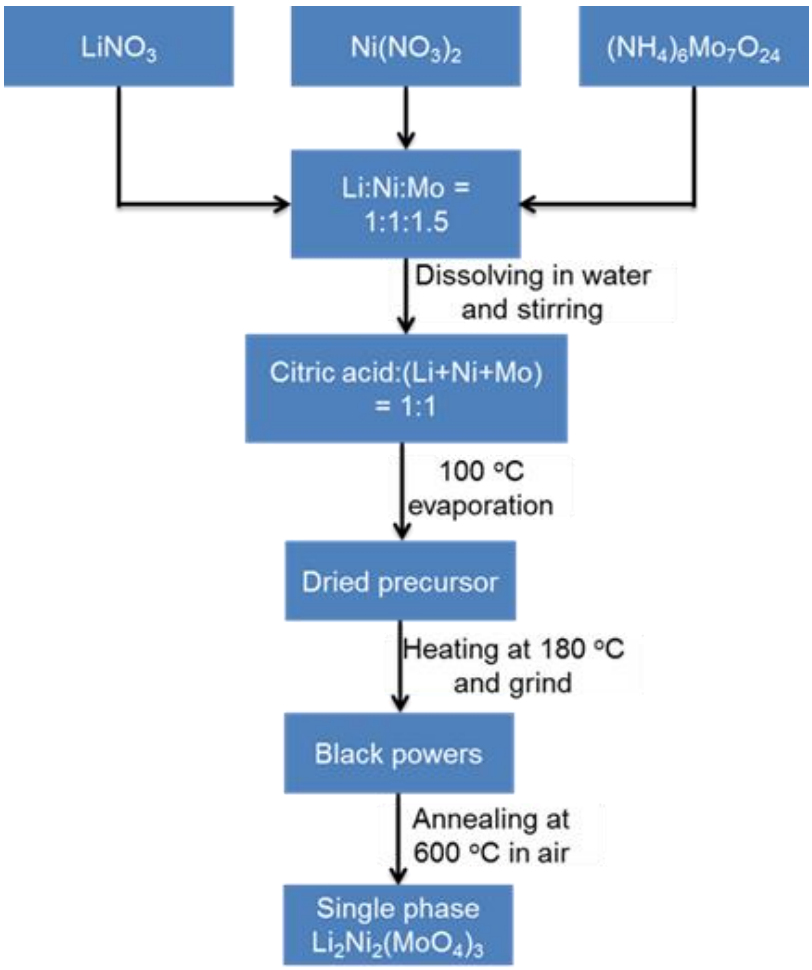

Scheme 5.1 Schematic illustration of $Li_2Ni_2(MoO_4)_3$ synthesis process.

5.2.2 Electrode preparation

The working electrode was prepared by mixing the as-synthesized $Li_2Ni_2(MoO_4)_3$ or $Na_2Ni_2(MoO_4)_3$ powders with acetylene black and PTFE at a mass ratio of 85 : 10 : 5 in water under magnetic stirring to make the slurry. The slurry was then coated onto a piece of Ni foam (1 × 1 cm^2), pressed at 10 MPa, and finally dried at 60 °C in a vacuum oven overnight. The mass loading of the active materials on the Ni foam was 1-2 mg cm^{-2}.

5.2.3 Assemble of $Li_2Ni_2(MoO_4)_3$//AC asymmetric supercapacitor

To fabricate the ASC, the as-prepared $Li_2Ni_2(MoO_4)_3$ electrode and an AC electrode were used as positive electrode and negative electrode, respectively. The AC negative electrode was obtained by mixing the AC (Black Pearl 2000, Cabot) and PTFE at a mass ratio of 95 : 5 in water under constant magnetic stirring. The prepared slurry was spread onto a Ni foam (1×1 cm^2) and then pressed at 10 MPa and dried at 60 ^oC overnight under vacuum. To assemble the full cell, the negative electrode and positive electrode were face to face placed into a container in which the electrolyte was added.

5.2.4 Physical characterization

Thermal analysis was obtained on a NETZSCH F3 thermal analyzer using simultaneous TG and DSC. The phase formation of the products was identified by XRD on a Panalytical X'Pert Pro Multi-Purpose Diffractometer (MPD) with Cu Kalpha1 radiation working at 45 kV and 40 mA. SEM (ZEISS SUPRA 55-VP) was applied to observe the sample morphology. The elemental compositions were analyzed by EDX attached to the SEM.

5.2.5 Electrochemical measurements

The electrochemical measurements of the as-prepared $Li_2Ni_2(MoO_4)_3$ electrode was performed with a conventional three-electrode cell configuration in different alkaline electrolytes. Besides the $Li_2Ni_2(MoO_4)_3$ working electrode, a piece of Pt mesh (1 × 1 cm^2) and an Ag/AgCl electrode (sat. KCl) were served as counter and reference electrodes, respectively. CV, GCD and EIS measurements were carried out on a Solartron 1470E/1455 multichannel cell test system. Impedance spectroscopy tests were performed in the frequency range from 100 kHz to 0.01 Hz with a potential amplitude of 5 mV at open circuit potential. The electrochemical performances of the ASC were analyzed under a two-electrode mode with $Li_2Ni_2(MoO_4)_3$ as the positive electrode and AC electrode as negative electrode. All the measurements were performed at room temperature in 2 M LiOH or NaOH aqueous solution.

5.3 Results and discussion

5.3.1 Physical characterization of $Li_2Ni_2(MoO_4)_3$

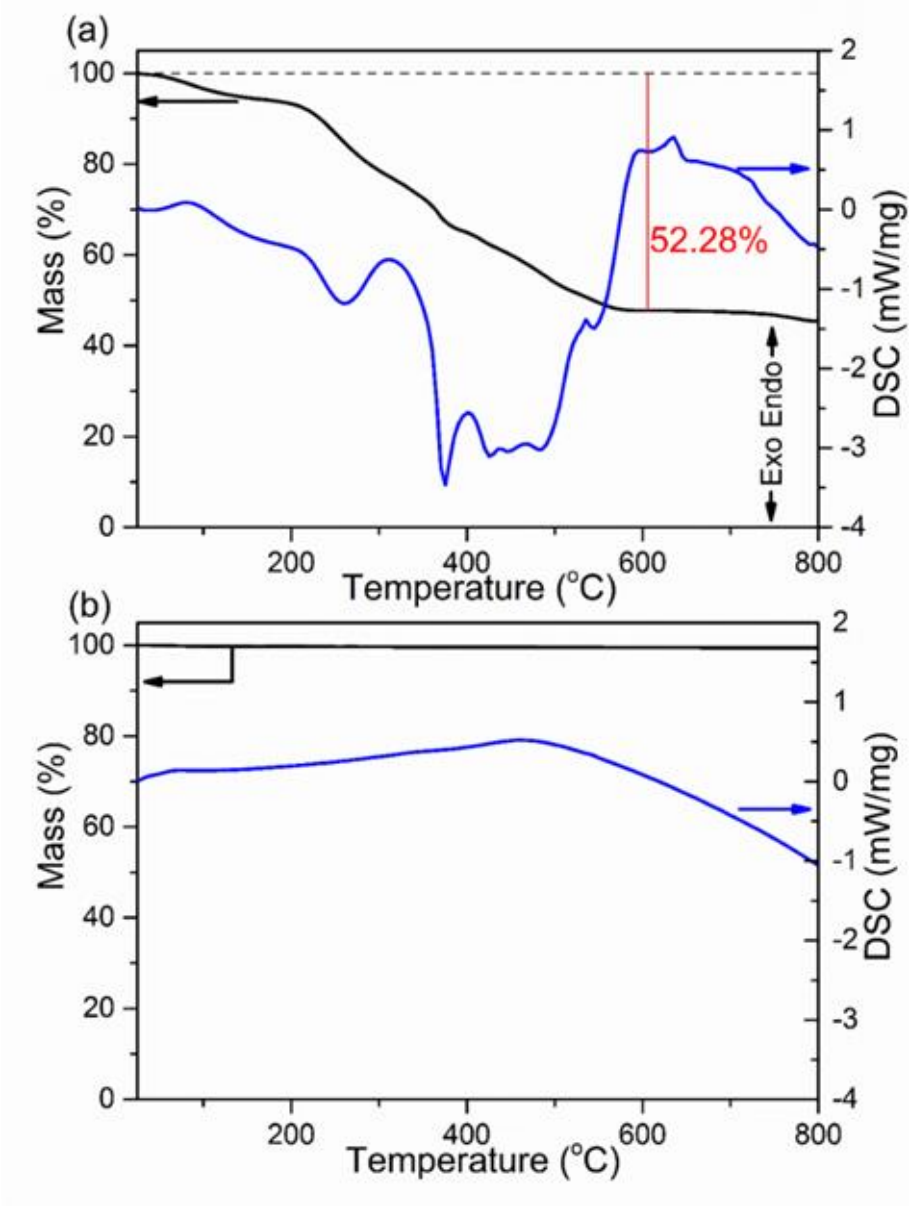

Fig. 5.1 TG and DSC curves of (a) the $Li_2Ni_2(MoO_4)_3$ precursor complex and (b) the 600 oC annealed $Li_2Ni_2(MoO_4)_3$.

The thermal stability and phase formation process of the $Li_2Ni_2(MoO_4)_3$ was evaluated by simultaneous TG and DSC. Fig. 5.1a shows the typical TG-DSC curves of the $Li_2Ni_2(MoO_4)_3$ precursor complex, the small endothermic peak at ~81 ^oC is due to desorption of adsorbed water while the exothermic peaks between 200 and 600 ^oC can be attributed to the decomposition of the precursors. The total

weight loss is about 52%, and it terminates at 590 ^{o}C, indicating the completion of the phase formation reaction. Therefore, the products were annealed at 600 ^{o}C and the corresponded TG-DSC curves are in Fig. 5.1b. The phase purity and structure of the synthesized $Li_2Ni_2(MoO_4)_3$ were examined by XRD. It can be seen from Fig. 5.2a, the observed peaks of the sample are consistent with the peaks from the orthorhombic $Li_2Ni_2(MoO_4)_3$ (ICCD 04-009-2490), confirming the formation of a well crystalline single-phase with orthorhombic structure. In addition, the polyhedral structure of $Li_2Ni_2(MoO_4)_3$ drawn by CrystalMaker Software is shown in Fig. 5.2b. The 3D framework is composed of MoO_4 tetrahedron and NiO_6 octahedron with Li atoms occupying the sites between them. This open structure could favor the intercalation/deintercalation of small-sized ions such as Li^+ ions which has been confirmed in previous studies [263, 264]. Not only for lithium ion battery, this property can also be used to develop electrode materials for supercapacitors.

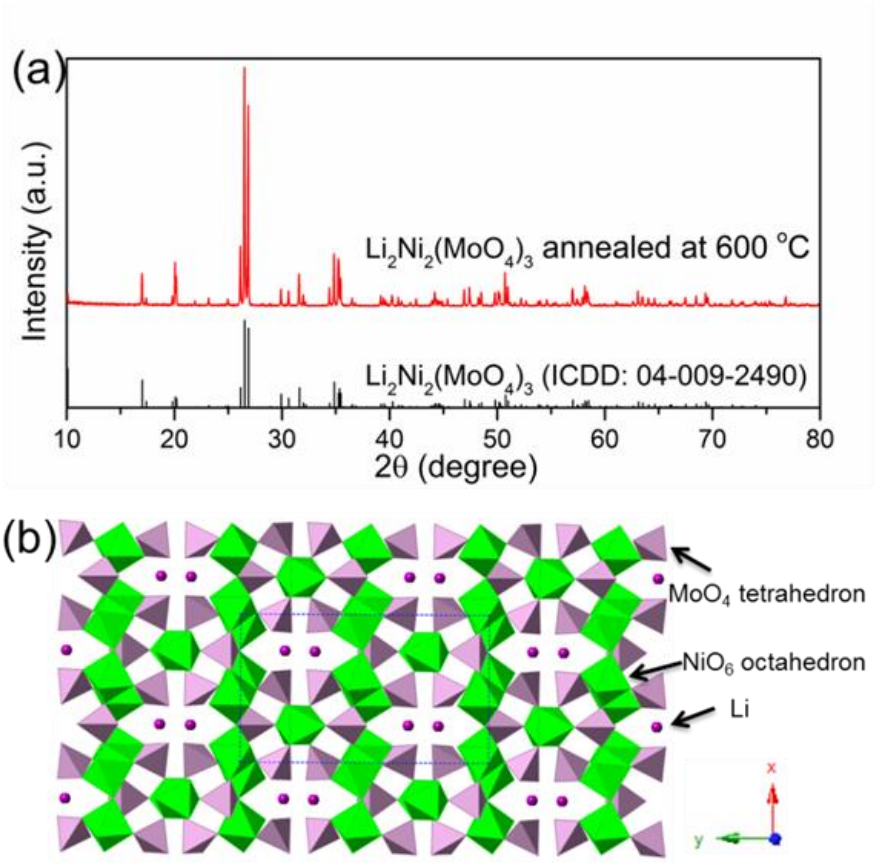

Fig. 5.2 (a) XRD patterns of the $Li_2Ni_2(MoO_4)_3$ after annealed at 600 ^{o}C and (b) crystal structure of $Li_2Ni_2(MoO_4)_3$.

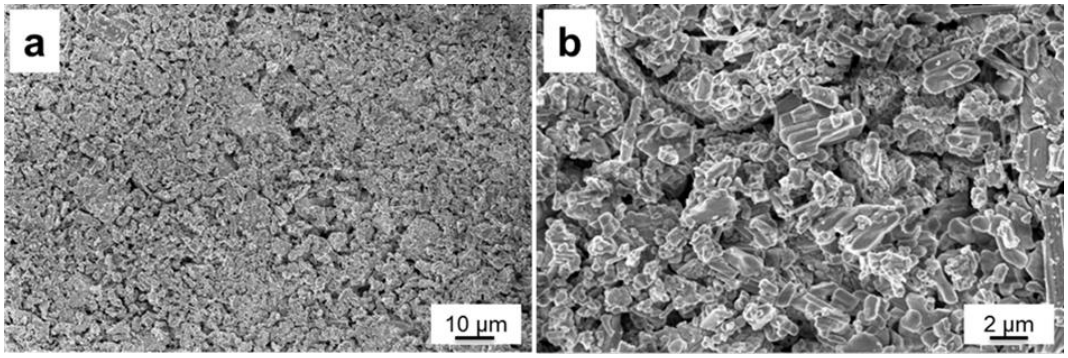

Fig. 5.3 Typical SEM images of the $Li_2Ni_2(MoO_4)_3$ at (a) low and (b) high magnification.

The morphology of the synthesized $Li_2Ni_2(MoO_4)_3$ were investigated by SEM. Fig. 5.3 exhibits the SEM images of the sample at different magnifications. It is clear that the sample is composed of fiber-like grains, which is consistent with those in the literatures [263, 265]. Fig. 5.3b indicates the grains are loosely agglomerated which could facilitate electrolyte access during the electrochemical test. In addition, each grain is well connected with the others, which could lead to improved conductivity. The average secondary particle size is roughly 1-2 μm. Energy-dispersive X-ray spectroscopy studies (EDX) on selected area indicates the existence of Ni, Mo and O elements (Fig. 5.4a). The element mapping demonstrates the Ni, Mo and O are distributed uniformly over the selected region, confirming the well formation of $Li_2Ni_2(MoO_4)_3$ (Fig. 5.4b-e).

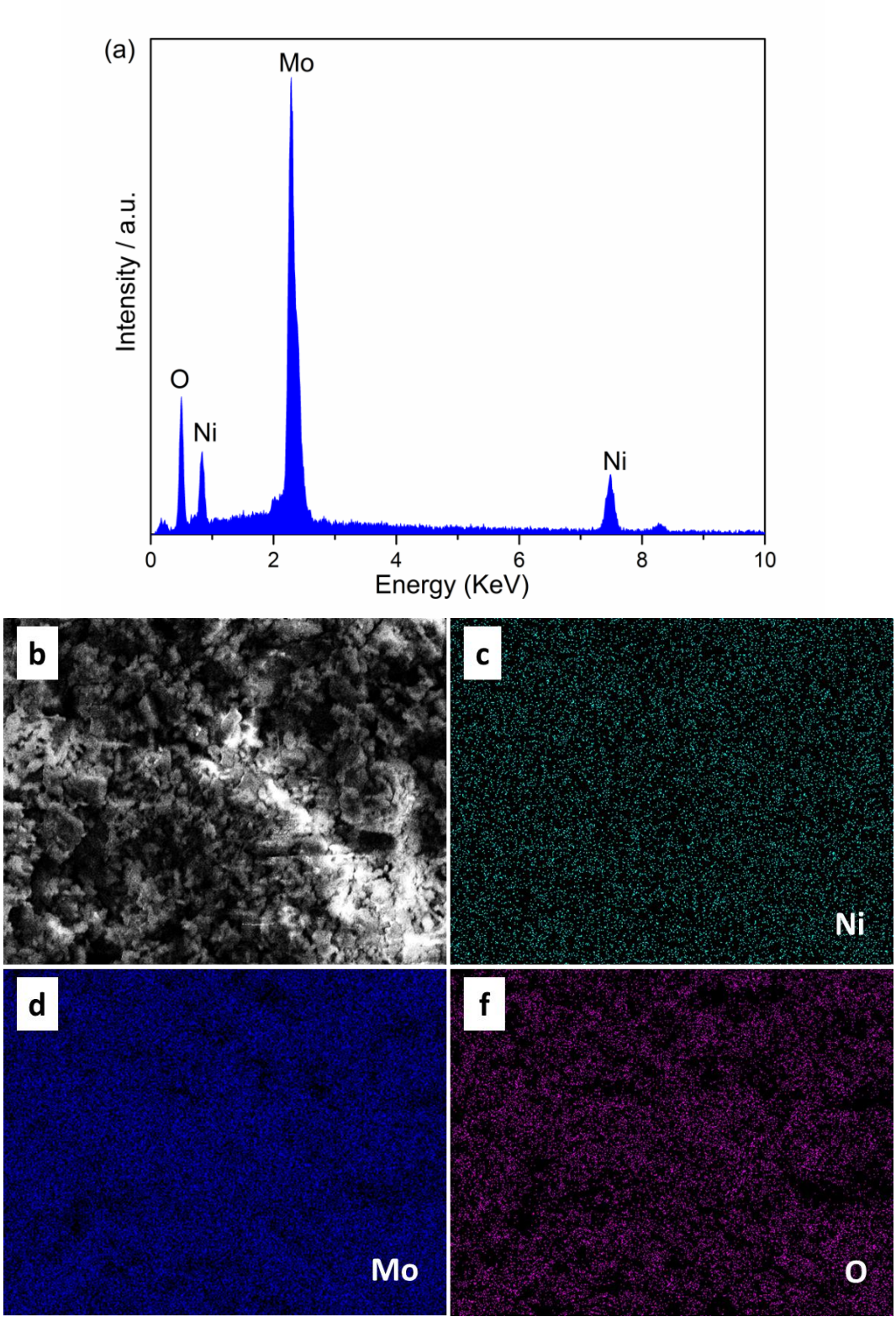

Fig. 5.4 (a) EDX spectrum $Li_2Ni_2(MoO_4)_3$ and (b-f) the corresponding mappings of Ni, Mo and O elements for the selected region.

5.3.2 Electrochemical performances of $Li_2Ni_2(MoO_4)_3$

To explore the electrochemical properties of the $Li_2Ni_2(MoO_4)_3$ material, the prepared electrode was tested using a typical three-electrode system. Fig. 5.5a presents the CV curves of $Li_2Ni_2(MoO_4)_3$ electrode at various scan rates from 1 to 10 mV s^{-1} at the potential range between 0 to 0.5 V vs. Ag/AgCl in 2 M LiOH aqueous solution. The anodic and cathodic peaks indicate the pseudocapacitive behavior of the $Li_2Ni_2(MoO_4)_3$, showing good reversibility. The peak positions are slightly changed with the increase of the scan rate but still reversible, which can be attributed to the low polarization effect of the electrode [266]. In terms of the CV curves in 2 M NaOH solution (Fig. 5.5c), similar results are obtained. Noticeably, the CV curve in Li-based electrolyte displays larger enclosed area than that in Na-based electrolyte at the same scan rate, implying higher capacitance, which means that the charge delivered by the intercalation/deintercalation of Li^+ ions is higher than that of Na^+ ions. The possible reason is that, Li^+ ions are much smaller than Na^+ ions thus would be easier to be intercalated/deintercalated in the $Li_2Ni_2(MoO_4)_3$ lattice.

Fig. 5.5b shows the GCD curves at various current densities from 1 to 20 A g^{-1} in 2 M LiOH aqueous solution. Nonlinear charge-discharge profiles were observed in GCD curves, which further supports the pseudocapacitive characteristics of the $Li_2Ni_2(MoO_4)_3$. The specific capacitance of the electrode was calculated from the GCD curves according to equation 3.10. Fig. 5.5d compares GCD curves at 1 A g^{-1} in 2 M LiOH and NaOH aqueous solutions. The specific capacitances of the electrode in LiOH and NaOH electrolytes are shown in Fig. 5.5e. The capacitance decreases from 1137 F g^{-1} (1.7 F cm^{-2}) at 1 A g^{-1} to 717 F g^{-1} (1.08 F cm^{-2}) at 20 A g^{-1} with a capacitance retention of 63%. The impact of the ion size is also reflected on the GCD curves, the capacitances in 2 M NaOH electrolyte are 860 F g^{-1} (1.3 F cm^{-2}) at 1 A g^{-1} and 488 F g^{-1} (0.73 F cm^{-2}) at 20 A g^{-1}, which is much lower than the values obtained in 2 M LiOH electrolyte, which is consistent with the CV results. Overall, it can be concluded that the small Li^+ ions are easier to be intercalated into the $Li_2Ni_2(MoO_4)_3$ lattice, which also originally contains Li in the structure. The reversible intercalation/deintercalation of Li^+ ions into the $Li_2Ni_2(MoO_4)_3$ lattice can be expressed by the following reaction:

$$Li_2Ni_2(MoO_4)_3 - xLi^+ \leftrightarrow Li_{2-x}Ni_2(MoO_4)_3 + xe^- \quad (5.1)$$

To further understand the electrochemical behavior of the $Li_2Ni_2(MoO_4)_3$ electrode, EIS measurement was carried out in the frequency range from 100 kHz to 0.01 Hz at open circuit potential with the amplitude at 5 mV. From Fig. 5.5f, in both LiOH and NaOH electrolytes, the Nyquist plots of the $Li_2Ni_2(MoO_4)_3$ electrode are composed of two parts, namely, a semicircle in high-frequency region followed by a linear component in low-frequency region. An equivalent circuit for the Nyquist plots is shown in inset (top) of Fig. 5.5f, where R_s is the equivalent series resistance, R_{ct} is the charge transfer resistance, W_o is the Warburg impedance, C_{dl} is the electric double layer capacitance, C_p is the faradaic capacitance, and R_L is the leakage resistance [161, 267]. The leakage resistance represents the resistance of self-discharge of a cell [268, 269]. Basically, lower leakage resistance implies a higher leakage current that causes the cell to self-discharge faster [268, 269]. The simulated curves based on the equivalent circuit are compared with the exponential curves in Fig. 5.6. Obviously, the simulated curves are consistent with the experimental data in both LiOH and NaOH electrolytes, indicating the accuracy of the proposed equivalent circuit. The R_s, representing the ionic resistance of the electrolyte, intrinsic resistance of active materials and the contact resistance between the active materials and current collector, can be evaluated by the intercept of the plots at the real axis represents [270-272]. The R_s in LiOH electrolyte is 0.71 Ω while that in NaOH electrolyte is 0.78 Ω, almost the same, which can be attributed to the small ionic resistance difference between LiOH and NaOH electrolytes. In terms of the R_{ct}, it represents the charge transfer resistance of the system, which can be estimated by the diameter of the semicircle [270-272]. The corresponding R_{ct} values of the $Li_2Ni_2(MoO_4)_3$ electrode in LiOH and NaOH solutions are 4.2 Ω and 5.2 Ω respectively, implying the easier and more rapid charge transfer in LiOH solution. In the low-frequency region, the straight line indicates the W_o, associating with the diffusive resistance of the electrolyte ions along the bulk $Li_2Ni_2(MoO_4)_3$ [270-272]. The steeper slope of the straight line exhibited in LiOH electrolyte demonstrates a smaller diffusive resistance of the ions in LiOH electrolyte, which explains the improved electrochemical performance of the $Li_2Ni_2(MoO_4)_3$ electrode in LiOH electrolyte.

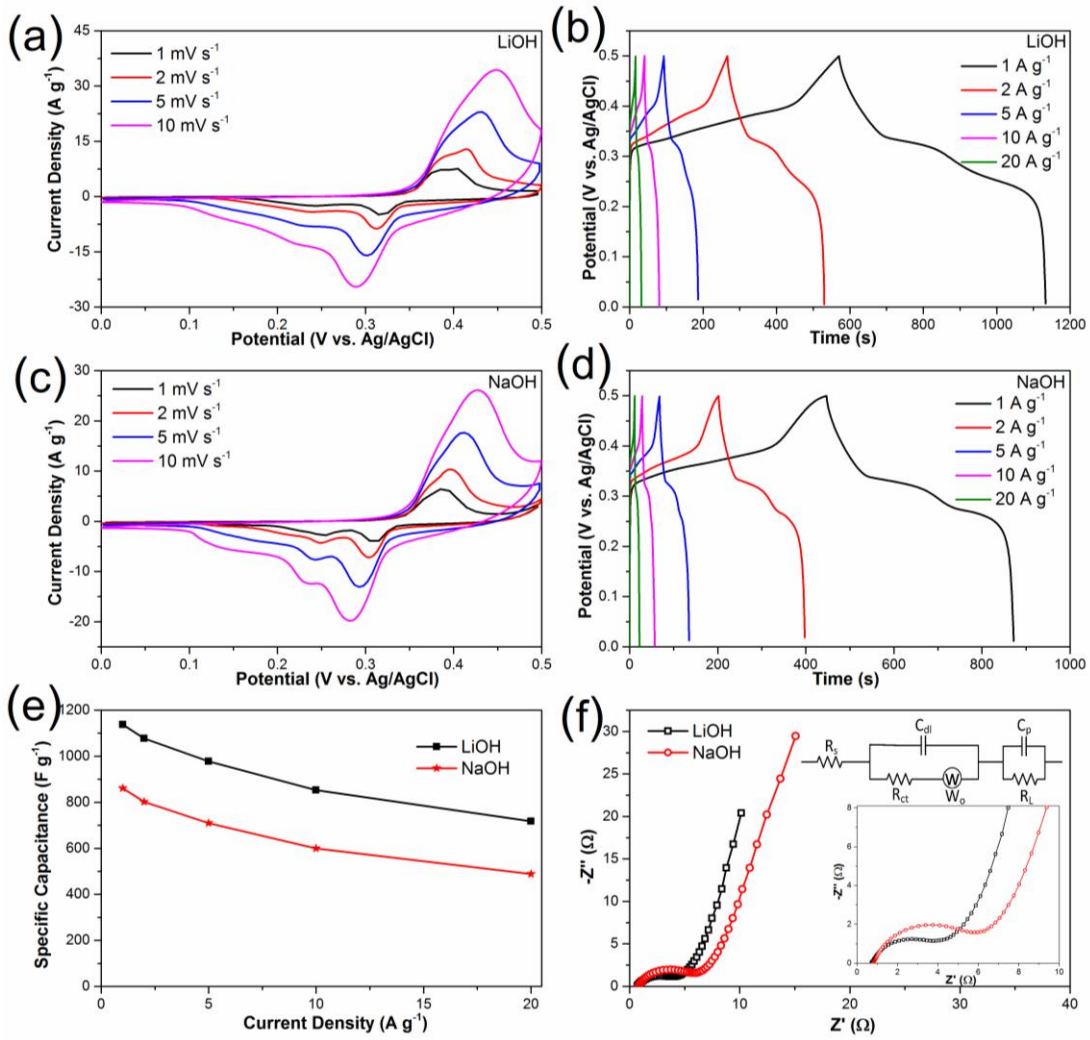

Fig. 5.5 Electrochemical performance of the $Li_2Ni_2(MoO_4)_3$ electrode in a three-electrode cell system. (a-b) CV curves at different scan rates and GCD curves at various current densities of $Li_2Ni_2(MoO_4)_3$ in 2 M LiOH solution; (c) CV curves at 10 mV s^{-1} in LiOH and NaOH electrolytes; (d) GCD curves at a current density of 1 A g^{-1} in LiOH and NaOH electrolytes; (e) Specific capacitances at various current densities in LiOH and NaOH electrolytes; (f) Nyquist plots of $Li_2Ni_2(MoO_4)_3$ electrode carried out at open circuit potential in the frequency range of 100 kHz to 0.01 Hz in LiOH solution. The insets of (f) show the impedance in high-frequency region (bottom) and the equivalent circuit (top).

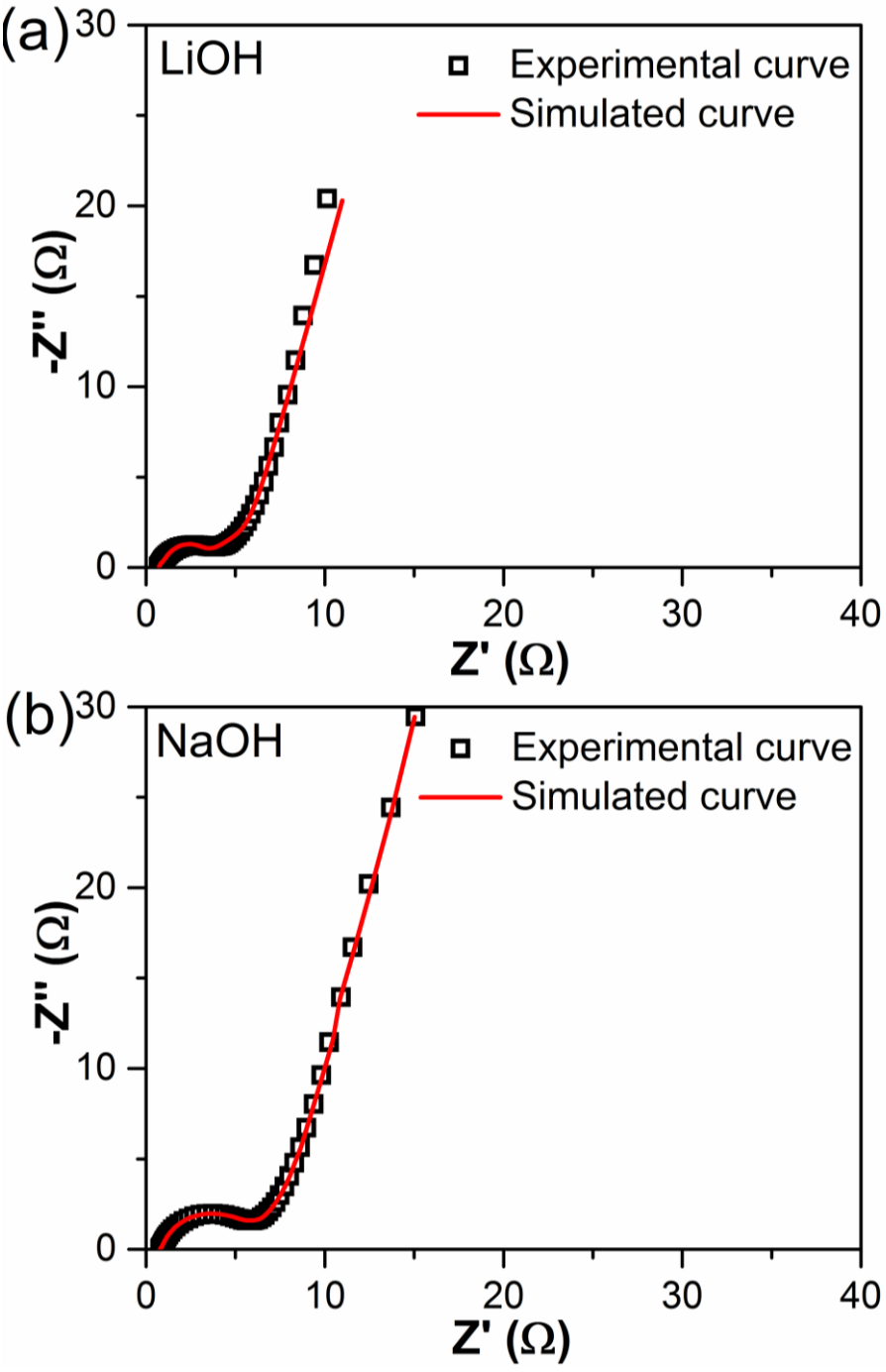

Fig. 5.6 Experimental and simulated Nyquist plots of the $Li_2Ni_2(MoO_4)_3$ electrode in (a) 2 M LiOH solution and (b) 2 M NaOH solution.

The high electrochemical performances of $Li_2Ni_2(MoO_4)_3$ electrode such as high capacitance and outstanding rate capability can be attributed to well-connected fiber-like structure, which improves the ion transport. Moreover, the $Li_2Ni_2(MoO_4)_3$, as a NASICON-type material, supplies the channels for the intercalation/deintercalation of Li^+ ions without structure destruction.

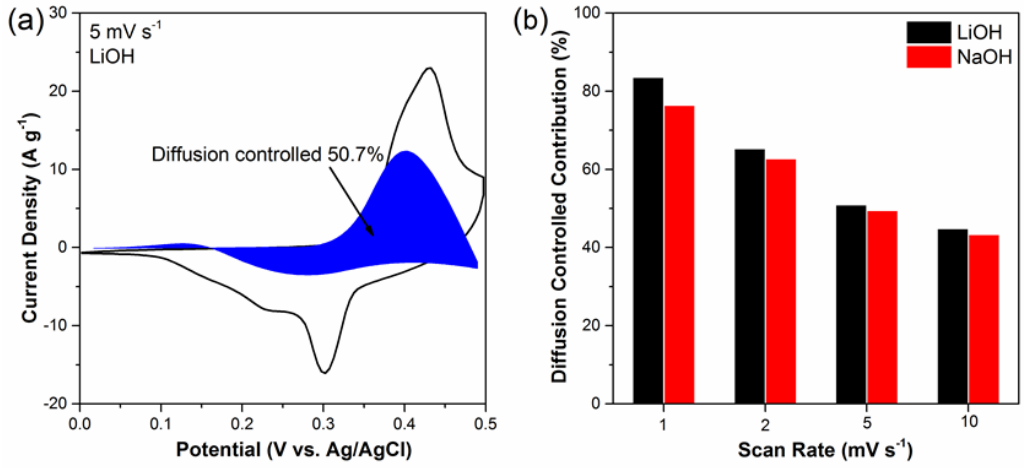

Fig. 5.7 (a) Typical separation of capacitive and diffusion-controlled charge storage process of the $Li_2Ni_2(MoO_4)_3$ electrode at scan rate of 5 mV s^{-1} in LiOH electrolyte. (b) Contribution ratio of diffusion-controlled charge storage at various scan rate in LiOH and NaOH electrolytes.

It is known that the charge stored in the electrode is contributed by diffusion-controlled faradaic process and capacitive process. The specific contribution of diffusion-controlled process and surface-controlled capacitive effect could be quantified by using equation 2.6 and 2.7. The terms $k_1\nu$ and $k_2\nu^{1/2}$represent at a given potential, the current response due to the surface-controlled capacitive effect and the diffusion-controlled faradaic process, respectively. The $k_1$and k_2 can be calculated by plotting $i/\nu^{1/2}$ $vs.\nu^{1/2}$, thus the fraction of the charge from the surface-controlled capacitive effect and the diffusion-controlled faradaic process could be determined. Fig. 5.7a demonstrates the diffusion-controlled contribution to the overall charge storage on $Li_2Ni_2(MoO_4)_3$ at a scan rate of 5 mV S^{-1} in LiOH electrolyte. 50.7% of the capacitance is contributed by the faradaic process and the remaining portion is from the surface-controlled capacitive effect. Fig. 5.7b compares the diffusion-controlled process contribution at different scan rates in both LiOH and NaOH electrolytes. It is clear that the diffusion-controlled process dominates the capacitance at lower scan rate, specifically, around 80% is occupied at 1 mV s^{-1} in both LiOH and NaOH electrolytes. While the capacitive properties increase gradually with the increasing scan rates due to the restriction of diffusion of electrolyte ions at fast scan rates. It should be noted that at each specific scan rate, the diffusion-controlled contribution in LiOH electrolyte is higher than that

in NaOH electrolyte, suggesting that the intercalation/deintercalation of the smaller Li^+ ions are easier than Na^+ ions in the $Li_2Ni_2(MoO_4)_3$, which is in agreement with the previous CV and GCD results.

5.3.3 Physical characterization of $Na_2Ni_2(MoO_4)_3$

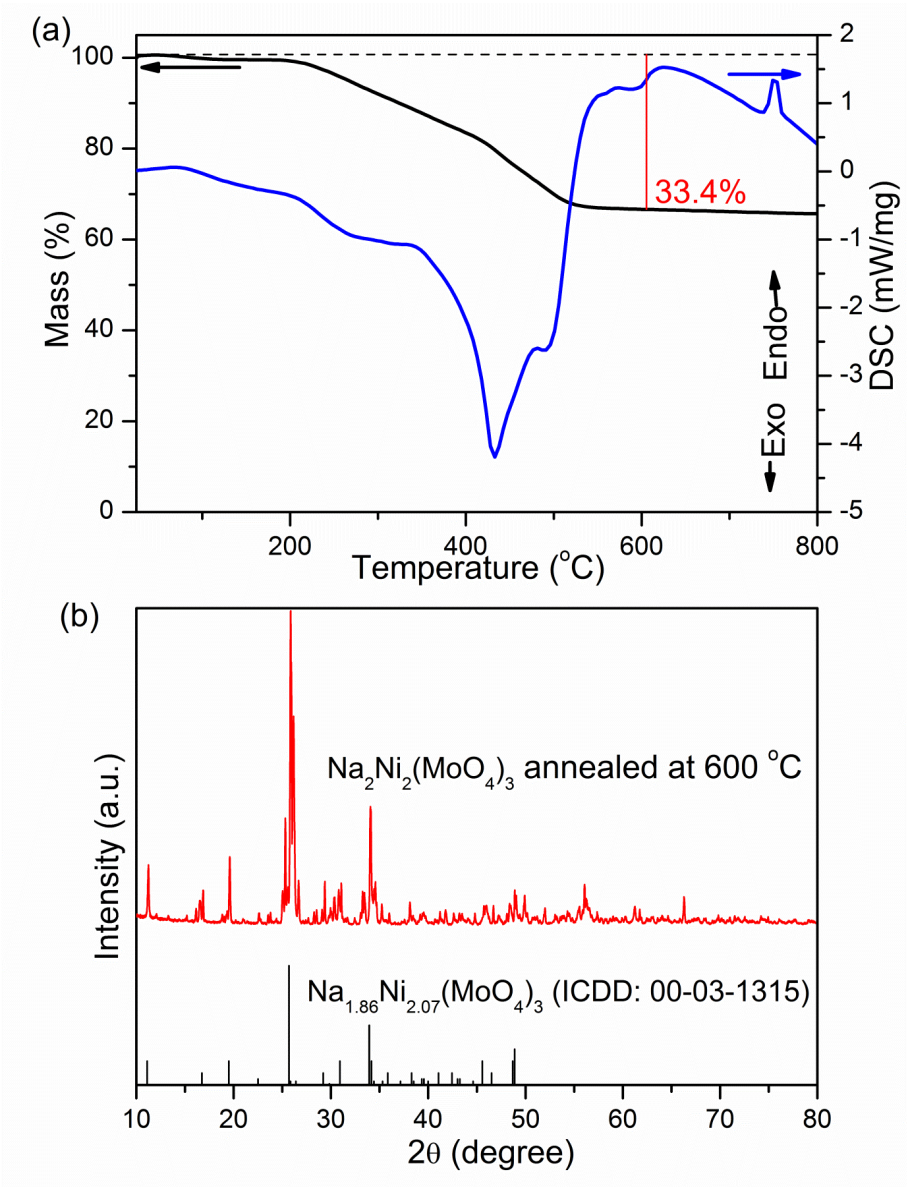

Fig. 5.8 (a) TG and DSC curves of the $Na_2Ni_2(MoO_4)_3$ precursor complex and (b) XRD patterns of the $Na_2Ni_2(MoO_4)_3$ after annealed at 600 ^oC.

For comparison, a Na-containing NASICON material $Na_2Ni_2(MoO_4)_3$ was synthesised using the same method. Fig. 5.8a shows TG and DSC curves of the $Na_2Ni_2(MoO_4)_3$ precursor complex. Obviously, the $Na_2Ni_2(MoO_4)_3$ precursor

exhibits very similar thermal properties to the $Li_2Ni_2(MoO_4)_3$ precursor. The small endothermic peak below 100 ^oC is resulted from desorption of adsorbed water. The exothermic peaks between 200 and 550 ^oC are due to the precursor decomposition. The weight stabilizes at around 550 ^oC with an overall weight loss of 33.4%, suggesting the completion of the phase transformation. Based on these results, the products were annealed at 600 ^oC and the corresponded XRD patterns are presented in Fig. 5.8b. As no standard data were indexed for the $Na_2Ni_2(MoO_4)_3$ from the database, it is hard to confirm if the single-phase is obtained. Nevertheless, majority of the observed peaks of the sample are consistent with the peaks from $Na_{1.86}Ni_{2.07}(MoO_4)_3$ (ICDD: 00-031-1315), which may prove that there is a similar structure between the two materials. According to the Na_2MoO_4–$NiMoO_4$–$Fe_2(MoO_4)_3$ phase diagram, the solubility limit of $Na_2Ni_2(MoO_4)_3$ solid solution lies at 0 $0 \leq x \leq 0.7$ [273]. Therefore $Na_{1.86}Ni_{2.07}(MoO_4)_3$ (x = 0.07) and $Na_2Ni_2(MoO_4)_3$ (x = 0) should exhibit the same structure.

5.3.4 Electrochemical performances of $Na_2Ni_2(MoO_4)_3$

The electrochemical properties of $Na_2Ni_2(MoO_4)_3$ in different LiOH and NaOH electrolytes are demonstrated in Fig. 5.9. Anodic and cathodic peaks are observed between 0 to 0.5 V vs. Ag/AgCl in the CV curves in both LiOH and NaOH electrolytes (Fig. 5.9a), indicating the pseudocapacitive behavior of the $Na_2Ni_2(MoO_4)_3$. At a current density of 5 A g^{-1}, the $Na_2Ni_2(MoO_4)_3$ performs longer discharge time in the LiOH solution (Fig. 5.9b), which means that more charges can be stored in LiOH electrolyte. The specific capacitances calculated according to GCD curves with equation 3.10 are shown in Fig. 5.9c. The specific capacitance reaches 835 F g^{-1} at 1 A g^{-1} in LiOH electrolyte, when the current density increases to 20 A g^{-1}, around 60% of the capacitance is retained. In NaOH electrolyte, the specific capacitance decreases from 625 F g^{-1} at 1 A g^{-1} to 379 F g^{-1} at 20 A g^{-1}. Obviously, the $Na_2Ni_2(MoO_4)_3$ exhibits higher capacitance in LiOH electrolyte than in NaOH electrolyte, implying the charge delivered by the intercalation/deintercalation of Li^+ ions is higher than that of Na^+ ions. It can be deduced that in the $Na_2Ni_2(MoO_4)_3$ lattice, Li^+ ions are easier to be intercalated/deintercalated than Na^+ ions, which could be attributed to the smaller size of Li^+ ions. It should be noted that the highest specific capacitance of

$Na_2Ni_2(MoO_4)_3$ performed is 835 F g^{-1} at 1 A g^{-1} in LiOH electrolyte, which is still lower than the value obtained by $Li_2Ni_2(MoO_4)_3$ (1137 F g^{-1}).

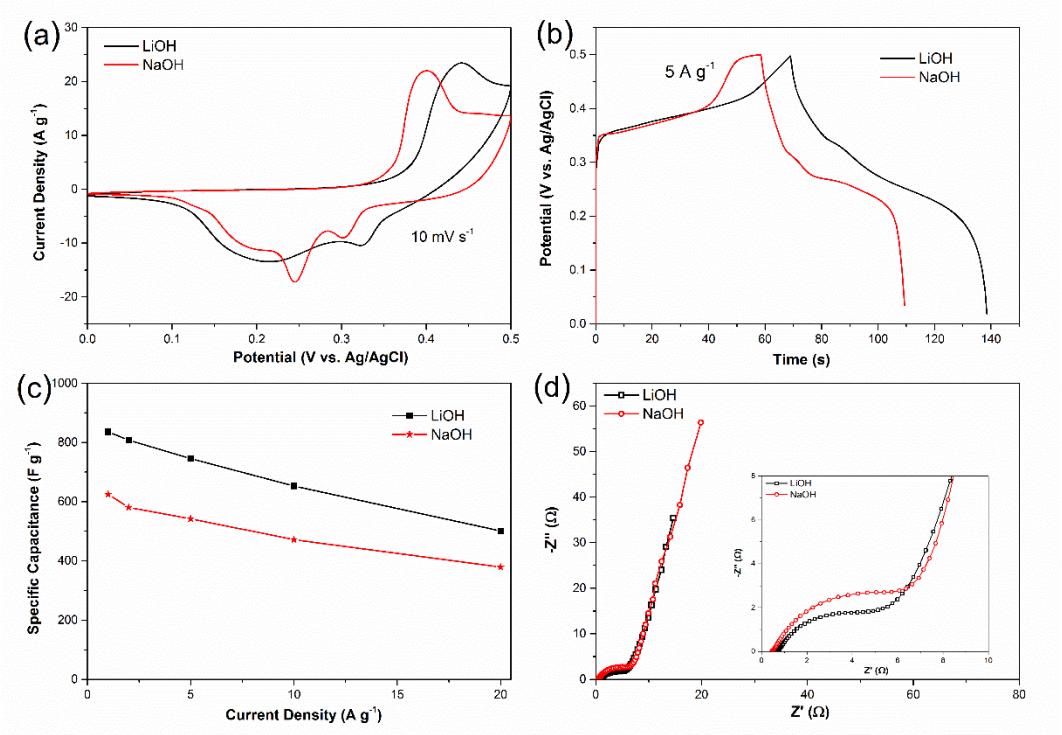

Fig. 5.9 Electrochemical performance of the $Na_2Ni_2(MoO_4)_3$ electrode in a three-electrode cell system. (a) CV curves at 10 mV s^{-1} and (b) GCD curves at 5 A g^{-1} of $Na_2Ni_2(MoO_4)_3$ in 2 M LiOH and 2 M NaOH solutions; (c) Specific capacitances at various current densities in LiOH and NaOH electrolytes; (d) Nyquist plots of $Li_2Ni_2(MoO_4)_3$ electrode carried out at open circuit potential in the frequency range of 100 kHz to 0.01 Hz in LiOH and NaOH electrolytes. The inset of (d) shows the impedance in high-frequency region.

EIS measurement of the $Na_2Ni_2(MoO_4)_3$ was conducted in the frequency range from 100 kHz to 0.01 Hz at open circuit potential with the amplitude at 5 mV (Fig. 5.9d). Due to the similarity of the two electrolytes, the equivalent series resistances (R_S) in LiOH and NaOH electrolytes are very close. The charge transfer resistances (R_{ct}) obtained from the diameter of the semicircle are 6.9 Ω and 9.7 Ω in LiOH and NaOH electrolytes respectively, indicating the easier and rapid charge transfer in LiOH electrolyte. However, this value is still lower than the 4.2 Ω of $Li_2Ni_2(MoO_4)_3$ obtained in LiOH electrolyte.

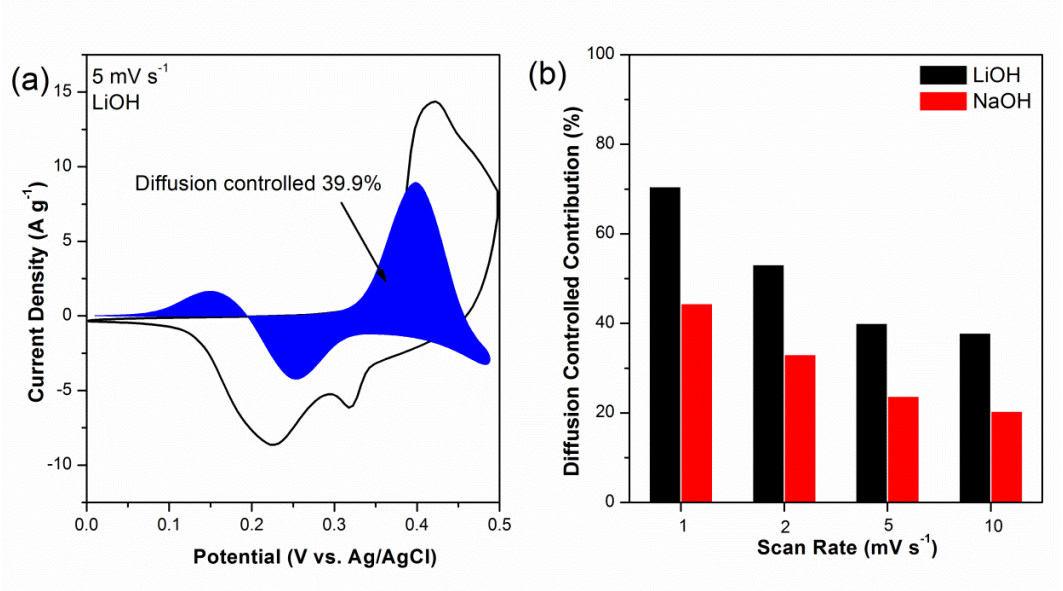

Fig. 5.10 (a) Typical separation of capacitive and diffusion-controlled charge storage process of the $Na_2Ni_2(MoO_4)_3$ electrode at scan rate of 5 mV s^{-1} in LiOH electrolyte; (b) Contribution ratio of diffusion-controlled charge storage at various scan rate in LiOH and NaOH electrolytes.

Based on equation 2.6 and 2.7, the capacitance contributed by the surface-controlled capacitive effect and diffusion-controlled process was further analyzed. Fig. 5.10a presents the diffusion-controlled contribution to the overall charge storage in $Na_2Ni_2(MoO_4)_3$ at a scan rate of 5 mV s^{-1} in LiOH electrolyte. 39.9% of the capacitance is contributed by the diffusion-controlled faradaic process while the remaining portion is produced by the surface-controlled capacitive effect. The percentages of the diffusion-controlled faradaic process in LiOH and NaOH electrolytes at difference scan rates are shown in Fig. 5.10b. Due to shorter diffusion time at higher scan rates, the capacitance contributed by the diffusion-controlled faradaic process keeps decreasing from 1 to 10 mV s^{-1} in both LiOH and NaOH electrolytes. Interestingly, at each same scan rate, the diffusion-controlled contribution in LiOH electrolyte is higher than that in NaOH electrolyte, which further confirms the easier intercalation/deintercalation of the Li^+ ions in the $Na_2Ni_2(MoO_4)_3$. Besides, it is found that the diffusion-controlled contribution in the $Li_2Ni_2(MoO_4)_3$ is higher than that in the $Na_2Ni_2(MoO_4)_3$ under same conditions, for instance, 80% for the $Li_2Ni_2(MoO_4)_3$ at 1 mV s^{-1} in LiOH electrolyte vs. 70% for the $Na_2Ni_2(MoO_4)_3$ at 1 mV s^{-1} in LiOH electrolyte, suggesting the

easier intercalation/deintercalation of the Li^+ ions in $Li_2Ni_2(MoO_4)_3$, which further supports the high charge storage capability of the $Li_2Ni_2(MoO_4)_3$. Based on the abovementioned observations, it can be concluded that the overall performance of $Li_2Ni_2(MoO_4)_3$ is superior to that of $Na_2Ni_2(MoO_4)_3$.

5.3.5 Electrochemical performances of $Li_2Ni_2(MoO_4)_3$//AC asymmetric supercapacitor

To further investigate the electrochemical performances of $Li_2Ni_2(MoO_4)_3$ under practical conditions, we have assembled an ASC by employing the prepared $Li_2Ni_2(MoO_4)_3$ electrode as the positive electrode and AC electrode as the negative electrode. In order to obtain high electrochemical performance, the charge should be balanced between the positive and the negative electrodes. The charge stored at the electrode can be calculated by the following equation [215]:

$$q = C_s \times \Delta V \times m \tag{5.2}$$

where C_s is the specific capacitance (F g^{-1}), ΔV is the constant potential range of charge-discharge process (V), m is the mass of the active materials (g). As $q_+ = q_-$, the mass ratio of active material on the positive and negative electrode in the ASC can be calculated based on equation 5.2 [274]:

$$\frac{m_+}{m_-} = \frac{C_- \times \Delta V_-}{C_+ \times \Delta V_+} \tag{5.3}$$

The electrochemical properties of AC electrode exhibit typical features of EDLCs (see more details in Chapter 4). A series of CV measurements at different voltage windows were performed at 5 mV s^{-1} to determine the optimal working potential of the ASC. According to the results in Fig. 5.11a, a stable operating voltage window can be extended as high as 1.7 V, and the polarization curve becomes very obvious when the potential increases to 1.8 V, indicating the electrolysis of water. Therefore, all the measurements of the ASC were carried out between 0 and 1.7 V. Fig. 5.11b depicts the CV behaviors of the ASC at different scan rates ranging from 1 to 20 mV s^{-1}. It should be noticed that the ASC performs quasi-rectangular CV curves in all scans, illustrating that the capacitance is contributed by both EDL capacitance and pseudocapacitance. The charge-discharge curves measured at the current densities from 0.5 to 20 A g^{-1} are shown in Fig. 5.11c. The discharge curves are nonlinear especially at lower current densities, suggesting combination effects of the EDL capacitance and pseudocapacitance for the ASC, which coincides with

the above CV results. The specific capacitance of the ASC was calculated from the discharge curves with equation 3.10, where m is the total mass of the active material in positive and negative electrodes (g). The specific capacitance of the ASC at different current density is presented in Fig. 5.11d. The capacitance is 93 F g^{-1} at a current density of 0.5 A g^{-1}, and the value gradually deceases to 73 F g^{-1} at 2 A g^{-1}, which is comparable with some previous ASCs [275, 276]. Impressively, the as-fabricated ASC reveals excellent rate capability from 5 to 20 A g^{-1}: the capacitances are 67, 64, 62 and 59 F g^{-1} at current densities of 5, 10, 15 and 20 A g^{-1}, respectively.

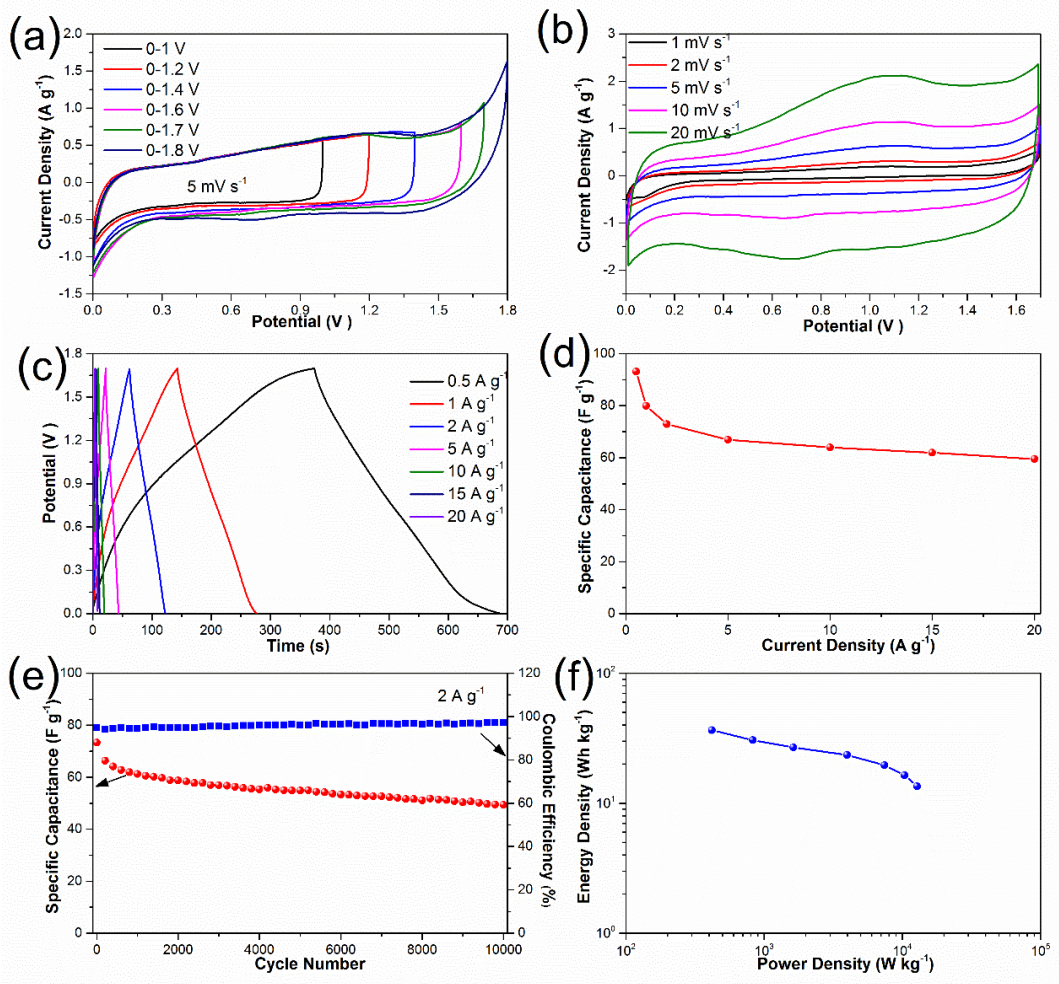

Fig. 5.11 Electrochemical properties of $Li_2Ni_2(MoO_4)_3$//AC ASC. (a) CV curves at various voltage windows at 5mV s^{-1}; (b) CV curves with a voltage window of 0-1.7 V at various scan rate; (c) GCD curves at various current densities; (d) Specific capacitance at various current densities. (e) Cycling stability and coulombic efficiency of the ASC for 10000 cycles at 2 A g^{-1}; (f) Ragone plots of the supercapacitor.

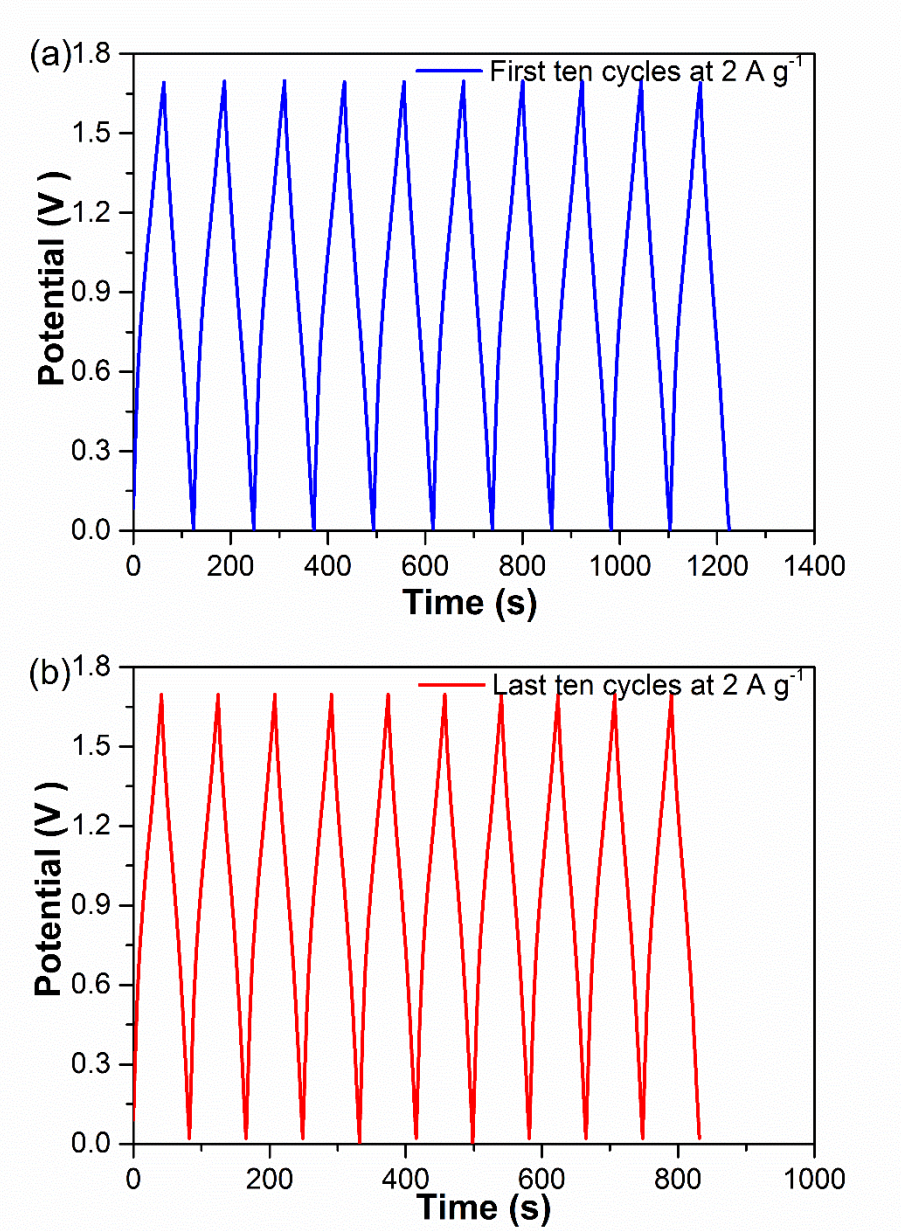

Fig. 5.12 (a) First and (b) last ten charge-discharge curves of the $Li_2Ni_2(MoO_4)_3$//AC ASC at a current density of 2 A g^{-1}.

To further investigate the durability of the ASC, the cycling stability and coulombic efficiency were evaluated at 2 A g^{-1} for 10000 cycles (Fig. 5.11e). The specific capacitance decreases about 20% of the initial value for the first 2000 cycles, which might be caused by the dissolution of the active materials [277] and the structure destruction of the electrode under rapid redox reactions [145]. The electrode experiences a decrease around 10% of the capacitance during the rest 8000 cycles, demonstrating excellent electrochemical stability. The overall specific capacitance retention is 68% after 10000 cycles, which can also be

evidenced by first and last ten charge-discharge curves (Fig. 5.12). The performance decay could be caused by the irreversibility of the faraday reaction or the structure destruction of electrode after numerous redox reactions [145, 278]. The coulombic efficiency remains over 95% during all cycles. The energy densities and corresponding power densities of the ASC were calculated using equation 3.12 and 3.13. The Ragone-plots of the ASC are displayed in Fig. 5.11f. A maximum energy density of 36.5 Wh kg^{-1} is delivered at a power density of 420 W kg^{-1}. It maintains 13.5 Wh kg^{-1} at a high power density of 12783 W kg^{-1}.

5.4 Conclusions

In this chapter, we have successfully synthesized the $Li_2Ni_2(MoO_4)_3$ through a combustion method. The $Li_2Ni_2(MoO_4)_3$ electrode exhibits excellent electrochemical performances and it displays higher specific capacitance in LiOH electrolyte than in NaOH electrolyte, which can be attributed to the easier intercalation/deintercalation of small Li^+ ions in the NASICON-type structure. The specific capacitance reaches 1137 F g^{-1} at 1 A g^{-1} in 2 M LiOH solution, and still maintains 63% at 20 A g^{-1}. Moreover, in an ASC with an AC electrode as the negative electrode, it delivers an energy density as high as 36.5 Wh kg^{-1} at an average power density of 420 W kg^{-1}. After 10000 cycles at 2 A g^{-1}, the capacitance retains 68% of the initial value, and the coulombic efficiency keeps over 95% during all cycles, showing reasonably good stability and electrochemical reversibility. All above results suggest the potential of $Li_2Ni_2(MoO_4)_3$ as a high-performance electrode material for supercapacitors.

CHAPTER 6 Preparation of hybrid $Cu_2O/CuMoO_4$ nanosheet electrode for high-performance asymmetric supercapacitors

6.1 Introduction

It is known that the demand of high quality supercapacitors with improved energy density is increasing. The ASCs are considered as one of the best alternatives because the redox reactions during charge-discharge processes can lead to larger specific capacitance [279, 280]. In a typical ASC, one electrode is derived from carbon-based materials while the other one is made of pseudocapacitive materials. It can combine the advantages of the two types of materials to exhibit high operating potential, and achieve high energy density.

Many efforts have been made to explore the pseudocapacitive materials for supercapacitors, and transition-metal oxides/hydroxides are the commonly used materials [34, 85, 281, 282]. In particular, mixed metal oxides/hydroxides usually can offer better electrical performances because of the improved conductivity as well as their synergic effects [145, 183, 283-285]. For example, Liu *et al.* found that $CoMoO_4$-$NiMoO_4$ exhibited higher specific capacitance than $CoMoO_4$ and better rate capability than $NiMoO_4$ [286]. Similarly, the investigation on Co-Ni double hydroxides has proved that the hybrid hydroxide electrodes significantly outperform either $Co(OH)_2$ or $Ni(OH)_2$ alone [32, 287, 288]. Nevertheless, the performance of pseudocapacitive materials still suffer from intrinsic poor electric conductivity and insufficient diffusion of the electrolyte into the active materials, namely, a large portion of the active materials are not accessible to the electrolyte to take faradaic reactions during the charge-discharge process thus no contribution to the specific capacitance [266]. Developing nanostructured materials with large surface area is regarded as an effective strategy to overcome these issues. Additionally, directly growing the active materials on a conductive substrate can reduce internal resistance and make full use of the active materials, therefore improving the capacitance and stability [289-291]. Among different oxide materials for supercapacitors, copper oxides have drawn many attentions due to

the low-cost, environment benignity and abundance [292-294]. Shinde *et al.* prepared a 3D-flower-like CuO on copper foil which exhibited 498 F g^{-1} at 5 mV s^{-1} [295]. Wang *et al*. measured the properties of CuO nanosheet, and a specific capacitance of 569 F g^{-1} was obtained at a current density of 5 mA cm^{-2} in 6.0 M KOH electrolyte [296]. However, it is still a big challenge on commercial utilization of Cu oxide supercapacitors, and more studies should be conducted to achieve the commercial requirements.

By combining aforementioned strategies, it can be deduced that better performance would be obtained if nanostructured copper oxide hybrids can be directly grown on conductive substrates. On the other hand, to the best of our knowledge, the application of $CuMoO_4$ for supercapacitors has not been reported. In this chapter, $Cu_2O/CuMoO_4$ nanosheets directly grown on Ni foam has been synthesized. The as-prepared electrode exhibits high specific and areal capacitance and rate capability. In addition, excellent electrical performances are obtained in an ASC with AC as the negative electrode. An energy density of 75.1 Wh kg^{-1} and power density of 420 W kg^{-1} can be achieved with voltage window at 1.7 V. Taking the fascinating performances and easy fabrication procedures into account, the hybrid $Cu_2O/CuMoO_4$ nanosheet electrode is promising for commercial application in high energy storage in the future.

6.2 Experimental

6.2.1 Preparation of hybrid $Cu_2O/CuMoO_4$ nanosheets on Ni foam

All the reagents were used without further purification. $Cu_2O/CuMoO_4$ nanosheets were synthesized by a facile hydrothermal method. Prior to the synthesis, the Ni foam (1×1 cm^2) was cleaned by ultra-sonication in 2 M HCl solution, ethanol and deionized water for several minutes respectively. The solution containing 0.05 M $Cu(NO_3)_2$ and 0.05 M Na_2MoO_4 was obtained by dissolving Copper(II) nitrate hemi(pentahydrate) and Sodium molybdate dihydrate in deionized water under constant stirring. The prepared solution was transferred into a Teflon lined stainless steel autoclave. Ni foam was immersed in the homogeneous solution, and then the autoclave was heated at 160 ^oC for 15 h and naturally cooled down to room temperature. The Ni foam was taken out and washed with water and ethanol

to remove surface ions and molecules, and then followed by drying at 60 ^{o}C overnight in a vacuum oven. Finally, the Ni foam with the as-grown hydrate precursors was calcined at 450 ^{o}C for 2 h in Argon atmosphere with heating and cooling rate of 1 ^{o}C min^{-1}. The mass loading of the active materials was obtained by comparing the weight of the Ni foam before the hydrothermal reaction and after the calcination, which was determined at around 2.2 mg cm^{-2}. For comparison, the precursor solution without Na_2MoO_4 was applied to fabricate electrodes by the same process.

6.2.2 Assemble of $Cu_2O/CuMoO_4$//AC asymmetric supercapacitor

To fabricate the ASC, the as-prepared $Cu_2O/CuMoO_4$ electrode was used as the positive electrode and an AC electrode was acted as the negative electrode. The AC electrode was obtained by mixing the activated carbon (Black Pearl 2000, Cabot) and PTFE at a mass ratio of 95 : 5 in water under constant magnetic stirring. The prepared slurry was spread onto a Ni foam (1×1 cm^2) and then pressed and dried at 60 ^{o}C overnight under vacuum. To assemble the full cell, the negative electrode and positive electrode were face to face placed into a container in which 2 M KOH was added as the electrolyte.

6.2.3 Physical characterization

XRD was carried out to identify the crystal structures on a Panalytical X'Pert Pro Multi-Purpose Diffractometer (MPD) with Cu Kalpha1 radiation working at 45 kV and 40 mA. SEM (ZEISS SUPRA 55-VP) and TEM (JEOL 2100) were applied to observe the morphologies. EDX attached to the SEM was employed to analyze the elemental compositions.

6.2.4 Electrochemical measurements

The electrochemical properties of the as-prepared $Cu_2O/CuMoO_4$ electrode were studied under a conventional three-electrode cell configuration. Specifically, the $Cu_2O/CuMoO_4$ electrode was used as the working electrode, which was activated for 1000 CV loops in 2 M KOH before test. A piece of Pt mesh (1 × 1 cm^2) and an Ag/AgCl electrode (sat. KCl) were used as counter and reference electrodes, respectively. The electrochemical performances of the $Cu_2O/CuMoO_4$//AC ASC

were explored under a two-electrode mode. All the measurements were performed in 2 M KOH solution at room temperature and recorded on a Solartron 1470E/1455 multichannel cell test system. The a.c. impedance was recorded at open circuit voltage with 5 mV amplitude in a frequency range of 100 kHz to 0.01 Hz.

6.3 Results and discussion

6.3.1 Physical characterization of $Cu_2O/CuMoO_4$ nanosheets

Fig. 6.1 shows the SEM images of the bare Ni foam. The Ni foam demonstrates a nice 3D porous structure (Fig. 6.1a) and its surface is flat and clean after acid treatment (Fig. 6.1b-c). SEM images of the $Cu_2O/CuMoO_4$ nanosheet electrode at different magnifications are shown in Fig. 6.2. The images at low magnification (Fig. 6.2a and b) indicate that the Ni foam surface becomes rough after the synthesis procedure as plenty of materials are deposited on it, which proves that the applied hydrothermal process can facilitate growing materials on the substrate. From the enlarged pictures (Fig. 6.2c and d), it can be seen that nanosheet clusters are uniformly distributed on the surface forming grass-like morphology. Moreover, the nanosheets are interconnected with each other and ultimately producing porous texture. Thus, large surface area is generated and most of the nanosheet surface could be easily accessed by the electrolyte during the electrochemical test. It should be noted that the electrode was washed and calcinated after hydrothermal process, the overall nanostructure is still well defined, which indicates excellent stability. Fig. 6.3 exhibits the surface structures of Cu_2O grown on Ni foam when only $Cu(NO_3)_2$ was used as precursor solution. Obviously, the surface is covered by grain shaped crystals with the size at around 10 μm. The difference on microstructures between the two samples reveals that the addition of MoO_4^{2-} ions can significantly affect the growth process, facilitating the formation of nanosheets. Basically, when there are no MoO_4^{2-} ions, Cu^{2+} ions are directly converted into Cu_2O and Cu in the form of large grain sized particles on the Ni foam. With the dispersal of MoO_4^{2-} ions in the solution, some Cu^{2+} ions will react with MoO_4^{2-} ions to form $CuMoO_4$, this process is slower and provides sufficient time to form nanosheets on the Ni foam.

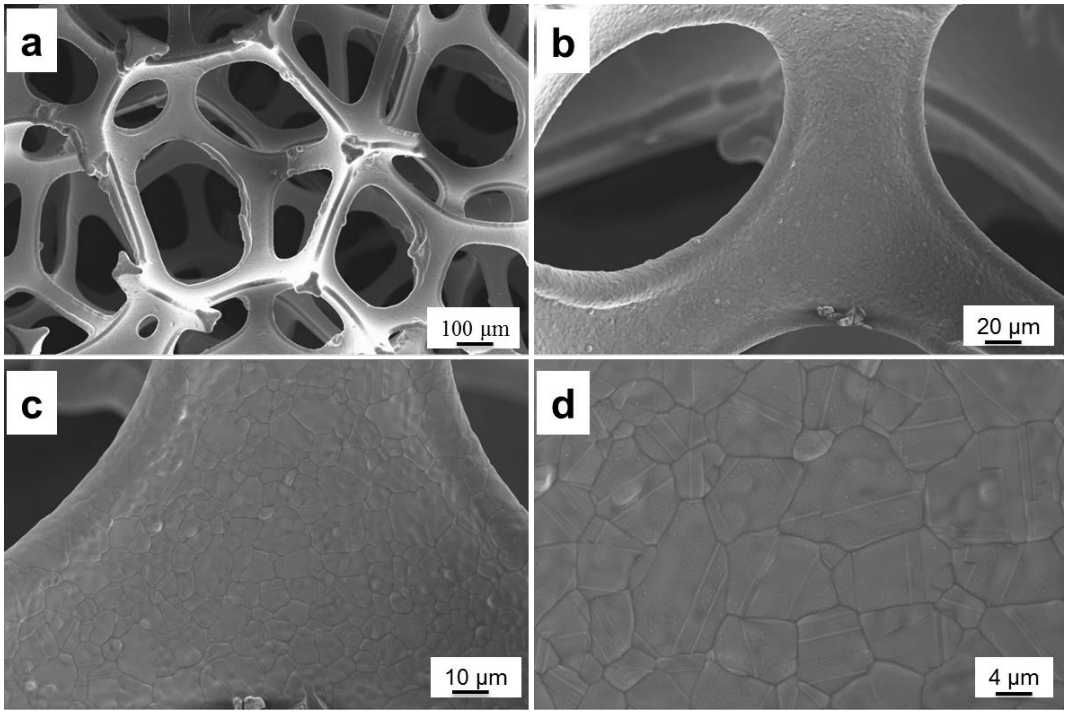

Fig. 6.1 Typical SEM images of bare Ni foam.

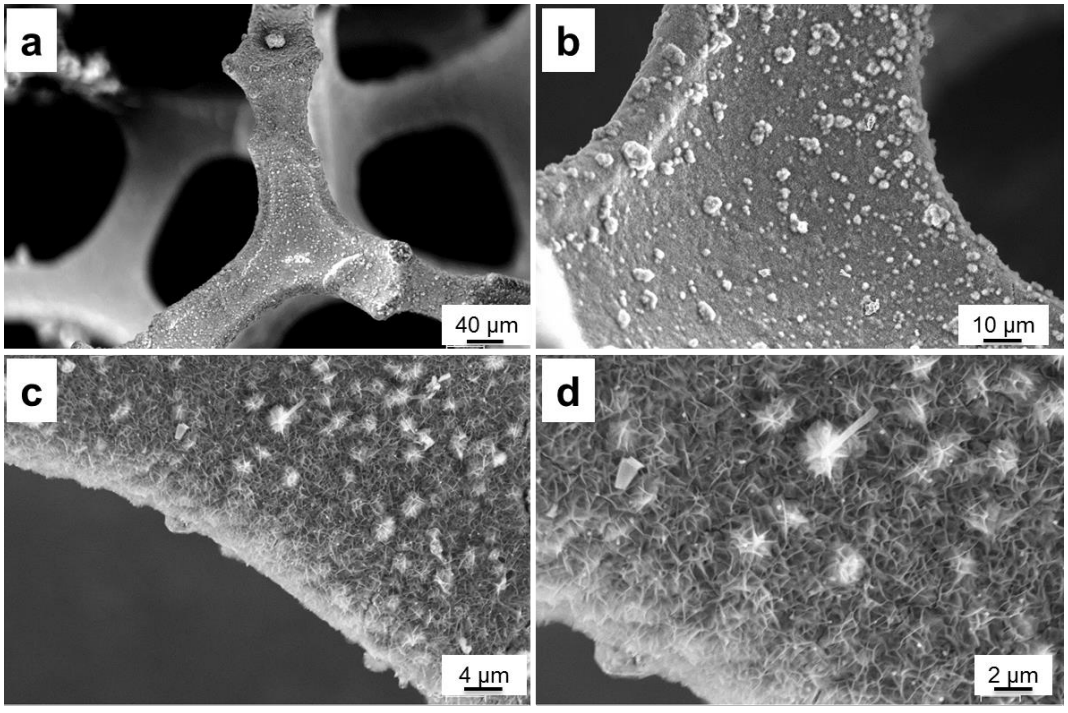

Fig. 6.2 Typical SEM images of $Cu_2O/CuMoO_4$ nanosheets on Ni foam at different magnifications.

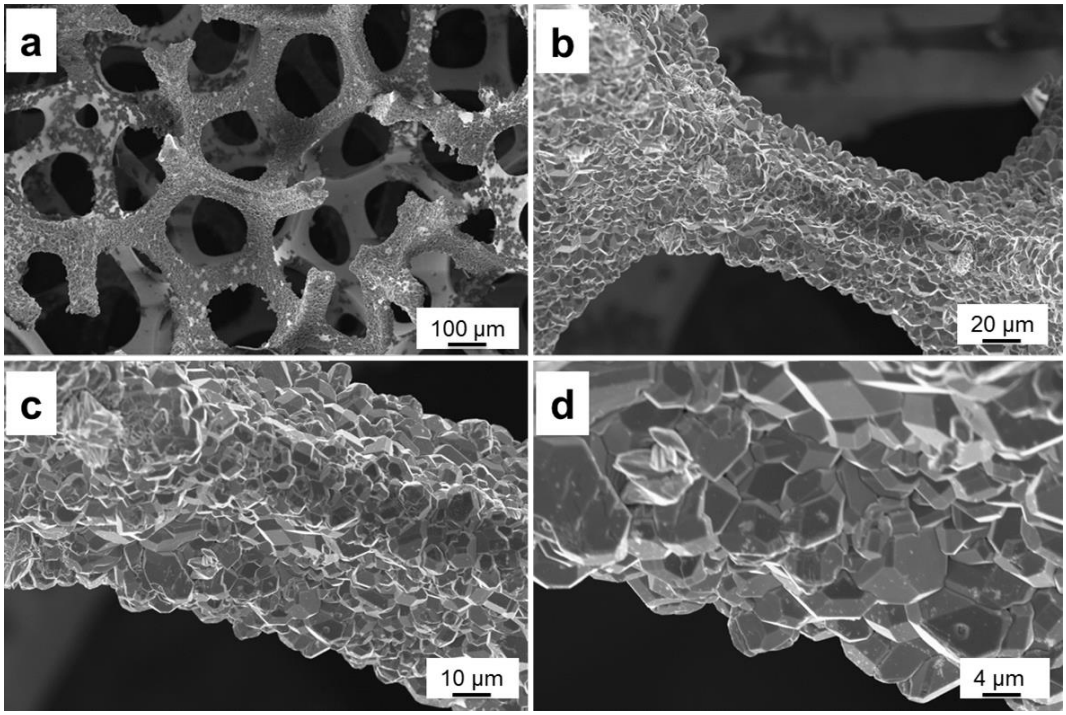

Fig. 6.3 Typical SEM images of Cu_2O grown on Ni foam.

To identify the element compositions of the materials grown on Ni foam, EDX analysis was conducted on the electrode and the results are shown in Fig. 6.4. The EDX spectrum indicates the nanosheets are composed of Ni, Cu, Mo, and O elements (Fig. 6.4a), which is also confirmed by the EDX mapping (Fig. 6.4b-f). All the elements are distributed uniformly in the electrode, suggesting the well formation of the hybrid $Cu_2O/CuMoO_4$. Besides the Ni signal derived from Ni foam, the results are consistent with the raw materials used for the hydrothermal reaction. For comparison, only Ni, Cu, and O elements are observed on the Cu_2O electrode (Fig. 6.5), which is in good agreement with experimental reagents. Apparently, the Ni signal is also from the Ni foam substrate.

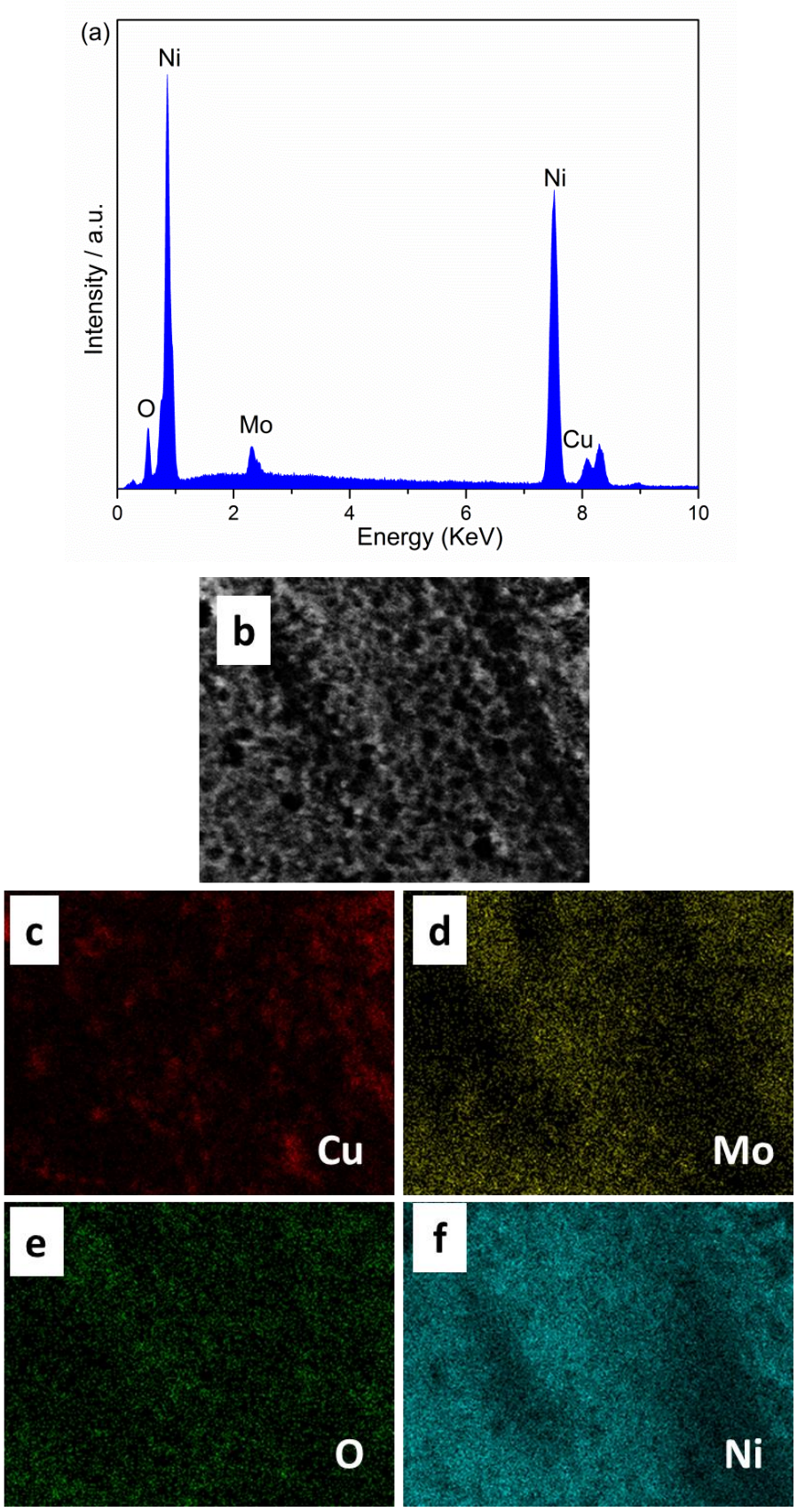

Fig. 6.4 (a) EDX spectrum and (b-f) corresponding mappings of Cu, Mo, O and Ni elements of $Cu_2O/CuMoO_4$ nanosheets on Ni foam.

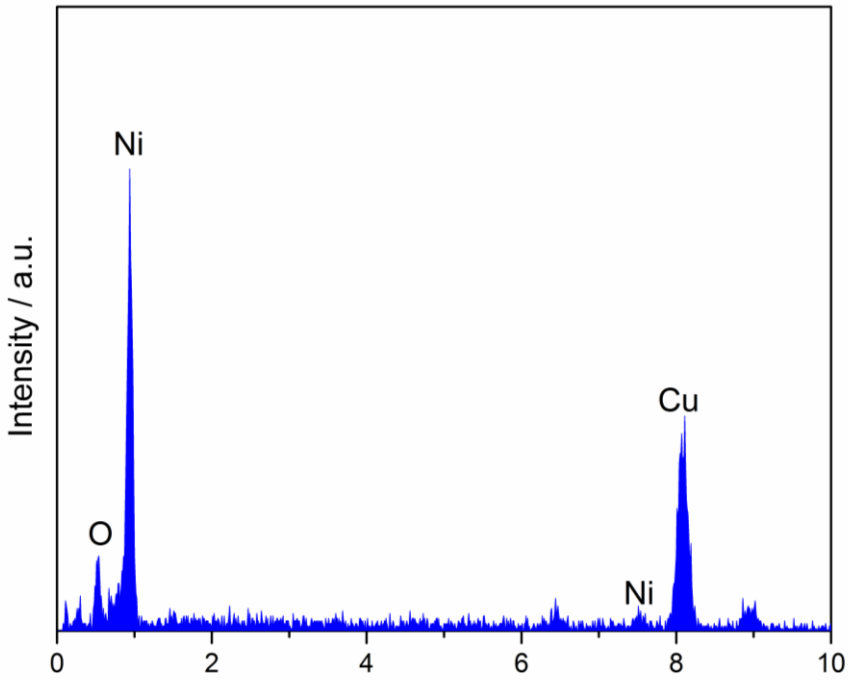

Fig. 6.5 EDX spectrum of the Cu_2O grown on Ni foam.

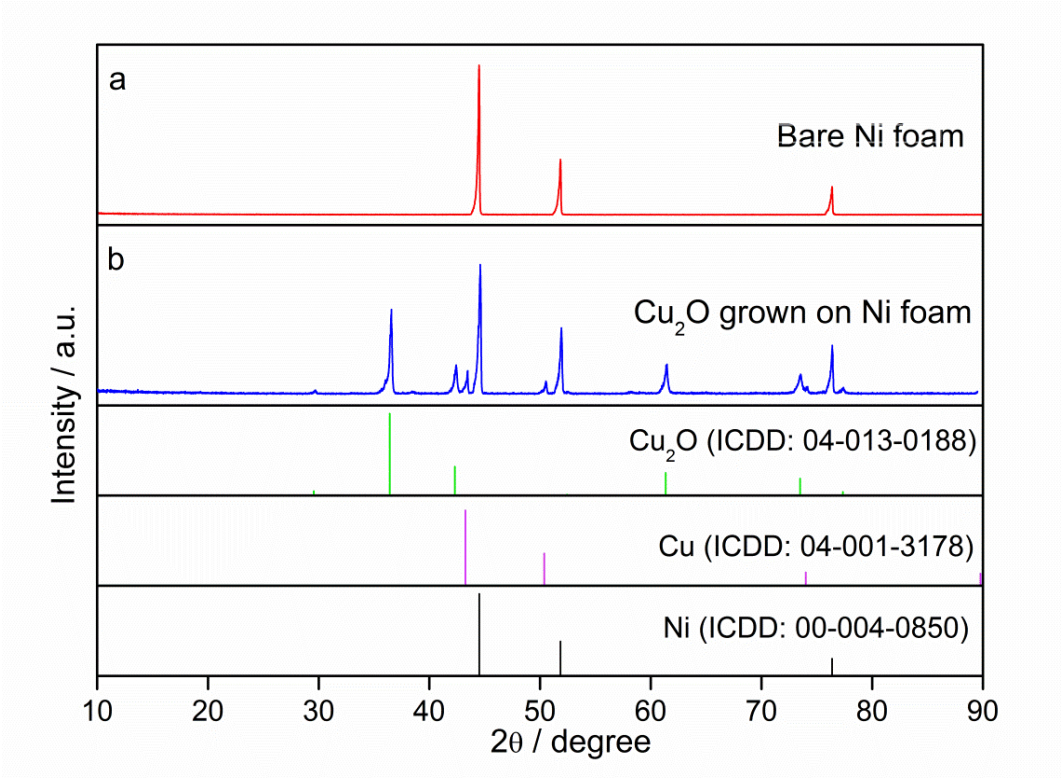

Fig. 6.6 XRD patterns of (a) bare Ni foam and (b) the as-synthesized Cu_2O grown on Ni foam.

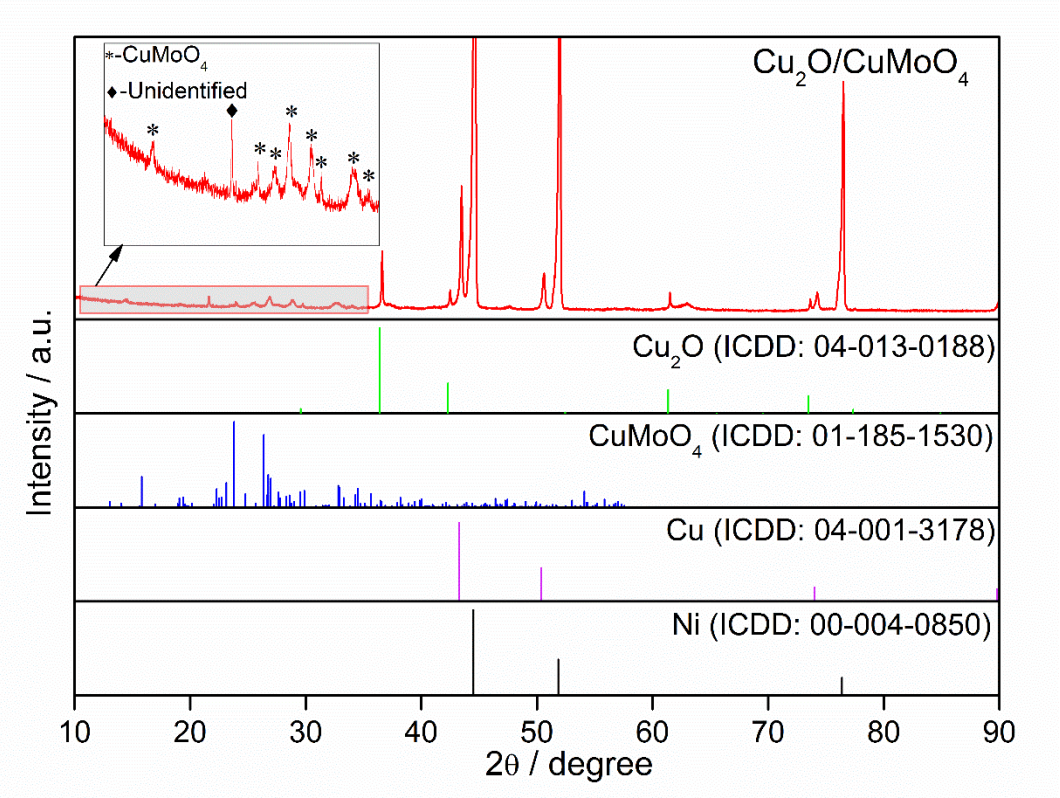

Fig. 6.7 XRD patterns of the as-synthesized $Cu_2O/CuMoO_4$ nanosheet electrode.

Next, the compositions of the grown materials were identified by XRD. No impurities are detected on the bare Ni foam substrate except the Ni peaks (Fig. 6.6a). In terms of the sample prepared with only $Cu(NO_3)_2$ solution as precursor (Fig. 6.6b), Cu_2O and Cu are found. A weak peak at $2\theta \approx 27.1°$ was not identified, which may need further investigation. XRD patterns of the as-synthesized $Cu_2O/CuMoO_4$ nanosheet electrode is shown in Fig. 6.7, the background of the Ni foam is very strong, but the diffraction patterns still reveal that the compositions of the grown materials are the hybrid of Cu_2O, $CuMoO_4$ and Cu as these peaks can be assigned to the standard Cu_2O (ICDD 04-013-0188), $CuMoO_4$ (ICD 00-047-0511) and Cu (ICDD: 00-004-0850).

The $CuMoO_4$ phase is not well crystallized, its existence was further confirmed by TEM. Fig. 6.8a shows that the $Cu_2O/CuMoO_4$ removed from the Ni foam by ultrasonication is supported on a lacy carbon support grid. The selected area diffraction pattern indicates that lots of different d-spacings exist in the sample, confirming the hybrid compositions (Fig. 6.8b). It can be seen that the sample

surface is covered by plentily of particles with a size of 20-50 nm (Fig. 6.8c and d). The HRTEM images with lattice fringes are presented in Fig. 6.8e and f, and the corresponding Fourier transform patterns are shown in inset of Fig. 6.8f. The interplanar distances observed are around 0.457, 0.379, 0.399, 0.408 and 0.512 nm, which can be indexed as the (110), (201), $(\bar{1}02)$, (002) and $(1\bar{1}1)$ planes of $CuMoO_4$. It can be deduced that during the hydrothermal process, some Cu^{2+} ions are converted into Cu_2O and Cu, while the addition of MoO_4^{2-} ions can simultaneously produce $CuMoO_4$. It is known that Cu would be electro-oxidized to Cu_2O in KOH electrolyte by employing CV test [219, 292], therefore the electrolyte accessible Cu on the Ni foam are converted to Cu_2O after the activation step while the remaining Cu can be functioned as a part of the current collector to improve the electrode conductivity. The active materials here are therefore denoted as $Cu_2O/CuMoO_4$.

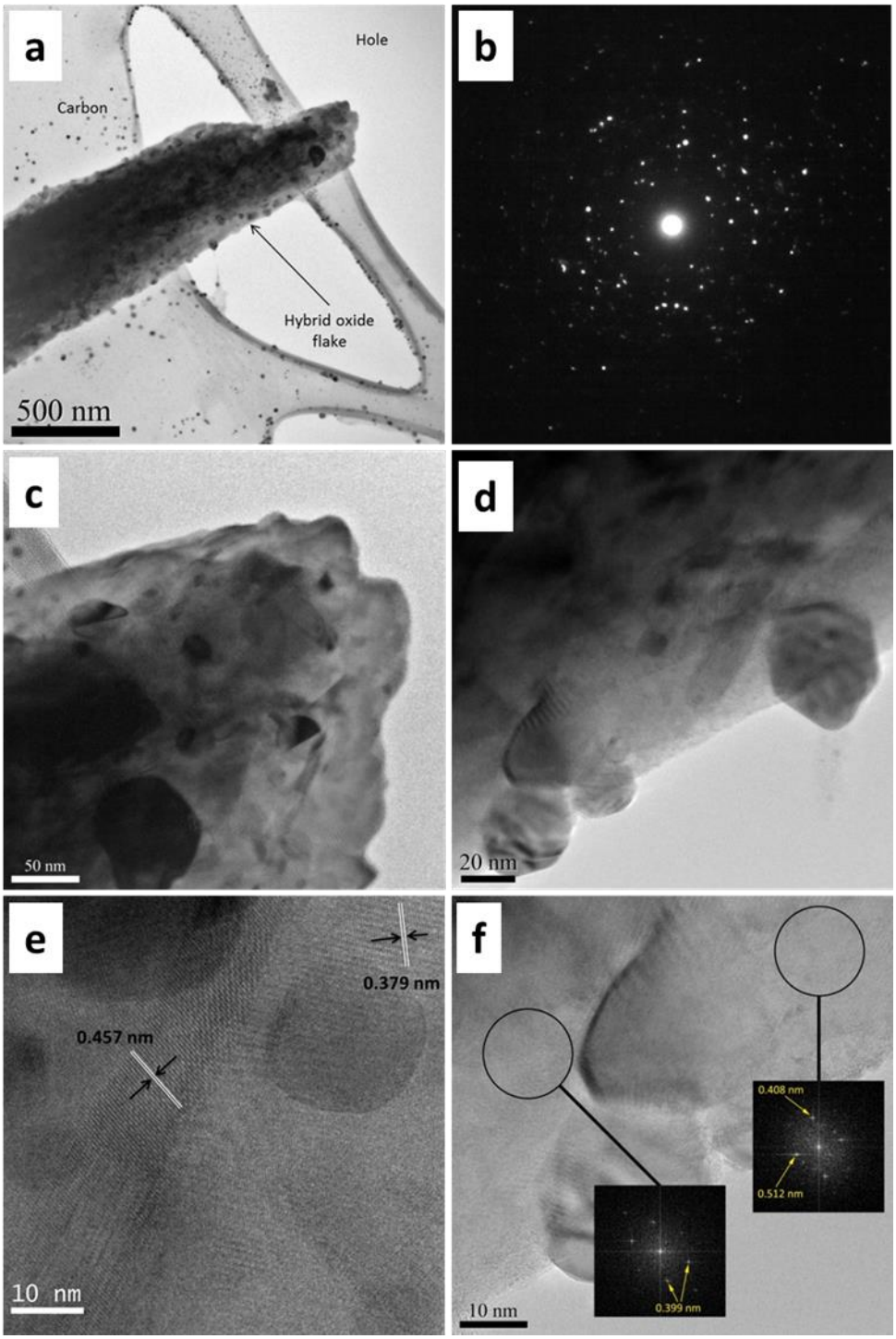

Fig. 6.8 (a, c-f) Typical TEM images of $Cu_2O/CuMoO_4$ nanosheets and (b) the selected area diffraction pattern. The inset of presents the corresponding Fourier transform patterns.

6.3.2 Electrochemical performances of $Cu_2O/CuMoO_4$ nanosheets

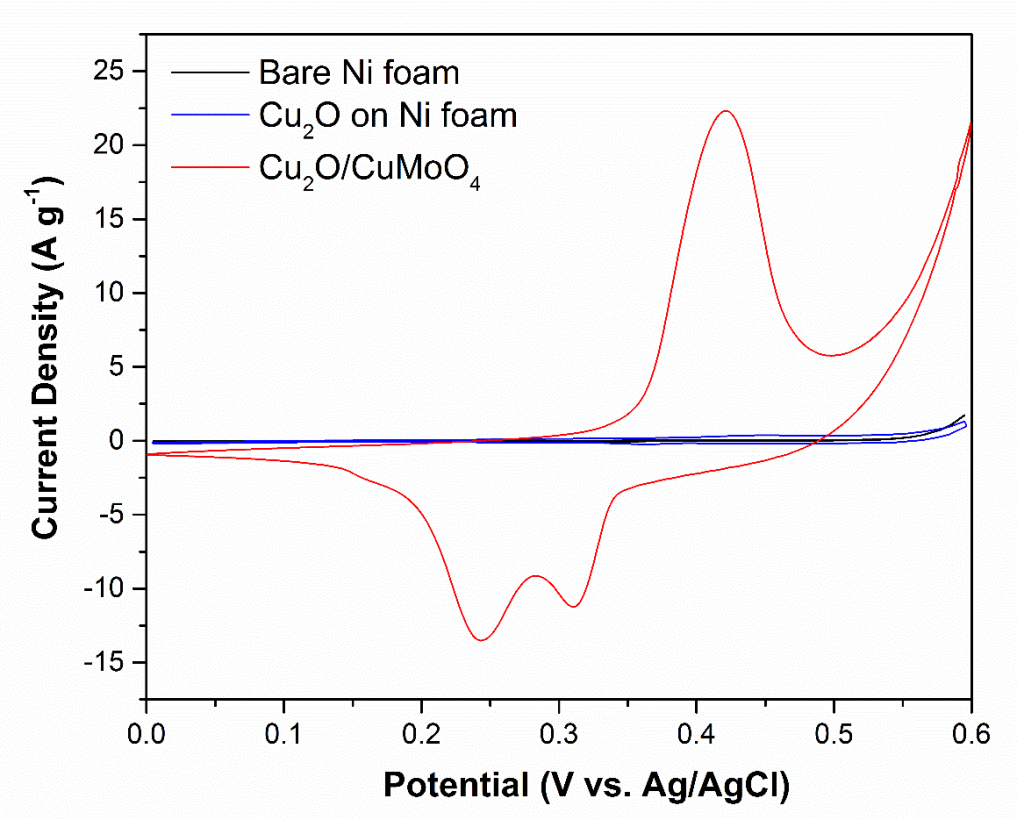

Fig. 6.9 Cyclic voltammograms (CV) of bare Ni foam after annealing in Argon at 450 ^oC for 2h, Cu_2O grown on Ni foam and hybrid $Cu_2O/CuMoO_4$ nanosheet electrode in a potential range of 0 to 0.6 V at a scan rate of 1 mV s^{-1}.

To evaluate the electrochemical performances of the $Cu_2O/CuMoO_4$ nanosheet electrode, the synthesized electrode was measured in a three-electrode cell configuration in 2M KOH aqueous solution. It should be pointed that the Ni foam substrate contributes negligible capacitance under the conditions applied in this work. The CV curves of the bare Ni foam electrode (1 × 1 cm^2, calculated as 1 mg), the Cu_2O-Ni foam electrode and the hybrid $Cu_2O/CuMoO_4$ nanosheet electrode at 1 mV s^{-1} are compared in Fig. 6.9, it is obvious that the current density on the bare Ni foam and Cu_2O electrodes are far lower than that on the $Cu_2O/CuMoO_4$ nanosheet electrode.

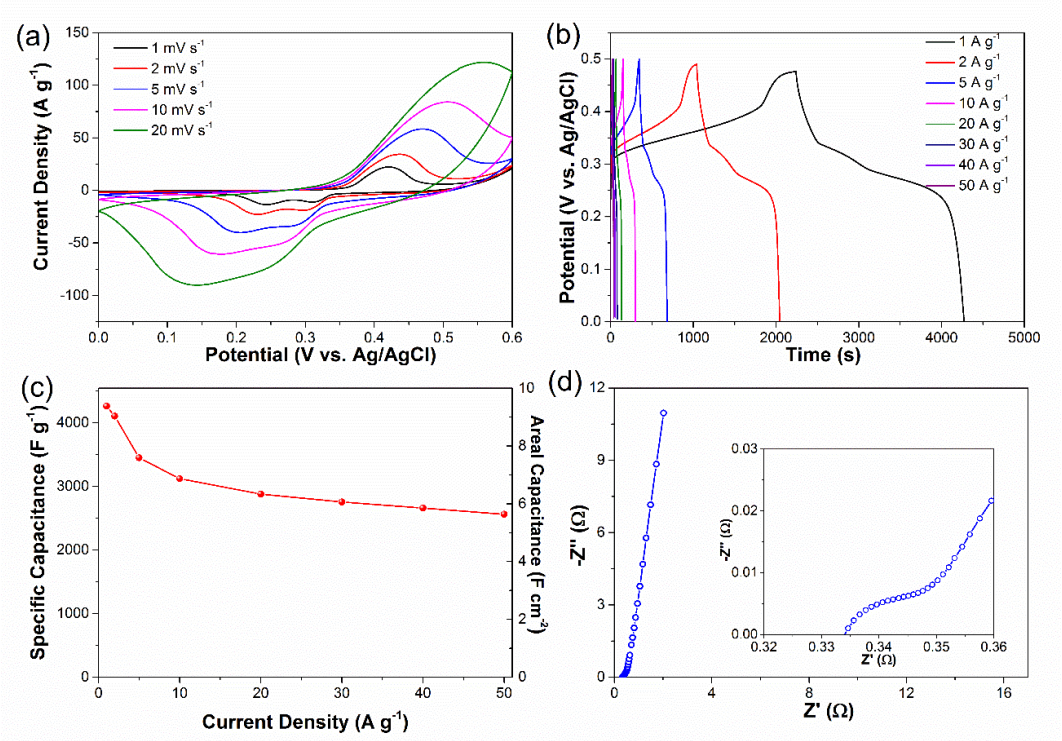

Fig. 6.10 Electrochemical performance of the $Cu_2O/CuMoO_4$ nanosheet electrode with a three-electrode mode in 2 M KOH. (a) CV curves of $Cu_2O/CuMoO_4$ nanosheet electrode at different scan rates; (b) GCD of the $Cu_2O/CuMoO_4$ electrode at various current densities; (c) Specific and areal capacitances at various current densities; (d) Nyquist plots of $Cu_2O/CuMoO_4$ electrode carried out at open circuit potential in the frequency range of 100 kHz to 0.01 Hz. The inset of (d) shows the impedance in high-frequency region.

The CV curves of the $Cu_2O/CuMoO_4$ electrode at different scan rates from 1 to 20 mV s^{-1} are shown in Fig. 6.10a. The appearance of the distinct redox peaks between 0 to 0.6 V vs. Ag/AgCl confirms the pseudocapacitive behaviour of the materials and implies good electrochemical reversibility. Herein, the pseudocapacitive behavior of the $Cu_2O/CuMoO_4$ is associated with its reversible reactions with KOH [219, 297]:

$$\frac{1}{2}Cu_2O + OH^- \leftrightarrow CuO + \frac{1}{2}H_2O + e^- \quad (6.1)$$

$$CuO + H_2O \leftrightarrow Cu(OH)_2 \quad (6.2)$$

$$Cu^{2+} + 2OH^- \leftrightarrow Cu(OH)_2 \quad (6.3)$$

$$Cu(OH)_2 + OH^- \leftrightarrow CuOOH + H_2O + e^- \quad (6.4)$$

Obviously, the current density increases with the increasing scan rate, while the anodic and cathodic peaks slightly shift towards the more positive and negative potentials respectively, which is supposed to be related to the internal resistance of the electrode [219] and limitation of charge transfer kinetic [266]. Fig. 6.10b shows the GCD curves at various current densities from 1 to 50 A g^{-1}. The nonlinear charge-discharge profiles further support the pseudocapacitive characteristics of the electrode, which is in good agreement with the CV curves in Fig. 6.10a. Based on the discharge curves, the specific capacitance of the electrode was calculated according to equation 3.10, and the areal capacitance can be calculated accordingly:

$$C_A = C_s A \tag{6.5}$$

where C_A is the areal capacitance (F cm^{-2}), C_s is the specific capacitance (F g^{-1}) and A is the mass loading of the electrode (mg cm^{-2}). The corresponded specific and areal capacitances against current density are plotted in Fig. 6.10c. The specific capacitance is 4264 F g^{-1} (9.38 F cm^{-2}) at a current density of 1 A g^{-1}, and it decreases to 3121 F g^{-1} (6.87 F cm^{-2}) when the current density increases to 10 A g^{-1}. It is believed that the degradation of capacitance with the increase of the current density is mainly due to the incremental iR drop and insufficient active material involved in redox reaction at high current densities [266]. However, as the current density keeps increasing, the electrode exhibits remarkable rate capability, namely, the specific capacitance still remains 2563 F g^{-1} (5.64 F cm^{-2}) at a current density of as high as 50 A g^{-1}. The present capacitance values here are much higher than those reported in previous studies using similar materials: Cu_2O/Cu nanoneedle arrays (510.2 F g^{-1}, 0.88 F cm^{-2} at 2.9 A g^{-1}) [219]; mesoporous NiO nanosheet (2504.3 F g^{-1}, 0.376 F cm^{-2} at 13.4 A g^{-1}) [218]; $NiMoO_4$ nanowires (3298 F g^{-1}, 4.94 F cm^{-2} at 5.33 A g^{-1}) [266]; $MnCo_2O_4$/$Ni(OH)_2$ core–shell nanoflowers (2124 F g^{-1}, 3.19 F cm^{-2} at 5 A g^{-1}) [145]; $NiCoO_2$ (508 F g^{-1} at 0.5 A g^{-1}) [275].

To further investigate the electrochemical behavior of the Cu_2O/$CuMoO_4$ electrode, EIS measurement was carried out in the frequency range from 100 kHz to 0.01 Hz at open circuit potential with the amplitude at 5 mV. As shown in Fig. 6.10d, the Nyquist plots of the Cu_2O/$CuMoO_4$ electrode are composed of a semicircle in

high-frequency region and a linear component in low-frequency region. The intercept of the plots at the real axis represents the equivalent series resistance (R_s), including the ionic resistance of the electrolyte, intrinsic resistance of active materials and the contact resistance between the active materials and current collector [270-272], which is determined at 0.334 Ω (inset of Fig. 6.10d). In terms of the semicircle, its diameter indicates the charge transfer resistance (R_{ct}) of system [270-272]. The corresponding R_{ct} of $Cu_2O/CuMoO_4$ electrode is only 0.02 Ω, implying the easy and rapid charge transfer on the electrode. In the low-frequency region, the straight line presents the Warburg impedance (W_o) [270-272], associated with the diffusive resistance of the electrolyte ions along the $Cu_2O/CuMoO_4$ nanosheets. The large slope of the straight line exhibited in Fig. 6.10d demonstrates a very small W_o of the electrolyte ion. The small values of R_s, R_{ct} and W_o suggest that there are large electro-active surface area and higher electrical conductivity with the $Cu_2O/CuMoO_4$ nanosheets, which could extend the reaction zone of the electrode, making more electrode materials available for charge-discharge, leading to high capacitance.

The dramatic high capacitance and outstanding rate capability of the $Cu_2O/CuMoO_4$ hybrid electrode can be attributed to its synthesis technique, nanostructure, and the synergistic effect from Cu_2O and $CuMoO_4$ components. The active materials are directly grown on the Ni foam current collector without any binders and conductive additives, which greatly reduce the contact resistance and improve the electrical conductivity of each nanosheet, leading to excellent conductivity of the electrode. Additionally, the specific surface area is significantly expanded with the nanosheets, which not only increases the electrolyte/electrode contact areas but also creates more active sites for rapid redox reactions with the anions and water molecules, enhancing the utilization of the $Cu_2O/CuMoO_4$ active materials. Moreover, the nanostructure could effectively facilitate the transport of electrolyte ions and electrons, and simultaneously, it is compatible with larger volume change during fast surface-dependent faradaic processes.

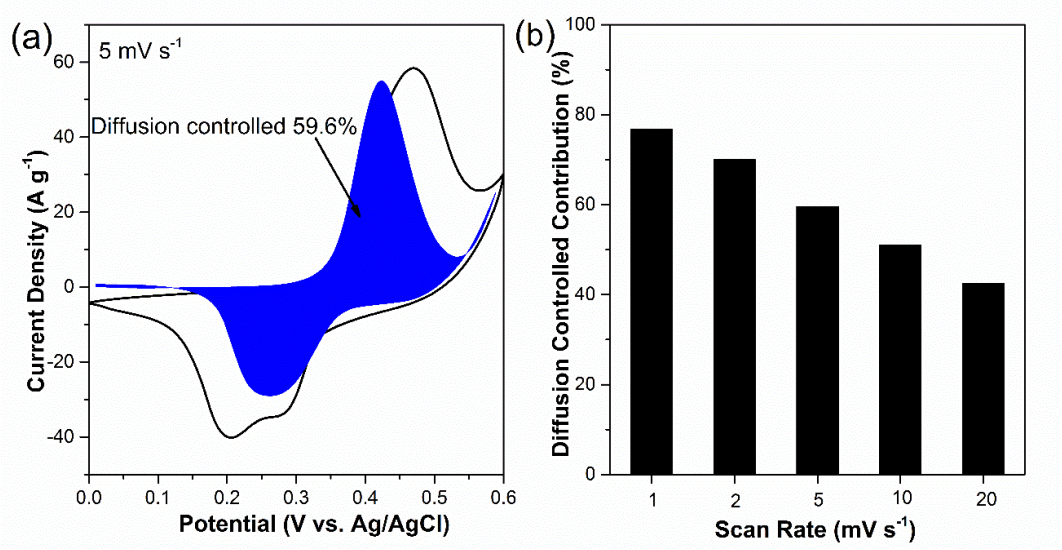

Fig. 6.11 (a) Typical separation of capacitive and diffusion-controlled charge storage process at scan rate of 5 mV s^{-1} in the $Cu_2O/CuMoO_4$ electrode (b) Contribution ratio of diffusion-controlled faradaic process to the total charge storage of the $Cu_2O/CuMoO_4$ electrode at various scan rates.

Generally, there are two different types of charge storage mechanisms for a supercapacitor material, namely, the surface-controlled capacitive process and the diffusion-controlled faradaic process. The surface-controlled capacitive process is the reaction occurred near or at the surface of the active materials. On the contrary, the diffusion-controlled faradaic process is the reversible redox reaction happened in the bulk materials. Distinct redox peaks are observed in the CV curves of the $Cu_2O/CuMoO_4$ electrode, suggesting the contribution of the diffusion-controlled faradaic process to the charge storage. However, large surface area is generated by the nanosheet structure, which could be involved in surface-controlled capacitive process. To quantify the capacitance contribution of the two processes, the CV curves of the $Cu_2O/CuMoO_4$ electrode were further analyzed according to equation 2.6 and 2.7. By plotting $i/v^{1/2}$ *vs.* $v^{1/2}$, k_1 and k_2 can be obtained as the slope and y-intercept, respectively. The fraction of the charge storage contributed by the surface-controlled capacitive process and the diffusion-controlled faradaic process can be calculated accordingly. Fig. 6.11a presents the percentage of charge stored by the diffusion-controlled faradaic process (blue area) on the $Cu_2O/CuMoO_4$ electrode at a scan rate of 5 mV s^{-1}. Around 59.6% of the capacitance is contributed by the diffusion-controlled faradaic process, and the remaining 40.4% is produced

by the surface-controlled capacitive process. The contribution ratio at different scan rates are shown in Fig. 6.11b. The percentage of diffusion-controlled contribution exhibits a high value of 76.7% at 1 mV s^{-1}, and then it gradually decreases to 42.4% at 20 mV s^{-1}. It is reasonable that the diffusion-controlled contribution declines with the increase of scan rates because the diffusion time is limited at high scan rates. This phenomenon has been reported by many groups [127, 162].

6.3.3 Electrochemical performances of $Cu_2O/CuMoO_4$//AC asymmetric supercapacitor

An ASC was assembled using the prepared $Cu_2O/CuMoO_4$ electrode as the positive electrode and AC electrode as the negative electrode for further investigating the performances of $Cu_2O/CuMoO_4$ nanosheet electrode under practical conditions. The electrochemical performance of the AC electrode presents a typical feature of carbon-based materials (see details in chapter 4). In order to find the optimal working potential, a series of CV measurements at different voltage windows were conducted at 5 mV s^{-1}. As seen from Fig. 6.12a, the operating windows are stable from 1.0 to 1.7 V. When it goes to 1.8 V, the polarization trend becomes very obvious, which means severe water electrolysis is under reacting. As a consequence, the best operating voltage window is determined as 1.7 V. Fig. 6.12b presents the CV performances of the ASC at different scan rates ranging from 1 to 20 mV s^{-1}. Unlike the single $Cu_2O/CuMoO_4$ or AC electrode, the ASC results quasi-rectangular CV curves in all scans, which means the capacitance is derived from both EDL capacitance and pseudocapacitance. The GCD curves of the ASC were measured at the current densities from 0.5 to 20 A g^{-1} (Fig. 6.12c). It can be seen that the discharge curves are nonlinear especially at low current densities, indicating the double contribution of EDL capacitance and pseudocapacitance, which is consistent with the CV results. The specific capacitance of the ASC was calculated from the GCD curves using equation 3.10. The specific capacitances at various current densities are plotted in Fig. 6.12d. The calculated capacitances are 191, 156, 114, 92, 83.7, 79.8 and 75.1 F g^{-1} at current densities of 0.5, 1, 2, 5, 10, 15 and 20 A g^{-1}, respectively. From 0.5 to 5 A g^{-1}, the specific capacitance experiences a significant decline,

losing around 50% of its initial value. This is due to the reduced availability of active materials for redox reaction at high current densities [266]. Nevertheless, it can be found that the as-fabricated ASC reveals excellent rate capability from 5 to 20 A g^{-1}. Since the surface-controlled capacitive process dominate the capacitance at high current densities, the capacitance becomes not sensitive to the current density.

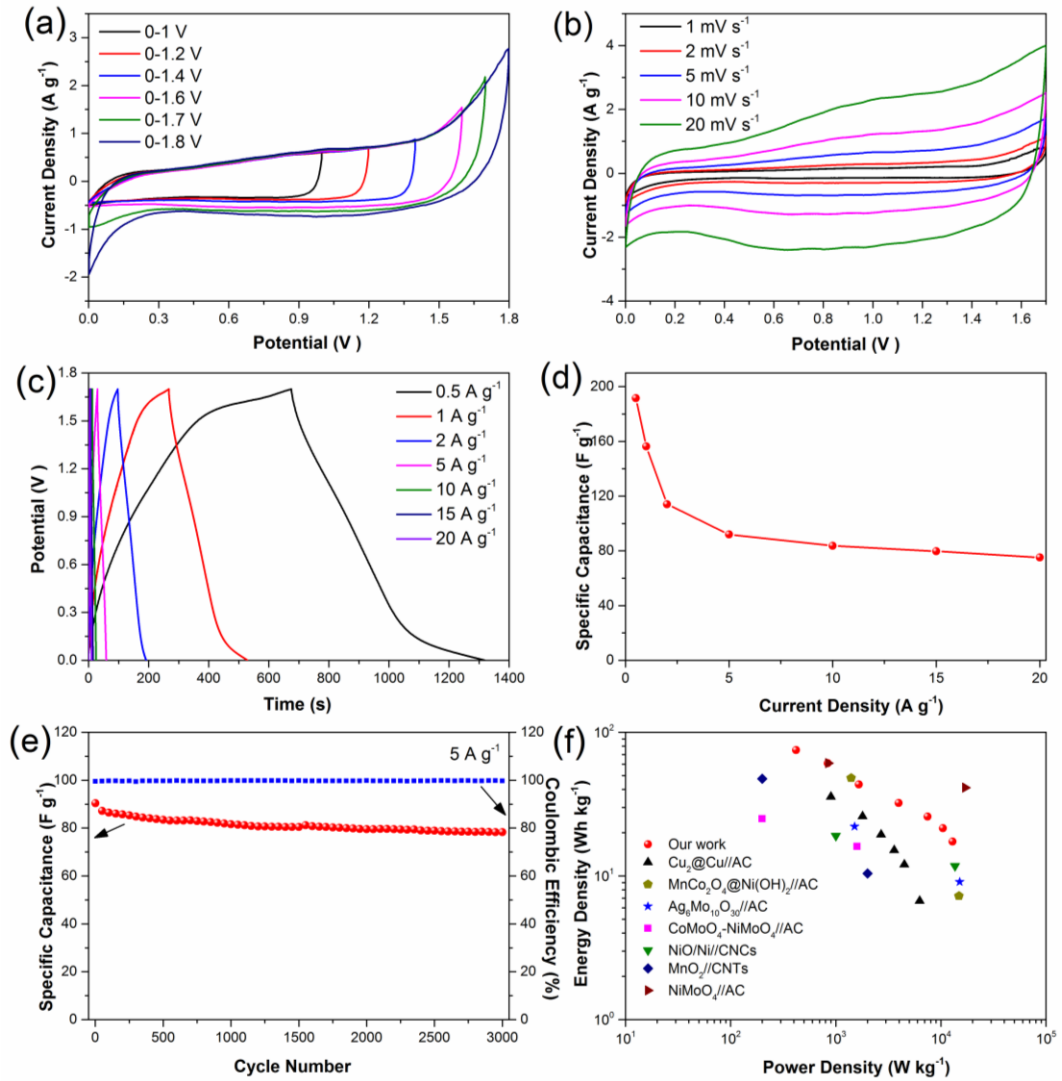

Fig. 6.12 Electrochemical properties of $Cu_2O/CuMoO_4$//AC ASC. (a) CV curves at various voltage windows at 5mV s^{-1}; (b) CV curves with a voltage window of 0-1.7 V at various scan rate; (c) GCD curves at various current densities; (d) Specific capacitance at various current densities. (e) Cycling stability and coulombic efficiency of the ASC for 3000 cycles at 5 A g^{-1}; (f) Ragone plots of our supercapacitor, compared with some other supercapacitors reported previously (CNCs: carbon nanocages, CNTs: carbon nanotubes).

To further investigate the durability of the ASC, its cycling stability and coulombic efficiency were recorded at 5 A g^{-1} (Fig. 6.12e). The specific capacitance still retains 86.6% of the initial value even after 3000 cycles, which demonstrates excellent electrochemical stability. It is believed the decline of the capacitance is caused by the loss of the electrical contact between the active materials and the Ni foam during numerous rapid redox reactions [31, 145]. This is also evidenced by first and last ten charge-discharge curves (Fig. 6.13). Furthermore, the $Cu_2O/CuMoO_4$//AC ASC maintains nearly 100% coulombic efficiency during the 3000 cycles, indicating its high electrochemical reversibility [247].

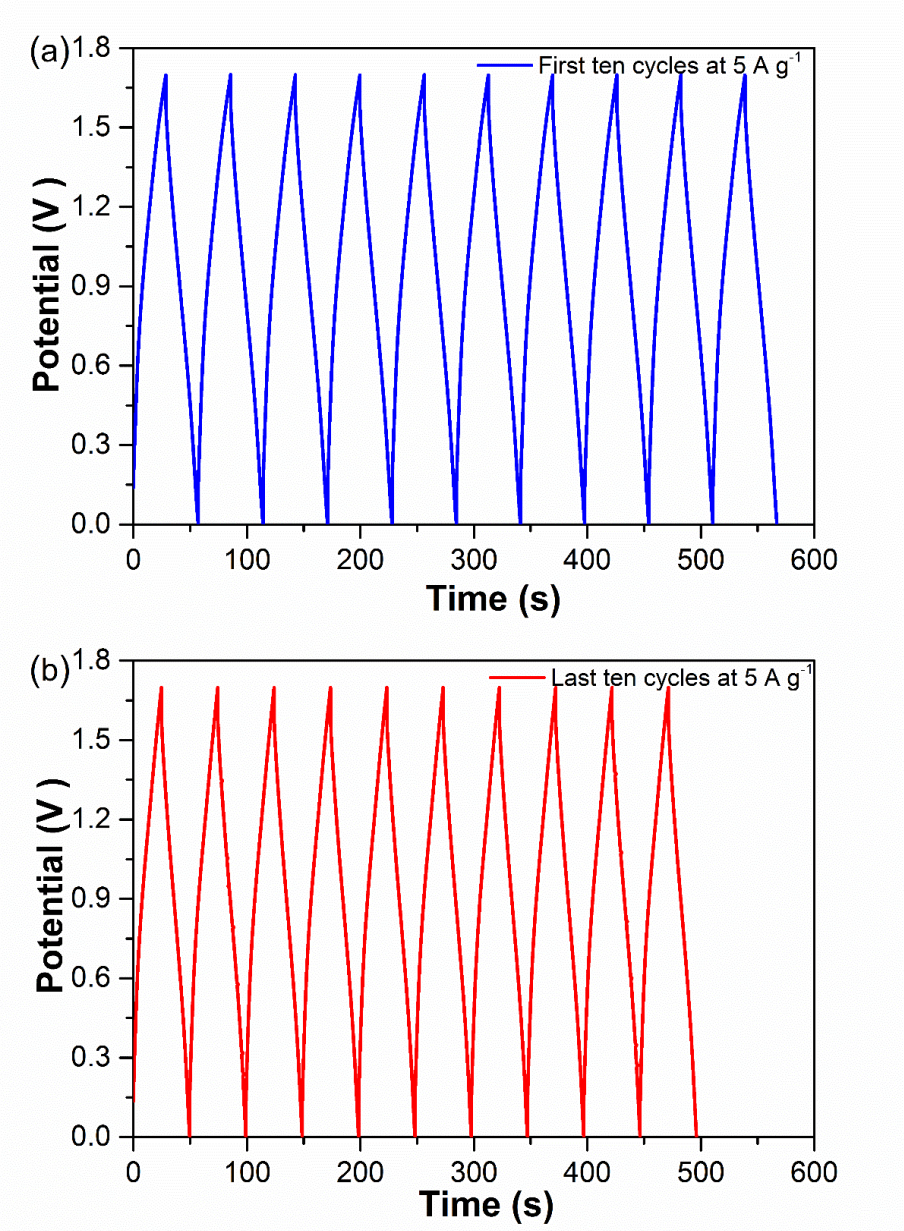

Fig. 6.13 (a) First and (b) last ten charge-discharge curves of the $Cu_2O/CuMoO_4$//AC ASC at a current density of 5 A g^{-1}.

Energy densities and power densities are crucial properties for an energy storage device. The energy densities and power densities of the ASC were obtained by equation 3.12 and 3.13. The Ragone plots of the ASC derived from discharge curves are displayed in Fig. 6.12f. The maximum energy density can be determined as 75.1 Wh kg^{-1} at an average power density of 420 W kg^{-1}. It can still maintain 21.5 Wh kg^{-1} even at a high power density of 10435 W kg^{-1}. It is found that the performance of $Cu_2O/CuMoO_4$//AC ASC is better than many previously reported systems, such as Cu_2O@Cu//AC [219], $MnCo_2O_4$@$Ni(OH)_2$//AC [145], $Ag_6Mo_{10}O_{30}$//AC [99], $CoMoO_4$-$NiMoO_4$//AC [286], NiO/Ni//CNCs [261] and MnO_2//CNTs [298].

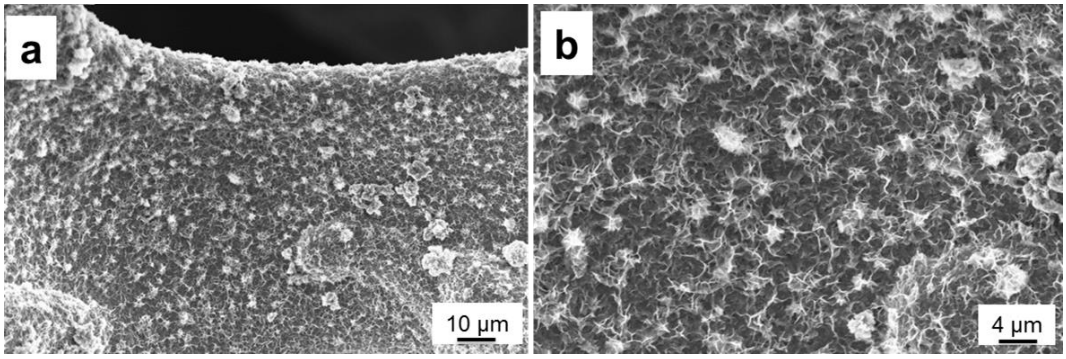

Fig. 6.14 SEM images of $Cu_2O/CuMoO_4$ nanosheet electrode after charge-discharge for 3000 cycles at a current density of 5 A g^{-1}.

To further probe the stability of the hybrid electrode, the sample after stability test was observed by SEM. Fig. 6.14 presents the SEM images after 3000 charge-discharge cycles at 5 A g^{-1}, it can be clearly seen that the physical microstructures of the electrode keep very well in comparison with Fig. 6.2, which are still in nanosheets. As no notable changes can be found on the electrode before and after the cycling measurements, it proves the good stability of the hybrid electrode.

6.4 Conclusions

In summary, we have successfully synthesized a hybrid $Cu_2O/CuMoO_4$ nanosheet electrode via a facile hydrothermal method and it exhibits remarkable improved specific and areal capacitance (up to 4264 F g^{-1} and 9.38 F cm^{-2} at a current density of 1 A g^{-1}). In addition, the electrode presents good rate capability, specifically, the capacitance still retains 2563 F g^{-1} (5.64 F cm^{-2}) at a current density as high as

50 A g^{-1}. Moreover, an ASC is fabricated using the $Cu_2O/CuMoO_4$ nanosheet electrode as the positive electrode and AC as the negative electrode. The operation voltage of the ASC could achieve 1.7 V, at which the energy density is 75.1 Wh kg^{-1} with a power density of 420 W kg^{-1}. The ASC also displays excellent rate capability, cycling stability and electrochemical reversibility. The capacitance maintains around 86.6% with nearly 100% coulombic efficiency after 3000 cycles at a current density of 5 A g^{-1}. Considering the fascinating performances of the $Cu_2O/CuMoO_4$ nanosheet electrode and easy fabrication procedures, the electrodes are promising for applications in renewable energy storage.

CHAPTER 7 Synthesis of $NiMoS_4$ as high-performance asymmetric supercapacitor materials

7.1 Introduction

As we introduced in the previous chapters, the demand for high-performance electrochemical energy storage devices is ever-growing as they are critical components for portable electronics, electric vehicles, and efficient storage mediums for energy from renewable sources [8]. Electrochemical supercapacitors have drawn tremendous amount of interest due to their high powder density, rapid charge-discharge rate and outstanding cycle life [3, 6, 299]. Currently, most commercial supercapacitors are SSCs based on carbon materials which possess better performance in terms of cycle life and power density, but the low specific capacitance and energy density limit their widespread applications [288]. It is supposed that developing ASCs could be a promising approach to fulfil the high energy density requirement without sacrificing the power density and cycle life [117].

Transition metal oxides are the most common pseudocapacitive materials and have been extensively studied due to their high theoretical capacities and low cost [3]. Many materials have been claimed holding good supercapacitor performances such as MnO_2 [300, 301], NiO [302, 303], MoO_3 [33, 34] etc. However, the performances of metal oxides often suffer from poor conductivity and mechanical stability especially at high rates [134]. It is known that the metal sulfides usually possess higher conductivity than the corresponding oxides. Therefore, plenty of sulfides have been applied as new pseudocapacitive materials with good performances being obtained. For instance, Pang *et al.* prepared a NiS_2 nanocube electrode via a microwave-assisted method, demonstrating a large specific capacitance of 695 F g^{-1} at 1.25 A g^{-1} and an excellent cycling performance of 93.4% retention after 3000 cycles [119]. Acerce *et al.*'s research indicates that chemically exfoliated nanosheets of MoS_2 can efficiently intercalate H^+, Li^+, Na^+ and K^+ ions to achieve high capacitance in a variety of aqueous electrolytes [124]. As $NiMoO_4$ has been confirmed as a good capacitive material [183, 266], it can be deduced that, its sulfide analogue, $NiMoS_4$ would also be a good candidate for

supercapacitors. $NiMoS_4$ has been applied in hydrogen evolution [304] and dye-sensitized solar cells [305] as previously reported.

In this chapter, we report a ternary compound $NiMoS_4$-A which was synthesized by a facile chemical co-precipitation process followed by calcining at 450 °C in Ar. Physical and electrochemical properties of sample $NiMoS_4$-A were extensively studied. The $NiMoS_4$-A electrode exhibits a high specific capacitance of 706.5 F g^{-1} at 1 A g^{-1} and good rate capability (83% retention at 10 A g^{-1}). EIS results indicate that the good performances could be attributed to the low internal and charge transfer resistances. Moreover, an ASC, with $NiMoS_4$-A as the positive electrode and AC as the negative electrode, was fabricated to investigate the performances in practical energy storage devices. The ASC displays a high energy density of 35 Wh kg^{-1} at an average power density of 400 W kg^{-1}. Meanwhile, an excellent cycle stability and electrochemical reversibility are observed: 82% of the initial capacitance and around 97% of the coulombic efficiency are retained after 10000 charge-discharge cycles even at a high current density of 5 A g^{-1}. These results indicate that $NiMoS_4$-A is a promising electrode material for high-performance energy storage devices.

7.2 Experimental

7.2.1 Synthesis of $(NH_4)_2MoS_4$

$(NH_4)_2MoS_4$ was synthesized following a previously reported method [304]. To prepare the $(NH_4)_2MoS_4$, 7.5 g $(NH_4)_6Mo_7O_{24}{\cdot}4H_2O$ was dissolved in 5 mL ammonia and 10 mL H_2O under constant stirring. Then 60 mL of 20% $(NH_4)_2S$ solution was added dropwise at room temperature. The system was kept in a water bath at 60 °C for 2 h. After that, the obtained red-brown solution was cooled in an ice-bath to allow the $(NH_4)_2MoS_4$ to crystallize. Finally, the resultant crystals were collected by centrifugation and washed with ethanol several times. The products were dried under vacuum at 30 °C. The mechanisms of the formation of $(NH_4)_2MoS_4$ crystal can be expressed by the following equations [306]:

$$(NH_4)_6Mo_7O_{24} + 8NH_3 \cdot H_2O \rightarrow 7(NH_4)_2MoO_4 + 4H_2O \quad (7.1)$$

$$(NH_4)_2MoO_4 + 4(NH_4)_2S + 4H_2O \rightarrow (NH_4)_2MoS_4 + 8NH_3 \cdot H_2O \quad (7.2)$$

7.2.2 Synthesis of $NiMoS_4$

Firstly, 4 mmol $(NH_4)_2MoS_4$ was dispersed in 30 mL water with 5 mL ethanol. Similarly, 4 mmol $Ni(NO_3)_2{\cdot}6H_2O$ was dissolved in 30 mL water with 5 mL ethanol. The $Ni(NO_3)_2$ solution was added into the $(NH_4)_2MoS_4$ solution under vigorous magnetic stirring and kept overnight. The black precipitate was collected by centrifugation, washed with distilled water and absolute ethanol several times, and finally vacuum dried at 30 ^oC. In addition, the $NiMoS_4$ was further calcined at 450 ^oC for 2 h under Ar atmosphere. For comparison, the calcined $NiMoS_4$ was denoted as $NiMoS_4$-A.

7.2.3 Electrode preparation

The working electrode was prepared as follows: a homogeneous slurry comprised of the active materials, acetylene black and PTFE in a mass ratio of 8 : 1 : 1 was coated onto Ni foam (1 × 1 cm^2), pressed at 10 MPa, and finally dried at 60 ^oC under vacuum. The mass loading of the active materials on each working electrode was 1-2 mg cm^{-2}.

7.2.4 Assemble of $NiMoS_4$-A//AC asymmetric supercapacitor

To fabricate the ASC, the as-prepared $NiMoS_4$-A electrode and an AC electrode were used as the positive electrode and the negative electrode, respectively. The AC negative electrode was obtained by mixing the AC (Black Pearl 2000, Cabot) and PTFE at a mass ratio of 95 : 5 in water under constant magnetic stirring. The prepared slurry was spread onto a Ni foam (1×1 cm^2) and then pressed at 10 MPa and dried at 60 ^oC overnight under vacuum. To assemble the full cell, the negative electrode and positive electrode were face to face placed into a container in which the electrolyte was added.

7.2.5 Physical characterization

XRD patterns were obtained on a Panalytical X'Pert Pro Multi-Purpose Diffractometer (MPD) with Cu Kalpha1 radiation working at 45 kV and 40 mA. The morphologies and microstructures of the as-synthesized materials were

identified using SEM (ZEISS SUPRA 55-VP). The elemental compositions were investigated by EDX attached to the SEM.

7.2.6 Electrochemical measurements

The performance of the prepared $NiMoS_4$ and $NiMoS_4$-A electrodes were investigated in a three-electrode system with a piece of Pt mesh (1×1 cm^2) and an Ag/AgCl electrode (sat. KCl) serving as counter and reference electrodes, respectively. The electrochemical performances of the $NiMoS_4$-A//AC ASC were explored under a two-electrode mode. The electrochemical measurements including CV, GCD and EIS, were carried out on a Solartron 1470E/1455 multichannel cell test system. Impedance spectroscopy were recorded with a potential amplitude of 5 mV at open circuit potential in a frequency range of 100 kHz to 0.01 Hz. All the measurements were performed at room temperature in 2 M KOH aqueous electrolyte.

7.3 Results and discussion

7.3.1 Physical characterization of $NiMoS_4$ and $NiMoS_4$-A

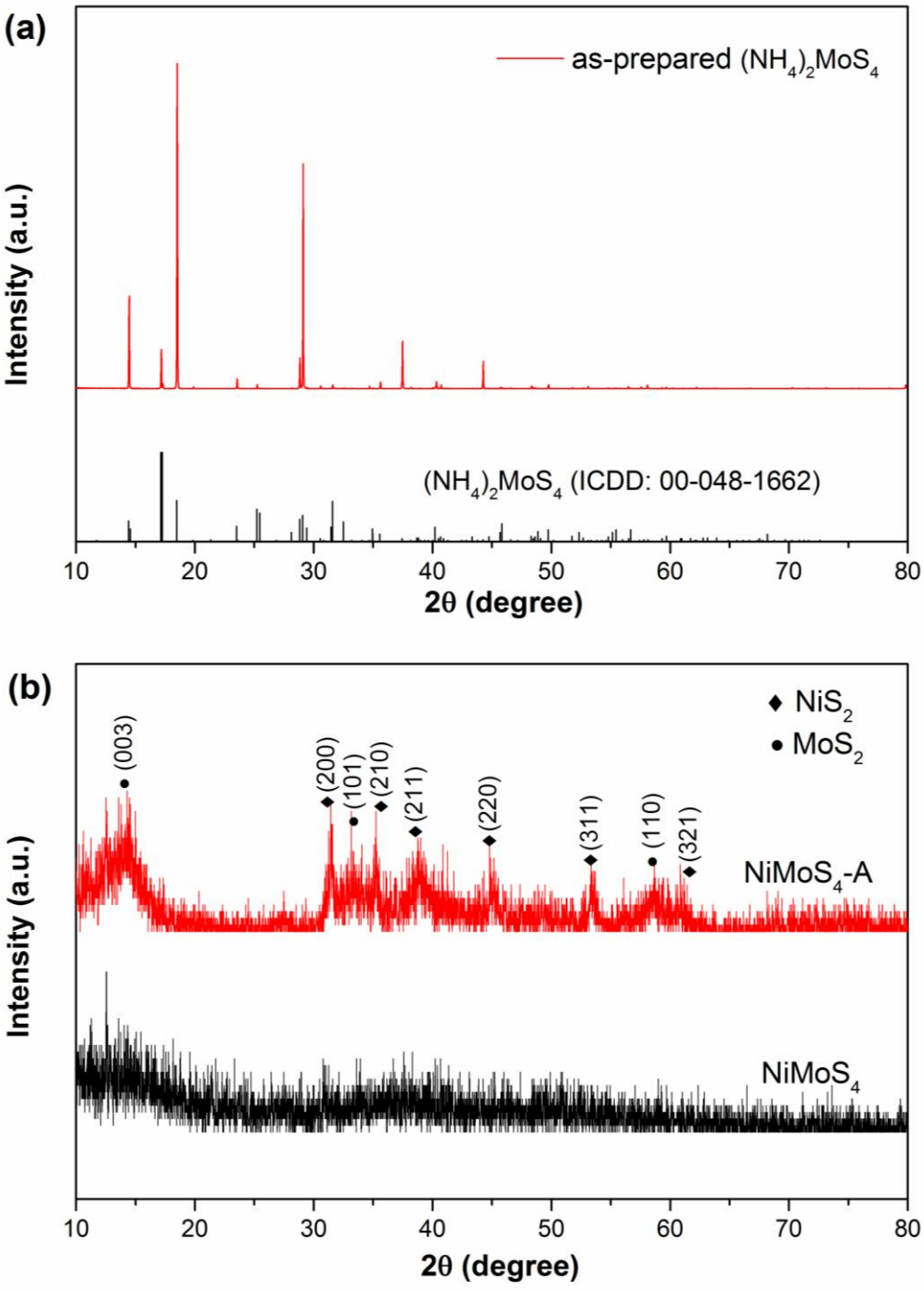

Fig. 7.1 XRD patterns of (a) $(NH_4)_2MoS_4$, (b) $NiMoS_4$ and $NiMoS_4$-A.

The compositions of the synthesized $(NH_4)_2MoS_4$ and $NiMoS_4$ were examined by XRD. As shown in Fig. 7.1a, the diffraction peaks of the as-prepared $(NH_4)_2MoS_4$

matched well with the orthorhombic $(NH_4)_2MoS_4$ (ICCD 00-048-1662), specifically, the major peaks at around 14.6°, 17.3°, 18.5°, 29.1° and 37.5° can be indexed to the (011) (111) (200) (040) and (400) crystal planes respectively. These results indicate that the $(NH_4)_2MoS_4$ was successfully prepared. $NiMoS_4$ was obtained by reacting $(NH_4)_2MoS_4$ with nickel nitrate. No peaks were found in the XRD patterns of $NiMoS_4$ (Fig. 7.1b), showing typical amorphous features, which is consistent with the results reported in the literature [304]. As the $NiMoS_4$ was further calcined at 450 °C, obvious diffraction peaks appeared in the $NiMoS_4$-A patterns (Fig. 7.1b). The peaks at 14.2°, 33.0° and 58.4° could be assigned to the (003) (101) and (110) planes of MoS_2 (ICDD 04-008-2233) while the peaks at 31.4°, 35.3°, 38.8°, 45.1°, 53.4° and 60.9° correspond to the (200) (210) (211) (220) (311) and (321) planes of NiS_2 (ICCD 04-003-1992). The results reveal that sample $NiMoS_4$-A contains small quantities of poorly crystalized NiS_2 and MoS_2.

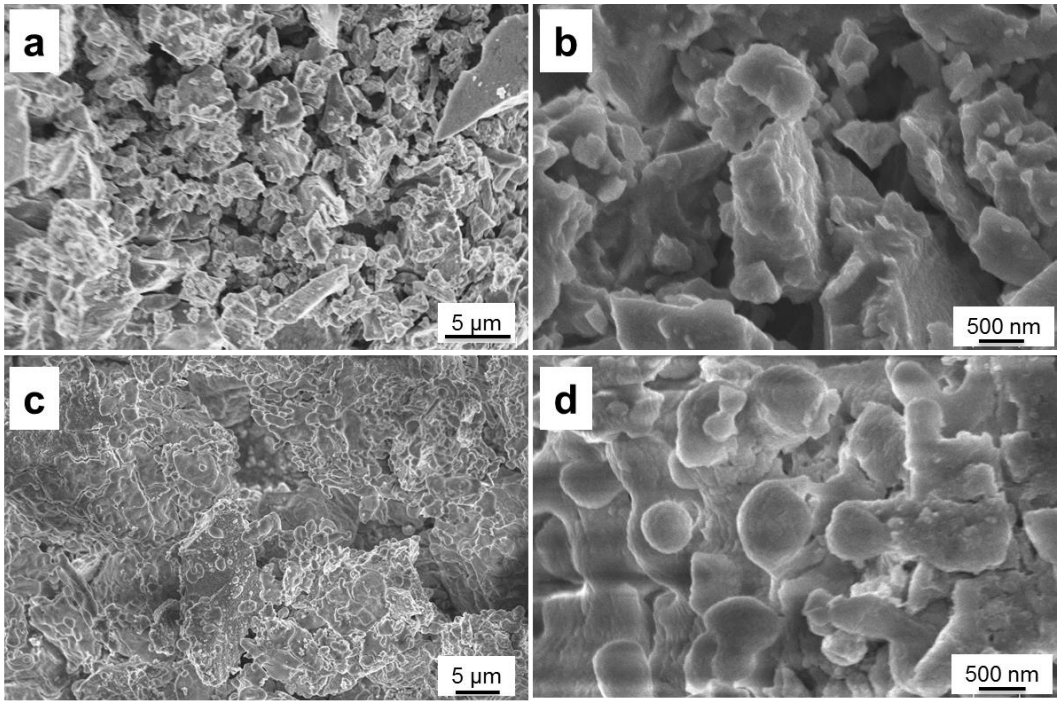

Fig. 7.2 SEM images of (a-b) $NiMoS_4$ and (c-d) $NiMoS_4$-A.

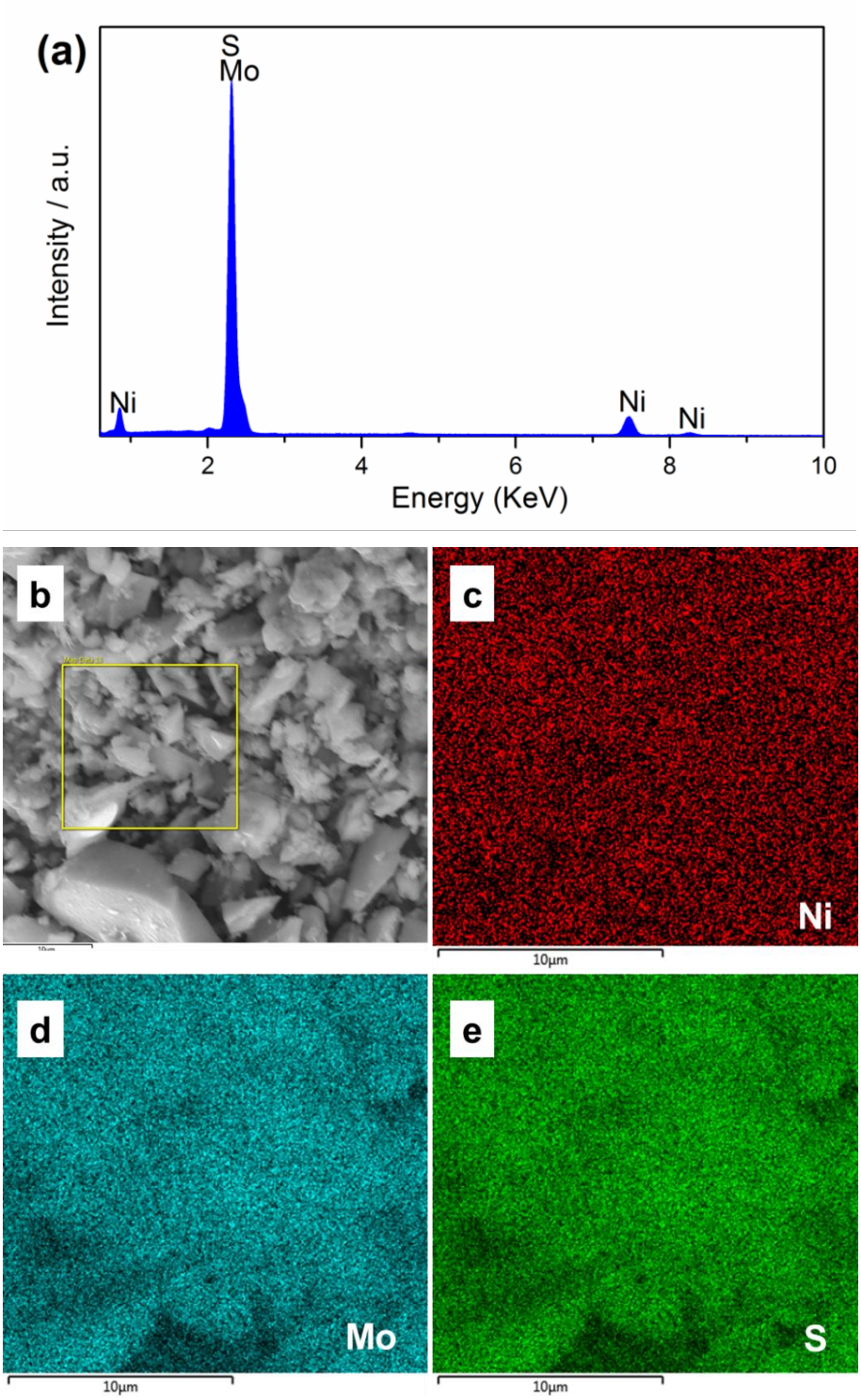

Fig. 7.3 (a) EDX spectrum and (b-f) corresponding mappings of Ni, Mo and S elements for the selected region of sample $NiMoS_4$.

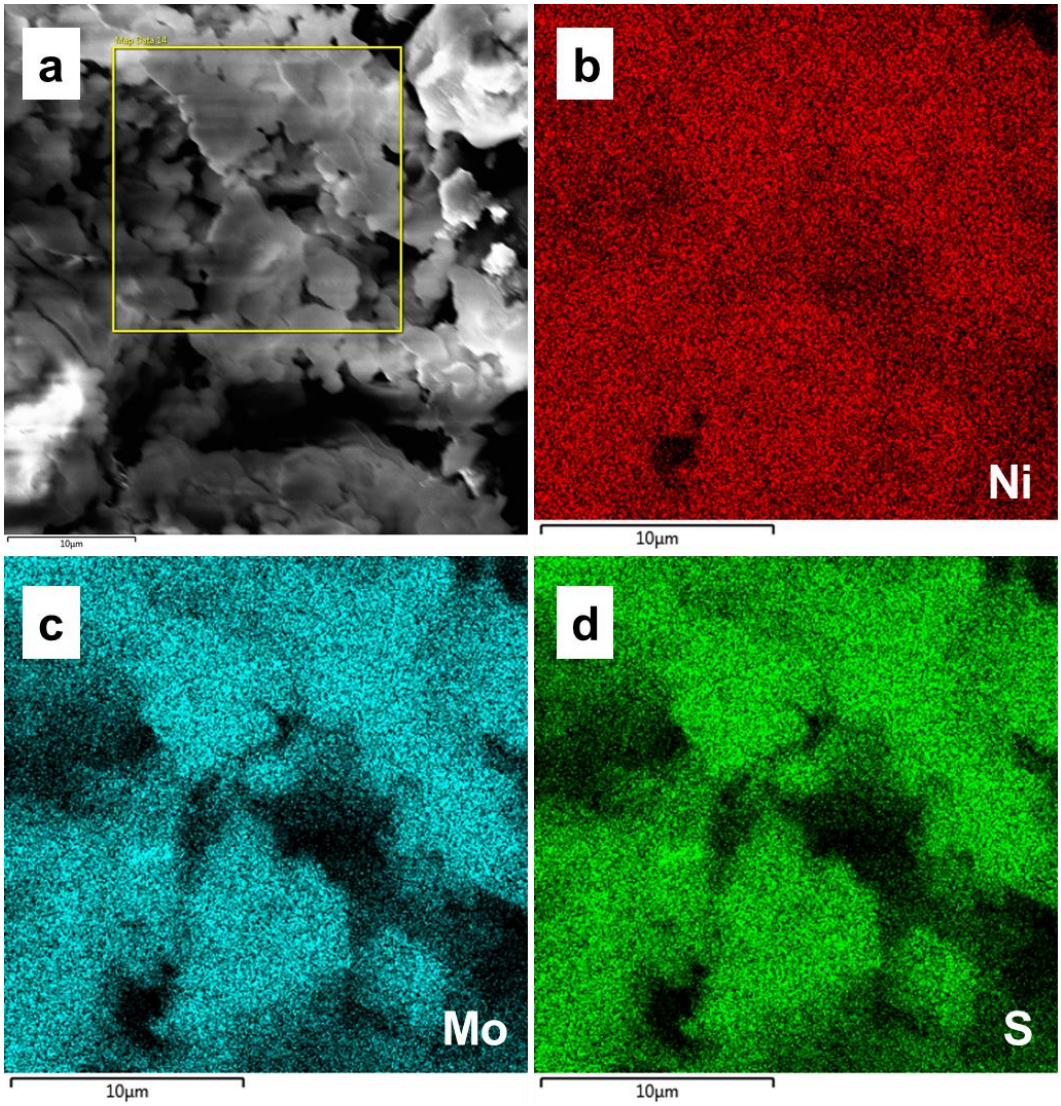

Fig. 7.4 EDX mappings of Ni, Mo and S elements of sample $NiMoS_4$-A.

To investigate morphology properties of the synthesized materials, SEM was carried out for samples $NiMoS_4$ and $NiMoS_4$-A. As shown in Fig. 7.2a and b, sample $NiMoS_4$ is composed of irregular particles. For sample $NiMoS_4$-A (Fig. 7.2c and d), the particles are loosely agglomerated forming porous structures, which could improve the access of the electrolyte into the material during charge-discharge, thus promoting energy storage performances. EDX were conducted to determine the element compositions in the samples. Elements Ni, Mo, and S are observed in $NiMoS_4$ according to the EDX spectrum (Fig. 7.3a), which is in good agreement with the reagents used in the preparation processes. The distribution of each element was identified through elemental mapping as shown in Fig. 7.3b-e. Clearly, the Ni, Mo, and S elements are uniformly distributed, the same result was

also found for sample $NiMoS_4$-A (Fig. 7.4), indicating that possible agglomeration of the segregated NiS_2 and MoS_2 is not significant.

7.3.2 Electrochemical performances of $NiMoS_4$ and $NiMoS_4$-A

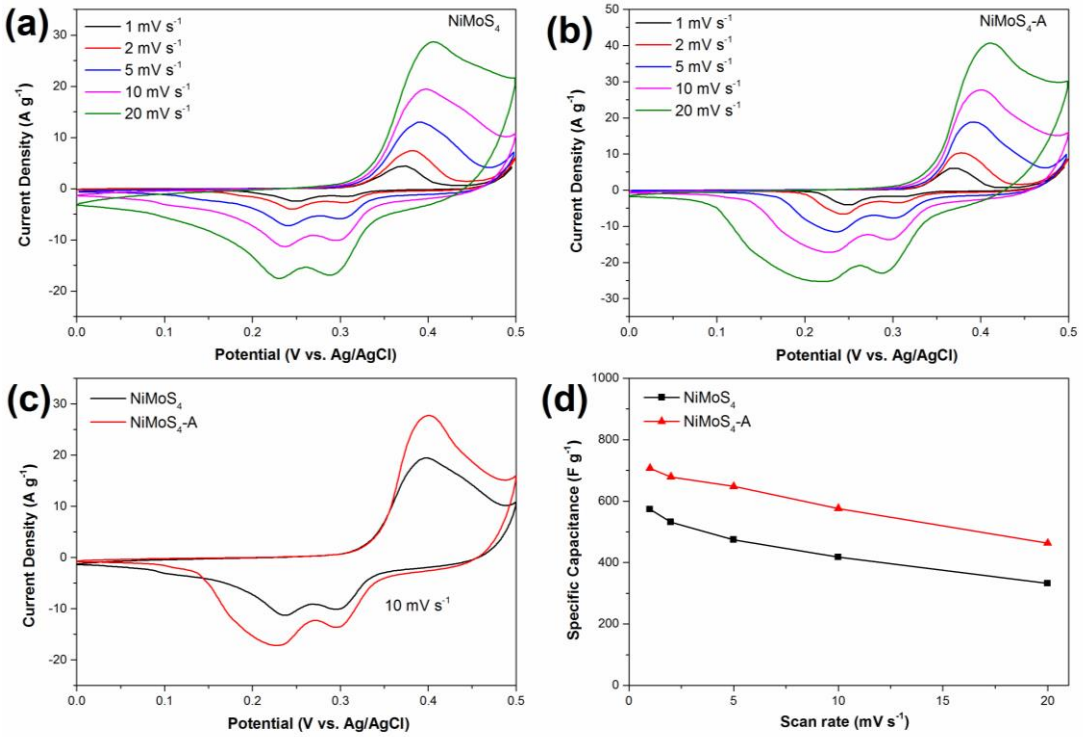

Fig. 7.5 CV curves at different scan rates of (a) $NiMoS_4$ and (b) $NiMoS_4$-A. (c) Comparison of CV curves of $NiMoS_4$ and $NiMoS_4$-A electrode at scan rate of 10 mV s^{-1}. (d) Specific capacitances at various san rates.

The prepared electrodes were examined in a three-electrode system using 2 M KOH electrolyte in order to explore the electrochemical properties. Fig. 7.5a indicates the CV curves of sample $NiMoS_4$ at different scan rates from 1 to 20 mV s^{-1} in a potential window of 0 to 0.5 V vs. Ag/AgCl. Redox peaks are found in the CV curves, demonstrating that the energy storage ability is mainly contributed by the faradaic redox reactions. It can be clearly seen that the CV curves exhibit a similar shape over all the scans, indicating good kinetic reversibility of the $NiMoS_4$ electrode [270, 307]. Moreover, it can be deduced that the electrode presents low polarization [307] and rapid electronic and ionic transportation [134, 308] since the anodic and cathodic peaks slightly shift towards the positive and negative potentials respectively at increasing scan rates. The CV curves of the $NiMoS_4$-A

electrode at different scan rates are presented in Fig. 7.5b. It is evident that CV behaviours similar to that of $NiMoS_4$ were observed. The redox peaks found here can be ascribed to the reversible reactions of Ni and Mo in different valences in KOH electrolyte, which can be described by the following equations [120, 309, 310]:

$$NiS_2 + OH^- \leftrightarrow NiOHS_2 + e^- \quad (7.3)$$

$$MoS_2 + xK^+ + xe^- \leftrightarrow K_xMoS_2 \quad (7.4)$$

Obviously, sample $NiMoS_4$-A exhibits larger current density responses than $NiMoS_4$ at each same scan rate. Fig. 7.5c displays the CV plots of $NiMoS_4$ and $NiMoS_4$-A at 10 mV s^{-1}. It is believed that the integral area of CV curves is proportional to the specific capacitance [311]. Obviously, the CV curve of $NiMoS_4$-A encloses a larger area than that of $NiMoS_4$, suggesting that more charges can be stored in the $NiMoS_4$-A electrode. The specific capacitance of the electrode can be calculated from the CV curves using equation 3.9. The specific capacitances of $NiMoS_4$ and $NiMoS_4$-A calculated based on the corresponding CV curves at different scan rates are shown in Fig. 7.5d. The specific capacitance of $NiMoS_4$-A is 706.6 F g^{-1} at 1 mV s^{-1}, larger than the value of $NiMoS_4$ (573.6 F g^{-1}). All the capacitances gradually decrease with increasing scan rates, reaching 462.9 F g^{-1} and 332.3 F g^{-1} at 20 mV s^{-1} for $NiMoS_4$-A and $NiMoS_4$ respectively. It can be seen that sample $NiMoS_4$-A performs better rate capability than sample $NiMoS_4$, namely, retaining 65.5% vs. 57.9% from 1 to 20 mV s^{-1}.

GCD measurements of samples $NiMoS_4$ and $NiMoS_4$-A with current densities ranging from 1 to 10 A g^{-1} are recorded in Fig. 7.6a and b respectively. It can be seen that both $NiMoS_4$ and $NiMoS_4$-A exhibit nonlinear GCD curves, which further support the faradaic behaviours of these materials. Fig. 7.6c compares the GCD curves of $NiMoS_4$ and $NiMoS_4$-A at a current density of 1 A g^{-1}. It shows that more charges can be stored in the $NiMoS_4$-A electrode due to its longer discharge time, which is consistent with the CV results shown above. The specific capacitance could also be determined from the GCD curves based on equation 3.10 as shown in Fig. 7.6d. Sample $NiMoS_4$-A exhibits a good specific capacitance of 706.5 F g^{-1} at a current density of 1 A g^{-1}. At current densities of 2, 4, 6, 8, and 10 A g^{-1}, the specific capacitances are 676.3, 647.2, 610.7, 596.4 and 584.5 F g^{-1}

respectively. This means that roughly 83% of the capacitance can be maintained with a 10-fold increase in the current density, implying an excellent rate capability of sample $NiMoS_4$-A. The gradual decrease in specific capacitance could be ascribed to insufficient active materials involved in the redox reaction as diffusion time is limited for electrolyte ions accessing the active materials at high charge-discharge rates [312]. Noticeably, sample $NiMoS_4$-A has a superior specific capacitance to that of sample $NiMoS_4$, specifically, only 501.5 F g^{-1} is achieved by $NiMoS_4$ at 1 A g^{-1} and 67% of the initial value is preserved when the current density increases to 10 A g^{-1}.

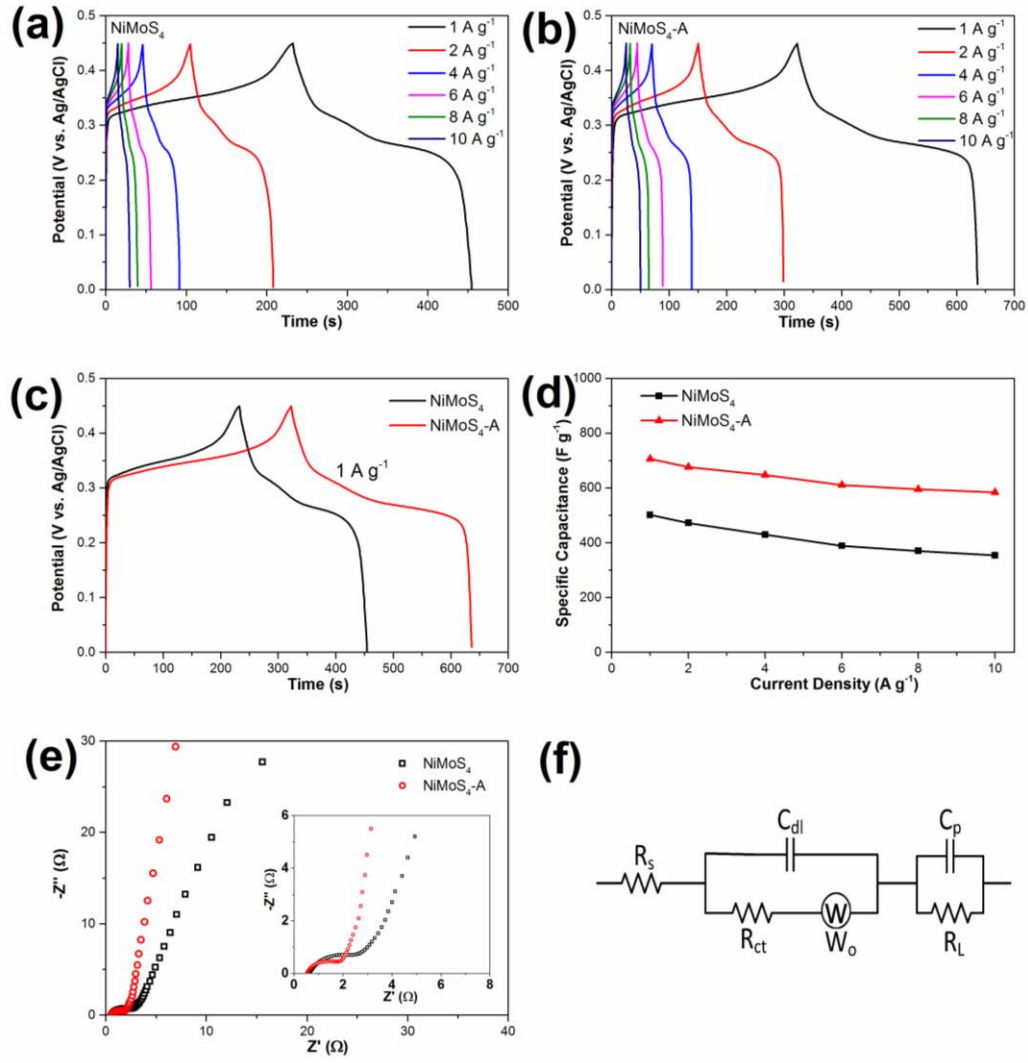

Fig. 7.6 GCD curves at different current density of (a) $NiMoS_4$ and (b) $NiMoS_4$-A. (c) Comparison of GCD curves of $NiMoS_4$ and $NiMoS_4$-A electrode at a current density of 1 A g^{-1}. (d) Specific capacitances at various current densities. (e) Nyquist plots at open circuit potential. (f) The equivalent circuit.

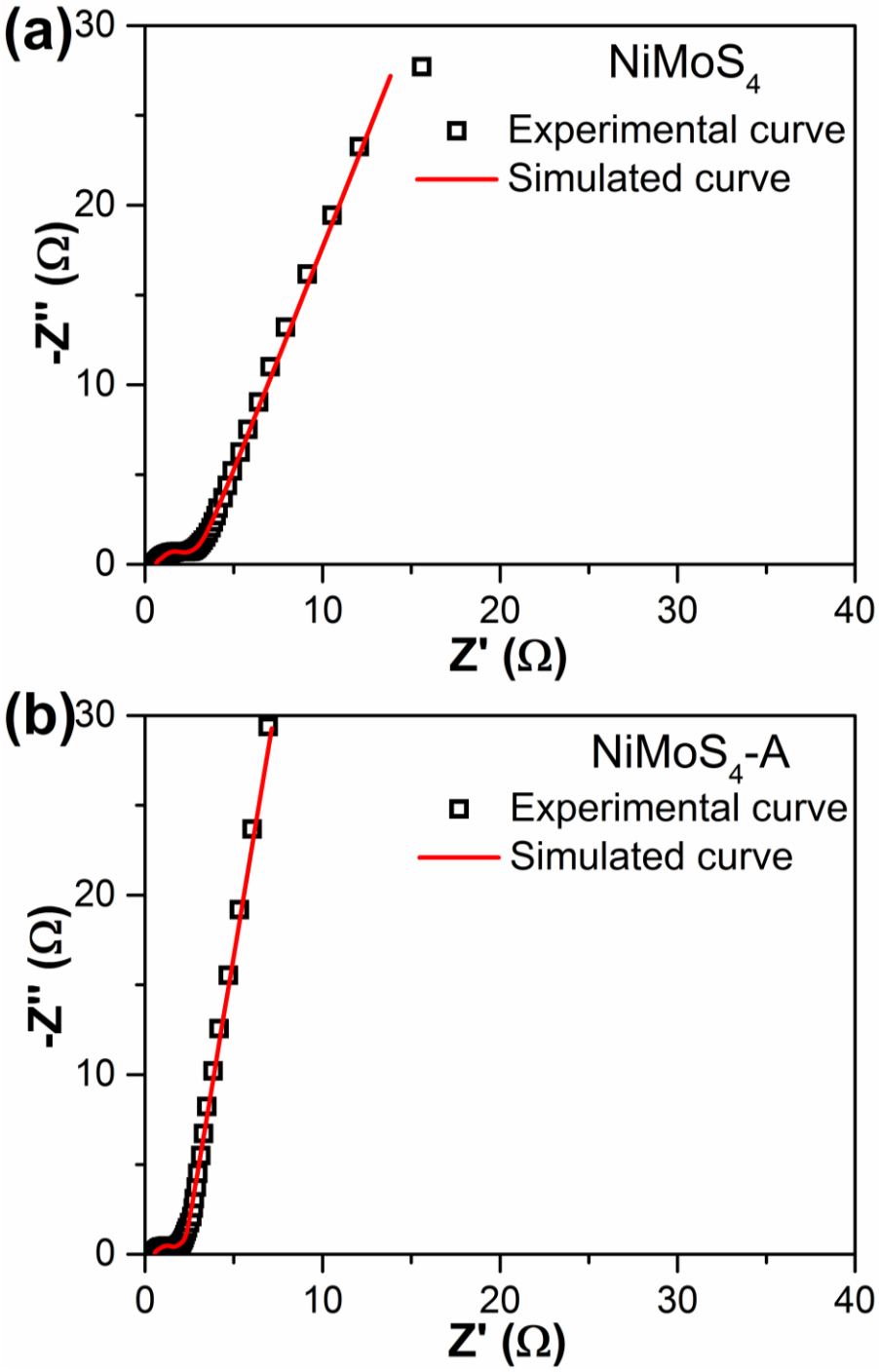

Fig. 7.7 Experimental and simulated Nyquist plots of (a) $NiMoS_4$ and (b) $NiMoS_4$-A.

The differences of electrochemical performance between samples $NiMoS_4$ and $NiMoS_4$-A are partially related to the impedance of the electrodes. Therefore, EIS measurement was carried out to further explore charge-transfer kinetics. Fig. 7.6e depicts the Nyquist plots of the $NiMoS_4$ and $NiMoS_4$-A electrodes at open circuit potential. It is evident that the graph is composed of a semicircle in high-frequency

region and a linear part in low-frequency region. An equivalent circuit for fitting the Nyquist plots is shown in Fig. 7.6f, where R_s is the internal resistance, which is also known as equivalent series resistance (ESR), R_{ct} is the charge transfer resistance, W_0 is the Warburg impedance, C_{dl} is the electric double layer capacity, C_p is the faradaic capacity, and R_L is the leakage resistance [161, 267]. The fitting curve and the experimental data match very well with each other (Fig. 7.7), confirming that the proposed equivalent circuit model is suitable for the electrodes. The internal resistance (R_s), containing the bulk resistance of the electrolyte, the intrinsic resistance of the active materials and the contact resistance from the interface of active material and current collector, could be estimated by the intersection of the curves on the real axis [134, 313]. The R_s for sample $NiMoS_4$-A is 0.53 Ω, slightly lower than 0.62 Ω for sample $NiMoS_4$, suggesting sample $NiMoS_4$-A may possess higher conductivity. The R_{ct}, demonstrating the rate of faradaic redox process at the electrode-electrolyte interface, can be evaluated by the diameter of the semicircle [161]. Sample $NiMoS_4$-A exhibits smaller R_{ct} (1.9 Ω) than that of sample $NiMoS_4$ (3.2 Ω), implying the faster electron transfer on the $NiMoS_4$-A electrode, possibly owning to the porous morphology of $NiMoS_4$-A, which could facilitate the diffusion of electrolyte into the active materials, thus lowering the charge resistance. The straight line at low frequencies is associated with the Warburg impedance (W_o), which is supposed to describe the diffusive resistance of electrolyte ions within the electrode [314]. Sample $NiMoS_4$-A exhibits a more vertical line, showing lower mass-transfer resistance in the host materials. Overall, the better impedance performances in terms of R_s, R_{ct} and W_o for $NiMoS_4$-A should lead to improved electrochemical properties, which has been confirmed by the previous CV and GCD results.

Normally, the total charge stored in the electrode is contributed by two different processes: the surface capacitive process and the diffusion-controlled faradaic effect. CV data could provide the insight into the charge storage mechanism. By using equation 2.6 and 2.7, the fraction of the charge stored from capacitive effect and diffusion-controlled faradaic process could be extracted quantitatively. In Fig. 7.8a, the current response of diffusion-controlled process (blue area) on the $NiMoS_4$-A electrode is compared with total current at a scan are of 5 mV s^{-1}. The diffusion-controlled process occupies around 61% of the total charge storage and

the remaining portion is originated from the surface capacitive effect. Based on the same approach, the contribution percentages of diffusion-controlled process on $NiMoS_4$ and $NiMoS_4$-A electrodes at various scan rates are compared in Fig. 7.8b. The two materials present quite similar tendency, namely, the diffusion-controlled process contribution gradually decreases with the increase in scan rate, reaching around 40% at a scan rate of 20 mV s^{-1}. In other words, the faradaic redox process dominates at lower scan rates while the capacitive effect matters at higher scan rates. However, at each specific scan rate, the percentage of diffusion-controlled process is slightly higher in sample $NiMoS_4$-A than that in sample $NiMoS_4$, suggesting easier redox reactions on the $NiMoS_4$-A electrode, which is well in accordance with the impedance results.

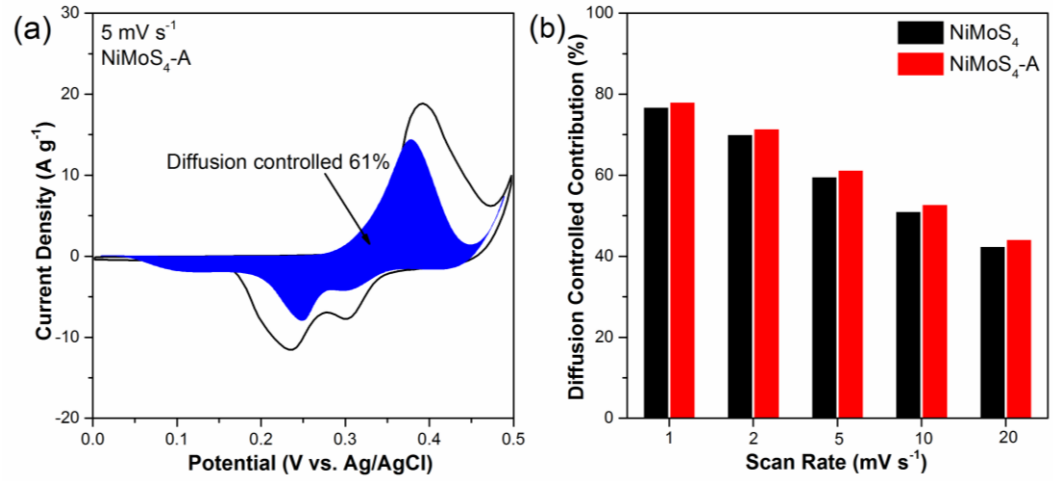

Fig. 7.8 (a) Typical separation of capacitive and diffusion-controlled charge storage process at scan rate of 5 mV s^{-1} of $NiMoS_4$-A. (b) Faradaic diffusion-controlled process contribution to the total charge stored at various scan rate in $NiMoS_4$ and $NiMoS_4$-A.

Clearly, as an energy storage material, the electrochemical performance of $NiMoS_4$-A is superior to that of $NiMoS_4$, which could be related to the heating process. XRD shows that weak peaks of NiS_2 and MoS_2 appear after heating in Ar. It is supposed that the interaction between the MoS_2 and NiS_2 components could promote the activity and improve its conductivity [304]. The lower resistance of sample $NiMoS_4$-A have been confirmed by our impedance results. Therefore, it can be concluded that the synergistic effect between the small amount of MoS_2

and NiS_2 in sample $NiMoS_4$-A improves the electrochemical performance of the electrode, resulting in a higher specific capacitance of the $NiMoS_4$-A electrode than that of the $NiMoS_4$ electrode.

7.3.3 Electrochemical performances of $NiMoS_4$-A//AC asymmetric supercapacitor

To further explore the electrochemical properties of the $NiMoS_4$-A electrode in a practical energy storage device, an ASC was fabricated using $NiMoS_4$-A as the positive electrode and AC as the negative electrode. The AC electrode performs a typical feature of EDLC (Fig. 7.9), details of its performances were discussed in chapter 4. In order to achieve high electrochemical performance of the ASC, the mass ratio between the $NiMoS_4$-A and AC electrodes was optimized by balancing the charge stored at the electrodes according to equation 5.3.

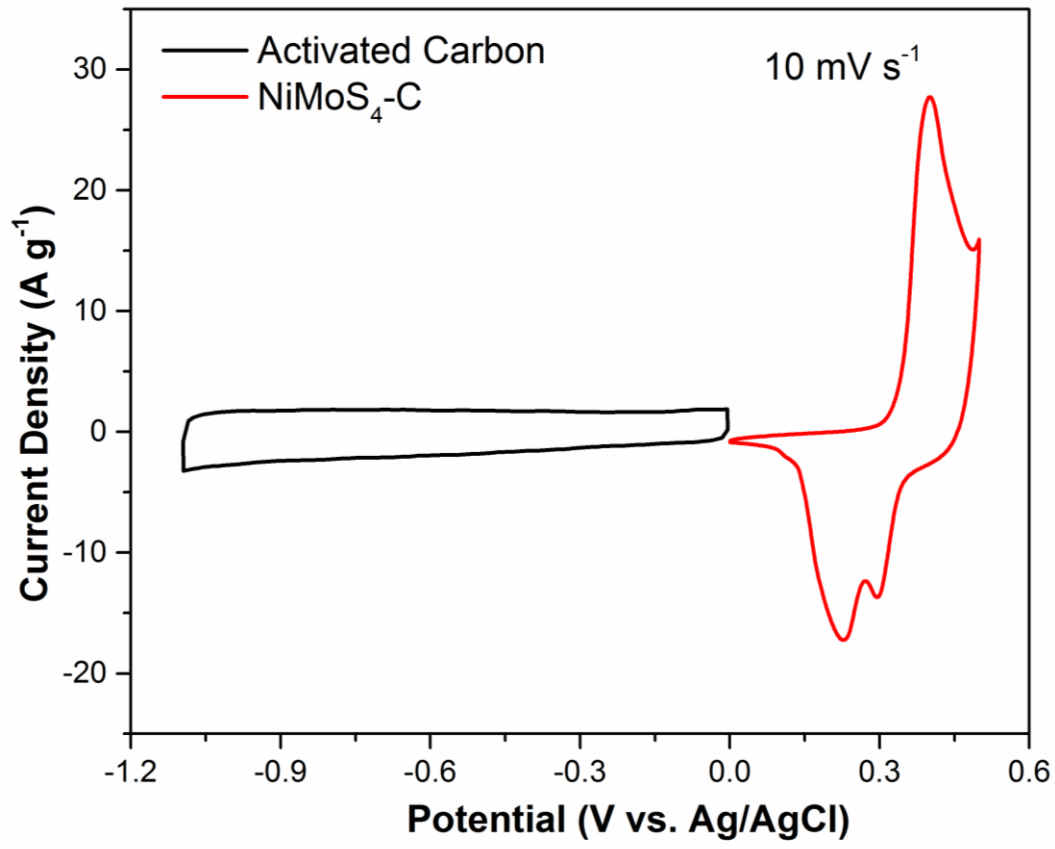

Fig. 7.9 Comparative CV curves of activated carbon and $NiMoS_4$-A electrodes performed in 2 M KOH at a scan rate of 10 mV s^{-1}.

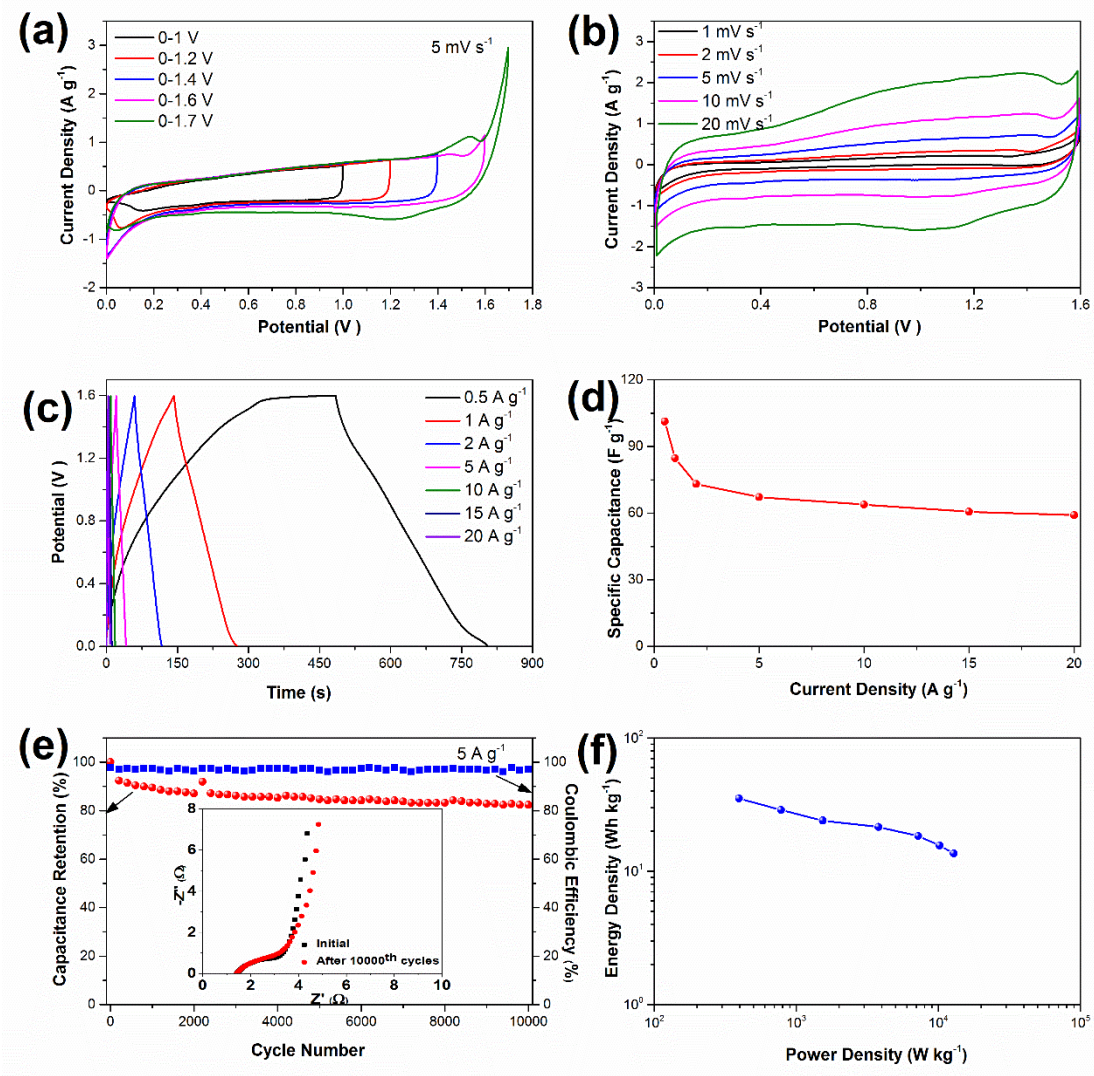

Fig. 7.10 Electrochemical properties of $NiMoS_4$-A//AC ASC. (a) CV curves at various voltage windows at 5mV s^{-1}; (b) CV curves with a voltage window of 0-1.6 V at various scan rate; (c) Galvanostatic charge–discharge curves at various current densities; (d) Specific capacitance at various current densities; (e) Cycling stability and coulombic efficiency of the ASC for 10000 cycles at 5 A g^{-1}; (f) Ragone plots of the supercapacitor.

Fig. 7.10a demonstrates CV curves of the $NiMoS_4$-A//AC ASC with different voltages ranging from 1.0 to 1.7 V at a scan rate of 5 mV s^{-1}. Obviously, the ASC has a stable performance with a voltage up to 1.6 V, however, when the voltage extends to 1.7 V, a polarization curve appears with a much higher current response, suggesting that a severe side reaction of water electrolysis is taking place. Consequently, the operating voltage window for the ASC is selected as 0 to 1.6 V.

The CV curves of the ASC at various scan rates are shown in Fig. 7.10b. The quasi-rectangular CV shape at all scans reveals that the energy stored in this ASC originates from hybrid effects of EDL and faradaic redox effects, this is further confirmed by the GCD curves (Fig. 7.10c). The lower the current densities, the more obviously non-linear the charge-discharge curves are. The specific capacitances of the ASC were calculated based on equation 3.10. The obtained specific capacitances at different current densities are plotted in Fig. 7.10d. There is a significant decrease from 0.5 to 2 A g^{-1}, but from 2 to 20 A g^{-1}, the values remain stable, indicating a good rate capability. Specifically, 101.3, 84.6, 73.1, 67.1, 63.8, 60.5, and 59.1 F g^{-1} are achieved at current density of 0.5, 1, 2, 5,10,15, and 20 A g^{-1} respectively, higher than those of other similar ASCs, such as $CoMoS_4$//rGO (77 F g^{-1} at 0.5 A g^{-1}) [136] and $NiMoO_4$-rGO//N-doped graphene (84 F g^{-1} at 0.5 A g^{-1}) [311]. The cycling durability and coulombic efficiency of the ASC were evaluated over 10000 cycles at a current density of 5 A g^{-1} (Fig. 7.10e). As seen from the graph, about 8% of the initial capacitance is lost during the first 200 cycles, after that, the value remains almost constant, showing an overall capacitance retention of 82% after 10000 cycles. The coulombic efficiency maintains around 97% during the 10000 cycles, indicating the high electrochemical reversibility of the ASC [247]. The impedance spectra before and after the cyclic test are shown in the inset of Fig. 7.10e. The R_s is nearly unchanged and the R_{ct} increases by about only 0.6 Ω after the 10000 cycle test, confirming the outstanding stability. The first and last ten cycles of the GCD curves are presented in Fig. 7.11. The excellent electrochemical stability could be attributed to the structural features of the materials. In particular, the effective interfacial area between the active materials and the electrolyte could facilitate the electrolyte accessing the active sites. Moreover, the porous structure could buffer the volume change during rapid charge-discharge process and prevent structural collapse.

Specific energy and power densities are two key parameters to investigate in an electrochemical energy storage device [119]. The energy densities and corresponding power densities of the ASC were calculated by equation 3.12 and 3.13. The Ragone plots of the ASC are displayed in Fig. 7.10f. The obtainable highest energy density is 35 Wh kg^{-1} at a power density of 400 W kg^{-1}, which is comparable to those of previously reported devices, such as Co_9S_8 nanoflakes//AC

(31.4 Wh kg^{-1} at 200 W kg^{-1}) [314], $CoMoS_4$//rGO (27.2 Wh kg^{-1} at 400 W kg^{-1}) [136] and $CoMoO_4$-graphene//AC (21.1 Wh kg^{-1} at 300 W kg^{-1}) [290]. The high energy density should benefit from the high capacitance of the $NiMoS_4$-A electrode. The ASC still delivers an energy density of 13.5 Wh kg^{-1} at a very high power density around 13000 W kg^{-1}.

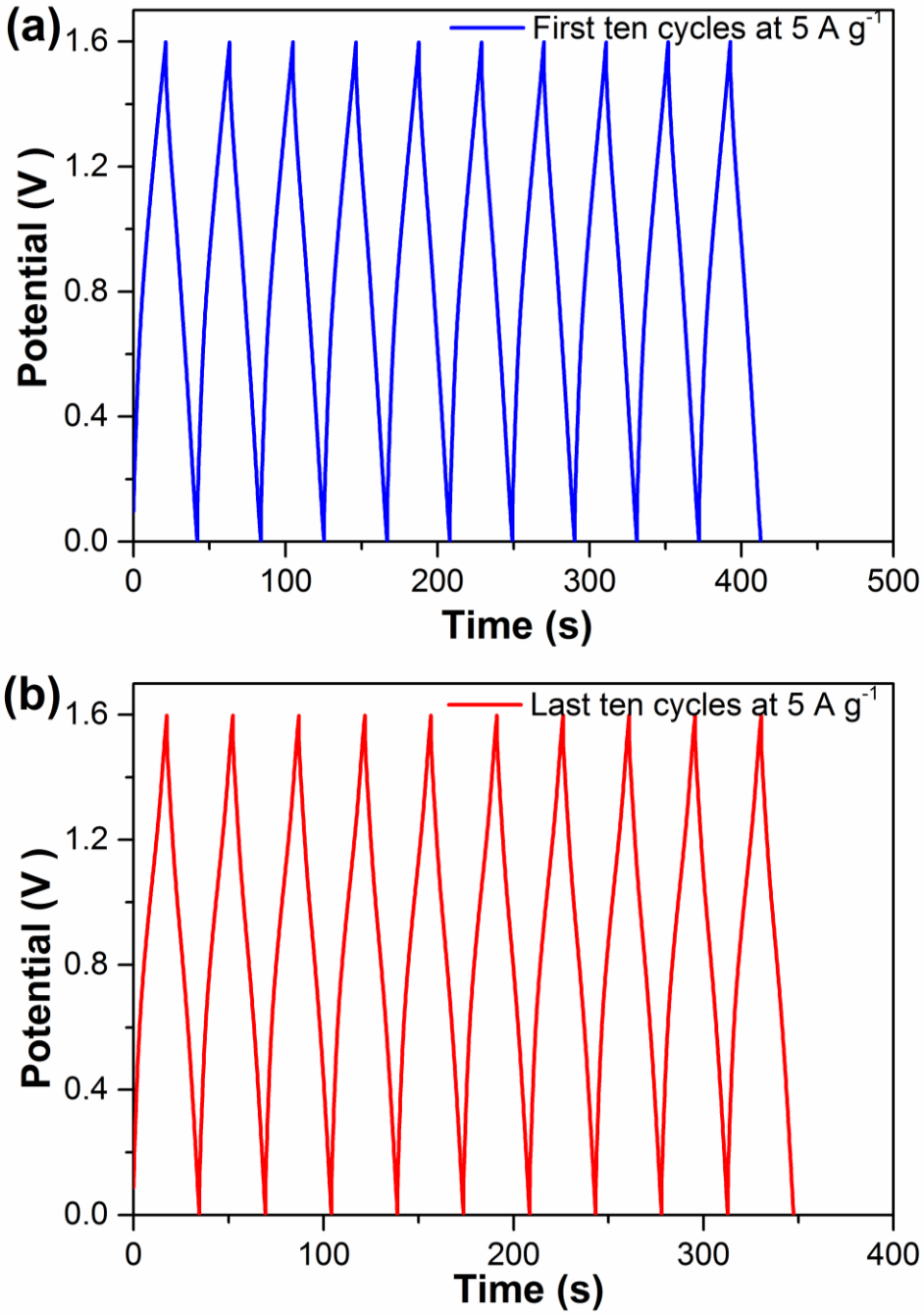

Fig. 7.11 (a) First and (b) last ten charge-discharge curves of the $NiMoS_4$-A//AC hybrid supercapacitor at a current density of 5 A g^{-1}.

7.4 Conclusions

In this chapter, we have synthesized sample $NiMoS_4$-A through a facile chemical co-precipitation process followed by calcining at 450 ^oC. XRD analysis indicates it is composed of NiS_2 and MoS_2. The $NiMoS_4$-A electrode performs a good specific capacitance of 706.5 F g^{-1} at 1 A g^{-1} while still maintains 83% of the capacitance at 10 A g^{-1} in an aqueous KOH electrolyte. The detailed charge storage mechanism analysis reveals that surface capacitive process and diffusion-controlled faradaic reaction contribute together to the energy storage, and that the faradaic redox process dominates at lower scan rates (78% at 1 mV s^{-1}) while the capacitive effect matters at higher scan rate (56% 20 mV s^{-1}). Furthermore, an ASC was fabricated using $NiMoS_4$-A as the positive electrode and AC as the negative electrode. The ASC delivers a cell voltage of 1.6 V and an energy density of 35 Wh kg^{-1} at a power density of 400 W kg^{-1}. Additionally, the ASC exhibits good cycle stability and electrochemical reversibility, retaining 82% of the initial capacitance with coulombic efficiency around 97% after 10000 charge-discharge cycles even at a high current density of 5 A g^{-1}. These good electrochemical performances indicate the great potential of $NiMoS_4$-A for ASC applications.

CHAPTER 8 Preparation of nanoporous nickel-copper sulfide on carbon cloth for high-performance asymmetric supercapacitors

8.1 Introduction

As we previously introduced, the performance of a supercapacitor is primarily determined by the electrode materials. The demand for electrode materials with high specific capacitance, good conductivity and outstanding cycling stability is increasing. Transition metal sulfides, such as nickel sulfides, cobalt sulfides and copper sulfides have been investigated as promising electrode materials due to their higher electrical conductivity and richer redox chemistry [117, 119, 121, 315]. Compared with their oxide or hydroxide counterparts, transition metal sulfides usually have better electrochemical performance. For instance, Yang *et. al* synthesized $Ni(OH)_2$ and NiS electrodes for supercapacitor application via a facile hydrothermal method, and the results demonstrate that NiS exhibited higher specific capacitance, lower resistance and better rate capability [118].

Moreover, it has been reported that binary metal compounds can exhibit better electrochemical performance than unitary metal compounds due to the synergistic effect and combined capacitive contribution of the individual components [100]. For example, Chen *et al.* observed that $NiCo_2S_4$ not only presented much higher conductivity than $NiCo_2O_4$, but also performed a higher capacitance than its corresponding single component sulfides (NiS_x and CoS_x) [316]. Many other binary metal compounds have also been explored for supercapacitor applications, such as $NiMoO_4$ [311], $NiMoS_4$ [317], $CoMoO_4$ [318], $CoMoS_4$ [306], $MnCo_2O_4$ [319], $MnCo_2S_4$ [133], $CuCo_2O_4$ [320], $CuCo_2S_4$ [321], etc.

In addition to the material type, the electrode structure is a key factor which determines the supercapacitor performance. Directly growing nanostructured materials on a conductive substrate is a highly preferred strategy for electrode preparation as the nanostructured morphology can increase the utilization efficiency of electroactive material. Simultaneously, the binder free electrode can

reduce the contact resistance, enhance the electron transport and electrolyte diffusion, leading to improved electrochemical performance [181, 322]. In addition, plenty of electrode materials developed by this method have been reported by other groups, such as nanoporous $Ni(OH)_2$ supported on graphite foam [31], $NiCo_2O_4$ nanowires supported on carbon fiber paper [323], Ni_3S_2 nanosheets supported on Ni foam [120], $MnCo_2S_4$ supported on carbon cloth [133], and so on.

It was found that that binary Ni-Cu possessed improved catalytic activity for methanol and ammonia electrooxidation [324-326], as well as water electrolysis [327]. However, to the best of our knowledge, reports on binary Ni-Cu sulfides in supercapacitor applications are scarce. Inspired by the above ideas, in this chapter we have successful prepared nanoporous Ni-Cu sulfides ($Ni_{0.8}Cu_{0.2}$−S) on carbon cloth via sulfurizing the Ni-Cu carbonate hydroxide precursor with an anion exchange reaction. The as-fabricated $Ni_{0.8}Cu_{0.2}$−S electrode exhibits a high specific capacitance of 938.6 F g^{-1} at a current density of 1 A g^{-1}, good rate capability of 76% at 10 A g^{-1}, as well as excellent flexibility with negligible capacitance loss at a bending angel up to 180^o. Charge storage analysis demonstrates that both the surface-controlled capacitive process and the diffusion-controlled faradaic process contribute to the capacitance. Furthermore, an ASC based on $Ni_{0.8}Cu_{0.2}$−S as the positive electrode and NG as the negative electrode delivers a high cell voltage up to 1.7 V with a maximum energy density of 35.3 Wh kg^{-1} and a maximum power density of 12700 W kg^{-1}. Additionally, the ASC displays good cycling stability and electrochemical reversibility, retaining 69% of the initial capacitance with about 92% coulombic efficiency after 10000 charge-discharge cycles at 2 A g^{-1}. These results suggest that the Ni-Cu sulfides are promising candidates for high-performance supercapacitor applications.

8.2 Experimental

8.2.1 Synthesis of Ni-Cu carbonate hydroxide nanowires on carbon cloth

All the chemicals were supplied by Alfa Aesar in analytical grade and used without further purification. The Ni-Cu carbonate hydroxide was directly grown on carbon cloth substrate via a simple one-step hydrothermal method. Prior to the synthesis, commercial carbon cloth (1071 HCB) was carefully cleaned with acetone, deionized water, and ethanol for several minutes, respectively. In a typical process, 1.2 mmol nickel(II) nitrate hexahydrate and 0.3 mmol copper(II) nitrate hemi(pentahydrate) were dissolved in 15 mL de-ionized water. Subsequently, 0.225 g urea and 0.375 g cetyltrimethylammonium bromide (CTAB) were added and the mixer was kept stirring until a transparent solution was obtained. The solution was then transferred into a 30 mL Teflon-lined stainless-steel autoclave. A piece of carbon cloth with a size of 1 × 1 cm^2 was immersed in the solution and the autoclave was maintained at 120 ^oC for 12 h. After cooling down to room temperature naturally, the carbon cloth was taken out and washed with water and ethanol several times. Finally, the carbon cloth was dried at 60 ^oC under vacuum overnight. To optimize the Ni-Cu ratio, different precursor solutions with Ni^{2+}/Cu^{2+} in the mole ratio of 10:0, 9:1, 8:2, 7:3, 6:4, 5:5 (the total Ni^{2+} and Cu^{2+} ions were kept at 1.5 mmol) were used. The corresponding samples are denoted as $Ni_{1.0}Cu_0$−CH, $Ni_{0.9}Cu_{0.1}$−CH, $Ni_{0.8}Cu_{0.2}$−CH, $Ni_{0.7}Cu_{0.3}$−CH, $Ni_{0.6}Cu_{0.4}$−CH and $Ni_{0.5}Cu_{0.5}$−CH, respectively.

8.2.2 Synthesis of nanoporous Ni-Cu sulfides on carbon cloth

The nanoporous Ni-Cu sulfides were prepared by applying a further hydrothermal process on the as-obtained $Ni_{0.8}Cu_{0.2}$−CH sample. Specifically, 0.25 g Na_2S was dissolved in 15 mL de-ionized water. The solution was then transferred into a 30 mL Teflon-lined stainless-steel autoclave followed by placing the $Ni_{0.8}Cu_{0.2}$−CH sample inside. The autoclave was heated at 160 ^oC for 12 h. The obtained sample was washed with water and ethanol several times to remove the surface ions and molecules, and dried at 60 ^oC in a vacuum oven. The Ni-Cu sulfides are denoted as $Ni_{0.8}Cu_{0.2}$−S.

The mass loading of the active materials grown on the carbon cloth was obtained by comparing the weight of the carbon cloth before and after the hydrothermal process. The mass loading for all the Ni-Cu working electrodes was 1-2 mg cm^{-2}.

8.2.3 Assemble of $Ni_{0.8}Cu_{0.2}$−S//NG asymmetric supercapacitor

To fabricate the $Ni_{0.8}Cu_{0.2}$−S//NG ASC, the as-prepared $Ni_{0.8}Cu_{0.2}$−S electrode and a NG electrode were used as positive electrode and negative electrode, respectively. NG was prepared via the method described in chapter 4. The synthesized NG was mixed with carbon black (Super P) and PTFE at a weight ratio of 90 : 5 : 5. The formed slurry was then coated on Ni foam (1 × 1 cm^2), pressed at 10 MPa, and finally dried at 60 ^oC under vacuum. To assemble the full cell, the positive and negative electrodes were face to face placed into a container in which 2 M KOH aqueous solution was added.

8.2.4 Physical characterization

The crystal structures of the products were characterized by XRD spectra (Panalytical X'Pert Pro Multi-Purpose Diffractometer (MPD), Cu Kalpha1 radiation, λ = 1.5406 Å). UV–visible spectra of the solid samples were obtained using a spectrophotometer (Shimadzu UV-2600) with an integrating sphere. The morphologies and microstructures of the samples were investigated with SEM (ZEISS SUPRA 55-VP) and TEM (JEOL 2100). EDX attached to the SEM were recorded to analyze the elemental compositions.

8.2.5 Electrochemical measurements

The electrochemical performance of synthesized electrodes was examined in both three-electrode and two-electrode modes. In a three-electrode system, the carbon cloth supported Ni-Cu samples were directly used as the working electrodes. A platinum mesh and a standard Ag/AgCl electrode (sat. KCl) were used as the counter electrode and reference electrode respectively. In the two-electrode mode, the $Ni_{0.8}Cu_{0.2}$−S//NG ASC device was fabricated. CV, GCD and EIS measurements were conducted with a Solartron 1470E/1455 multichannel cell test system. Impedance spectroscopy was performed in the frequency range from 100 kHz to 0.01 Hz with a potential amplitude of 5 mV at open circuit potential. All

the electrochemical measurements were carried out at room temperature in 2 M KOH aqueous solution electrolyte.

8.3 Results and discussion

8.3.1 Physical characterization of $Ni_{1-x}Cu_x$–CH

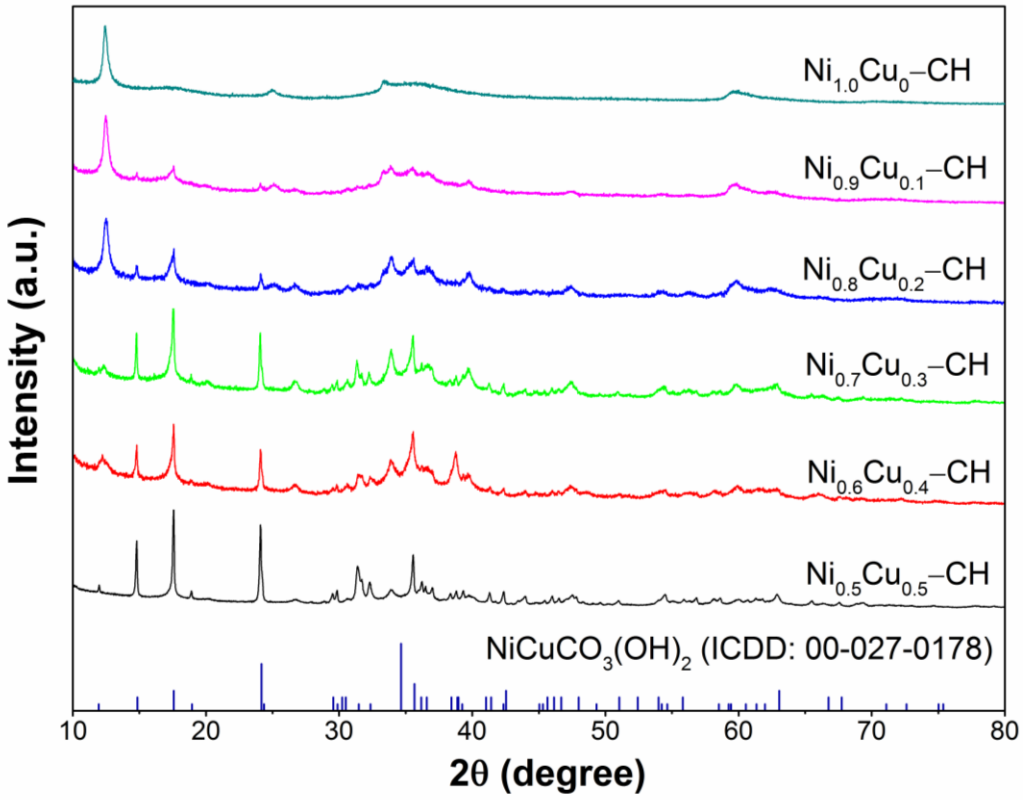

Fig. 8.1 XRD patterns of $Ni_{1-x}Cu_x$–CH (x = 0, 0.1, 0.2, 0.3, 0.4, and 0.5).

With the starting chemical precursors, the formation of Ni-Cu carbonate hydroxides can be described by the following reactions [328]:

$$CO(NH_2)_2 + 3H_2O \rightarrow 2NH_4^+ + CO_2 + 2OH^- \quad (8.1)$$

$$CO_2 + 2OH^- \rightarrow CO_3^{2-} + H_2O \quad (8.2)$$

$$2Ni^{2+} + CO_3^{2-} + 2OH^- \rightarrow Ni_2CO_3(OH)_2 \quad (8.3)$$

$$2Cu^{2+} + CO_3^{2-} + 2OH^- \rightarrow Cu_2CO_3(OH)_2 \quad (8.4)$$

The urea in this synthesis was used as a source for the generation of carbonate and hydroxyl anions [316, 329]. After the first hydrothermal step, the obtained $Ni_{1-x}Cu_x$–CH (x = 0, 0.1, 0.2, 0.3, 0.4, and 0.5) samples were examined by XRD

measurement, as shown in Fig. 8.1. All the samples exhibit very similar patterns, except that the peak intensities vary with different ratios of nickel and copper. For instance, when the Cu content increases from 0 to 0.5, the peak at 12.0° gets weaker while the peaks at 14.9°, 17.6° and 24.2° get stronger. Nevertheless, all the diffraction peaks can be well indexed to the nickel-copper carbonate hydroxide (ICDD 00-027-0178), which indicates that the substitution between Ni and Cu only slightly changes the lattice parameters while maintaining the crystal structure [316]. Meanwhile, UV-vis absorption spectra of the $Ni_{1-x}Cu_x$−CH samples are shown in Fig. 8.2. The samples present similar absorption curves while the differences are caused by the different Cu content. The absorption peak at 389 nm gradually disappears with the increase of Cu content, confirming the successful formation of the Ni-Cu compounds.

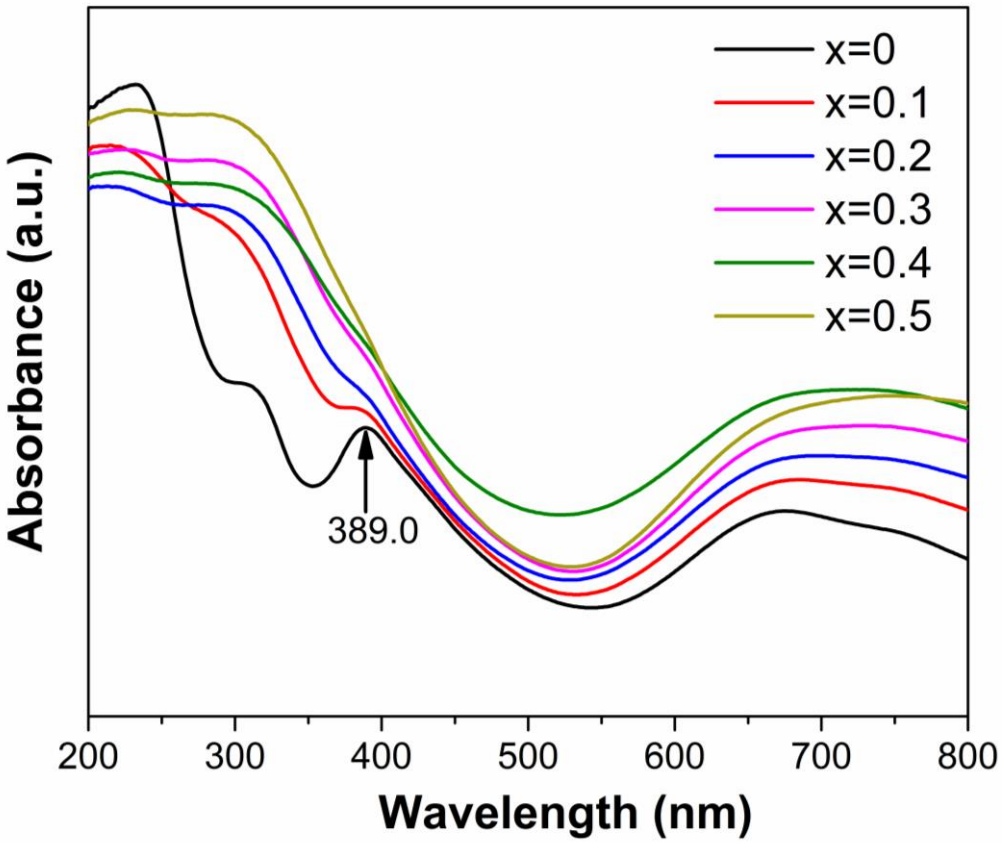

Fig. 8.2 UV-vis absorption spectra of $Ni_{1-x}Cu_x$−CH (x = 0, 0.1, 0.2, 0.3, 0.4, and 0.5).

The morphology and microstructure of the $Ni_{1-x}Cu_x$−CH (x = 0, 0.1, 0.2, 0.3, 0.4, and 0.5) were investigated by SEM and the images are shown in Fig. 8.3. Obviously, the surface of carbon cloth fiber is covered by the active materials, indicating the successfully preparation of the $Ni_{1-x}Cu_x$−CH/carbon cloth electrodes. The microstructures are influenced by the Ni-Cu ratio. At low Cu content (x = 0 and 0.1), the sample surfaces are uneven, while when x = 0.2, 0.3, 0.4 and 0.5, the active materials are uniformly distributed on the substrate. All the Ni-Cu materials exhibit a nanowire structure, which could benefit the access of electrolyte ions during charge-discharge.

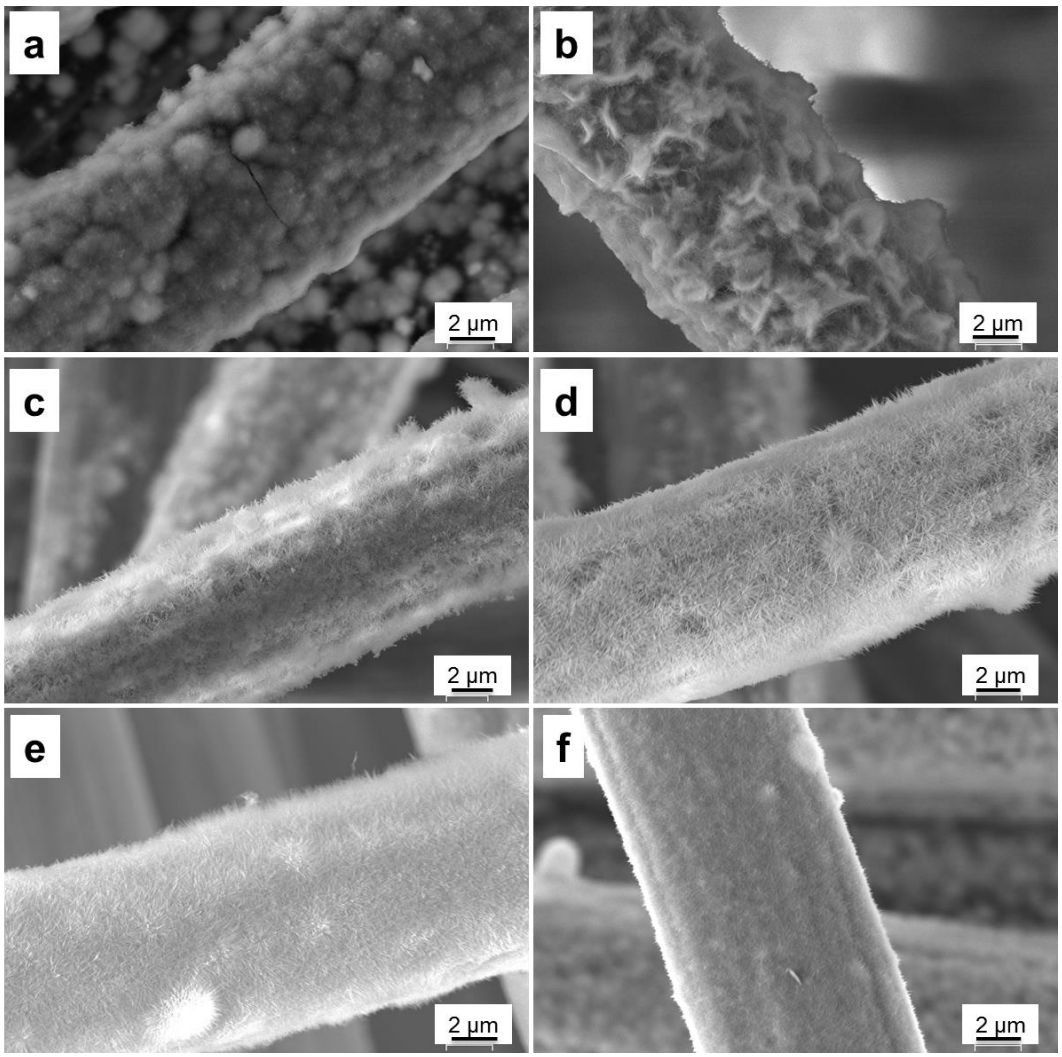

Fig. 8.3 SEM images of $Ni_{1-x}Cu_x$−CH with x value at: (a) 0, (b) 0.1, (c) 0.2, (d) 0.3, (e) 0.4 and (f) 0.5.

8.3.2 Electrochemical performances of $Ni_{1-x}Cu_x$–CH

To find the optimal composition of the $Ni_{1-x}Cu_x$–CH for charge storage, the electrochemical properties of the electrodes based on different ratio of Ni and Cu (x = 0, 0.1, 0.2, 0.3, 0.4, and 0.5) were measured in 2 M KOH aqueous solution with a three-electrode cell configuration. Fig. 8.4a demonstrates the CV curves of $Ni_{1-x}Cu_x$–CH in the potential range of 0 to 0.5 V vs. Ag/AgCl at a scan rate of 10 mV s^{-1}. The redox peaks are explicitly defined in each curve, which can be attributed to the combined contribution of Ni and Cu based redox reactions, namely [330-332]:

$$Ni_2CO_3(OH)_2 + 4OH^- \leftrightarrow 2NiOOH + CO_3^{2-} + 2H_2O + 2e^- \quad (8.5)$$

$$Cu_2CO_3(OH)_2 + 4OH^- \leftrightarrow 2CuOOH + CO_3^{2-} + 2H_2O + 2e^- \quad (8.6)$$

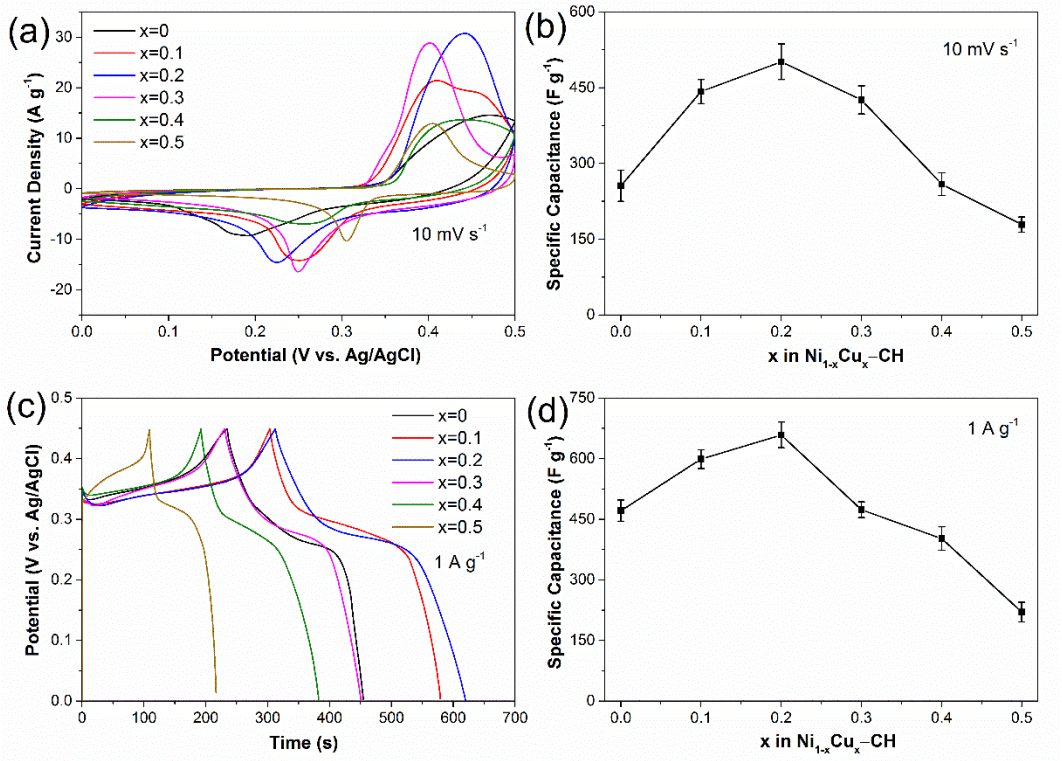

Fig. 8.4 (a) CV curves and (b) corresponding specific capacitances of $Ni_{1-x}Cu_x$–CH (x = 0, 0.1, 0.2, 0.3, 0.4, and 0.5) at a scan rate of 10 mV s^{-1}. (c) Galvanostatic charge–discharge curves and (d) corresponding specific capacitances of $Ni_{1-x}Cu_x$–CH (x = 0, 0.1, 0.2, 0.3, 0.4, and 0.5) at a current density of 1 A g^{-1}.

Although two different reactions are involved at the electrodes during charge-discharge, only one pair of redox peaks are observed, which is due to the well

mixing of Ni-Cu composites. The redox peak positions and intensities vary with different Ni-Cu ratios, revealing that the electrochemical behavior of the composites can be controlled by changing their compositions. As is known, the charge stored in an electrode is proportional to its enclosed area by CV. Obviously, when x = 0.2, the composite of $Ni_{0.8}Cu_{0.2}$−CH exhibits the largest integrated area by CV, suggesting that more charges can be stored in the $Ni_{0.8}Cu_{0.2}$−CH electrode. The specific capacitance of the electrode can be determined by CV curves according to equation 3.9. The corresponding specific capacitances of $Ni_{1-x}Cu_x$−CH (x = 0, 0.1, 0.2, 0.3, 0.4, and 0.5) are shown in Fig. 8.4b. When x increases from 0 to 0.5, the specific capacitance experiences an increase at first then followed by a decline, reaching the highest value of 501.5 F g^{-1} at x = 0.2. The superior performance of $Ni_{0.8}Cu_{0.2}$−CH is further confirmed by the GCD results as presented in Fig. 8.4c. At a current density of 1 A g^{-1}, sample $Ni_{0.8}Cu_{0.2}$−CH exbibits the longest discharge time, suggesting the highest charge storage ability. The specific capacitance could also be calculated from the GCD curves by equation 3.10. It is found that the specific capacitance of sample $Ni_{0.8}Cu_{0.2}$−CH achieves 658.8 F g^{-1}, higher than the values of 471.4, 598.9, 473.7, 402.4, 220.2 F g^{-1} for samples $Ni_{1.0}Cu_0$−CH, $Ni_{0.9}Cu_{0.1}$−CH, $Ni_{0.7}Cu_{0.3}$−CH, $Ni_{0.6}Cu_{0.4}$−CH, and $Ni_{0.5}Cu_{0.5}$−CH, respectively (Fig. 8.4d). The CV and GCD results demonstrate that sample $Ni_{0.8}Cu_{0.2}$−CH presents the highest capacitance, which is in good agreement with our previous study of Ni-Cu hydroxides toward electrochemical oxidation of ammonia [324, 326]. It was found that sample $Ni_{0.8}Cu_{0.2}$ exhibited higher electrochemical surface area thus performing higher catalytic activity, which could also be the reason for its high capacitance here.

8.3.3 Physical characterization of $Ni_{0.8}Cu_{0.2}$−CH and $Ni_{0.8}Cu_{0.2}$−S

The nanopourous $Ni_{0.8}Cu_{0.2}$−S was synthesized by sulfurizing the $Ni_{0.8}Cu_{0.2}$−CH nanowires with Na_2S via a further hydrothermal process. XRD measurements were conducted to determine the phase property (Fig. 8.5). As can be seen, the diffraction peaks at 16.2°, 26.6°, 31.2°, 37.9°, 46.9°, 49.9°, 54.7°, 64.3°, 68.5° and 77.2° can be assigned to the respective (111), (220), (311), (400), (422), (511), (440), (533), (444) and (553) planes of the cubic Ni_3S_4 (ICDD 04-004-5623). The remaining peaks at 27.1°, 27.7°, 29.2°, 31.7°, 32.8°, 47.9°, 52.6° and 59.2° are in

good agreement with the standard hexagonal CuS phase (ICDD 04-008-8149), corresponding to the (100), (101), (102), (103), (006), (110), (108) and (116) planes. Notably, no other impurities have been detected, indicating that sample $Ni_{0.8}Cu_{0.2}$−S is a mixture of Ni_3S_4 and CuS.

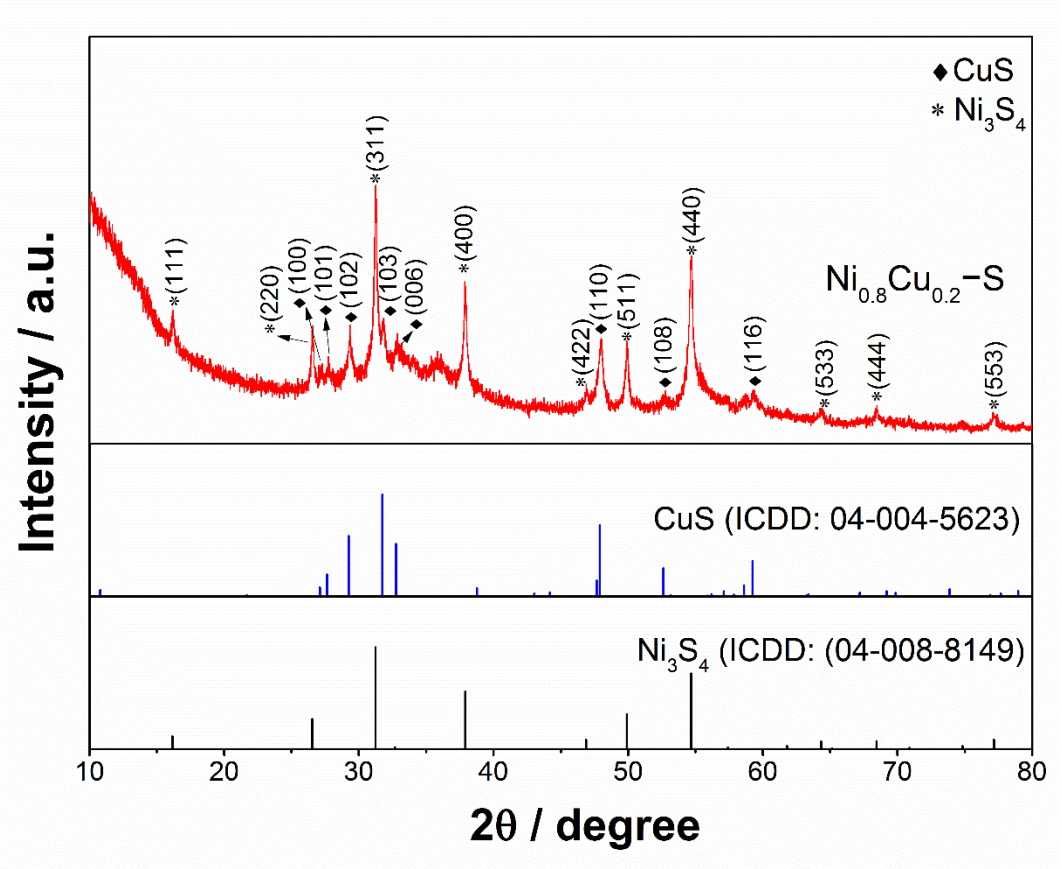

Fig. 8.5 XRD patterns of $Ni_{0.8}Cu_{0.2}$−S.

SEM and TEM were employed to compare the morphology and microstructure of the $Ni_{0.8}Cu_{0.2}$−CH and $Ni_{0.8}Cu_{0.2}$−S. Fig. 8.6a shows the typical SEM image of $Ni_{0.8}Cu_{0.2}$−CH grown on carbon cloth. Obviously, the $Ni_{0.8}Cu_{0.2}$−CH are in nanowire clusters and uniformly distributed on the carbon cloth surface forming grass-like morphology. TEM indicates that each cluster is composed of numerous nanowires grown from the substrate center (Fig. 8.6b). The nanowires are about 100-200 nm in length and 5-10 nm in width (Fig. 8.6c). Unlike $Ni_{0.8}Cu_{0.2}$−CH nanowires, SEM image demonstrates that the $Ni_{0.8}Cu_{0.2}$−S presents a porous structure (Fig. 8.6d). The particles are firmly connected to the carbon cloth substrate, which could result in high conductivity. Interestingly, TEM investigation indicates that the particles are composed of nanoparticles with numerous pores among them, forming a nanoporous structure (Fig. 8.6e). The

nanoporous structure could be favorable for the diffusion of electrolyte throughout the whole electrode, leading to extensive contact of electrolyte with active materials, which will improve the utilization efficiency of active materials. HRTEM image show that the primary particles are well distributed with a size range of 10-20 nm (Fig. 8.6f). The interplanar distances between the lattice fringes are measured to be 0.286 nm and 0.548 nm, which can be ascribed to the (311) and (111) planes of Ni_3S_4, respectively. Simultaneously, the corresponding Fourier Transform patterns of the selected area gives an interplanar distance of 0.282 nm (inset of Fig. 8.6f), which can be assigned to the (103) plane of CuS. These observations are consistent with the XRD results.

Energy-dispersive X-ray spectroscopy (EDX) mapping was applied to determine the element distribution in the samples. Elements Ni, Cu, and O are evenly distributed in sample $Ni_{0.8}Cu_{0.2}$−CH (Fig. 8.7). Similarly, uniform distribution of elements Ni, Cu and S is observed in sample $Ni_{0.8}Cu_{0.2}$−S (Fig. 8.8), confirming the successful conversion of sulfides from carbonate hydroxide precursors.

According to the above results, the conversion of $Ni_{0.8}Cu_{0.2}$−CH nanowires into nanoporous $Ni_{0.8}Cu_{0.2}$−S can be explained by the anion-exchange reaction mechanism [164]. The S^{2-} anions in the solution exchange with CO_3^{2-} and OH^- to form $Ni_{0.8}Cu_{0.2}$−S at the surface, and then the produced CO_3^{2-} and OH^- react with hydrogen cations to form CO_2 and H_2O. In addition to supplying the sulfur source, the S^{2-} anions here can also act as an etching agent during the reaction [333]. The growth of $Ni_{0.8}Cu_{0.2}$−S at the outer region and the etching effect of S^{2-} anions break the nanowire structure and generate void space inside. With the further diffusion of S^{2-}, the $Ni_{0.8}Cu_{0.2}$−CH has been completely converted into $Ni_{0.8}Cu_{0.2}$−S, simultaneously, the nanowire clusters have become nanoparticles in a porous structure.

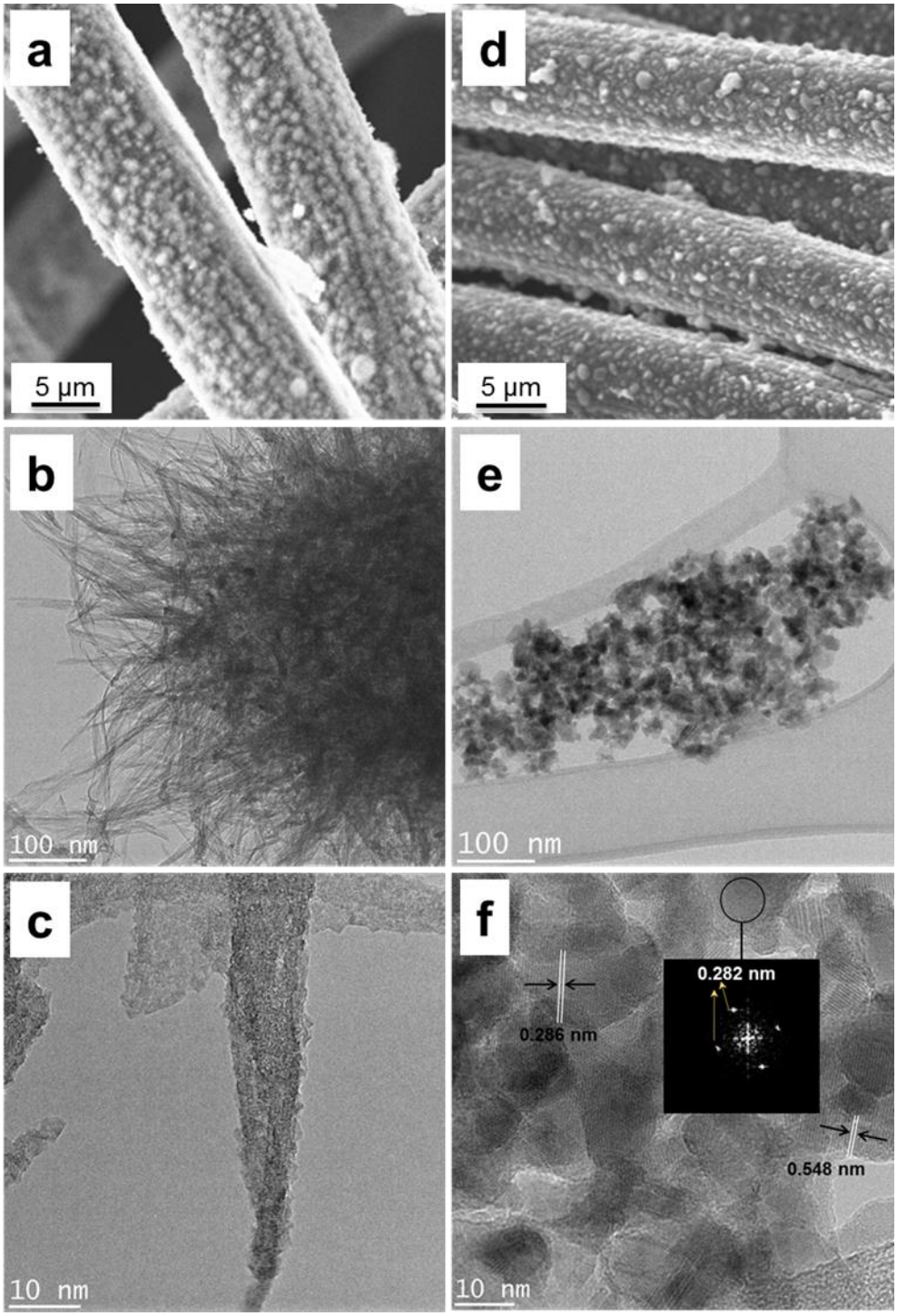

Fig. 8.6 (a) SEM and (b and c) TEM images of $Ni_{0.8}Cu_{0.2}$−CH nanowires. (d) SEM and (e and f) TEM images of nanoporous $Ni_{0.8}Cu_{0.2}$−S grown on carbon cloth. The inset of (f) is the corresponding Fourier Transform patterns.

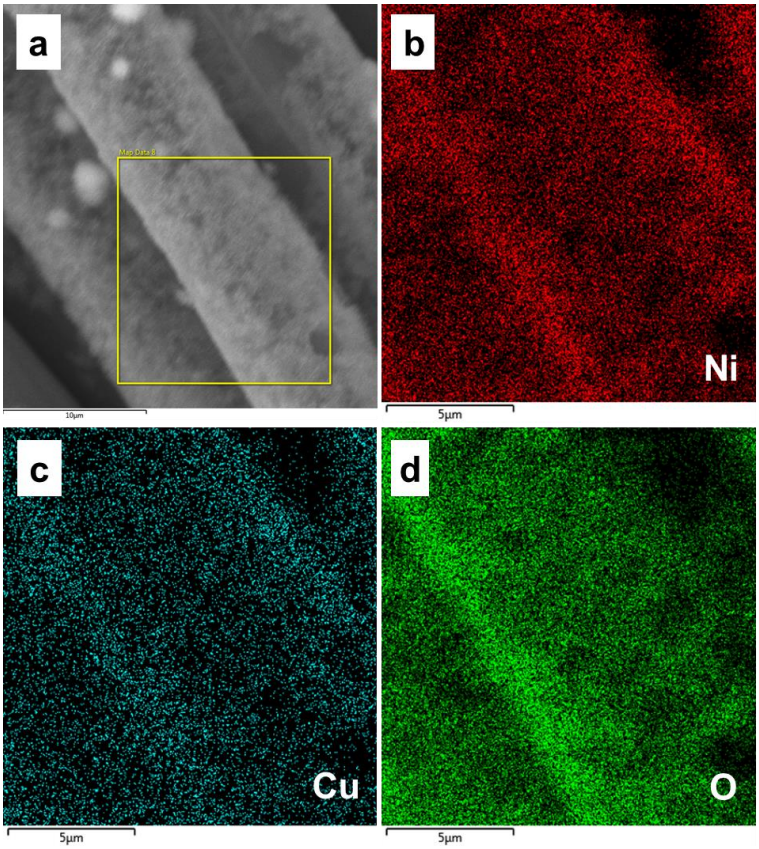

Fig. 8.7 EDX mappings Ni, Cu and O elements of $Ni_{0.8}Cu_{0.2}$−CH.

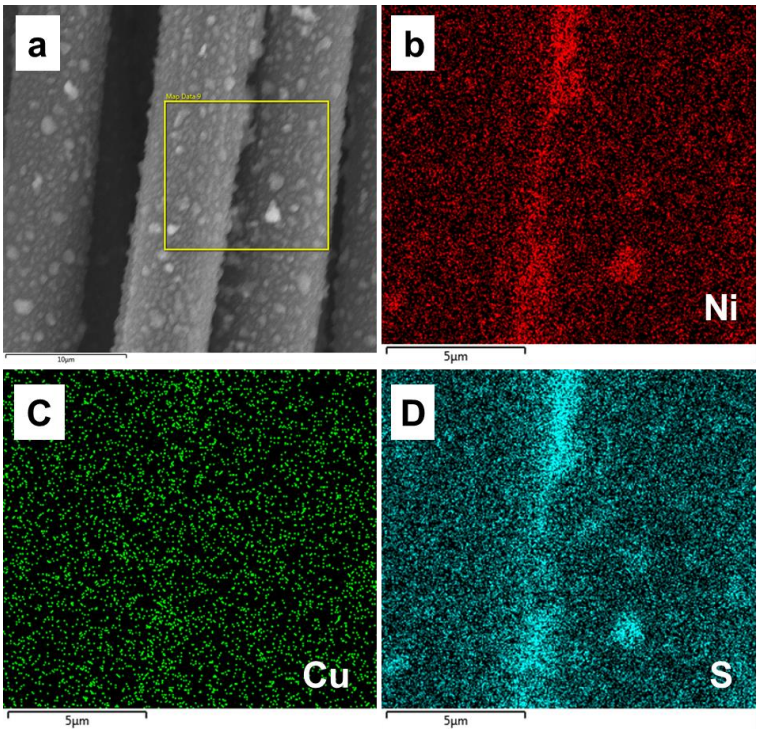

Fig. 8.8 EDX mappings Ni, Cu and O elements of $Ni_{0.8}Cu_{0.2}$−S.

8.3.4 Electrochemical performances of $Ni_{0.8}Cu_{0.2}$−CH and $Ni_{0.8}Cu_{0.2}$−S

The electrochemical performances of samples $Ni_{0.8}Cu_{0.2}$−CH and $Ni_{0.8}Cu_{0.2}$−S were evaluated by CV and GCD measurements. Typical CV curves of $Ni_{0.8}Cu_{0.2}$−CH and $Ni_{0.8}Cu_{0.2}$−S measured at scan rates of 1, 2 5, 10, and 20 mV s^{-1} are shown in Fig. 8.9a and b, respectively. The distinct redox peaks can be observed in all CVs, indicating that the energy storage ability of the active materials mainly originates from faradaic processes [323]. The redox reactions for the peaks in CVs of sample $Ni_{0.8}Cu_{0.2}$−CH are described as equation 8.5 and 8.6, while the peaks observed in CVs of sample $Ni_{0.8}Cu_{0.2}$−S can be ascribed to the reversible reactions between the sulfides and the KOH electrolyte [120, 334]:

$$Ni_3S_4 + 3OH^- \leftrightarrow Ni_3S_4(OH)_3 + 3e^- \quad (8.7)$$

$$CuS + OH^- \leftrightarrow CuSOH + e^- \quad (8.8)$$

There are two different reactions involved during the charge-discharge, only one pair of redox peaks are observed, indicating the well mixing of the Ni-Cu composites, which can be supported by the above EDS mappings. Apparently, the current response increases and maintains a similar curve shape with increasing scan rates, implying good electrochemical reversibility [317]. At high scan rates, the anodic and cathodic peaks slightly shift towards more positive and negative potentials respectively, which is due to the low polarization effect of the electrodes [266].

A comparison of CV plots of $Ni_{0.8}Cu_{0.2}$−CH and $Ni_{0.8}Cu_{0.2}$−S at 10 mV s^{-1} is demonstrated in Fig. 8.9c. Both of the two electrodes demonstrate one pair of redox peaks, but their peak positions are different. Compared with $Ni_{0.8}Cu_{0.2}$−CH, the anodic and cathodic peaks in $Ni_{0.8}Cu_{0.2}$−S slightly shit to more negative potential, which can be attributed to the difference of the redox potentials of Ni and Cu in carbonate hydroxides and sulfides. In addition, sample $Ni_{0.8}Cu_{0.2}$−S enclose a larger area than sample $Ni_{0.8}Cu_{0.2}$−CH, showing a better charge storage capability.

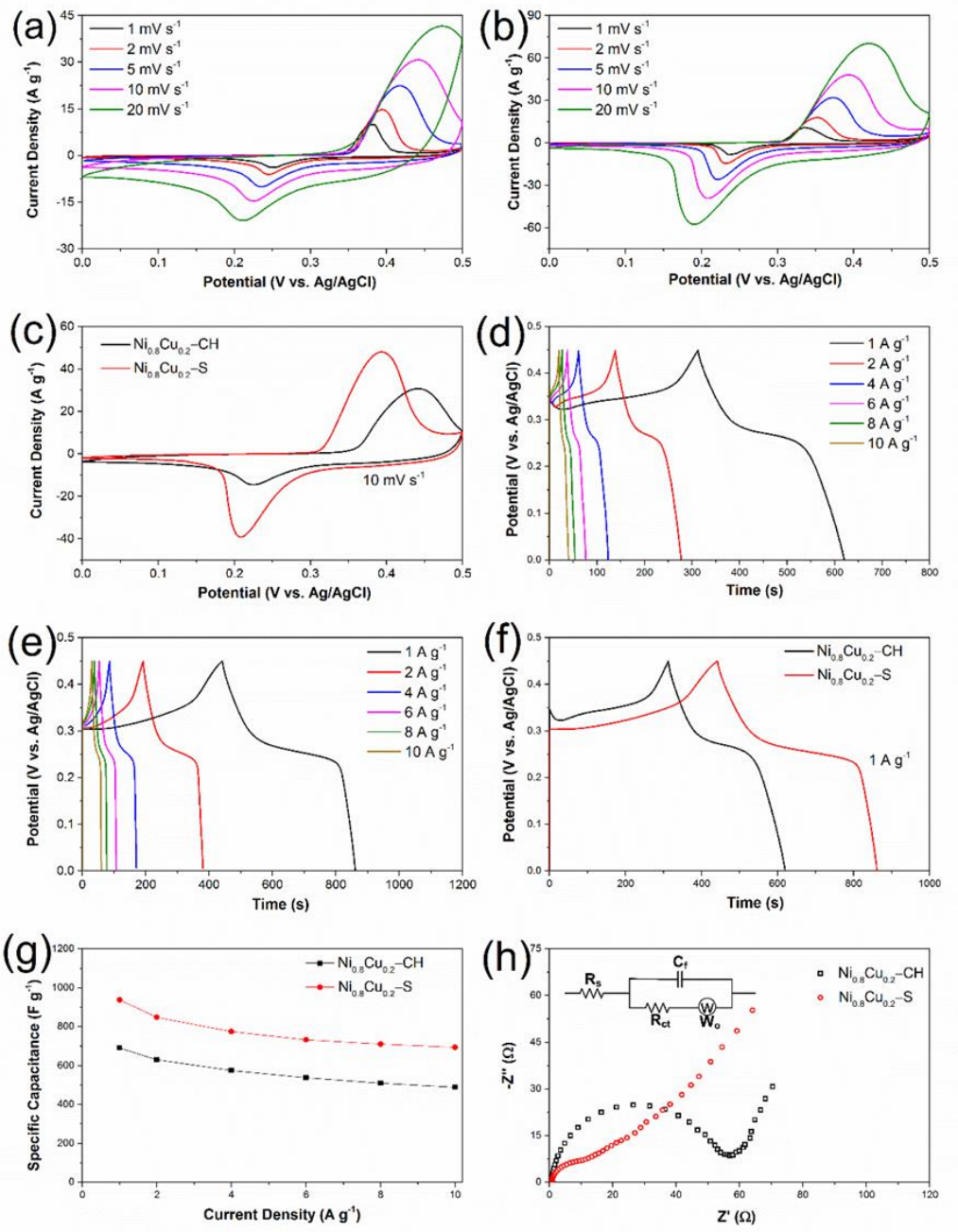

Fig. 8.9 CV curves at different scan rates of (a) $Ni_{0.8}Cu_{0.2}$−CH and (b) $Ni_{0.8}Cu_{0.2}$−S. (c) Comparison of CV curves of $Ni_{0.8}Cu_{0.2}$−CH and $Ni_{0.8}Cu_{0.2}$−S at a scan rate of 10 mV s^{-1}. GCD curves at different current density of (d) $Ni_{0.8}Cu_{0.2}$−CH and (e) $Ni_{0.8}Cu_{0.2}$−S. (f) Comparison of GCD curves of $Ni_{0.8}Cu_{0.2}$−CH and $Ni_{0.8}Cu_{0.2}$−S at a current density of 1 A g^{-1}. (g) Specific capacitances of $Ni_{0.8}Cu_{0.2}$−CH and $Ni_{0.8}Cu_{0.2}$−S at various current densities. (h) Nyquist plots of $Ni_{0.8}Cu_{0.2}$−CH and $Ni_{0.8}Cu_{0.2}$−S at open circuit potential (inset is the equivalent circuit).

Fig. 8.9d and e display the GCD curves of samples $Ni_{0.8}Cu_{0.2}$−CH and $Ni_{0.8}Cu_{0.2}$−S

at various current densities from 1 to 10 A g^{-1}. Consistent with the CV results, the voltage plateaus in charge-discharge curves further verify the existence of faradaic behaviours [335]. Fig. 8.9f compares the GCD curves of $Ni_{0.8}Cu_{0.2}$−CH and $Ni_{0.8}Cu_{0.2}$−S at a current density of 1 A g^{-1}. Clearly, sample $Ni_{0.8}Cu_{0.2}$−S possesses higher capacitance due to its longer discharge time, which is in good agreement with the above CV results. Based on the GCD curves and equation 3.10, the specific capacitances of $Ni_{0.8}Cu_{0.2}$−S can be calculated to 938.6, 848.8, 775.1, 732.4, 710.9, and 694.6 F g^{-1} at current densities of 1, 2, 4, 6, 8, and 10 A^{-1}, respectively, as plotted in Fig. 8.9g. It can be seen that around 76% of the capacitance is maintained for a 10-fold increase in the charge-discharge rate, implying good rate capability of the $Ni_{0.8}Cu_{0.2}$−S electrode. In terms of sample $Ni_{0.8}Cu_{0.2}$−CH, its specific capacitance achieves 690.7 F g^{-1} at 1 A g^{-1} with 70% retention at 10 A g^{-1}. Basically, the degradation of specific capacitance at high rates can be attributed to the low diffusion of electrolyte ions [316]. There is insufficient access of electrolyte ions to the active materials due to the limited diffusion time at high charge-discharge rates, therefore only the outer active surface is utilized for charge storage, resulting in a reduced specific capacitance. Here, the high capacitance and good rate capability of the $Ni_{0.8}Cu_{0.2}$−S electrode can be attributed to its specific features. The conversion of carbonate hydroxides to sulfides could improve the materials' conductivity. Additionally, the nanoporous structure could short the electrolyte diffusion paths, provide more active sites for rapid redox reactions and offer high electroactive materials utilization efficiency. Moreover, the nanoporous $Ni_{0.8}Cu_{0.2}$−S was directly grown on the carbon cloth substrate without any binder, which can reduce the contact resistance. Depending on the combined contribution of these factors, a $Ni_{0.8}Cu_{0.2}$−S electrode with high conductivity and large amounts of active sites is obtained. Such an electrode could effectively enhance the charge storage performance, especially at high charge-discharge rates.

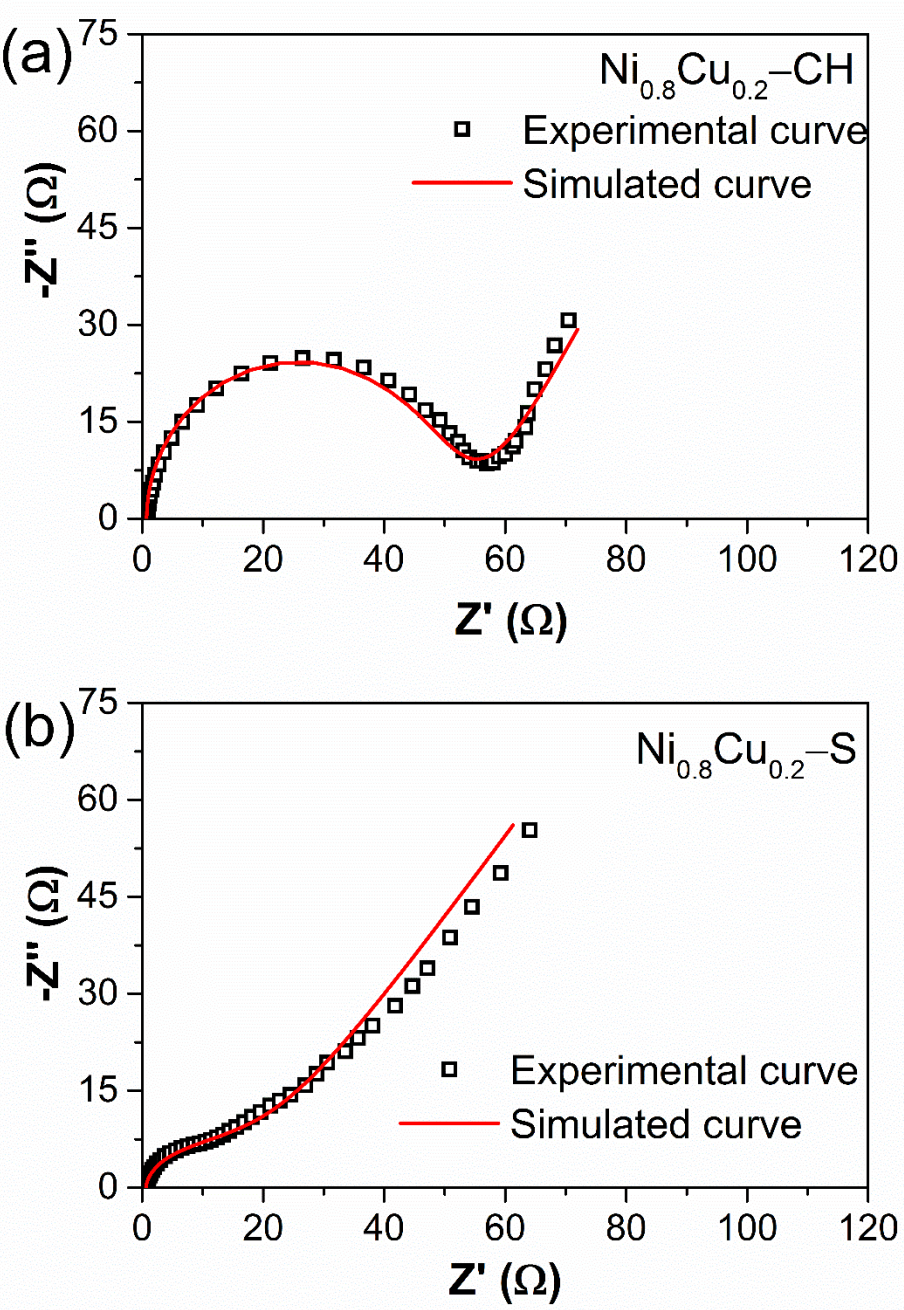

Fig. 8.10 Experimental and simulated Nyquist plots of (a) $Ni_{0.8}Cu_{0.2}$–CH and (b) $Ni_{0.8}Cu_{0.2}$–S.

To further understand the electrochemical properties of the electrodes, EIS was carried out at open circuit potential. Fig. 8.9h displays the Nyquist plots of $Ni_{0.8}Cu_{0.2}$–CH and $Ni_{0.8}Cu_{0.2}$–S. The two electrodes show similar EIS profiles with a semicircle in the high frequency range and a linear part in the low frequency range. The data can be fitted by an equivalent circuit model (inset of Fig. 8.9h), consisting of an equivalent series resistance R_S, a charge transfer resistance R_{ct}, a

capacitance C_f, and a Warburg resistance W_o [36, 336]. As shown in Fig. 8.10, the simulated results based on the equivalent circuit are in good agreement with the experimental data, proving the accuracy of proposed equivalent circuit. The equivalent series resistance (R_S), representing the combination of the intrinsic resistance of the electrode materials, the bulk solution resistance, and the contact resistance between electrode and current collector, can be evaluated by the real axis intercept [36]. The $Ni_{0.8}Cu_{0.2}$−S electrode exhibits a R_s of 0.64 Ω, slightly lower than that of the $Ni_{0.8}Cu_{0.2}$−CH electrode (0.71 Ω), which indicates its higher conductivity. The charge transfer resistance (R_{ct}), which is caused by faradaic reactions, indicating the rate of redox process at the electrode-electrolyte interface, can be estimated by the diameter of the semicircle [271]. The R_{ct} observed at the $Ni_{0.8}Cu_{0.2}$−S electrode is 15.6 Ω, which is noticeably lower than 54.9 Ω for the $Ni_{0.8}Cu_{0.2}$−CH electrode, suggesting the fast ion transport across the $Ni_{0.8}Cu_{0.2}$−S electrode. Overall, better impedance performances have been achieved at the $Ni_{0.8}Cu_{0.2}$−S electrode, which further supports the improved supercapacitor performances obtained by above CV and GCD results.

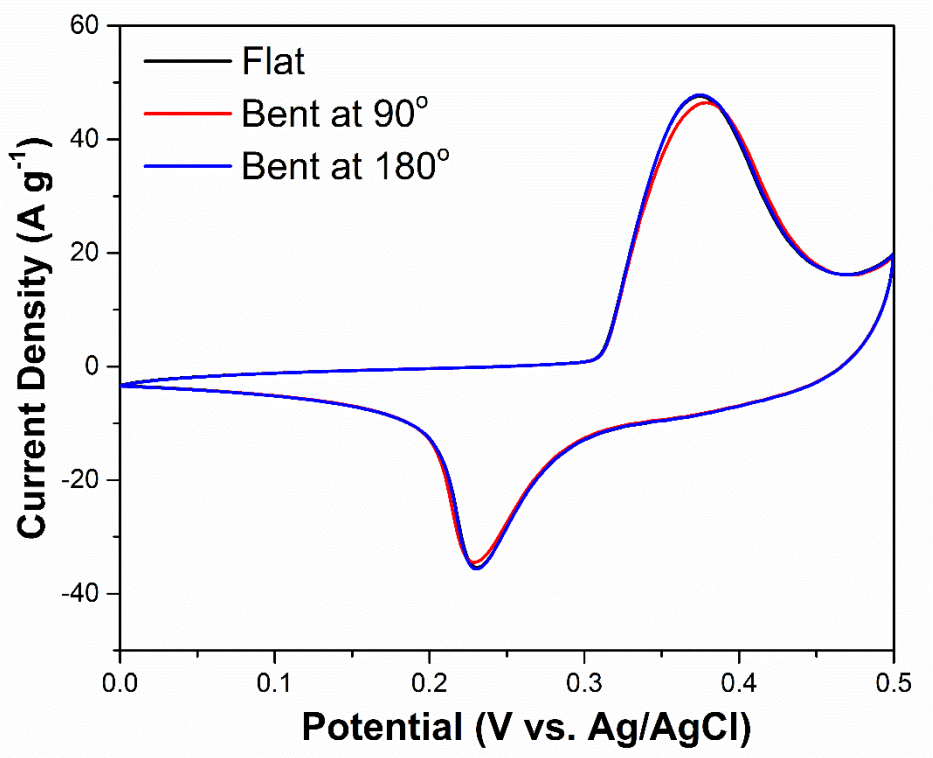

Fig. 8.11 Flexible performance of $Ni_{0.8}Cu_{0.2}$−S electrode under different bending conditions.

The electrode demonstrates good flexibility since it was prepared with a flexible carbon cloth substrate. Fig. 8.11 presents the CV curves of the $Ni_{0.8}Cu_{0.2}$−S electrode examined at different statical curvatures of 0 °, 90 ° and 180° at a scan rate of 10 mV s^{-1}. Obviously, negligible difference can be found for all the curves even at a large bending angle of 180°, indicating good electrochemical performance reliability of the electrode during bending. The high flexibility makes the $Ni_{0.8}Cu_{0.2}$−S electrode a suitable candidate for wearable supercapacitor applications.

It is known that there are two types of energy storage modes in the electrode materials: the surface-controlled capacitive process and diffusion-controlled faradaic process [37]. Typically, the surface-controlled capacitive process includes the reversible charge storage by EDL and the pseudocapacitive redox process, which take place near or at the surface of the active materials. While the diffusion-controlled faradaic process is based on the redox reactions occurred in the bulk materials. It should be noted that obvious redox peaks appeared in the CV curves of the $Ni_{0.8}Cu_{0.2}$−CH and $Ni_{0.8}Cu_{0.2}$−S electrodes, indicating the diffusion-controlled faradaic behaviours of the materials. Nevertheless, it is believed that nanostructured materials can exhibit extrinsic pseudocapacitive behaviours due to the decrease in diffusion distances [16, 28]. To investigate the charge storage mechanisms of samples $Ni_{0.8}Cu_{0.2}$−CH and $Ni_{0.8}Cu_{0.2}$−S, we conducted further analysis of their CV results according to equation 2.6 and 2.7. The fraction of charge storage contributed by the capacitive and diffusion-controlled processes is calculated.

The charge storage contributed by the diffusion-controlled process (blue area) on the $Ni_{0.8}Cu_{0.2}$−S electrode at a scan rate of 5 mV s^{-1} is shown in Fig. 8.12a. Around 50.9% of the capacitance is delivered by the diffusion-controlled faradaic process and the remaining 49.1% is from the surface-controlled capacitive effect. By using the same technique, the contribution ratios of diffusion-controlled process on $Ni_{0.8}Cu_{0.2}$−CH and $Ni_{0.8}Cu_{0.2}$−S electrodes at different scan rates are quantified as shown in Fig. 8.12b. A similar trend is observed for the two electrodes, namely, the diffusion-controlled property decreases gradually with the increase in scan rates, varying from 80.0% to 47.2% for $Ni_{0.8}Cu_{0.2}$−CH and 69.8% to 34.1% for

$Ni_{0.8}Cu_{0.2}$–S from 1 to 20 mV s^{-1}. At high scan rates, diffusion-controlled faradaic reactions are insufficient due to the limited diffusion time, therefore the charge storage ability is mainly accomplished by the capacitive process occurring at the active materials' surface. Moreover, at the same scan rate, sample $Ni_{0.8}Cu_{0.2}$–CH has a larger portion of diffusion-controlled contribution (or smaller portion of capacitive contribution) compared with sample $Ni_{0.8}Cu_{0.2}$–S, suggesting that sample $Ni_{0.8}Cu_{0.2}$–S exhibits more pseudocapacitive properties. Considering the better capacitance performance of sample $Ni_{0.8}Cu_{0.2}$–S obtained by the above CV and GCD results, it can be deduced that the increase in capacitance of the $Ni_{0.8}Cu_{0.2}$–S is largely derived from the capacitive effect. The nonaporous structure and possible higher conductivity of the sulfides offer more active sites to yield extrinsic pseudocapacitance.

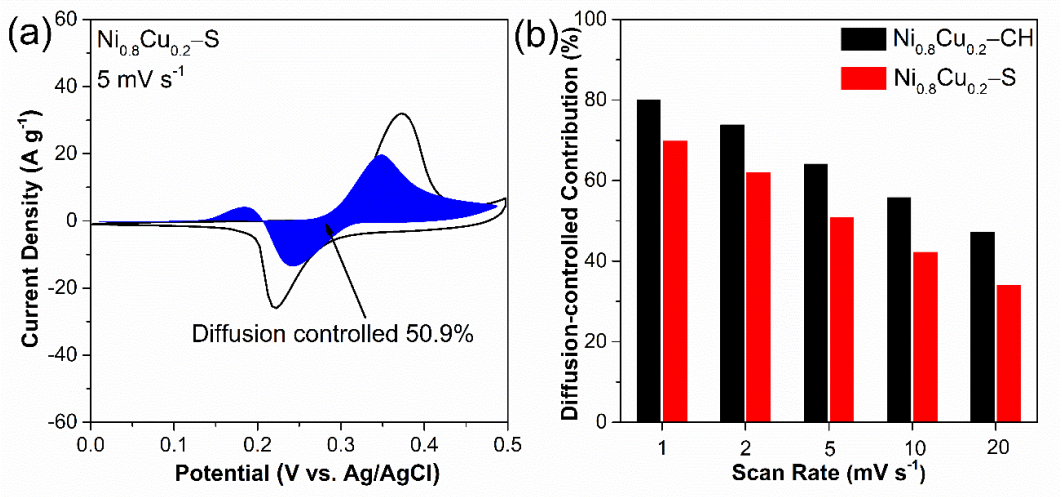

Fig. 8.12 (a) Typical separation of capacitive and diffusion-controlled charge storage process at scan rate of 5 mV s^{-1} of $Ni_{0.8}Cu_{0.2}$–S (b) Contribution ratio of diffusion-controlled faradaic process to the total charge storage of $Ni_{0.8}Cu_{0.2}$–CH and $Ni_{0.8}Cu_{0.2}$–S at various scan rates.

8.3.5 Electrochemical performances of $Ni_{0.8}Cu_{0.2}$−S//NG asymmetric supercapacitor

To further evaluate the electrochemical properties toward practical application of the $Ni_{0.8}Cu_{0.2}$−S electrode, an ASC was assembled by employing the $Ni_{0.8}Cu_{0.2}$−S electrode as the positive electrode and a NG electrode as the negative electrode. Prior to the fabrication, the mass ratio between the positive and negative electrodes was optimized by balancing the charge stored at each electrode using equation 5.3. The NG exhibits typical properties of an EDLC with rectangular CV curves and linear GCD curves (see details in chapter 4).

Fig. 8.13a presents the CV curves of the $Ni_{0.8}Cu_{0.2}$−S//NG ASC with different voltage windows from 1.0 to 1.8 V at a scan rate of 5 mV s^{-1}. Clearly, the ASC delivers a stable performance from 1.0 to 1.7 V. When the operating potential goes to 1.8 V, the dramatically increased current response forms a sharp peak, indicating the polarization of the electrode as well as the serve water electrolysis [335]. Therefore, the working voltage of the full cell was chosen as 1.7 V, which is higher than the conventional carbon-based supercapacitors in aqueous electrolytes (~1.0 V) [11]. Fig. 8.13b illustrates CV curves of the ASC device at various scan rates of 1 to 50 mV s^{-1}. Interestingly, the ASC shows quasi-rectangular CV shape, implying the combined contributions of EDL and faradaic redox reactions. Additionally, the CV shapes from 1 to 50 mV s^{-1} are not obviously changed, suggesting the good rate capability of the device [184].

GCD measurements at different current densities of 2 to 20 A g^{-1} were conducted to further explore the performance of the ASC (Fig. 8.13c). The nearly linear and symmetric charge and discharge curves again demonstrate the mixed capacitance contributions. Based on the discharging parameters and the total mass of the two electrodes, the specific capacitance of the $Ni_{0.8}Cu_{0.2}$−S//NG ASC is plotted in Fig. 8.13d. At a current density 2 A g^{-1}, the cell capacitance can reach as high as 95.9 F g^{-1}, and it still maintains over 80% of this value (77.0 F g^{-1}) when the current density increases to 20 A g^{-1}, indicating good capability of the fabricated ASC device. These performances are superior to those previously reported sulfides based devices, such as NiS//AC (57.7 F g^{-1} at 2 A g^{-1} and 30.2 F g^{-1} at 10 A g^{-1})

[118], CuS//AC (42.3 F g^{-1} at 2 A g^{-1} and 37 F g^{-1} at 8 A g^{-1}) [337], and $NiMoS_4$//AC (73.1 F g^{-1} at 2 A g^{-1} and 59.1 F g^{-1} at 20 A g^{-1}) [317].

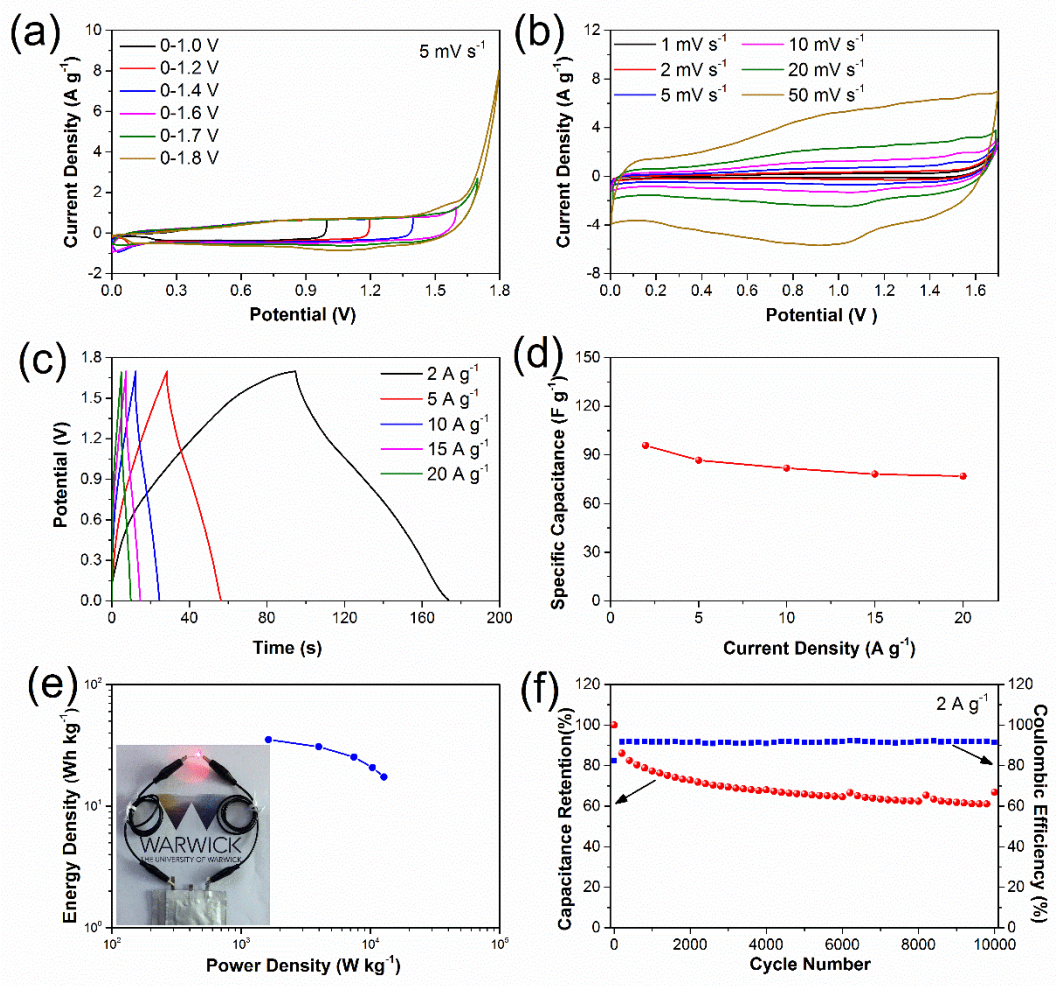

Fig. 8.13 Electrochemical performance of $Ni_{0.8}Cu_{0.2}$−S//NG ASC. (a) CV curves at different potential windows at 5mV s^{-1}; (b) CV curves with a voltage window of 0-1.7 V at various scan rates; c) GCD profiles at various current densities; (d) Specific capacitance at various current densities; (e) Ragone plots of the supercapacitor (inset is the optical image of the $Ni_{0.8}Cu_{0.2}$−S//NG ASC lighting a red LED); (f) Long-term cycling stability and coulombic efficiency of the ASC for 10000 cycles at 2 A g^{-1}.

The energy and power densities are key parameters used to evaluate an electrochemical energy storage device [184]. Energy and power density of $Ni_{0.8}Cu_{0.2}$−S//NG ASC device was calculated using equation 3.12 and 3.13, which is given by Ragone plot in Fig. 8.13e. The device delivers an energy density as

high as 35.3 Wh kg^{-1} at a power density of 1627 W kg^{-1}, which is comparable to other supercapacitors reported previously, such as $NiCo_2S_4$//rGO (31.5 Wh kg^{-1} at 156.6 W kg^{-1}) [164], NiS//AC (31 Wh kg^{-1} at 900 W kg^{-1}) [118], CuS//AC (17.7 Wh kg^{-1} at 504 W kg^{-1})[338], and $NiCo_2O_4$@MnO_2//AC (37.5 Wh kg^{-1} at 187.5 W kg^{-1}) [184]. Moreover, the ASC still keeps an energy density of 17.3 Wh kg^{-1} even at a high power density of up to 12700 W kg^{-1}. These results can be attributed to the high capacitance of the $Ni_{0.8}Cu_{0.2}$−S electrode and wide potential window of the ASC. In practical applications, a red round light-emitting diode (LED) was successfully illuminated by two $Ni_{0.8}Cu_{0.2}$−S//NG ASCs assembled in series after charging (inset in Fig. 8.13e).

The long-term cycling stability and coulombic efficiency of our ASC were tested by 10000 GCD cycles at a current density of 2 A g^{-1} (Fig. 8.13f). The ASC device exhibits a significant capacitance decrease for the first 200 cycles, namely, about 14% of the initial capacitance has been lost. Then the value gradually decreases in the next 1800 cycles, giving an 73% capacitance retention at the 2000th cycle. After this stage, the capacitance almost keeps constant during the following 8000 cycles, finally retaining approximate 69% of the maximum capacitance after 10000 cycles. Its coulombic efficiency is stable, maintaining around 92% during all the 10000 cycles, demonstrating good electrochemical reversibility. The first and last ten GCD curves are presented in Fig. 8.14. The capacitance degradation at the beginning of the cycle test, especially for the first 200 cycles, can be related to the volume expansion and shrinkage of the active materials during the repeated charge-discharge processes which causes the detachment of some weak-connected active materials from the carbon cloth substrate [32]. This can be supported by the black powders found in the electrolyte after test, this issue can be further solved by using a solid-state polymer electrolyte [108]. Nevertheless, The ASC shows good stability during the last 8000 cycles. The structural integrity and basic morphology of the $Ni_{0.8}Cu_{0.2}$−S are overall well preserved with little structural deformation as shown in Fig. 8.15.

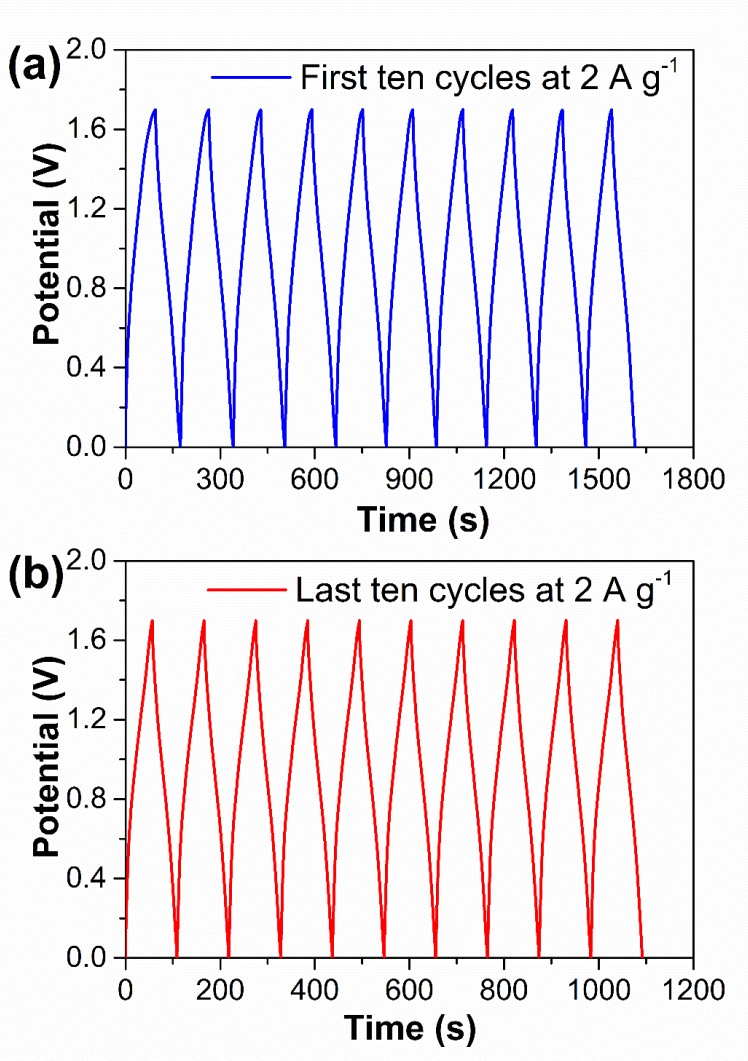

Fig. 8.14 (a) First and (b) last ten charge-discharge curves of the $Ni_{0.8}Cu_{0.2}$–S//NG ASC at a current density of 2 A g^{-1}.

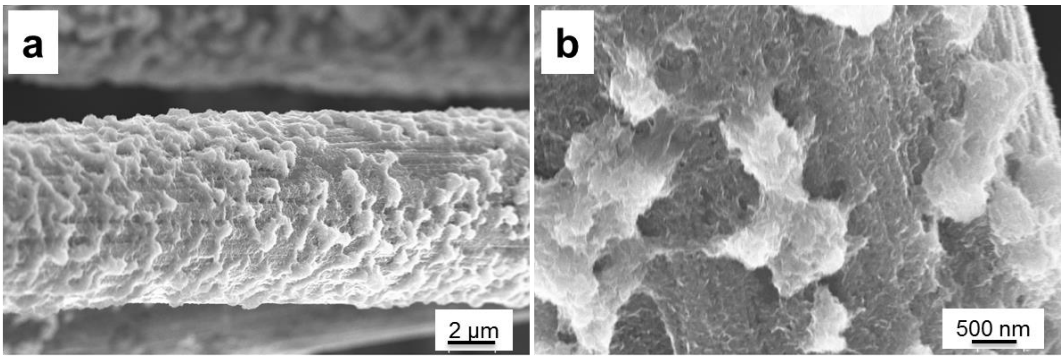

Fig. 8.15 SEM images of the $Ni_{0.8}Cu_{0.2}$–S electrode after charge-discharge for 10000 cycles at a current density of 2 A g^{-1}.

8.4 Conclusions

In this chapter, nanoporous $Ni_{0.8}Cu_{0.2}$−S on carbon cloth has been successful prepared via sulfurizing the Ni-Cu carbonate hydroxide precursor with an anion exchange reaction. The as-fabricated $Ni_{0.8}Cu_{0.2}$−S electrode exhibits a high specific capacitance of 938.6 F g^{-1} at a current density of 1 A g^{-1} and good rate capability of 76% at 10 A g^{-1}, as well as excellent flexibility with negligible performance loss at a bending angle up to 180°. The charge storage process in the $Ni_{0.8}Cu_{0.2}$−S electrode is quantitatively analysed, and the results demonstrate that the total capacitance is contributed to by the combination of surface-controlled capacitive process and diffusion-controlled faradaic process. Compared with the carbonate hydroxide precursor, the capacitance increase of the sulfides is largely from the captive effect, which can be attributed to its nanoporous structure and high conductivity that offers more active sites to yield extrinsic pseudocapacitance. Furthermore, an ASC based on the $Ni_{0.8}Cu_{0.2}$−S positive electrode and a NG negative electrode was assembled, delivering a high cell voltage up to 1.7 V with a maximum energy density of 35.3 Wh kg^{-1} and a maximum power density of 12700 W kg^{-1}. Additionally, the ASC presents good cycle stability and electrochemical reversibility, retaining 69% of the initial capacitance with about 92% coulombic efficiency after 10000 charge-discharge cycles at 2 A g^{-1}. The performances we achieved suggest that the nanoporous $Ni_{0.8}Cu_{0.2}$−S has deep potential for high-performance supercapacitor applications.

CHAPTER 9 Conclusions and future work

9.1 Conclusions

In this thesis, we have developed four novel electrode materials based on the transition metals of Ni and Cu for supercapacitor applications, including the metal oxides ($Li_2Ni_2(MoO_4)_3$ and $Cu_2O/CuMoO_4$) and metal sulfides ($NiMoS_4$ and Ni-Cu-S). These materials were prepared via different techniques, such as combustion, chemical co-precipitation and hydrothermal. Their physical properties were characterized by XRD, SEM, EDX, TEM, TG and UV-Vis, and the electrochemical behaviours were evaluated by cyclic CV, GCD and EIS. To measure the performance in practical energy storage devices, the materials were tested with a two-electrode configuration. All the four materials were used as positive electrodes, which were paired with proper AC or NG negative electrodes to assemble ASCs. Detailed performances are summarised as below.

In terms of the $Li_2Ni_2(MoO_4)_3$, it was synthesized through a combustion method. The working electrode was made by coating mixture of $Li_2Ni_2(MoO_4)_3$ powders, acetylene black and PTFE onto Ni foam. Electrochemical performances of the $Li_2Ni_2(MoO_4)_3$ electrode were investigated in aqueous LiOH and NaOH electrolytes. Results demonstrate that higher specific capacitance is obtained in LiOH electrolyte, which can be attributed to the easier intercalation/deintercalation of small Li^+ ions in the framework of $Li_2Ni_2(MoO_4)_3$. Its specific capacitance reaches 1137 F g^{-1} at 1 A g^{-1} in 2 M LiOH solution (only 717 F g^{-1} in 2 M NaOH solution), and still maintains 63% of the value at 20 A g^{-1}. An ASC was further fabricated by applying the $Li_2Ni_2(MoO_4)_3$ electrode as the positive electrode and an AC electrode as the negative electrode. The device delivers energy density as high as 36.5 W h kg^{-1} at an average power density of 420 W kg^{-1}. Its capacitance retains 68% with coulombic efficiency over 95% after 10000 GCD cycles at 2 A g^{-1}, showing reasonably good stability and electrochemical reversibility.

The $Cu_2O/CuMoO_4$ nanosheets electrode was prepared via a facile hydrothermal method. Since the active materials are directly grown on the Ni foam current collector without any binders and conductive additives, the contact resistance is

greatly reduced which results in excellent conductivity of the electrode. In addition, the nanosheet structure creates more active sites and facilitate the transport of electrolyte ions and electrons, enhancing the utilization of the $Cu_2O/CuMoO_4$. It exhibits remarkable improved specific capacitance (up to 4264 F g^{-1} at a current density of 1 A g^{-1}) with good rate capability (2563 F g^{-1} at a current density of as high as 50 A g^{-1}). Moreover, an ASC was fabricated using the $Cu_2O/CuMoO_4$ nanosheet electrode as the positive electrode and AC as the negative electrode. The operation voltage of the ASC could achieve 1.7 V, at which the energy density is 75.1 Wh kg^{-1} with a power density of 420 W kg^{-1}. The ASC also displays excellent rate capability, cycling stability and electrochemical reversibility. The capacitance maintains around 86.6% with nearly 100% coulombic efficiency after 3000 cycles at a current density of 5 A g^{-1}. Overall, the high capacitance of the $Cu_2O/CuMoO_4$ hybrid electrode achieved can be attributed to its synthesis technique, nanostructure, as well as the synergistic effect between Cu_2O and $CuMoO_4$.

The $NiMoS_4$-A was synthesized through a chemical co-precipitation process followed by calcining at 450 ^oC. Simultaneously, an electrode prepared using the same method except the calcination process was applied for comparison ($NiMoS_4$). Results show that the $NiMoS_4$-A electrode exhibits better electrochemical performances than the $NiMoS_4$ electrode, specifically, a specific capacitance of 706.5 F g^{-1} at 1 A g^{-1} with 83% of capacitance retention at 10 A g^{-1} is observed for $NiMoS_4$-A, while only 501.5 F g^{-1} at 1 A g^{-1} with 70% capacitance retention at 10 A g^{-1} is achieved by $NiMoS_4$. EIS measurements demonstrate that the calcination process of $NiMoS_4$-A decreases its internal resistance, charge transfer resistance and Warburg impedance, leading to the improved electrochemical properties. Next, the charge storage mechanism of the $NiMoS_4$-A electrode was analysed based on the CV curves. It reveals that the surface capacitive process and diffusion-controlled faradaic reaction contribute together to the energy storage. The faradaic redox process dominates at lower scan rates (78% at 1 mV s^{-1}) while the capacitive effect matters at higher scan rate (56% at 20 mV s^{-1}). Furthermore, an ASC was fabricated using $NiMoS_4$-A as the positive electrode and AC as the negative electrode. The ASC delivers a cell voltage of 1.6 V and an energy density of 35 Wh kg^{-1} at a power density of 400 W kg^{-1}. Additionally, the ASC exhibits good cycle stability and electrochemical reversibility, retaining 82% of the initial

capacitance with coulombic efficiency around 97% after 10000 GCD cycles even at a high current density of 5 A g^{-1}.

Different atomic ratio of Ni-Cu carbonate hydroxide nanowires ($Ni_{1-x}Cu_x$−CH, x= 0, 0.1, 0.2, 0.3, 0.4, and 0.5) were directly grown on carbon cloth substrates via a hydrothermal method. Their electrochemical properties, including CV and GCD, were measured in 2 M KOH solution. Since the composite of $Ni_{0.8}Cu_{0.2}$−CH exhibits the highest capacitance (690.8 F g^{-1} at 1 A g^{-1}), it was further converted into sulfides through an anion exchange reaction with Na_2S ($Ni_{0.8}Cu_{0.2}$−S). SEM and TEM indicate sample $Ni_{0.8}Cu_{0.2}$−S exhibits a nanoporous structure which could be due to the etching effect of the S^{2-} anions. The as-fabricated $Ni_{0.8}Cu_{0.2}$−S electrode exhibits a high specific capacitance of 938.6 F g^{-1} at a current density of 1 A g^{-1} and good rate capability of 76% at 10 A g^{-1}. Moreover, basing on the flexible carbon cloth substrate, the $Ni_{0.8}Cu_{0.2}$−S electrode shows excellent flexibility with negligible performance loss at a bending angle up to 180^o, which makes it a suitable candidate for wearable supercapacitor applications. Similar to the $NiMoS_4$-A electrode, the charge storage process in the Ni-Cu electrodes was quantitatively analysed, and the results demonstrate that the total capacitance is contributed to by the combination of surface controlled capacitive process and diffusion-controlled faradaic process. Compared with the $Ni_{0.8}Cu_{0.2}$−CH precursor, the capacitance increase of sample $Ni_{0.8}Cu_{0.2}$−S is largely from the captive effect, which can be attributed to its nanoporous structure and high conductivity that offers more active sites to yield extrinsic pseudocapacitance. Furthermore, an ASC based on the $Ni_{0.8}Cu_{0.2}$−S positive electrode and NG negative electrode was assembled, delivering a high cell voltage up to 1.7 V with a maximum energy density of 35.3 Wh kg^{-1} and a maximum power density of 12700 W kg^{-1}. By assembling two $Ni_{0.8}Cu_{0.2}$−S//NG pouch cells in series, a red round LED was successfully illuminated. The ASC also presents good cycling stability, retaining 69% of the initial capacitance after 10000 GCD cycles at 2 A g^{-1}.

In summary, the charge storage capability of the four materials is mainly based on the reversible faradaic processes. Their electrochemical performances are compared in Table 9.1. The $Cu_2O/CuMoO_4$ nanosheets electrode exhibits the highest specific capacitance among the four electrodes. Although the remaining

three electrodes perform lower specific capacitances, the values are still much higher than the results obtained by carbon materials such as the AC and NG measured in chapter 4. It should be noted that the $Ni_{0.8}Cu_{0.2}$−S electrode demonstrates good flexibility. More importantly, the operation potential of the ASCs fabricated based on these electrodes is greatly improved, reaching up to 1.7 V (except the 1.6 V of the $NiMoS_4$-A//AC ASC), which is higher than the 1.2 V of the AC//AC and NG//NG SSCs. Accordingly, the ASCs exhibit improved energy and power densities. The highest energy density is delivered by the $Cu_2O/CuMoO_4$//AC ASC at 75.1 Wh kg^{-1}, over 10 times larger than the value of the NG//NG SSC. However, the stability of the ASCs is worse than the AC//AC and NG//NG SSCs. Both of the two SSCs exhibit a capacitance retention over 100%, owing to their EDLC properties which can reversibly adsorb/desorb ions at the electrode/electrolyte interface without damaging the active materials' microstructure. On the contrary, the numerous rapid faradaic reactions of the ASCs could cause destruction of the active materials, leading to decline of capacitances. The best stability among the four ASCs is achieved by the $NiMoS_4$-A//AC, demonstrating 82% after 10000 cycles. Considering the high initial energy density delivered by the ASCs, they can still offer higher energy density even after thousands of cycles in comparison with the carbon-based SSCs. From this point of view, the four materials we developed in this thesis are promising for high-performance supercapacitor applications.

Table 9.1 Summarized performance of supercapacitors fabricated in this thesis.

Electrode	Specific capacitance	Electrolyte	Supercapacitor type	Operating voltage	Energy density	Power density	Cycling performance	Chapter
AC	133 F g^{-1} at 1 A g^{-1}	2 M KOH	AC//AC SSC	1.2 V	4.5 Wh kg^{-1} 1.4 Wh kg^{-1}	281 W kg^{-1} 2069 W kg^{-1}	126% after 2000 cycles	4
NG	187 F g^{-1} at 1 A g^{-1}	2 M KOH	NG//NG SSC	1.2 V	5.9 Wh kg^{-1} 2.0 Wh kg^{-1}	285 W kg^{-1} 2248 W kg^{-1}	108% after 2000 cycles	4
$Li_2Ni_2(MoO_4)_3$	1137 F g^{-1} at 1 A g^{-1}	2 M LiOH	$Li_2Ni_2(MoO_4)_3$//AC ASC	1.7 V	36.5 Wh kg^{-1} 13.5 Wh kg^{-1}	420 W kg^{-1} 12783 W kg^{-1}	68% after 10000 cycles	5
$Cu_2O/CuMoO_4$	4264 F g^{-1} at 1 A g^{-1}	2 M KOH	$Cu_2O/CuMoO_4$//AC ASC	1.7 V	75.1 Wh kg^{-1} 21.5 Wh kg^{-1}	420 W kg^{-1} 10435 W kg^{-1}	86.6% after 3000 cycles	6
$NiMoS_4$-A	706.5 F g^{-1} at 1 A g^{-1}	2 M KOH	$NiMoS_4$-A//AC ASC	1.6 V	35 Wh kg^{-1} 13.5 Wh kg^{-1}	400 W kg^{-1} 13000 W kg^{-1}	82% after 10000 cycles	7
$Ni_{0.8}Cu_{0.2}$−S	938.6 F g^{-1} at 1 A g^{-1}	2 M KOH	$Ni_{0.8}Cu_{0.2}$−S//NG ASC	1.7 V	35.3 Wh kg^{-1} 17.3 Wh kg^{-1}	1627 W kg^{-1} 12700 W kg^{-1}	69% after 10000 cycles	8

9.2 Future work

In this thesis, we focus on the electrode material synthesis for supercapacitors. However, in comparison with the matured technologies of batteries, the supercapacitor technology is still at an initial research stage, and many issues need to be addressed from the material synthesis to the prototype construction. Several suggestions for future research are proposed.

- The specific surface area is an important factor which significantly determines the supercapacitor performances. BET technique could be applied to study the porosity properties of the developed materials, such as specific surface area and pore size distribution, which would be very helpful for understanding their electrochemical behaviours and further performance improvement.
- The understanding of the reaction mechanisms of the developed materials is not sufficient. They can be further investigated by applying some in situ techniques, such as XRD, SEM. More valuable information about the change of the materials during charge-discharge process would be obtained, which can be useful for further improvement of their performances.
- Based on the current results, it can be found that the stability of the faradaic reaction involved materials is not perfect. More efforts should be made to improve their stability, such as enhancing the conductivity by making hybrid materials with graphene and CNTs, and redesigning the electrode structures.
- It is known that energy density can be largely improved by increasing the overall cell voltage. Some materials could suppress the water electrolysis thus achieving very high cell voltage in aqueous electrolytes, such as the $Na_{0.5}MnO_2$ and carbon-coated Fe_3O_4 discussed in chapter 2. Other transition metal-based compounds could be good alternatives for developing high-voltage supercapacitors with aqueous electrolytes which needs further investigation.
- Majority of the superactions in this work were fabricated in a beaker, and simple pouch cells were also prepared. But these attempts are very pristine. Besides the electrode materials, the cell structure is also a very significant

factor which influences the supercapacitor performances. More sophisticated designs, such as coin cells and cylindrical cells can be applied.

- In addition to the experimental exploration, computational simulation at a molecular level can be a powerful tool for further understanding the properties of a material, which could be helpful in designing high-performance electrodes and solving the current issues.

References

1. Guan, L., L. Yu, and G.Z. Chen, *Capacitive and non-capacitive faradaic charge storage.* Electrochimica Acta, 2016. **206**: p. 464-478.
2. Zhao, H., et al., *Recent advances in designing and fabricating self‐supported nanoelectrodes for supercapacitors.* Advanced Science, 2017.
3. Wang, G., L. Zhang, and J. Zhang, *A review of electrode materials for electrochemical supercapacitors.* Chemical Society Reviews, 2012. **41**(2): p. 797-828.
4. Choi, N.S., et al., *Challenges facing lithium batteries and electrical double‐layer capacitors.* Angewandte Chemie International Edition, 2012. **51**(40): p. 9994-10024.
5. Wang, Y. and Y. Xia, *Recent progress in supercapacitors: from materials design to system construction.* Advanced materials, 2013. **25**(37): p. 5336-5342.
6. Simon, P. and Y. Gogotsi, *Materials for electrochemical capacitors.* Nature materials, 2008. **7**(11): p. 845-854.
7. Zhao, C. and W. Zheng, *A review for aqueous electrochemical supercapacitors.* Frontiers in Energy Research, 2015. **3**: p. 23.
8. Yu, G., et al., *Hybrid nanostructured materials for high-performance electrochemical capacitors.* Nano Energy, 2013. **2**(2): p. 213-234.
9. Wang, Y., Y. Song, and Y. Xia, *Electrochemical capacitors: mechanism, materials, systems, characterization and applications.* Chemical Society Reviews, 2016. **45**(21): p. 5925-5950.
10. Zhang, L.L. and X. Zhao, *Carbon-based materials as supercapacitor electrodes.* Chemical Society Reviews, 2009. **38**(9): p. 2520-2531.
11. Wang, Y., et al., *Supercapacitor devices based on graphene materials.* The Journal of Physical Chemistry C, 2009. **113**(30): p. 13103-13107.
12. Yang, P., et al., *Low-cost high-performance solid-state asymmetric supercapacitors based on MnO_2 nanowires and Fe_2O_3 nanotubes.* Nano letters, 2014. **14**(2): p. 731-736.
13. Shi, F., et al., *Metal oxide/hydroxide-based materials for supercapacitors.* Rsc Advances, 2014. **4**(79): p. 41910-41921.
14. Li, W., et al., *Application of ultrasonic irradiation in preparing conducting polymer as active materials for supercapacitor.* Materials Letters, 2005. **59**(7): p. 800-803.
15. Sharma, R., A. Rastogi, and S. Desu, *Pulse polymerized polypyrrole electrodes for high energy density electrochemical supercapacitor.* Electrochemistry Communications, 2008. **10**(2): p. 268-272.
16. Sun, J., et al., *Recent progresses in high-energy-density all pseudocapacitive-electrode-materials-based asymmetric supercapacitors.* Journal of Materials Chemistry A, 2017. **5**(20): p. 9443-9464.
17. Choudhary, N., et al., *Asymmetric supercapacitor electrodes and devices.* Advanced Materials, 2017.
18. Yu, M., et al., *Recent progress in the development of anodes for asymmetric supercapacitors.* Journal of Materials Chemistry A, 2016. **4**(13): p. 4634-4658.
19. Kang, K., et al., *Electrodes with high power and high capacity for rechargeable lithium batteries.* Science, 2006. **311**(5763): p. 977-980.

20. Goodenough, J.B. and K.-S. Park, *The Li-ion rechargeable battery: a perspective.* Journal of the American Chemical Society, 2013. **135**(4): p. 1167-1176.
21. Helmholtz, H.v., *Annalen der Physik.* Leipzig, 1853. **89**: p. 21.
22. Gouy, M., *Sur la constitution de la charge électrique à la surface d'un électrolyte.* J. Phys. Theor. Appl., 1910. **9**(1): p. 457-468.
23. Stern, O., *The theory of the electrolytic double-layer.* Z. Elektrochem, 1924. **30**(508): p. 1014-1020.
24. Breitkopf, C. and K. Swider-Lyons, *Springer handbook of electrochemical energy*. 2016: Springer.
25. Guo, C.X. and C.M. Li, *A self-assembled hierarchical nanostructure comprising carbon spheres and graphene nanosheets for enhanced supercapacitor performance.* Energy & Environmental Science, 2011. **4**(11): p. 4504-4507.
26. Hulicova‐Jurcakova, D., et al., *Combined effect of nitrogen‐and oxygen‐containing functional groups of microporous activated carbon on its electrochemical performance in supercapacitors.* Advanced functional materials, 2009. **19**(3): p. 438-447.
27. Fan, Z., et al., *A three‐dimensional carbon nanotube/graphene sandwich and its application as electrode in supercapacitors.* Advanced materials, 2010. **22**(33): p. 3723-3728.
28. Augustyn, V., P. Simon, and B. Dunn, *Pseudocapacitive oxide materials for high-rate electrochemical energy storage.* Energy & Environmental Science, 2014. **7**(5): p. 1597-1614.
29. Conway, B., *Two-dimensional and quasi-two-dimensional isotherms for Li intercalation and upd processes at surfaces.* Electrochimica acta, 1993. **38**(9): p. 1249-1258.
30. Okubo, M., et al., *Nanosize effect on high-rate Li-ion intercalation in $LiCoO_2$ electrode.* Journal of the american chemical society, 2007. **129**(23): p. 7444-7452.
31. Ji, J., et al., *Nanoporous $Ni(OH)_2$ thin film on 3D ultrathin-graphite foam for asymmetric supercapacitor.* ACS nano, 2013. **7**(7): p. 6237-6243.
32. Cheng, Y., et al., *Improving the performance of cobalt–nickel hydroxide-based self-supporting electrodes for supercapacitors using accumulative approaches.* Energy & Environmental Science, 2013. **6**(11): p. 3314-3321.
33. Kim, H.-S., et al., *Oxygen vacancies enhance pseudocapacitive charge storage properties of MoO_{3-x}.* Nature materials, 2017. **16**(4): p. 454-460.
34. Brezesinski, T., et al., *Ordered mesoporous a-MoO_3 with iso-oriented nanocrystalline walls for thin-film pseudocapacitors.* Nature materials, 2010. **9**(2): p. 146-151.
35. Xu, H., et al., *Flexible asymmetric micro‐supercapacitors based on Bi_2O_3 and MnO_2 nanoflowers: larger areal mass promises higher energy density.* Advanced Energy Materials, 2015. **5**(6).
36. Zhang, X., et al., *A universal strategy for metal oxide anchored and binder-free carbon matrix electrode: a supercapacitor case with superior rate performance and high mass loading.* Nano Energy, 2017. **31**: p. 311-321.
37. Xia, X., et al., *Generic synthesis of carbon nanotube branches on metal oxide arrays exhibiting stable high‐rate and long‐cycle sodium‐ion storage.* Small, 2016. **12**(22): p. 3048-3058.

38. Zhang, Y., et al., *Progress of electrochemical capacitor electrode materials: A review.* International journal of hydrogen energy, 2009. **34**(11): p. 4889-4899.
39. Frackowiak, E., *Supercapacitors based on carbon materials and ionic liquids.* Journal of the Brazilian Chemical Society, 2006. **17**(6): p. 1074-1082.
40. Rouquerol, J., et al., *Recommendations for the characterization of porous solids (Technical Report).* Pure and Applied Chemistry, 1994. **66**(8): p. 1739-1758.
41. Eftekhari, A. and Z. Fan, *Ordered mesoporous carbon and its applications for electrochemical energy storage and conversion.* Materials Chemistry Frontiers, 2017. **1**(6): p. 1001-1027.
42. Kierzek, K., et al., *Electrochemical capacitors based on highly porous carbons prepared by KOH activation.* Electrochimica Acta, 2004. **49**(4): p. 515-523.
43. Raymundo-Pinero, E., et al., *Relationship between the nanoporous texture of activated carbons and their capacitance properties in different electrolytes.* Carbon, 2006. **44**(12): p. 2498-2507.
44. Salitra, G., et al., *Carbon electrodes for double‐layer capacitors i. Relations between ion and pore dimensions.* Journal of the Electrochemical Society, 2000. **147**(7): p. 2486-2493.
45. Largeot, C., et al., *Relation between the ion size and pore size for an electric double-layer capacitor.* Journal of the American Chemical Society, 2008. **130**(9): p. 2730-2731.
46. Rios, R.R.A., et al., *Tailoring activated carbon by surface chemical modification with O, S, and N containing molecules.* Materials Research, 2003. **6**(2): p. 129-135.
47. Pandolfo, A. and A. Hollenkamp, *Carbon properties and their role in supercapacitors.* Journal of power sources, 2006. **157**(1): p. 11-27.
48. Li, B., et al., *Nitrogen-doped activated carbon for a high energy hybrid supercapacitor.* Energy & Environmental Science, 2016. **9**(1): p. 102-106.
49. Gajewicz, A., et al., *Advancing risk assessment of engineered nanomaterials: application of computational approaches.* Advanced drug delivery reviews, 2012. **64**(15): p. 1663-1693.
50. Bordjiba, T., M. Mohamedi, and L.H. Dao, *New Class of Carbon‐Nanotube Aerogel Electrodes for Electrochemical Power Sources.* Advanced materials, 2008. **20**(4): p. 815-819.
51. Niu, C., et al., *High power electrochemical capacitors based on carbon nanotube electrodes.* Applied Physics Letters, 1997. **70**(11): p. 1480-1482.
52. Frackowiak, E., et al., *Enhanced capacitance of carbon nanotubes through chemical activation.* Chemical Physics Letters, 2002. **361**(1): p. 35-41.
53. An, K.H., et al., *Electrochemical properties of high-power supercapacitors using single-walled carbon nanotube electrodes.* Advanced functional materials, 2001. **11**(5): p. 387-392.
54. Saghafi, M., et al., *Preparation of vertically aligned carbon nanotubes and their electrochemical performance in supercapacitors.* Synthetic Metals, 2014. **195**: p. 252-259.
55. Zhang, H., et al., *Comparison between electrochemical properties of aligned carbon nanotube array and entangled carbon nanotube electrodes.* Journal of The Electrochemical Society, 2008. **155**(2): p. K19-K22.

56. Kim, B., H. Chung, and W. Kim, *Supergrowth of aligned carbon nanotubes directly on carbon papers and their properties as supercapacitors.* The Journal of Physical Chemistry C, 2010. **114**(35): p. 15223-15227.
57. Tang, Z., C.h. Tang, and H. Gong, *A high energy density asymmetric supercapacitor from nano‐architectured $Ni(OH)_2$/carbon nanotube electrodes.* Advanced Functional Materials, 2012. **22**(6): p. 1272-1278.
58. Cheng, Q., et al., *Graphene and carbon nanotube composite electrodes for supercapacitors with ultra-high energy density.* Physical Chemistry Chemical Physics, 2011. **13**(39): p. 17615-17624.
59. Li, D., et al., *Synthesis of nitrogen doped graphene from graphene oxide within an ammonia flame for high performance supercapacitors.* RSC Advances, 2014. **4**(98): p. 55394-55399.
60. Ji, H., et al., *Capacitance of carbon-based electrical double-layer capacitors.* Nature communications, 2014. **5**: p. 3317.
61. Bonaccorso, F., et al., *Graphene, related two-dimensional crystals, and hybrid systems for energy conversion and storage.* Science, 2015. **347**(6217): p. 1246501.
62. Lee, J.-S., et al., *Chemical vapor deposition of mesoporous graphene nanoballs for supercapacitor.* ACS nano, 2013. **7**(7): p. 6047-6055.
63. Dey, R.S., H.A. Hjuler, and Q. Chi, *Approaching the theoretical capacitance of graphene through copper foam integrated three-dimensional graphene networks.* Journal of Materials Chemistry A, 2015. **3**(12): p. 6324-6329.
64. Sun, L., et al., *Nitrogen-doped graphene with high nitrogen level via a one-step hydrothermal reaction of graphene oxide with urea for superior capacitive energy storage.* Rsc Advances, 2012. **2**(10): p. 4498-4506.
65. Conway, B.E., *Transition from "supercapacitor" to "battery" behavior in electrochemical energy storage.* Journal of the Electrochemical Society, 1991. **138**(6): p. 1539-1548.
66. Juodkazis, K., et al., *On the charge storage mechanism at RuO_2/0.5 M H_2SO_4 interface.* Journal of Solid State Electrochemistry, 2008. **12**(11): p. 1399-1404.
67. Zheng, J., P. Cygan, and T. Jow, *Hydrous ruthenium oxide as an electrode material for electrochemical capacitors.* Journal of the Electrochemical Society, 1995. **142**(8): p. 2699-2703.
68. Dmowski, W., et al., *Local atomic structure and conduction mechanism of nanocrystalline hydrous RuO2 from X-ray scattering.* The Journal of Physical Chemistry B, 2002. **106**(49): p. 12677-12683.
69. Hu, C.-C., W.-C. Chen, and K.-H. Chang, *How to achieve maximum utilization of hydrous ruthenium oxide for supercapacitors.* Journal of the Electrochemical Society, 2004. **151**(2): p. A281-A290.
70. Lee, H.Y. and J.B. Goodenough, *Supercapacitor behavior with KCl electrolyte.* Journal of Solid State Chemistry, 1999. **144**(1): p. 220-223.
71. Wu, M.-S., *Electrochemical capacitance from manganese oxide nanowire structure synthesized by cyclic voltammetric electrodeposition.* Applied Physics Letters, 2005. **87**(15): p. 153102.
72. Kashale, A.A., et al., *Binder free 2D aligned efficient MnO_2 micro flowers as stable electrodes for symmetric supercapacitor applications.* RSC Advances, 2017. **7**(59): p. 36886-36894.

73. Devaraj, S. and N. Munichandraiah, *Effect of crystallographic structure of MnO_2 on its electrochemical capacitance properties.* The Journal of Physical Chemistry C, 2008. **112**(11): p. 4406-4417.
74. Yang, Y., et al., *Graphene/MnO_2 composite prepared by a simple method for high performance supercapacitor.* Materials Research Innovations, 2016. **20**(2): p. 92-98.
75. Chen, W., et al., *High-performance nanostructured supercapacitors on a sponge.* Nano letters, 2011. **11**(12): p. 5165-5172.
76. Li, M., et al., *Controlling the formation of rodlike V_2O_5 nanocrystals on reduced graphene oxide for high-performance supercapacitors.* ACS applied materials & interfaces, 2013. **5**(21): p. 11462-11470.
77. Saravanakumar, B., K.K. Purushothaman, and G. Muralidharan, *Interconnected V_2O_5 nanoporous network for high-performance supercapacitors.* ACS applied materials & interfaces, 2012. **4**(9): p. 4484-4490.
78. Zhu, J., et al., *Building 3D structures of vanadium pentoxide nanosheets and application as electrodes in supercapacitors.* Nano letters, 2013. **13**(11): p. 5408-5413.
79. Liang, K., et al., *Ultrafine V_2O_5 Nanowires in 3D Current Collector for High‐Performance Supercapacitor.* ChemElectroChem, 2016. **3**(5): p. 704-708.
80. Chen, Z., et al., *Design and synthesis of hierarchical nanowire composites for electrochemical energy storage.* Advanced Functional Materials, 2009. **19**(21): p. 3420-3426.
81. Dubal, D.P., et al., *Decoration of spongelike $Ni(OH)_2$ nanoparticles onto MWCNTs using an easily manipulated chemical protocol for supercapacitors.* ACS applied materials & interfaces, 2013. **5**(7): p. 2446-2454.
82. Vijayakumar, S., S. Nagamuthu, and G. Muralidharan, *Supercapacitor studies on NiO nanoflakes synthesized through a microwave route.* ACS applied materials & interfaces, 2013. **5**(6): p. 2188-2196.
83. Yuan, C., et al., *Growth of ultrathin mesoporous Co_3O_4 nanosheet arrays on Ni foam for high-performance electrochemical capacitors.* Energy & Environmental Science, 2012. **5**(7): p. 7883-7887.
84. Hu, C.-C., J.-C. Chen, and K.-H. Chang, *Cathodic deposition of $Ni(OH)_2$ and $Co(OH)_2$ for asymmetric supercapacitors: importance of the electrochemical reversibility of redox couples.* Journal of Power Sources, 2013. **221**: p. 128-133.
85. Lu, Z., et al., *Beta-phased $Ni(OH)_2$ nanowall film with reversible capacitance higher than theoretical Faradic capacitance.* Chemical Communications, 2011. **47**(34): p. 9651-9653.
86. Liao, Q., et al., *All-solid-state symmetric supercapacitor based on Co_3O_4 nanoparticles on vertically aligned graphene.* Acs Nano, 2015. **9**(5): p. 5310-5317.
87. Lu, X., G. Li, and Y. Tong, *A review of negative electrode materials for electrochemical supercapacitors.* Science China Technological Sciences, 2015. **58**(11): p. 1799-1808.
88. Chen, Y.C., et al., *Novel iron oxyhydroxide lepidocrocite nanosheet as ultrahigh power density anode material for asymmetric supercapacitors.* Small, 2014. **10**(18): p. 3803-3810.

89. Li, Y., et al., *Fe_2O_3 nanoneedles on ultrafine nickel nanotube arrays as efficient anode for high‐performance asymmetric supercapacitors.* Advanced Functional Materials, 2017. **27**(14).
90. Lu, X., et al., *Oxygen‐deficient hematite nanorods as high‐performance and novel negative electrodes for flexible asymmetric supercapacitors.* Advanced Materials, 2014. **26**(19): p. 3148-3155.
91. Wang, Q., et al., *Fe_3O_4 nanoparticles grown on graphene as advanced electrode materials for supercapacitors.* Journal of Power Sources, 2014. **245**: p. 101-106.
92. Liu, R., et al., *Flexible Ti‐doped FeOOH quantum dots/graphene/bacterial cellulose anode for high‐energy asymmetric supercapacitors.* Particle & Particle Systems Characterization, 2017.
93. Wang, Q., et al., *Morphology evolution of urchin-like $NiCo_2O_4$ nanostructures and their applications as psuedocapacitors and photoelectrochemical cells.* Journal of Materials Chemistry, 2012. **22**(40): p. 21647-21653.
94. Mai, L.-Q., et al., *Hierarchical $MnMoO_4/CoMoO_4$ heterostructured nanowires with enhanced supercapacitor performance.* Nature communications, 2011. **2**: p. 381.
95. Wang, Z., et al., *One-step accurate synthesis of shell controllable $CoFe_2O_4$ hollow microspheres as high-performance electrode materials in supercapacitor.* Nano Research, 2016. **9**(7): p. 2026-2033.
96. Liu, B., et al., *New energy storage option: toward $ZnCo_2O_4$ nanorods/nickel foam architectures for high-performance supercapacitors.* ACS applied materials & interfaces, 2013. **5**(20): p. 10011-10017.
97. Guo, D., et al., *High performance $NiMoO_4$ nanowires supported on carbon cloth as advanced electrodes for symmetric supercapacitors.* Nano Energy, 2014. **8**: p. 174-182.
98. Wang, Y., et al., *Novel $FeMoO_4$/graphene composites based electrode materials for supercapacitors.* Composites Science and Technology, 2014. **103**: p. 16-21.
99. Kumar, V., et al., *Design of mixed‐metal silver decamolybdate nanostructures for high specific energies at high power density.* Advanced Materials, 2016. **28**(32): p. 6966-6975.
100. Zhang, Y., et al., *Binary metal oxide: advanced energy storage materials in supercapacitors.* Journal of Materials Chemistry A, 2015. **3**(1): p. 43-59.
101. Lu, X., et al., *Hydrogenated TiO_2 nanotube arrays for supercapacitors.* Nano letters, 2012. **12**(3): p. 1690-1696.
102. Sun, X., et al., *Atomic layer deposition of TiO_2 on graphene for supercapacitors.* Journal of the Electrochemical Society, 2012. **159**(4): p. A364-A369.
103. Chang, J., et al., *Asymmetric supercapacitors based on graphene/MnO_2 nanospheres and graphene/MoO_3 nanosheets with high energy density.* Advanced Functional Materials, 2013. **23**(40): p. 5074-5083.
104. Liu, R., et al., *Oxygen‐deficient bismuth oxide/graphene of ultrahigh capacitance as advanced flexible anode for asymmetric supercapacitors.* Advanced Functional Materials, 2017.

105. Senthilkumar, S., et al., *Fabrication of Bi_2O_3||AC asymmetric supercapacitor with redox additive aqueous electrolyte and its improved electrochemical performances.* Electrochimica Acta, 2014. **115**: p. 518-524.
106. Zhu, C., et al., *A 2.0 V capacitive device derived from shape-preserved metal nitride nanorods.* Nano Energy, 2016. **26**: p. 1-6.
107. Choi, D. and P.N. Kumta, *Nanocrystalline TiN derived by a two-step halide approach for electrochemical capacitors.* Journal of the Electrochemical Society, 2006. **153**(12): p. A2298-A2303.
108. Lu, X., et al., *Stabilized TiN nanowire arrays for high-performance and flexible supercapacitors.* Nano letters, 2012. **12**(10): p. 5376-5381.
109. Tian, F., et al., *Preparation and electrochemical capacitance of graphene/titanium nitride nanotube array.* Rsc Advances, 2014. **4**(79): p. 41856-41863.
110. Xu, Y., et al., *One-dimensional vanadium nitride nanofibers fabricated by electrospinning for supercapacitors.* Electrochimica Acta, 2015. **173**: p. 680-686.
111. Lu, X., et al., *High energy density asymmetric quasi-solid-state supercapacitor based on porous vanadium nitride nanowire anode.* Nano letters, 2013. **13**(6): p. 2628-2633.
112. Dong, S., et al., *TiN/VN composites with core/shell structure for supercapacitors.* Materials Research Bulletin, 2011. **46**(6): p. 835-839.
113. Zhou, X., et al., *Mesoporous coaxial titanium nitride-vanadium nitride fibers of core–shell structures for high-performance supercapacitors.* ACS applied materials & interfaces, 2011. **3**(8): p. 3058-3063.
114. Balogun, M.-S., et al., *Three-dimensional nickel nitride (Ni_3N) nanosheets: Free standing and flexible electrodes for lithium ion batteries and supercapacitors.* Journal of Materials Chemistry A, 2016. **4**(25): p. 9844-9849.
115. Xiao, X., et al., *Salt-templated synthesis of 2D metallic mon and other nitrides.* ACS nano, 2017. **11**(2): p. 2180-2186.
116. Śliwak, A., A. Moyseowicz, and G. Gryglewicz, *Hydrothermal-assisted synthesis of an iron nitride–carbon composite as a novel electrode material for supercapacitors.* Journal of Materials Chemistry A, 2017. **5**(12): p. 5680-5684.
117. Hu, H., B.Y. Guan, and X.W.D. Lou, *Construction of complex CoS hollow structures with enhanced electrochemical properties for hybrid supercapacitors.* Chem, 2016. **1**(1): p. 102-113.
118. Guan, B., et al., *Synthesis of hierarchical NiS microflowers for high performance asymmetric supercapacitor.* Chemical Engineering Journal, 2017. **308**: p. 1165-1173.
119. Pang, H., et al., *Microwave-assisted synthesis of NiS_2 nanostructures for supercapacitors and cocatalytic enhancing photocatalytic H_2 production.* Scientific reports, 2014. **4**: p. 3577.
120. Huo, H., Y. Zhao, and C. Xu, *3D Ni_3S_2 nanosheet arrays supported on Ni foam for high-performance supercapacitor and non-enzymatic glucose detection.* Journal of Materials Chemistry A, 2014. **2**(36): p. 15111-15117.
121. Rui, X., H. Tan, and Q. Yan, *Nanostructured metal sulfides for energy storage.* Nanoscale, 2014. **6**(17): p. 9889-9924.

122. Ji, Y., et al., *A facile template-free approach for the solid-phase synthesis of CoS_2 nanocrystals and their enhanced storage energy in supercapacitors.* RSC Advances, 2014. **4**(91): p. 50220-50225.
123. Li, H., et al., *Vapor-phase atomic layer deposition of Co_9S_8 and its application for supercapacitors.* Nano letters, 2015. **15**(10): p. 6689-6695.
124. Acerce, M., D. Voiry, and M. Chhowalla, *Metallic 1T phase MoS_2 nanosheets as supercapacitor electrode materials.* Nature nanotechnology, 2015. **10**(4): p. 313-318.
125. da Silveira Firmiano, E.G., et al., *Supercapacitor electrodes obtained by directly bonding 2D MoS_2 on reduced graphene oxide.* Advanced Energy Materials, 2014. **4**(6).
126. Huang, K.-J., et al., *Synthesis of polyaniline/2-dimensional graphene analog MoS_2 composites for high-performance supercapacitor.* Electrochimica Acta, 2013. **109**: p. 587-594.
127. Javed, M.S., et al., *Tracking pseudocapacitive contribution to superior energy storage of MnS nanoparticles grown on carbon textile.* ACS Applied Materials & Interfaces, 2016. **8**(37): p. 24621-24628.
128. Masikhwa, T.M., et al., *Asymmetric supercapacitor based on VS_2 nanosheets and activated carbon materials.* RSC Advances, 2016. **6**(45): p. 38990-39000.
129. Javed, M.S., et al., *A high-performance flexible solid-state supercapacitor based on Li-ion intercalation into tunnel-structure iron sulfide.* Electrochimica Acta, 2016. **219**: p. 742-750.
130. Huang, K.-J., J.-Z. Zhang, and Y. Fan, *One-step solvothermal synthesis of different morphologies CuS nanosheets compared as supercapacitor electrode materials.* Journal of Alloys and Compounds, 2015. **625**: p. 158-163.
131. Khalil, A., et al., *Metallic 1T-WS_2 nanoribbons as highly conductive electrodes for supercapacitors.* RSC Advances, 2016. **6**(54): p. 48788-48791.
132. Chen, W., C. Xia, and H.N. Alshareef, *One-step electrodeposited nickel cobalt sulfide nanosheet arrays for high-performance asymmetric supercapacitors.* ACS nano, 2014. **8**(9): p. 9531-9541.
133. Elshahawy, A.M., et al., *Controllable $MnCo_2S_4$ nanostructures for high performance hybrid supercapacitors.* Journal of Materials Chemistry A, 2017. **5**(16): p. 7494-7506.
134. Guo, M., et al., *Facile fabrication of Co_2CuS_4 nanoparticle anchored N-doped graphene for high-performance asymmetric supercapacitors.* Journal of Materials Chemistry A, 2016. **4**(44): p. 17560-17571.
135. Hu, X., et al., *Superior electrical conductivity in hydrogenated layered ternary chalcogenide nanosheets for flexible all‐solid‐state supercapacitors.* Angewandte Chemie International Edition, 2016. **55**(19): p. 5733-5738.
136. Xu, X., et al., *Amorphous $CoMoS_4$ for a valuable energy storage material candidate.* Chemical Engineering Journal, 2016. **301**: p. 266-275.
137. Wang, K., J. Huang, and Z. Wei, *Conducting polyaniline nanowire arrays for high performance supercapacitors.* The Journal of Physical Chemistry C, 2010. **114**(17): p. 8062-8067.

138. Sharma, R., A. Rastogi, and S. Desu, *Manganese oxide embedded polypyrrole nanocomposites for electrochemical supercapacitor.* Electrochimica Acta, 2008. **53**(26): p. 7690-7695.
139. Zhu, Z.-z., et al., *Fabrication and electrochemical characterization of polyaniline nanorods modified with sulfonated carbon nanotubes for supercapacitor applications.* Electrochimica Acta, 2011. **56**(3): p. 1366-1372.
140. Wang, Z., et al., *Nanocellulose coupled flexible polypyrrole@graphene oxide composite paper electrodes with high volumetric capacitance.* Nanoscale, 2015. **7**(8): p. 3418-3423.
141. Cong, H.-P., et al., *Flexible graphene–polyaniline composite paper for high-performance supercapacitor.* Energy & Environmental Science, 2013. **6**(4): p. 1185-1191.
142. Horng, Y.-Y., et al., *Flexible supercapacitor based on polyaniline nanowires/carbon cloth with both high gravimetric and area-normalized capacitance.* Journal of Power Sources, 2010. **195**(13): p. 4418-4422.
143. Zhang, H., et al., *Tube-covering-tube nanostructured polyaniline/carbon nanotube array composite electrode with high capacitance and superior rate performance as well as good cycling stability.* Electrochemistry Communications, 2008. **10**(7): p. 1056-1059.
144. Kovalenko, I., D.G. Bucknall, and G. Yushin, *Detonation nanodiamond and onion‐like‐carbon‐embedded polyaniline for supercapacitors.* Advanced Functional Materials, 2010. **20**(22): p. 3979-3986.
145. Zhao, Y., et al., *Preparation of $MnCo_2O_4$@$Ni(OH)_2$ core–shell flowers for asymmetric supercapacitor materials with ultrahigh specific capacitance.* Advanced Functional Materials, 2016. **26**(23): p. 4085-4093.
146. Subramanian, V., et al., *Supercapacitors from activated carbon derived from banana fibers.* The Journal of Physical Chemistry C, 2007. **111**(20): p. 7527-7531.
147. Owusu, K.A., et al., *Low-crystalline iron oxide hydroxide nanoparticle anode for high-performance supercapacitors.* Nature communications, 2017. **8**.
148. Li, L., et al., *A bismuth oxide nanosheet-coated electrospun carbon nanofiber film: a free-standing negative electrode for flexible asymmetric supercapacitors.* Journal of Materials Chemistry A, 2016. **4**(42): p. 16635-16644.
149. Zhong, C., et al., *A review of electrolyte materials and compositions for electrochemical supercapacitors.* Chemical Society Reviews, 2015. **44**(21): p. 7484-7539.
150. Galiński, M., A. Lewandowski, and I. Stępniak, *Ionic liquids as electrolytes.* Electrochimica acta, 2006. **51**(26): p. 5567-5580.
151. Balducci, A., et al., *High temperature carbon–carbon supercapacitor using ionic liquid as electrolyte.* Journal of Power Sources, 2007. **165**(2): p. 922-927.
152. González, A., et al., *Review on supercapacitors: technologies and materials.* Renewable and Sustainable Energy Reviews, 2016. **58**: p. 1189-1206.
153. Yang, P. and W. Mai, *Flexible solid-state electrochemical supercapacitors.* Nano Energy, 2014. **8**: p. 274-290.

154. Zhou, X., et al., *A core-shell structured polysulfonamide-based composite nonwoven towards high power lithium ion battery separator.* Journal of The Electrochemical Society, 2013. **160**(9): p. A1341-A1347.
155. Yi, T., et al., *Structural and thermodynamic stability of $Li_4Ti_5O_{12}$ anode material for lithium-ion battery.* Journal of Power Sources, 2013. **222**: p. 448-454.
156. Sun, X., et al., *Effects of separator on the electrochemical performance of electrical double-layer capacitor and hybrid battery-supercapacitor.* Acta Physico-Chimica Sinica, 2014. **30**(3): p. 485-491.
157. Mandake, P. and P.B. Karandikar, *Significance of separator thickness for supercapacitor.* International Journal for Research in Applied Science & Engineering Technology, 2016. **4**(2): p. 214-218.
158. Calvo, E., et al., *Optimizing the electrochemical performance of aqueous symmetric supercapacitors based on an activated carbon xerogel.* Journal of Power Sources, 2013. **241**: p. 776-782.
159. Chodankar, N.R., et al., *Flexible all-solid-state MnO_2 thin films based symmetric supercapacitors.* Electrochimica Acta, 2015. **165**: p. 338-347.
160. Bello, A., et al., *Symmetric supercapacitors based on porous 3D interconnected carbon framework.* Electrochimica Acta, 2015. **151**: p. 386-392.
161. Wang, W., et al., *Hydrous ruthenium oxide nanoparticles anchored to graphene and carbon nanotube hybrid foam for supercapacitors.* Scientific reports, 2014. **4**: p. 4452.
162. Shan, X., et al., *Bivalence Mn_5O_8 with hydroxylated interphase for high-voltage aqueous sodium-ion storage.* Nature communications, 2016. **7**.
163. Cao, J., et al., *High voltage asymmetric supercapacitor based on MnO_2 and graphene electrodes.* Journal of Electroanalytical Chemistry, 2013. **689**: p. 201-206.
164. Chen, H., et al., *In situ growth of $NiCo_2S_4$ nanotube arrays on Ni foam for supercapacitors: maximizing utilization efficiency at high mass loading to achieve ultrahigh areal pseudocapacitance.* Journal of Power Sources, 2014. **254**: p. 249-257.
165. Yang, C., et al., *All-solid-state asymmetric supercapacitor based on reduced graphene oxide/carbon nanotube and carbon fiber paper/polypyrrole electrodes.* Journal of Materials Chemistry A, 2014. **2**(5): p. 1458-1464.
166. Wang, Y.-G., Z.-D. Wang, and Y.-Y. Xia, *An asymmetric supercapacitor using RuO_2/TiO_2 nanotube composite and activated carbon electrodes.* Electrochimica Acta, 2005. **50**(28): p. 5641-5646.
167. Wang, W., et al., *A novel exfoliation strategy to significantly boost the energy storage capability of commercial carbon cloth.* Advanced Materials, 2015. **27**(23): p. 3572-3578.
168. Nagaraju, D.H., et al., *Two-dimensional heterostructures of V_2O_5 and reduced graphene oxide as electrodes for high energy density asymmetric supercapacitors.* Journal of Materials Chemistry A, 2014. **2**(40): p. 17146-17152.
169. Gu, T. and B. Wei, *High-performance all-solid-state asymmetric stretchable supercapacitors based on wrinkled MnO_2/CNT and Fe_2O_3/CNT macrofilms.* Journal of Materials Chemistry A, 2016. **4**(31): p. 12289-12295.

170. Zhu, C., et al., *All metal nitrides solid‐state asymmetric supercapacitors.* Advanced Materials, 2015. **27**(31): p. 4566-4571.
171. Jabeen, N., et al., *High‐performance 2.6 v aqueous asymmetric supercapacitors based on in situ formed $Na_{0.5}MnO_2$ nanosheet assembled nanowall arrays.* Advanced Materials, 2017.
172. Tomiyasu, H., et al., *An aqueous electrolyte of the widest potential window and its superior capability for capacitors.* Scientific Reports, 2017. **7**.
173. Li, Y., et al., *Novel dual-ion hybrid supercapacitor based on a $NiCo_2O_4$ nanowire cathode and MoO_2–C nanofilm anode.* ACS applied materials & interfaces, 2016. **8**(44): p. 30232-30238.
174. Yu, N. and L. Gao, *Electrodeposited PbO_2 thin film on Ti electrode for application in hybrid supercapacitor.* Electrochemistry communications, 2009. **11**(1): p. 220-222.
175. Naoi, K., et al., *High-rate nano-crystalline $Li_4Ti_5O_{12}$ attached on carbon nano-fibers for hybrid supercapacitors.* Journal of Power Sources, 2010. **195**(18): p. 6250-6254.
176. Kim, H., et al., *High‐performance hybrid supercapacitor based on graphene‐wrapped $Li_4Ti_5O_{12}$ and activated carbon.* ChemElectroChem, 2014. **1**(1): p. 125-130.
177. Zuo, W., et al., *Directly grown nanostructured electrodes for high volumetric energy density binder-free hybrid supercapacitors: a case study of CNTs//$Li_4Ti_5O_{12}$.* Scientific reports, 2015. **5**: p. 7780.
178. Tang, W., et al., *$LiMn_2O_4$ nanotube as cathode material of second-level charge capability for aqueous rechargeable batteries.* Nano letters, 2013. **13**(5): p. 2036-2040.
179. Wang, Y.-g. and Y.-y. Xia, *A new concept hybrid electrochemical surpercapacitor: Carbon/$LiMn_2O_4$ aqueous system.* Electrochemistry Communications, 2005. **7**(11): p. 1138-1142.
180. Zhang, W., et al., *Nitrogen‐superdoped 3d graphene networks for high‐performance supercapacitors.* Advanced Materials, 2017.
181. Zhang, Y., et al., *High-performance symmetric supercapacitor based on manganese oxyhydroxide nanosheets on carbon cloth as binder-free electrodes.* Journal of Power Sources, 2016. **311**: p. 121-129.
182. Patil, S.S., et al., *Ag:$BiVO_4$ dendritic hybrid-architecture for high energy density symmetric supercapacitors.* Journal of Materials Chemistry A, 2016. **4**(20): p. 7580-7584.
183. Peng, S., et al., *Controlled growth of $NiMoO_4$ nanosheet and nanorod arrays on various conductive substrates as advanced electrodes for asymmetric supercapacitors.* Advanced Energy Materials, 2015. **5**(2).
184. Zhang, Y., et al., *Full synergistic contribution of electrodeposited three-dimensional $NiCo_2O_4$@MnO_2 nanosheet networks electrode for asymmetric supercapacitors.* Nano Energy, 2016. **27**: p. 627-637.
185. Hercule, K.M., et al., *Interconnected nanorods–nanoflakes $Li_2Co_2(MoO_4)_3$ framework structure with enhanced electrochemical properties for supercapacitors.* Advanced Energy Materials, 2015. **5**(10).
186. Peng, H., et al., *Low-cost and high energy density asymmetric supercapacitors based on polyaniline nanotubes and MoO_3 nanobelts.* Journal of Materials Chemistry A, 2014. **2**(27): p. 10384-10388.

187. Wang, R., et al., *A hybrid supercapacitor based on flower-like Co(OH)$_2$ and urchin-like VN electrode materials.* Journal of Materials Chemistry A, 2014. **2**(32): p. 12724-12732.
188. *Bragg's law*. 30 August 2017; Available from: https://en.wikipedia.org/wiki/Bragg%27s_law.
189. Huebschen, G., et al., *Materials characterization using Nondestructive Evaluation (NDE) methods*. 2016: Woodhead Publishing.
190. Lyman, C.E., et al., *Scanning electron microscopy, X-ray microanalysis, and analytical electron microscopy: a laboratory workbook*. 2012: Springer Science & Business Media.
191. Vernon-Parry, K., *Scanning electron microscopy: an introduction.* III-Vs Review, 2000. **13**(4): p. 40-44.
192. Khouchaf, L., *Scanning electron microscopy*. 2012: InTech.
193. Reimer, L., *Scanning electron microscopy: physics of image formation and microanalysis*. Vol. 45. 2013: Springer.
194. Goldstein, J., et al., *Scanning electron microscopy and X-ray microanalysis: a text for biologists, materials scientists, and geologists*. 2012: Springer Science & Business Media.
195. *Scanning electron microscope*. 30 August 2017; Available from: https://en.wikipedia.org/wiki/Scanning_electron_microscope.
196. Thomas, S., et al., *Microscopy methods in nanomaterials characterization*. 2017: Elsevier.
197. Vernon-Parry, K. and A. Wright, *TEM: an introduction part 2.* III-Vs Review, 2001. **14**(1): p. 48-51.
198. Reimer, L., *Transmission electron microscopy: physics of image formation and microanalysis*. Vol. 36. 2013: Springer.
199. Smith, D.J., *Characterization of nanomaterials using transmission electron microscopy.* 2015.
200. Fahlman, B.D., *Materials chemistry*. 2011: Springer.
201. Wendlandt, W.W., *Thermal methods of analysis*. 1974: Wiley-Interscience. New York.
202. Kaufmann, E.N., *Characterization of materials*. 2003: Wiley-Interscience.
203. Coats, A.W. and J.P. Redfern, *Thermogravimetric analysis. A review.* Analyst, 1963. **88**(1053): p. 906-924.
204. Sommer, L., *Analytical absorption spectrophotometry in the visible and ultraviolet: the principles*. Vol. 8. 2012: Elsevier.
205. Larason, T.C., et al., *Spectroradiometric detector measurements*. 1998: US Department of Commerce, National Institute of Standards and Technology.
206. Reusch, W. *Visible and ultraviolet spectroscopy*. 2013 30 August 2017; Available from: https://www2.chemistry.msu.edu/faculty/reusch/virttxtjml/spectrpy/uv-vis/spectrum.htm.
207. Lewis, G.F., *Analytical chemistry: an introduction*. 1985: Macmillan.
208. Perkampus, H.-H., *UV-Vis spectroscopy and its applications*. 2013: Springer Science & Business Media.
209. Heinze, J., *Cyclic voltammetry—"electrochemical spectroscopy". New analytical methods (25).* Angewandte Chemie International Edition in English, 1984. **23**(11): p. 831-847.
210. Bard, A.J., et al., *Electrochemical methods: fundamentals and applications*. Vol. 2. 1980: wiley New York.

211. Dip, D.S. *Cyclic voltammetry*. 2013 30 August 2017; Available from: http://urrjaa.blogspot.co.uk/2013/08/cyclic-voltammetry-urrjaa-p0110-2013.html.
212. Aristov, N. and A. Habekost, *Cyclic voltammetry-A versatile electrochemical method investigating electron transfer processes.* World Journal of Chemical Education, 2015. **3**(5): p. 115-119.
213. Gosser, D.K., *Cyclic voltammetry: simulation and analysis of reaction mechanisms*. Vol. 43. 1993: VCH New York.
214. Pyun, S.-I., et al., *Electrochemistry of insertion materials for hydrogen and lithium*. 2012: Springer Science & Business Media.
215. Fan, Z., et al., *Asymmetric supercapacitors based on graphene/MnO_2 and activated carbon nanofiber electrodes with high power and energy density.* Advanced Functional Materials, 2011. **21**(12): p. 2366-2375.
216. Li, R., et al., *Carbon‐stabilized high‐capacity ferroferric oxide nanorod array for flexible solid‐state alkaline battery–supercapacitor hybrid device with high environmental suitability.* Advanced Functional Materials, 2015. **25**(33): p. 5384-5394.
217. Rajkumar, M., et al., *Advanced materials for aqueous supercapacitors in the asymmetric design.* Progress in Natural Science: Materials International, 2015. **25**(6): p. 527-544.
218. Cheng, G., et al., *Ultrathin mesoporous NiO nanosheet-anchored 3D nickel foam as an advanced electrode for supercapacitors.* Journal of Materials Chemistry A, 2015. **3**(33): p. 17469-17478.
219. Dong, C., et al., *3D binder-free Cu_2O@Cu nanoneedle arrays for high-performance asymmetric supercapacitors.* Journal of Materials Chemistry A, 2014. **2**(43): p. 18229-18235.
220. Wang, Y., Z. Ye, and Y. Ying, *New trends in impedimetric biosensors for the detection of foodborne pathogenic bacteria.* Sensors, 2012. **12**(3): p. 3449-3471.
221. Barsoukov, E. and J.R. Macdonald, *Impedance spectroscopy: theory, experiment, and applications*. 2005: John Wiley & Sons.
222. Wang, H., T. Maiyalagan, and X. Wang, *Review on recent progress in nitrogen-doped graphene: synthesis, characterization, and its potential applications.* Acs Catalysis, 2012. **2**(5): p. 781-794.
223. Lu, Y.-F., et al., *Nitrogen-doped graphene sheets grown by chemical vapor deposition: synthesis and influence of nitrogen impurities on carrier transport.* ACS nano, 2013. **7**(8): p. 6522-6532.
224. Lai, L., et al., *Exploration of the active center structure of nitrogen-doped graphene-based catalysts for oxygen reduction reaction.* Energy & Environmental Science, 2012. **5**(7): p. 7936-7942.
225. Hou, S., et al., *Nitrogen-doped graphene for dye-sensitized solar cells and the role of nitrogen states in triiodide reduction.* Energy & Environmental Science, 2013. **6**(11): p. 3356-3362.
226. Gao, H., et al., *Synthesis of nitrogen-doped graphene from ployacrylonitrile.* Materials Letters, 2013. **109**: p. 182-185.
227. Yu, D., Q. Zhang, and L. Dai, *Highly efficient metal-free growth of nitrogen-doped single-walled carbon nanotubes on plasma-etched substrates for oxygen reduction.* Journal of the American Chemical Society, 2010. **132**(43): p. 15127-15129.

228. Lin, Y.-C., C.-Y. Lin, and P.-W. Chiu, *Controllable graphene N-doping with ammonia plasma.* Applied Physics Letters, 2010. **96**(13): p. 133110.
229. Li, N., et al., *Large scale synthesis of N-doped multi-layered graphene sheets by simple arc-discharge method.* Carbon, 2010. **48**(1): p. 255-259.
230. Subrahmanyam, K., et al., *Simple method of preparing graphene flakes by an arc-discharge method.* The Journal of Physical Chemistry C, 2009. **113**(11): p. 4257-4259.
231. Du, X., H.-Y. Liu, and Y.-W. Mai, *Ultrafast synthesis of multifunctional N-doped graphene foam in an ethanol flame.* ACS nano, 2015. **10**(1): p. 453-462.
232. Wei, D., et al., *Synthesis of N-doped graphene by chemical vapor deposition and its electrical properties.* Nano letters, 2009. **9**(5): p. 1752-1758.
233. Zhang, Y., et al., *Sandwich-like nitrogen-doped porous carbon/graphene nanoflakes with high-rate capacitive performance.* Nanoscale, 2016. **8**(15): p. 7889-7898.
234. Marcano, D.C., et al., *Improved synthesis of graphene oxide.* ACS Nano, 2010. **4**(8): p. 4806-4814.
235. Shu, Y., et al., *Single and competitive adsorption of Cd (II) and Pb (II) from aqueous solution by activated carbon prepared with Salix matsudana Kiodz.* Water Science and Technology, 2016. **74**(12): p. 2751-2761.
236. Qi, B., et al., *Dry plasma reduction to prepare a high performance Pd/C catalyst at atmospheric pressure for CO oxidation.* Journal of Materials Chemistry A, 2014. **2**(30): p. 11885-11890.
237. Shang, H., et al., *Preparing high surface area porous carbon from biomass by carbonization in a molten salt medium.* RSC Advances, 2015. **5**(92): p. 75728-75734.
238. Palmre, V., et al., *Electroactive polymer actuators with carbon aerogel electrodes.* Journal of Materials Chemistry, 2011. **21**(8): p. 2577-2583.
239. Ali, G.A., et al., *Electrochemical performance studies of MnO_2 nanoflowers recovered from spent battery.* Materials Research Bulletin, 2014. **60**: p. 5-9.
240. Ali, G.A., et al., *High performance supercapacitor using catalysis free porous carbon nanoparticles.* Journal of Physics D: Applied Physics, 2014. **47**(49): p. 495307.
241. Stoller, M.D. and R.S. Ruoff, *Best practice methods for determining an electrode material's performance for ultracapacitors.* Energy & Environmental Science, 2010. **3**(9): p. 1294-1301.
242. Zhang, J., et al., *A high-performance asymmetric supercapacitor fabricated with graphene-based electrodes.* Energy & Environmental Science, 2011. **4**(10): p. 4009-4015.
243. Tian, K., et al., *Membranes of carbon nanofibers with embedded MoO_3 nanoparticles showing superior cycling performance for all-solid-state flexible supercapacitors.* Materials Today Energy, 2017. **6**: p. 27-35.
244. Dai, Z., et al., *Template synthesis of shape-tailorable NiS_2 hollow prisms as high-performance supercapacitor materials.* ACS applied materials & interfaces, 2015. **7**(45): p. 25396-25401.
245. Ma, C., et al., *High-performance supercapacitor electrodes based on porous flexible carbon nanofiber paper treated by surface chemical etching.* Chemical Engineering Journal, 2014. **249**: p. 216-225.

246. Shao, J., et al., *Mechanism analysis of the capacitance contributions and ultralong cycling-stability of the isomorphous MnO_2@MnO_2 core/shell nanostructures for supercapacitors.* Journal of Materials Chemistry A, 2015. **3**(11): p. 6168-6176.
247. Zhang, C., et al., *Ion intercalation into graphitic carbon with a low surface area for high energy density supercapacitors.* Journal of The Electrochemical Society, 2014. **161**(10): p. A1486-A1494.
248. Hassan, F.M., et al., *Pyrrolic-structure enriched nitrogen doped graphene for highly efficient next generation supercapacitors.* Journal of Materials Chemistry A, 2013. **1**(8): p. 2904-2912.
249. Canty, R., et al., *Reduction expansion synthesis as strategy to control nitrogen doping level and surface area in graphene.* Materials, 2015. **8**(10): p. 7048-7058.
250. Long, C., et al., *Porous layer-stacking carbon derived from in-built template in biomass for high volumetric performance supercapacitors.* Nano Energy, 2015. **12**: p. 141-151.
251. Yan, J., et al., *Advanced asymmetric supercapacitors based on $Ni(OH)_2$/graphene and porous graphene electrodes with high energy density.* Advanced Functional Materials, 2012. **22**(12): p. 2632-2641.
252. Cherusseri, J. and K.K. Kar, *Self-standing carbon nanotube forest electrodes for flexible supercapacitors.* RSC Advances, 2015. **5**(43): p. 34335-34341.
253. Zhu, Y., et al., *Carbon-based supercapacitors produced by activation of graphene.* Science, 2011. **332**(6037): p. 1537-41.
254. Chen, S., et al., *Nanostructured morphology control for efficient supercapacitor electrodes.* Journal of Materials Chemistry A, 2013. **1**(9): p. 2941-2954.
255. Zhang, Q., et al., *A high rate 1.2 V aqueous sodium-ion battery based on all NASICON structured $NaTi_2(PO_4)_3$ and $Na_3V_2(PO_4)_3$.* Electrochimica Acta, 2016. **196**: p. 470-478.
256. Wang, N., et al., *CVD-grown polypyrrole nanofilms on highly mesoporous structure MnO_2 for high performance asymmetric supercapacitors.* Chemical Engineering Journal, 2017. **307**: p. 105-112.
257. Zhang, P., et al., *Constructing highly-efficient electron transport channels in the 3D electrode materials for high-rate supercapacitors: The case of $NiCo_2O_4$@$NiMoO_4$ hierarchical nanostructures.* Chemical Engineering Journal, 2017. **307**: p. 687-695.
258. Lin, T., et al., *Nitrogen-doped mesoporous carbon of extraordinary capacitance for electrochemical energy storage.* Science, 2015. **350**(6267): p. 1508-1513.
259. Stoller, M.D., et al., *Graphene-based ultracapacitors.* Nano letters, 2008. **8**(10): p. 3498-3502.
260. Xiang, C., et al., *A reduced graphene oxide/Co_3O_4 composite for supercapacitor electrode.* Journal of Power Sources, 2013. **226**: p. 65-70.
261. Lai, H., et al., *Mesostructured NiO/Ni composites for high-performance electrochemical energy storage.* Energy & Environmental Science, 2016. **9**(6): p. 2053-2060.
262. Lukatskaya, M.R., et al., *Cation intercalation and high volumetric capacitance of two-dimensional titanium carbide.* Science, 2013. **341**(6153): p. 1502-1505.

263. Prabaharan, S., et al., *New NASICON-type $Li_2Ni_2(MoO_4)_3$ as a positive electrode material for rechargeable lithium batteries.* Solid State Ionics, 2004. **171**(3): p. 157-165.
264. Begam, K. and S. Prabaharan, *Improved cycling performance of nano-composite $Li_2Ni_2(MoO_4)_3$ as a lithium battery cathode material.* Journal of power sources, 2006. **159**(1): p. 319-322.
265. Begam, K., et al., *New lithiated NASICON-Type $Li_2Ni_2(MoO_4)_3$ for rechargeable lithium batteries synthesis, structural, and electrochemical properties.* Electrochemical and solid-state letters, 2004. **7**(8): p. A242-A246.
266. Guo, D., et al., *$NiMoO_4$ nanowires supported on Ni foam as novel advanced electrodes for supercapacitors.* Journal of Materials Chemistry A, 2013. **1**(32): p. 9024-9027.
267. Niu, Z., et al., *Compact-designed supercapacitors using free-standing single-walled carbon nanotube films.* Energy & Environmental Science, 2011. **4**(4): p. 1440-1446.
268. Kötz, R., M. Hahn, and R. Gallay, *Temperature behavior and impedance fundamentals of supercapacitors.* Journal of Power Sources, 2006. **154**(2): p. 550-555.
269. Ike, I.S., I. Sigalas, and S. Iyuke, *Understanding performance limitation and suppression of leakage current or self-discharge in electrochemical capacitors: a review.* Physical Chemistry Chemical Physics, 2016. **18**(2): p. 661-680.
270. Moosavifard, S.E., et al., *3D ordered nanoporous $NiMoO_4$ for high-performance supercapacitor electrode materials.* RSC Advances, 2014. **4**(94): p. 52555-52561.
271. Zhang, X., Y. Zhao, and C. Xu, *Surfactant dependent self-organization of Co_3O_4 nanowires on Ni foam for high performance supercapacitors: from nanowire microspheres to nanowire paddy fields.* Nanoscale, 2014. **6**(7): p. 3638-3646.
272. Liu, M.-C., et al., *Facile synthesis of $NiMoO_4 \cdot xH_2O$ nanorods as a positive electrode material for supercapacitors.* RSC Advances, 2013. **3**(18): p. 6472-6478.
273. Kozhevnikova, N. and A. Imekhenova, *Interactions in the subsolidus region of the Na_2MoO_4-$NiMoO_4$-$Fe_2(MoO_4)_3$ system.* Russian Journal of Inorganic Chemistry, 2009. **54**(4): p. 638-643.
274. Khomenko, V., E. Raymundo-Pinero, and F. Béguin, *Optimisation of an asymmetric manganese oxide/activated carbon capacitor working at 2V in aqueous medium.* Journal of Power Sources, 2006. **153**(1): p. 183-190.
275. Xu, Y., et al., *A Facile approach to $NiCoO_2$ intimately standing on nitrogen doped graphene sheets by one-step hydrothermal synthesis for supercapacitors.* Journal of Materials Chemistry A, 2015. **3**(13): p. 7121-7131.
276. Kazemi, S.H., et al., *An advanced asymmetric supercapacitor based on a binder-free electrode fabricated from ultrathin $CoMoO_4$ nano-dandelions.* RSC Advances, 2016. **6**(75): p. 71156-71164.
277. Li, Y., et al., *Facile one-pot synthesis of a $NiMoO_4$/reduced graphene oxide composite as a pseudocapacitor with superior performance.* RSC Advances, 2016. **6**(73): p. 69627-69633.

278. Li, Y., et al., *Synthesis of $NiMoO_4$ nanosheets on graphene sheets as advanced supercapacitor electrode materials.* Materials Letters, 2016. **184**: p. 21-24.
279. Wu, Z.-S., et al., *High-energy MnO_2 nanowire/graphene and graphene asymmetric electrochemical capacitors.* ACS nano, 2010. **4**(10): p. 5835-5842.
280. Su, Y.-Z., et al., *Amorphous $Ni(OH)_2$@three-dimensional Ni core–shell nanostructures for high capacitance pseudocapacitors and asymmetric supercapacitors.* Journal of Materials Chemistry A, 2014. **2**(34): p. 13845-13853.
281. Huang, M., et al., *Facile synthesis of hierarchical Co_3O_4@MnO_2 core–shell arrays on Ni foam for asymmetric supercapacitors.* Journal of Power Sources, 2014. **252**: p. 98-106.
282. Yu, L., et al., *Formation of yolk‐shelled Ni‐Co mixed oxide nanoprisms with enhanced electrochemical performance for hybrid supercapacitors and lithium ion batteries.* Advanced Energy Materials, 2015. **5**(21).
283. Bao, L., J. Zang, and X. Li, *Flexible Zn_2SnO_4/MnO_2 core/shell nanocable−carbon microfiber hybrid composites for high-performance supercapacitor electrodes.* Nano letters, 2011. **11**(3): p. 1215-1220.
284. Cai, D., et al., *Three-dimensional Co_3O_4@$NiMoO_4$ core/shell nanowire arrays on Ni foam for electrochemical energy storage.* ACS applied materials & interfaces, 2014. **6**(7): p. 5050-5055.
285. Huang, L., et al., *Hybrid composite $Ni(OH)_2$@$NiCo_2O_4$ grown on carbon fiber paper for high-performance supercapacitors.* ACS applied materials & interfaces, 2013. **5**(21): p. 11159-11162.
286. Liu, M.-C., et al., *Design and synthesis of $CoMoO_4$–$NiMoO_4 \cdot xH_2O$ bundles with improved electrochemical properties for supercapacitors.* Journal of Materials Chemistry A, 2013. **1**(4): p. 1380-1387.
287. Xiong, X., et al., *Three-dimensional ultrathin $Ni(OH)_2$ nanosheets grown on nickel foam for high-performance supercapacitors.* Nano Energy, 2015. **11**: p. 154-161.
288. Chen, H., et al., *Nickel–cobalt layered double hydroxide nanosheets for high‐performance supercapacitor electrode materials.* Advanced Functional Materials, 2014. **24**(7): p. 934-942.
289. Yu, M., et al., *Mesoporous $NiCo_2O_4$ nanoneedles grown on 3D graphene-nickel foam for supercapacitor and methanol electro-oxidation.* Electrochimica Acta, 2015. **151**: p. 99-108.
290. Yu, X., B. Lu, and Z. Xu, *Super long‐life supercapacitors based on the construction of nanohoneycomb‐like strongly coupled $CoMoO_4$‐3D graphene hybrid electrodes.* Advanced Materials, 2014. **26**(7): p. 1044-1051.
291. Jiang, J., et al., *CNT/Ni hybrid nanostructured arrays: synthesis and application as high-performance electrode materials for pseudocapacitors.* Energy & Environmental Science, 2011. **4**(12): p. 5000-5007.
292. Dong, C., et al., *Flexible and ultralong-life cuprous oxide microsphere-nanosheets with superior pseudocapacitive properties.* RSC Advances, 2015. **5**(8): p. 6207-6214.
293. Pendashteh, A., M.F. Mousavi, and M.S. Rahmanifar, *Fabrication of anchored copper oxide nanoparticles on graphene oxide nanosheets via an*

electrostatic coprecipitation and its application as supercapacitor. Electrochimica Acta, 2013. **88**: p. 347-357.
294. Wang, K., et al., *Facile synthesis of Cu_2O/RGO/$Ni(OH)_2$ nanocomposite and its double synergistic effect on supercapacitor performance.* Electrochimica Acta, 2015. **165**: p. 314-322.
295. Shinde, S.K., et al., *Hierarchical 3D-flower-like CuO nanostructure on copper foil for supercapacitors.* RSC Advances, 2015. **5**(6): p. 4443-4447.
296. Wang, G., et al., *Preparation and supercapacitance of CuO nanosheet arrays grown on nickel foam.* Journal of Power Sources, 2011. **196**(13): p. 5756-5760.
297. Pramanik, A., S. Maiti, and S. Mahanty, *Reduced graphene oxide anchored $Cu(OH)_2$ as a high performance electrochemical supercapacitor.* Dalton Transactions, 2015. **44**(33): p. 14604-14612.
298. Jiang, H., et al., *A green and high energy density asymmetric supercapacitor based on ultrathin MnO_2 nanostructures and functional mesoporous carbon nanotube electrodes.* Nanoscale, 2012. **4**(3): p. 807-812.
299. Winter, M. and R.J. Brodd, *What are batteries, fuel cells, and supercapacitors?* 2004, ACS Publications.
300. Choi, C., et al., *Elastomeric and dynamic MnO_2/CNT core–shell structure coiled yarn supercapacitor.* Advanced Energy Materials, 2016.
301. Ye, Z., et al., *Micropore-dominant vanadium and iron Co-doped MnO_2 hybrid film electrodes for high-performance supercapacitors.* Journal of The Electrochemical Society, 2016. **163**(13): p. A2725-A2732.
302. Meng, G., et al., *Hierarchical mesoporous NiO nanoarrays with ultrahigh capacitance for aqueous hybrid supercapacitor.* Nano Energy, 2016. **30**: p. 831-839.
303. Kannan, V., et al., *Facile route to NiO nanostructured electrode grown by oblique angle deposition technique for supercapacitors.* ACS applied materials & interfaces, 2016. **8**(27): p. 17220-17225.
304. Shao, L., et al., *Low-cost and highly efficient $CoMoS_4$/$NiMoS_4$-based electrocatalysts for hydrogen evolution reactions over a wide pH range.* Electrochimica Acta, 2016. **213**: p. 236-243.
305. Zheng, X., et al., *Low-cost and high-performance $CoMoS_4$ and $NiMoS_4$ counter electrodes for dye-sensitized solar cells.* Chemical Communications, 2013. **49**(83): p. 9645-9647.
306. Dai, Y.-H., et al., *Simple synthesis of a $CoMoS_4$ based nanostructure and its application for high-performance supercapacitors.* RSC Advances, 2016. **6**(9): p. 7633-7642.
307. Lei, Y., et al., *Rapid microwave-assisted green synthesis of 3D hierarchical flower-shaped $NiCo_2O_4$ microsphere for high-performance supercapacitor.* ACS applied materials & interfaces, 2014. **6**(3): p. 1773-1780.
308. Cao, Y., et al., *$MnMoO_4{\cdot}_4H2O$ nanoplates grown on a Ni foam substrate for excellent electrochemical properties.* Journal of Materials Chemistry A, 2014. **2**(48): p. 20723-20728.
309. Zeng, Z., et al., *$NiCo_2S_4$ nanoparticles//activated balsam pear pulp for asymmetric hybrid capacitors.* CrystEngComm, 2016. **18**(13): p. 2363-2374.

310. Hercule, K.M., et al., *Synergistic effect of hierarchical nanostructured $MoO_2/Co(OH)_2$ with largely enhanced pseudocapacitor cyclability.* Nano letters, 2013. **13**(11): p. 5685-5691.
311. Liu, T., et al., *Rapid microwave-assisted synthesis of mesoporous $NiMoO_4$ nanorod/reduced graphene oxide composites for high-performance supercapacitors.* Electrochimica Acta, 2015. **180**: p. 998-1006.
312. Wang, J.-G., et al., *Rational synthesis of MnO_2/conducting polypyrrole@carbon nanofiber triaxial nano-cables for high-performance supercapacitors.* Journal of Materials Chemistry, 2012. **22**(33): p. 16943-16949.
313. Khalid, S., et al., *Microwave assisted synthesis of mesoporous $NiCo_2O_4$ nanosheets as electrode material for advanced flexible supercapacitors.* RSC Advances, 2015. **5**(42): p. 33146-33154.
314. Rakhi, R., et al., *Nanostructured cobalt sulfide-on-fiber with tunable morphology as electrodes for asymmetric hybrid supercapacitors.* Journal of Materials Chemistry A, 2014. **2**(38): p. 16190-16198.
315. Zhu, T., et al., *Arrays of ultrafine CuS nanoneedles supported on a CNT backbone for application in supercapacitors.* Journal of Materials Chemistry, 2012. **22**(16): p. 7851-7855.
316. Chen, H., et al., *Highly conductive $NiCo_2S_4$ urchin-like nanostructures for high-rate pseudocapacitors.* Nanoscale, 2013. **5**(19): p. 8879-8883.
317. Du, D., et al., *Synthesis of $NiMoS_4$ for high-performance hybrid supercapacitors.* Journal of The Electrochemical Society, 2017. **164**(12): p. A2881-A2888.
318. Xia, X., et al., *One-step synthesis of $CoMoO_4$/graphene composites with enhanced electrochemical properties for supercapacitors.* Electrochimica Acta, 2013. **99**: p. 253-261.
319. Mondal, A.K., et al., *Mesoporous $MnCo_2O_4$ with a Flake‐Like Structure as Advanced Electrode Materials for Lithium‐Ion Batteries and Supercapacitors.* Chemistry-A European Journal, 2015. **21**(4): p. 1526-1532.
320. Pendashteh, A., et al., *Highly ordered mesoporous $CuCo_2O_4$ nanowires, a promising solution for high-performance supercapacitors.* Chemistry of Materials, 2015. **27**(11): p. 3919-3926.
321. Zhu, Y., et al., *Controllable preparation of highly uniform $CuCo_2S_4$ materials as battery electrode for energy storage with enhanced electrochemical performances.* Electrochimica Acta, 2017. **249**: p. 64-71.
322. Wang, Q., et al., *$NiCo_2O_4$ nanowire arrays supported on Ni foam for high-performance flexible all-solid-state supercapacitors.* Journal of Materials Chemistry A, 2013. **1**(7): p. 2468-2473.
323. Huang, L., et al., *Nickel–cobalt hydroxide nanosheets coated on $NiCo_2O_4$ nanowires grown on carbon fiber paper for high-performance pseudocapacitors.* Nano letters, 2013. **13**(7): p. 3135-3139.
324. Xu, W., et al., *Electrodeposited NiCu bimetal on carbon paper as stable non-noble anode for efficient electrooxidation of ammonia.* Applied Catalysis B: Environmental, 2017: p. doi.org/10.1016/j.apcatb.2016.11.003.
325. Zhao, X., et al., *Electrocatalytic activity of the conductive alumina/ncn composite electrode by electro‐depositing nicu particles for methanol*

oxidation. Journal of the American Ceramic Society, 2011. **94**(4): p. 1167-1172.
326. Xu, W., et al., *Directly growing hierarchical nickel-copper hydroxide nanowires on carbon fibre cloth for efficient electrooxidation of ammonia.* Applied Catalysis B: Environmental, 2017. **218**: p. 470-479.
327. Ahn, S.H., et al., *Electrochemically fabricated NiCu alloy catalysts for hydrogen production in alkaline water electrolysis.* International Journal of Hydrogen Energy, 2013. **38**(31): p. 13493-13501.
328. Xiong, S., et al., *Mesoporous Co_3O_4 and CoO@C topotactically transformed from chrysanthemum‐like $Co(CO_3)_{0.5}(OH) \cdot 0.11H_2O$ and their lithium‐storage properties.* Advanced Functional Materials, 2012. **22**(4): p. 861-871.
329. Xiong, X., et al., *Controlled synthesis of $NiCo_2S_4$ nanostructured arrays on carbon fiber paper for high-performance pseudocapacitors.* Nano Energy, 2015. **16**: p. 71-80.
330. Zheng, X., et al., *Ultrafine nickel–copper carbonate hydroxide hierarchical nanowire networks for high-performance supercapacitor electrodes.* Chemical Engineering Journal, 2016. **290**: p. 353-360.
331. Gurav, K., et al., *Room temperature chemical synthesis of $Cu(OH)_2$ thin films for supercapacitor application.* Journal of Alloys and Compounds, 2013. **573**: p. 27-31.
332. Liu, S., et al., *Facile synthesis of microsphere copper cobalt carbonate hydroxides electrode for asymmetric supercapacitor.* Electrochimica Acta, 2016. **188**: p. 898-908.
333. He, W., et al., *Ultrathin and porous $Ni_3S_2/CoNi_2S_4$ 3D‐network structure for superhigh energy density asymmetric supercapacitors.* Advanced Energy Materials, 2017.
334. Qian, L., et al., *High specific capacitance of CuS nanotubes in redox active polysulfide electrolyte.* RSC Advances, 2013. **3**(6): p. 1703-1708.
335. Du, D., et al., *Preparation of a hybrid $Cu_2O/CuMoO_4$ nanosheet electrode for high-performance asymmetric supercapacitors.* Journal of Materials Chemistry A, 2016. **4**(45): p. 17749-17756.
336. Yang, J., et al., *Electrochemical performances investigation of NiS/rGO composite as electrode material for supercapacitors.* Nano Energy, 2014. **5**: p. 74-81.
337. Zhang, J., et al., *Solvothermal synthesis of three-dimensional hierarchical CuS microspheres from a Cu-based ionic liquid precursor for high-performance asymmetric supercapacitors.* ACS applied materials & interfaces, 2015. **7**(39): p. 21735-21744.
338. Fu, W., et al., *Nanostructured CuS networks composed of interconnected nanoparticles for asymmetric supercapacitors.* Physical Chemistry Chemical Physics, 2016. **18**(35): p. 24471-24476.